A Tale of Two Dopings

The Microwave Charge Conductivity of $YBa_2Cu_3O_{6.5}$ (underdoped) and $YBa_2Cu_3O_{6.993}$ (overdoped) in the Superconducting State

by

Richard Graydon Harris

B.Sc., McMaster University, 1997
M.Sc., The University of British Columbia,1999

A THESIS SUBMITTED IN PARTIAL FULFILMENT OF
THE REQUIREMENTS FOR THE DEGREE OF

DOCTOR OF PHILOSOPHY

in

The Faculty of Graduate Studies

(Department of Physics and Astronomy)

We accept this thesis as conforming
to the required standard

THE UNIVERSITY OF BRITISH COLUMBIA

December 12, 2003

Abstract

The microwave charge conductivity of the high temperature superconducting cuprate $YBa_2Cu_3O_{6+x}$ for currents flowing parallel to the $\widehat{ab}$ oriented $(CuO_2)^{2-}$ planes has been investigated experimentally at two particular oxygen concentrations x: *Ortho-II* ordered $YBa_2Cu_3O_{6.5}$ (underdoped, $T_c = 60\,K$) and $YBa_2Cu_3O_{6.993}$ (overdoped, $T_c = 88\,K$). Measurements were performed by several members of the University of British Columbia Superconductivity Laboratory using a nonresonant broadband ($0.3 \rightarrow 22.5\,GHz$) bolometry technique and six different microwave cavity perturbation experiments operating at discrete frequencies (1.14, 2.25, 2.99, 13.4, 22.7 and $75.4\,GHz$). The data were then analyzed within a phenomenological electronic band-structure approach. The observation of sharp spectral features at low temperatures and the successful tracking of spectral weight as it is transferred between superfluid and normal fluid both indicate that the materials studied herein are clean (relatively defect-free) *d*-wave superconductors with well defined quasiparticles. However, an anomalous amount of quasiparticle oscillator strength survives to low temperatures for both of the oxygen concentrations studied. It is demonstrated that this so called 'residual oscillator strength' cannot be explained by the presence of dilute Coulomb defects in the crystalline lattice.

Contents

List of Tables

List of Figures

Glossary of Symbols

a, b, c ..... $YBa_2Cu_3O_{6+x}$ unit cell dimensions.
$\hat{a}, \hat{b}, \hat{c}$ ..... $YBa_2Cu_3O_{6+x}$ lattice vectors.
$c^\dagger_{i\sigma}$ $(c_{i\sigma})$ ..... Electron creator (annihilator) at site i of spin σ.
$c^\dagger_{\vec{k}\sigma}$ $(c_{\vec{k}\sigma})$ ..... Electron creator (annihilator) of momentum $\vec{k}$ and spin σ.
$c^\dagger_{i\vec{k}\sigma}$ $(c_{i\vec{k}\sigma})$ ..... Electron creator (annihilator) of momentum $\vec{k}$ and spin σ in band i.
$C^\dagger_{\vec{k}}$ $(C_{\vec{k}})$ ..... 2-component Nambu spinor creator (annihilator) of momentum $\vec{k}$.
$\mathbf{C}^\dagger_{\vec{k}}$ $(\mathbf{C}^\dagger_{\vec{k}})$ ..... N-component Nambu spinor creator (annihilator) of momentum $\vec{k}$.
e ..... Electron charge.
E_C ..... A high frequency cutoff in energy integrals.
$E_{\vec{k}}$ ..... d-wave quasiparticle kinetic energy.
f ..... Microwave frequency.
f_o ..... Resonant frequency of unloaded resonator.
$\hat{G} = G_0\hat{\tau}^0 + G_1\hat{\tau}^1 + G_3\hat{\tau}^3$ ..... Momentum integrated Green function.
$\hat{G}_p$ ..... Green function integrated over momenta near a single Fermi point.
$\hat{\mathcal{G}}_o(\vec{k}, \omega)$ ..... Unperturbed d-wave quasiparticle Green function.
$\hat{\mathcal{G}}(\vec{k}, \tilde{\omega})$ ..... Renormalized d-wave quasiparticle Green function.
$\hbar$ ..... Plank's constant.
H_{rf} ..... Magnitude of applied radio (or microwave) frequency magnetic field.
$\mathcal{H}$ ..... Electron Hamiltonian.
$\mathcal{H}_{plane}$ ..... Electron Hamiltonian on an isolated $(CuO_2)^{2-}$ plane.
$\hat{\imath}, \hat{x}, \hat{y}$ ..... Unit vectors: general, $\hat{a}$-axis, $\hat{b}$-axis.
$\vec{\mathcal{J}}$ ..... Charge current density.
J_{eff} ... Effective exchange coupling between nearest neighbour spins in $t - J$ model.
k_B ..... Boltzmann's constant.
k_F ..... Magnitude of Fermi wavevector.
$\vec{k} = (k_x, k_y)$ ..... Two dimensional wavevector.
$\vec{k}_{++}, \vec{k}_{-+}, \vec{k}_{+-}, \vec{k}_{--}$ ..... Wavevectors at Fermi points in d-wave superconductor.
$K(x)$ ..... Complete elliptic integral of the first kind.
ℓ ..... Electron mean free path.
$\vec{m}$ ..... Magnetic moment.
n ..... Electron density.
n_i ..... Electron occupation at site i (Chapter 1), defect density (Chapter 5).
ne^2/m^* ..... Total electronic spectral weight.
$n_n e^2/m^*$ ..... Total normal fluid or quasiparticle oscillator strength.
$n_s e^2/m^*$ ..... Total superfluid oscillator strength.
$N(\omega)$ ..... Density of states in the superconducting state normalized to N_o.

N_o ..... Density of states at the Fermi energy in the normal state.
$\vec{q}_{1D}^{\,min}$ ..... Smallest internode wavevector for a 1-dimensional band.
$\vec{q}_{2D}^{\,min}$ ..... Smallest internode wavevector for a 2-dimensional band.
q_c^{-1} ..... Screening lengthscale for a Coulomb defect.
q_{op}^{-1} ..... Decay lengthscale for order parameter supression around a defect.
$\vec{q}_{++}, \vec{q}_{-+}, \vec{q}_{+-}, \vec{q}_{--}$ ..... Internode scattering wavevectors.
Q ..... Quality factor of a resonance.
Q_i ..... Charge on an impurity (defect) site.
Q_o ..... Quality factor of an unloaded resonator.
R_s, R_{sa}, R_{sb} ..... Surface resistance: general, $\hat{a}$-axis, $\hat{b}$-axis.
$\vec{S}_i$ ..... Quantum spin operator acting on an electron at site i.
t_{chain} ..... Hopping energy between Cu^{2+} sites on a CuO chain.
t_{cp} ..... Hopping energy between a $(CuO_2)^{2-}$ plane and a CuO chain.
t_{eff} ..... Effective hopping energy in Hubbard or $t-J$ model.
t_{fold} ..... Hopping energy modulation due to *Ortho-II* ordering.
t_{plane} ..... Hopping energy between Cu^{2+} sites on a $(CuO_2)^{2-}$ plane.
t_{pp} ..... Hopping energy between two $(CuO_2)^{2-}$ planes.
t' ..... Hopping energy between second nearest neighbour Cu^{2+} sites.
t'' ..... Hopping energy between third nearest neighbour Cu^{2+} sites.
T ..... Temperature.
T_c ..... Superconducting transition temperature.
T_K ..... Kondo transition temperature.
T_o ..... A scaling temperature.
$\hat{T}(\vec{k}, \vec{k}', \omega)$ ..... $\hat{T}$-matrix element.
U_{eff} ..... Effective on-site Coulomb potential in Hubbard model.
$\vec{v}_F$ ..... Fermi velocity.
v_F ..... Magnitude of Fermi velocity.
$\vec{v}_F^{\,chain}$ ..... Fermi velocity in a chain derived band.
$\vec{v}_F^{\,plane}$ ..... Fermi velocity in a plane derived band.
v_Δ .... Band velocity in direction perpendicular to $\vec{v}_F$ in the superconducting state.
$\hat{V}(\vec{q})$ ..... Fourier transform of a general scattering potential.
$\hat{V}_o$ ..... $\vec{q}=0$ value of Fourier transform of Coulomb scattering potential.
$\hat{V}_{OPo}$ ..... $\vec{q}=0$ value of Fourier transform of order parameter supression.
$\hat{V}_{PB}$ ..... $\vec{q}=0$ value of Fourier transform of pair breaking potential.
$V_{\vec{k},\vec{k}'}$ ..... General electron pairing potential.
$\hat{V}_o$ ..... $\vec{q}=0$ value of $\hat{V}(\vec{q})$.
x ..... Oxygen concentration in the unit formula of $YBa_2Cu_3O_{6+x}$.
x_a, x_b, x_c ..... Dimensions of superconducting sample.
$y(T)$ ..... Exponent in phenomenological conductivity model.
$Z_s \equiv R_s + iX_s$ ..... Surface impedance.
α ..... Fermi liquid correction to electronic charge.
δ ..... Hole doping per Cu^{2+} site.
δf ..... Shift in resonance frequency.
$\delta\mathcal{H}$ ..... Perturbation to a Hamiltonian.

$\delta_{i,j}$ ..... Discrete δ-function in real space.
$\delta\Delta_{\vec{q}} = \delta\Delta_o \cos\phi_{\vec{q}}$. Fourier transform of order parameter supression around a defect.
$\Delta_{\vec{k}}$ ..... Order parameter or superconducting gap function.
$\tilde{\Delta}_{\vec{k}} = \Delta_{\vec{k}} + \Sigma_1(\tilde{\omega})$ ..... Renormalized order parameter.
Δ_o ..... d-wave superconducting gap amplitude.
Δf ..... Full width at half maximum of a resonance.
$\Delta\lambda(T)$ ..... Change in magnetic penetration depth.
ΔT ..... Change in temperature.
Δ_U ..... Superconducting gap of a quasiparticle involved in Umklapp process.
Γ ..... Normal state scattering rate.
$\kappa(T)$ ..... Thermal conductivity.
$\lambda(T)$,$\lambda_a(T)$,$\lambda_b(T)$ ..... Magnetic penetration depth: general, $\hat{a}$-axis, $\hat{b}$-axis.
$\lambda_L(T)$,$\lambda_L^a(T)$,$\lambda_L^b(T)$ ..... London penetration depth: general, $\hat{a}$-axis, $\hat{b}$-axis.
$\Lambda^{-1}(T)$ ..... Scattering rate in phenomenological conductivity model.
μ_o ..... Magnetic permeability of free space.
μ_{chain} ..... Energy shift for a CuO chain band.
μ_{plane} ..... Energy shift for a $(CuO_2)^{2-}$ plane band.
ω ..... Internal frequency.
$\omega' = \omega - \Omega$ ..... Shorthand for internal minus microwave frequency.
$\tilde{\omega} = \omega - \Sigma_0(\tilde{\omega})$ ..... Renormalized internal frequency.
ω_{peak} ..... Energy of a resonant feature in the quasiparticle self-energy.
Ω ..... Applied microwave field angular frequency.
ϕ ..... Angle in $(CuO_2)^{2-}$ plane with respect to $\hat{a}$-axis.
$\sigma \equiv \sigma_1 - i\sigma_2$ ..... General reference to charge conductivity.
$\sigma_1, \sigma_{1a}, \sigma_{1b}$ ..... Real part of conductivity: general, $\hat{a}$-axis, $\hat{b}$-axis.
σ_1^{1D} ..... Contribution to σ_1 from a quasi-1-dimensional band.
σ_1^{2D} ..... Contribution to σ_1 from 2-dimensional bands.
σ_2 ..... Imaginary part of conductivity.
σ_o ..... DC conductivity.
σ_{qp} ..... Quasiparticle contribution to charge conductvity.
σ_{sf} ..... Superfluid contribution to charge conductvity.
σ_{xy} ..... A component of the charge conductivity tensor.
$\hat{\Sigma} = \Sigma_0\hat{\tau}^0 + \Sigma_1\hat{\tau}^1 + \Sigma_3\hat{\tau}^3$ ..... Quasiparticle self-energy.
τ^{-1} ..... Electron/quasiparticle scattering rate in Drude model.
$\hat{\tau}^0, \hat{\tau}^1, \hat{\tau}^2, \hat{\tau}^3$ ..... Pauli spin matrices.
$\xi_{\vec{k}}$ ..... Electron dispersion.
$\tilde{\xi}_{\vec{k}} = \xi_{\vec{k}} + \Sigma_3(\tilde{\omega})$ ..... Renormalized electron dispersion.
$\xi_{\vec{k}}^i$ ..... Electron dispersion in band i.
$\xi_{\vec{k}}^{chain}$ ..... Electron dispersion on an isolated CuO chain band.
$\xi_{\vec{k}}^{fold}$ ..... Electron dispersion of a band generated by zone folding.
$\xi_{\vec{k}}^{plane}$ ..... Electron dispersion on an isolated $(CuO_2)^{2-}$ plane band.

Acknowledgements

The original insights presented herein into the general problem of superconductivity in the cuprates would not have been possible without the materials grown and experiments performed by the many persons in the University of British Columbia Superconductivity Laboratory. In particular, Dr. Ruixing Liang is responsible for the growth of the ultrahigh purity, highly crystalline samples of $YBa_2Cu_3O_{6+x}$ that have become the foundation for many of the definitive measurements of intrinsic properties of the cuprates. Patrick Turner is the principal figure in the development and operation of the broadband bolometric apparatus which has provided so much valuable and highly detailed data. Finally, the team of researchers responsible for the implementation and operation of the microwave cavity perturbation experiments (Dr. Saeid Kamal, 1.14 *GHz*; Pinder Dosanjh, 2.25 and 2.99 *GHz*; Dr. Ahmad Hosseini, 13.4 and 22.7 *GHz*; this author, 75.4 *GHz*) deserve recognition and I thank them all for sharing their data. Dr. Doug Bonn and Dr. Walter Hardy, the co-directors of the Superconductivity Laboratory, deserve special recognition for providing a stimulating environment and allowing me to follow through on my (sometimes overambitious) plans.

This thesis is somewhat theory heavy and the following parties are entirely to blame for providing stimulating conversations and encouragement on these matters; Dr. John Berlinsky (McMaster), Dr. Bill Atkinson (Trent), Dr. Daniel Sheehy (Colorado (Boulder)), Dr. Adam Durst (Yale) and Dr. Peter Hirschfeld (Florida). Dr. George Sawatzky (UBC) provided important feedback regarding bandstructure in the cuprates for which I am very thankful. Dr. Marcel Franz (UBC) acted as my primary filter and served as an important reality check on some of my more esoteric work. Dr. Jeff Young served as filter and reality check for my entire Ph.D. committee, being the only person in that group who was not part of the cuprate superconductor conspiracy at UBC.

Finally, I would like to thank NSERC for having provided financial support over much of my career as a graduate student and my wife, Adeline Chin, for teaching me that it's all about food.

Chapter 1

New Physics and the Cuprates

Superconductivity is a macroscopic quantum phenomenon characterized by perfect charge conduction at DC and the expulsion of an applied magnetic field via the Meissner effect [1]. These properties generally arise from an effective electron-electron pairing interaction that can occur in condensed matter systems under the right circumstances and the subsequent establishment of phase coherence between electron pairs. While the mechanism of superconductivity is reasonably well understood in the elemental superconductors (Al, Pb, Sn and others) and some metallic compounds (V_3Si and MgB_2, for example), the cuprate superconductors (such as $YBa_2Cu_3O_{6+x}$ and $Bi_2Sr_2CaCu_2O_{8+x}$) have yet to yield all of their secrets. Thus the cuprates have been, and still are, the subject of an intense search for novel physics in condensed matter systems.

1.1 Doping the Mott Insulator

The principal feature that is common amongst all of the cuprate superconductors is the presence of quasi-2-dimensional $(CuO_2)^{2-}$ planes separated by layers of other oxides. These latter layers maintain overall charge neutrality of a given structure and can have an important role to play in controlling charge doping. However, the $(CuO_2)^{2-}$ layers appear to be the stage upon which all of the interesting electronic drama occurs. Within the undoped parent compounds, for example $YBa_2Cu_3O_6$, the $(CuO_2)^{2-}$ layers consist of Cu^{2+} ions situated on an approximately square lattice with intervening O^{2-} ions, as depicted in Fig. 1.1. A single unpaired electron resides in each Cu $3d_{x^2-y^2}$ orbital while the O $2p_{x,y,z}$ orbitals are filled. The large σ-type overlap between the Cu $3d_{x^2-y^2}$ and O $2p_{x,y}$ orbitals mediates electron hopping between copper sites, thus allowing for electronic motion. However, these hopping events are known to be inhibited by on-site Coulomb repulsion at the Cu sites which discourages double occupancy of the $3d_{x^2-y^2}$ orbital. Given these few details, one can write a relatively simple expression for the electronic Hamiltonian which is known as the Hubbard Model [2]:

$$\mathcal{H} = -t_{eff} \sum_{<i,j>,\sigma} (c^{\dagger}_{i\sigma} c_{j\sigma} + c^{\dagger}_{j\sigma} c_{i\sigma}) + \frac{U_{eff}}{2} \sum_{i} (n_i - 1)^2 \ldots \tag{1.1}$$

where $c^{\dagger}_{i\sigma}$ ($c_{i\sigma}$) creates (annihilates) an electron of spin σ at site i and $n_i \equiv c^{\dagger}_{i\uparrow} c_{i\uparrow} + c^{\dagger}_{i\downarrow} c_{i\downarrow}$ is the electron number operator at site i. Eq.1.1 contains terms summing over nearest neighbour Cu-Cu hopping (as denoted by $< i, j >$) and Cu on-site Coulomb repulsion at each site i proportional to the occupancy of the $3d_{x^2-y^2}$ orbital at that site.

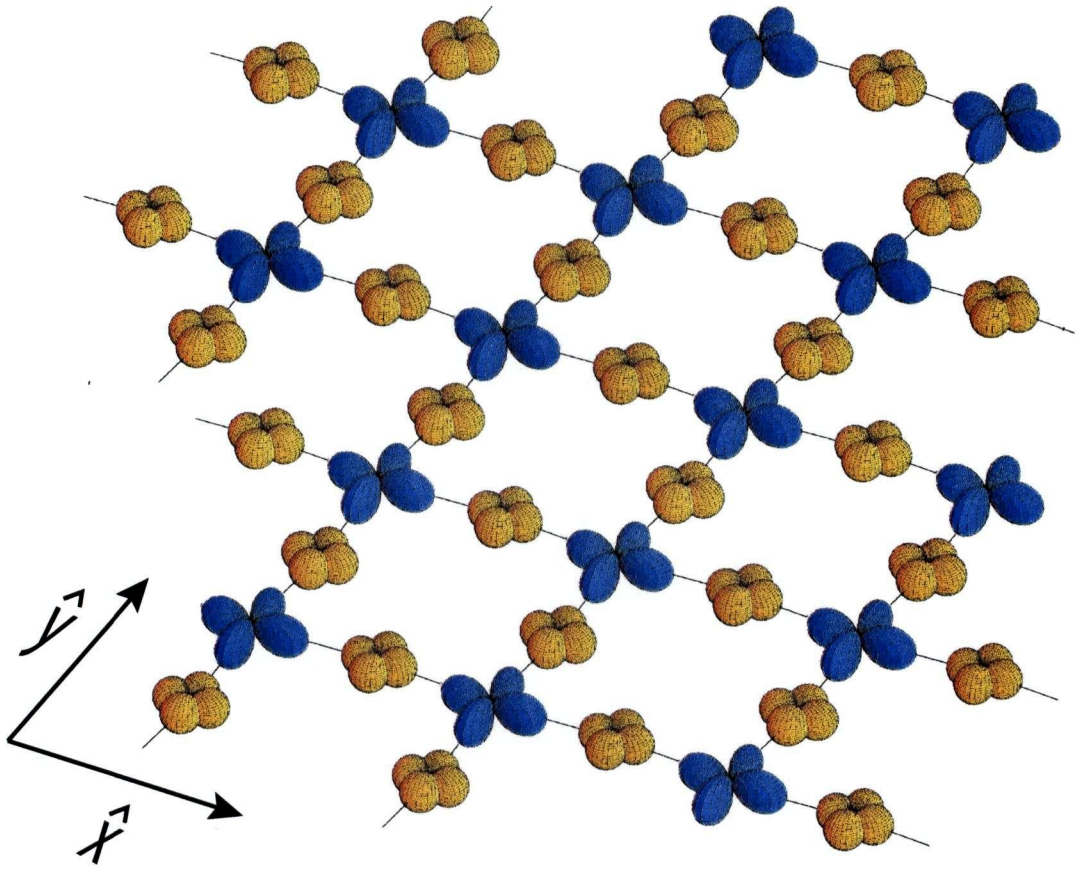

Figure 1.1: The $(CuO_2)^{2-}$ plane, the key electronic structure of the cuprate superconductors. The Cu-$3d_{x^2-y^2}$ and O-$2p_{x,y}$ orbitals are drawn schematically in blue and amber, respectively, with the $\widehat{xy}$ plane orientated as indicated. O-$2p_z$ orbitals are not shown.

The parameters t_{eff} and U_{eff} represent the effective nearest neighbour Cu-Cu hopping energy and effective Cu on-site Coulomb repulsion, respectively. This expression can contain next nearest neighbour couplings and so forth (...) which have been omitted here for the sake of simplicity. In the limit $t_{eff} \gg U_{eff}$ the physics in Eq. 1.1 will be governed by the hopping term and one can neglect the on-site Coulomb repulsion term. In this case, a $(CuO_2)^{2-}$ plane would appear to be a lattice of metal atoms with one weakly bound valence electron per site, which naturally gives rise to the metallic behaviour of a half filled band [3]. However, detailed calculations [4] and experimental evidence [5] indicate that, at least in the case of undoped $(CuO_2)^{2-}$ planes, that the cuprates satisfy the opposite limit, $t_{eff} \ll U_{eff}$. While the exact magnitudes of both t_{eff} and U_{eff} are matters of significant debate [6], the consequences for charge transport seem to be universally agreed upon:

1. The balance between on-site Coulomb repulsion and electron kinetic energy inevitably lead to localization of single electrons on Cu^{2+} sites, thus rendering the undoped $(CuO_2)^{2-}$ layer insulating.

2. Virtual hopping between Cu^{2+} sites via the O $2p_{x,y}$ orbitals leads to an effective antiferromagnetic superexchange coupling [7], thereby inducing long range ordering of the electronic spins.

Based upon the above information, it has been suggested by many that in the limit $t_{eff} \ll U_{eff}$ and close to half-filling (1 electron per Cu^{2+} site) that the low energy physics of Eq.1.1 can be expressed in terms of the t-J Hamiltonian [2]:

$$\mathcal{H} \approx -t_{eff} \sum_{<i,j>,\sigma} (c^{\dagger}_{i\sigma} c_{j\sigma} + c^{\dagger}_{j\sigma} c_{i\sigma}) + J_{eff} \sum_{<i,j>} (\vec{S}_i \cdot \vec{S}_j - \frac{1}{4} n_i n_j) \qquad (1.2)$$

where t_{eff} is the effective hopping introduced in Eq. 1.1 and $J_{eff} \approx 4t^2_{eff}/U_{eff} > 0$ is the effective nearest neighbour antiferromagnetic exchange energy between spins $\vec{S}_i$ and $\vec{S}_j$ at sites i and j, respectively. In deriving Eq.1.2 from Eq. 1.1 one casts away all wavefunctions involving doubly occupied sites ($n_i = 2$) for they possess an energy $\sim U_{eff}$ greater than the presumed true groundstate energy. Therefore, in the case of an undoped $(CuO_2)^{2-}$ plane the first term in Eq.1.2 can only give rise to virtual transitions (second order processes of the form $c^{\dagger}_{i\sigma} c_{j\sigma} c^{\dagger}_{j\sigma} c_{i\sigma}$) and $n_i n_j = 1$ (constant) for *all* pairs of nearest neighbours.

Given that the parent compounds of the cuprate superconductors are all antiferromagnetic insulators due to strong correlations between both electronic charge and spin, it is not obvious how the above story should change upon removing a small fraction ($\delta < 5\%$) of the solitary electrons from Cu^{2+} sites, thus producing holes. While this ought to allow charge to hop unhindered to adjacent unoccupied sites (due to the absence of on-site Coulomb repulsion), an intrepid electron must contend with nearest neighbour antiferromagnetic exchange correlations (see Fig. 1.2). The tradeoff between kinetic energy of the new found charge degrees of freedom and the potential energy cost due to restrictions on the spin degrees of freedom ultimately leads to complex behaviour that has yet to be described in a satisfactory manner.

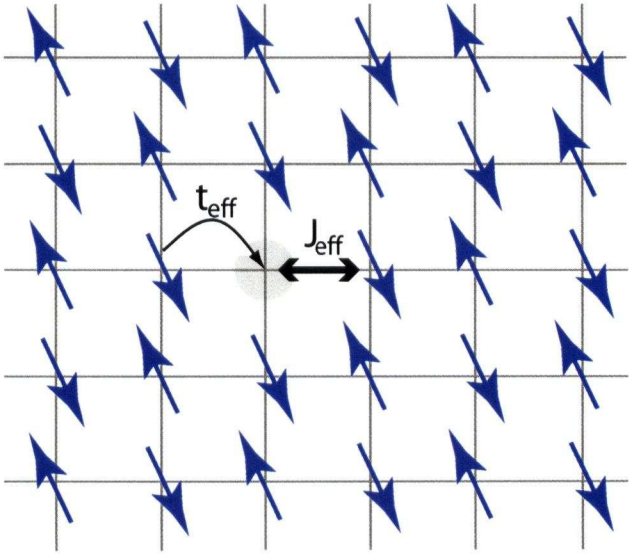

Figure 1.2: The motion of a single hole doped into an antiferromagnetic square lattice. Hopping of an electron (kinetic energy $-t_{eff}$) into the hole allows charge to move in the plane, but its motion is frustrated by the system's attempt to maintain long range antiferromagnetic order (potential energy J_{eff}).

Despite the complexity at low hole doping ($\delta < 5\%$), it appears that the $(CuO_2)^{2-}$ planes behave in a much more comprehensible manner at higher doping ($5\% < \delta < 30\%$), at least from the humble perspective of an experimentalist, for they become superconducting. This is a very significant shift in paradigms: At low doping the physics is governed by strong correlations that put the spin and charge degrees of freedom at odds, which suggests that whole electrons (comprised of spin $\hbar/2$ and charge e) are not the natural low energy objects in the system. On the other hand, superconductivity is generally recognized as a Fermi liquid state in which electronic correlations are sufficiently weak that they only result in perturbative renormalizations of single particle properties [8]. Therefore, something substantial occurs as a function of δ between the antiferromagnetic insulator at $\delta \to 0$ and the first whispers of superconductivity near $\delta \sim 5\%$.

1.2 Brief Survey of the Cuprate Phase Diagram

In the quest for definitive answers to the cuprate puzzle, many have presented arguments based upon trends in the doping-temperature (δ-T) phase diagram. There is an astounding variety of such diagrams available in the literature; however from an experimentalist's perspective they can, for the most part, be summarized as shown below in Fig. 1.3:

Here AFI and SC denote antiferromagnetic insulator and superconductor, respectively. With increasing temperatures one encounters second order phase transitions

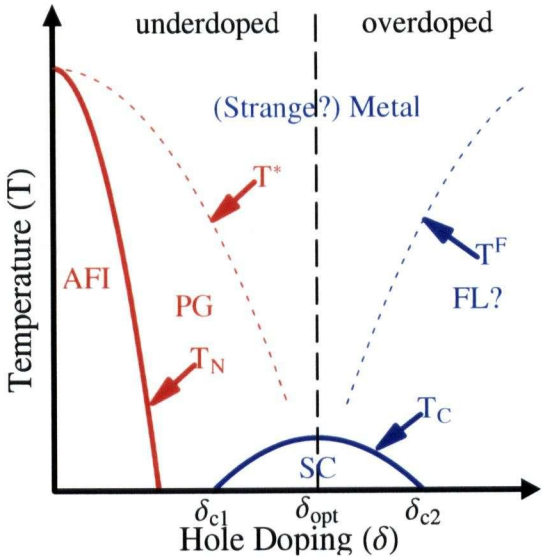

Figure 1.3: A experimentalist's schematic view of the cuprate δ-T phase diagram. Antiferromagnetic insulator (AFI) and superconductivity (SC) are distinct groundstates with transitions at T_N and T_C, respectively. The pseudogap phase (PG) has either a transition or a dynamical crossover at T^*. A possible Fermi Liquid (FL) state exists at high doping with a crossover at temperature T^F to an unconventional or strange metal state.

from either state at the Néel transition T_N and the superconducting transition T_C. To get a sense of scale, $T_N^{max} \sim 500\,K$ and $T_C^{max} \sim 100\,K$ for a typical cuprate. In addition, there is a so called pseudogap phase (PG) observable for $\delta < 0.2$ at intermediate temperatures, as evidenced by the partial development of a gap in many spectral properties (such as the depression of the optical conductivity at low frequency) below a temperature T^* [9]. Note that at $\delta = 0$ these systems can be described as a conventional insulating Heisenberg antiferromagnets with a Néel transition and no signature of the pseudogap. It is not known whether T^* is a true phase transition or is a crossover temperature whose magnitude may very well depend upon the nature of one's experimental probe [5]. Furthermore, it is a matter of speculation whether T^* has any relation to T_C. This last point has proven to be a key issue in the study of the cuprates and will be elaborated upon in due course. Finally, it should be noted that the region near $T = 0$ between the loss of antiferromagnetism and the onset of superconductivity at δ_{c1} is terra incognita. This region of the cuprate phase diagram has proven difficult to access experimentally and observations have suggested everything from fluctuating antiferromagnetism [10], fluctuating superconducting correlations to fluctuating charge stripes. It is not clear whether this region is part of the pseudogap phase or some (as of yet) unidentified electronic state.

At intermediate and high temperatures one encounters a phase that has been labelled as (Strange?) Metal, with the term '(Strange?)' indicating that while some

properties appear metallic-like they are nonetheless difficult to reconcile with conventional Fermi Liquid theory. Perhaps most ubiquitous is the anomalous linearity of the in-plane resistivity, $\rho_{ab}(T) \propto T$, over a broad temperature window, typically extending from the superconducting transition T_c to temperatures well beyond $300\,K$ in optimally doped $YBa_2Cu_3O_{6+x}$ [11]. A second peculiar observation is that the Hall angle varies quadratically with temperature over a comparable temperature range, $\theta_H(T) \propto T^2$ [12]. However, neither of these observations alone truly qualify the suggestion that this phase is 'Strange'. Rather, it is the recognition of an apparent disconnect of the transport scattering rate $1/\tau_{tr} \propto T$ from the Hall relaxation rate $1/\tau_H \propto T^2$ that clearly indicates that the fundamental charge carrying objects in these materials are not electrons in the conventional sense [13]. However, the 'Strangeness' does seem to subside at high doping δ where the cuprates show more conventional Fermi Liquid-like (FL) behaviour. The presumed crossover temperature from the FL to the (Strange?) Metal state has been denoted as T^F in Fig. 1.3.

Figure 1.3 also displays labels for two commonly used terms in the study of the cuprates: overdoped and underdoped. The nomenclature is directly related to the variation of the superconducting transition temperature T_c as a function of doping δ. Typically, T_c is maximized at $\delta_o \sim 0.2$ and falls off to zero at $\delta_o \pm 0.1$.

To progress beyond the few details suggested in Fig. 1.3, one must ascribe microscopic physics to each of the experimentally observed phases. In particular, identification of the pseudogap phase has proven to be the distinguishing feature among many theoretical approaches to the cuprate phase diagram [14]. While the gamut of cuprate theories is too numerous to explore in great detail herein, it can be argued that three general approaches to the δ-T phase diagram deserve particular attention.

1.2.1 Speculation I - The Role of Quantum Criticality

One general scenario that can be encountered in the literature assumes that T^* is a bone fide phase transition that is reduced to zero temperature at some critical doping, δ_{QCP}, known as a quantum critical point (QCP). Furthermore, a second phase transition, which this author has denoted as T^F, is frequently invoked as well and it covers the doping $\delta > \delta_{QCP}$. Within this picture the entire cuprate phase diagram can be described as thermal fluctuations away from the physics at $T = 0$, which is inherently quantum in nature. Regions to the left and right of δ_{QCP} are distinct quantum groundstates with the phase transition at δ_{QCP} driven purely by quantum critical fluctuations. Depending upon the strength of these fluctuations, the system may very well choose an alternate ground state in the vicinity of δ_{QCP}; the hope here being d-wave superconductivity. These features are in agreement with the picture of Emery and Kivelson in which T^* is attributed to the onset of microscopic phase separation into fluctuating quasi-1-dimensional Luttinger liquid 'stripes' separating antiferromagnetic domains [15].

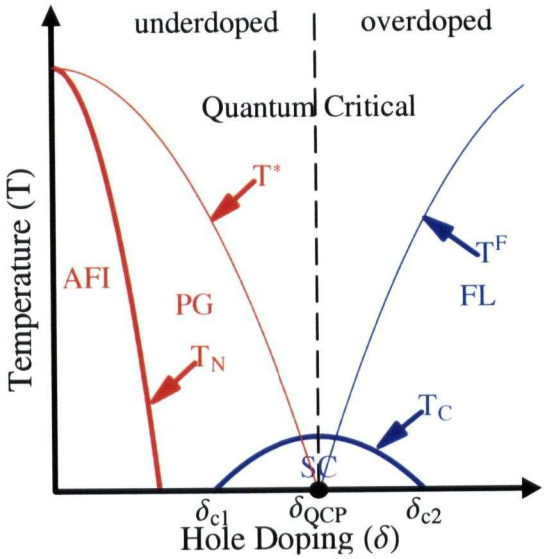

Figure 1.4: The plausible role of quantum criticality in the cuprate δ-T phase diagram. T^* is regarded as a true phase transition which is terminated at a critical doping δ_{QCP}. Superconductivity is supported only in the vicinity of δ_{QCP}.

Independent of these theoretical pictures, phase diagrams suggestive of superconductivity existing in the vicinity of a QCP have been experimentally determined for a number of heavy fermion systems [16]. Though there may be significant leaps between the physics of the cuprates and the heavy fermions, a phase diagram akin to that in Fig. 1.4 cannot be ruled out by experimental observations at this time.

1.2.2 Speculation II: Slave Bosons and Their Kin

A particularly intriguing approach to solving the cuprate conundrum invokes the concept of spin-charge separation. As mentioned previously, the spin and charge degrees of freedom appear to be at odds in the doped antiferromagnetic insulator, therefore it may be salient to redefine the natural excitations of the doped $(CuO_2)^{2-}$ plane as a (charge e, spin 0) boson (creation operator denoted as $b_i^\dagger$) and a (charge 0, spin 1/2) fermion (creation operator denoted as $\psi_{\alpha i}^\dagger$). Together these two objects form an electron $c_{\alpha i}^\dagger$:

$$c_{\alpha i}^\dagger \equiv b_i \psi_{\alpha i}^\dagger \tag{1.3}$$

One then attempts to diagonalize the effective low energy Hamiltonian Eq. 1.2 in terms of these so called holons and spinons using Eq. 1.3. While this approach can lead to exact results in one dimension [17], the case for spin-charge separation in two dimensions has not been proven. Nonetheless, this approach has a venerable history and significant gains have been made in recent years [18–20].

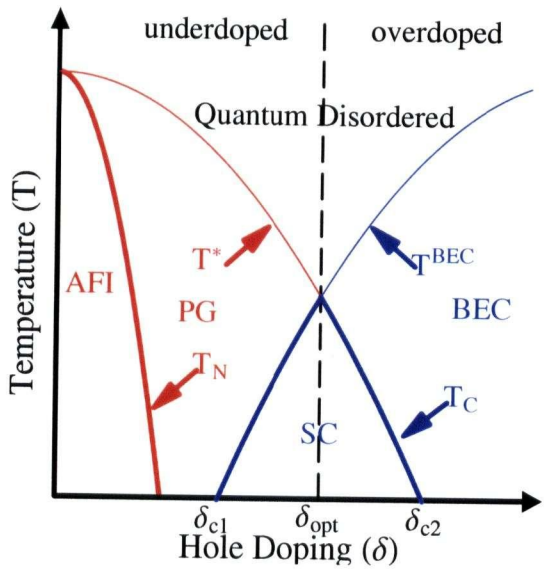

Figure 1.5: Spin-charge separation and the δ-T phase diagram. Superconductivity depends upon the condensation of the spin degrees of freedom (PG phase) being concomitant with condensation of the charge degrees of freedom (BEC).

A caricature of a typical slave-boson phase diagram is shown in Fig. 1.5. While T^* once again denotes a phase transition, the key difference between Fig. 1.4 and Fig. 1.5 is the relation between T^* and T_c. In the latter case the superconducting phase is entirely enveloped by T^*. Typically T^* and T^{BEC} are associated with the fermionic and bosonic degrees of freedom, respectively. For example, in the $SU(2)$ picture of Lee [19], the pseudogap is attributed to long range ordering of the staggered flux phase in which singlet pairing between spinons is established along each Cu^{2+}-Cu^{2+} bond. On the other hand, T^{BEC} represents Bose-Einstein condensation (BEC) of two species of chargons (completely vacant and doubly occupied Cu^{2+} sites). The union of the two condensates is then conjectured to produce a Fermi liquid condensate (superconductivity). While the connection between the staggered flux phase and d-wave superconductivity may seem tenuous, Lee *et al.* argue that the wavefunctions of the two states have considerable overlap and therefore have comparable groundstate energies [21]. In contrast to the QCP picture in which superconductivity exists near a phase transition between two distinct groundstates, slave boson pictures suggest that superconductivity exists in the same region of the phase diagram as a single alternate groundstate. However, the alternate groundstate is presumed to have a slightly higher energy for $\delta_{c1} < \delta < \delta_{c2}$ and yields to d-wave superconductivity.

1.2.3 Speculation III: Superconductivity as a Sovereign State

The theoretical pictures discussed thus far share a common philosophy in that they are primarily designed to explain the δ-T phase diagram at low doping and then consider the d-wave superconducting state almost as an afterthought. Indeed, there are many theorists who wish that superconductivity could be suppressed in experiments so as to reveal the 'true'groundstate at higher doping. However, the experimental evidence obtained thus far suggests that the superconducting state in the cuprates is very robust and its low temperature properties are similar to those of a Fermi liquid. Therefore, a reasonable approach to studying the cuprate phase diagram would be to take the d-wave superconducting state as the true groundstate and then describe nearby regions of the phase diagram perturbatively. There is then no need to invoke a phase transition at T^* - rather it is viewed as a crossover.

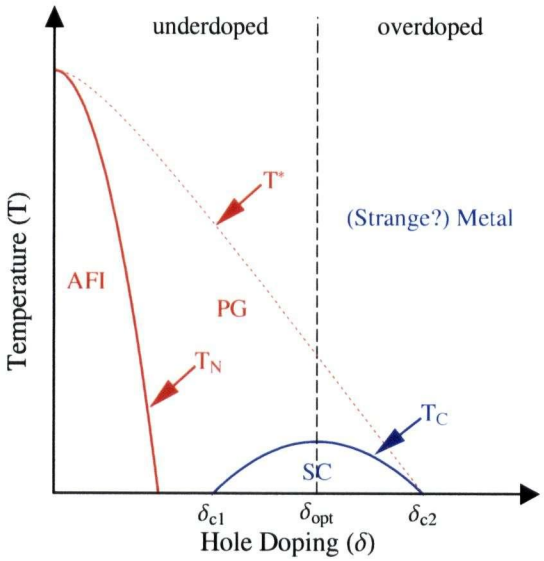

Figure 1.6: Perturbatively describing the cuprate δ-T phase diagram around the superconducting state. The PG phase is viewed as a disordered superconductor which has nonzero superfluid density but lacks long range correlations.

This approach is presently being championed by the QED-3 theory of Franz and Tésanoviç [22] and others [23]. Within this theory the transition at T_c is governed by disordering of the 2-dimensional superfluid phase via thermally excited vortex-antivortex pairs. The pseudogap phase then has finite superfluid density but lacks long range phase coherence. As such, this latter phase is not a new electronic state of matter. Interestingly, Herbut *et al.* claim that one obtains long wavelength spin density waves at low doping, which can be interpreted as antiferromagnetism [23]. However, QED-3 does not contain an explanation why T_c is reduced to zero at higher

doping δ_{c2}, nor does it explain how Cooper pairing is actually mediated. Nonetheless, this theory has been singled out here because it represents a very different philosophy which states that the physics of the cuprates can at least be described using standard many body techniques. The key to understanding the cuprates is then to be found in the details of the superconducting state, as opposed to the QCP and slave boson pictures that stress the importance of alternate electronic states of matter that reside in the same region of the $\delta - T$ phase diagram as superconductivity.

1.3 Connecting to Experiments in the Superconducting State

Given the variety of theoretical approaches to studying the cuprate phase diagram, there follows an equally numerous pantheon of predictions concerning the low temperature behaviour within the superconducting state. While all of the models discussed herein recognize that the observed *d*-wave superconducting state must behave similar to a Fermi liquid condensate, both scenarios I and II (Figs. 1.4 and 1.5) suggest that superconductivity has some built-in frailty in that the system would rather become an alternate electronic state of matter if provoked. Therefore, if the superconductivity were to be supressed, then the alternate groundstate(s) of the system must produce some observable consequences. This is very much the philosophy behind experiments performed upon cuprate superconductors in high magnetic fields (exceeding H_{c1}) for the superfluid density is driven to zero at the centre of a magnetic vortex. Within the vortex core it is anticipated that superconductivity gives way to the 'normal' state [1] - whatever it may be.

Similarly, one can argue that the details of how thermal excitations out of the *d*-wave superconducting condensate (quasiparticles) interact with crystalline defects ought to show some signature of the underlying groundstate since these are localized sites where the mean field behaviour (superconductivity) is disrupted. While defects such as impurities, atomic disorder, twinning and so forth are generally viewed as undesirable in research quality materials, the reader is reminded that defects control many of the experimental observables in groundbreaking experiments such as Fourier Transform Scanning Tunnelling Spectroscopy (FT-STS) [24]. Furthermore, crystalline defects ultimately dominate the low temperature limits of basic physical properties such as thermal conductivity [25] and charge conductivity [26], and their effects are unavoidable at some level.

1.4 Scope of Thesis

Given the wealth of information obtained recently on the real space electronic density near defects in a *d*-wave superconductor [24], it should now be possible to ask very detailed questions about how defects interact with the surrounding electronic system. This thesis is an attempt to address this very issue. It will be assumed that the superconducting state of the cuprates is a well defined Fermi liquid state and the

consequences of including elastic scattering of quasiparticles from static defects will be investigated. It will then be possible to answer the following key question: are there any significant inconsistencies between the Fermi liquid theory and experimental microwave (charge) conductivity data?

The first order of business will be to introduce the cuprate of choice for this study, $YBa_2Cu_3O_{6+x}$. Next, since the author will be playing the role of Devil's advocate (by assuming *a priori* that the Fermi liquid picture is entirely correct), it will be necessary to review some basic electronic band structure calculations as pertaining to $YBa_2Cu_3O_{6+x}$. The qualitative arguments developed therein will then be applied to experimental data on $YBa_2Cu_3O_{6.5}$ ($T_c = 56\,K$, underdoped) and $YBa_2Cu_3O_{6.993}$ ($T_c = 89\,K$, overdoped) to identify important features, such as the contribution to charge conduction from the $(CuO_2)^{2-}$ planes. The thesis then culminates in the calculation of the microwave conductivity at low temperatures using realistic model parameters suited to describe $YBa_2Cu_3O_{6.5}$ and $YBa_2Cu_3O_{6.993}$. The effects of including defects on the $(CuO_2)^{2-}$ planes are included via self-consistent renormalizations of the *d*-wave quasiparticle propagators. Results from scanning tunnelling microscopy (STM) experiments on cuprate superconductors are reviewed and details concerning cation substitution at Cu^{2+} sites in the $(CuO_2)^{2-}$ plane discussed. It is ultimately shown that the Fermi liquid picture does work remarkably well, however the defect required to successfully model the low temperature quasiparticle conductivity remains elusive. It is suggested that the novel physics that may arise from the breakdown of superconductivity near nonmagnetic defects in the $(CuO_2)^{2-}$ planes could provide the missing details.

Chapter 2

The Electronic Structure of $YBa_2Cu_3O_{6+x}$

2.1 Introducing $YBa_2Cu_3O_{6+x}$

There is an astounding variety of cuprate superconductors [27] and each seems to hold its particular advantages for different experimental probes. For example, the lanthanum compound $La_xSr_{1-x}CuO_4$ has often been the choice for neutron scattering [28] due to the availability of large ($> 1\,cm^2$) samples. The bismuth compounds such as $Bi_2Sr_2CaCu_2O_{8+x}$ are the choice for surface sensitive probes such as STM [24, 29] and ARPES [30] since they cleave easily parallel to the $(CuO_2)^{2-}$ planes and there are no surface states at the cleavage plane. In the case of microwave spectroscopy [31] the choice of materials is driven by the need for electronic homogeneity. Furthermore, the microwave techniques presented herein are most readily applied to materials whose electrical properties are not too anisotropic. $YBa_2Cu_3O_{6+x}$ has proven to be the best option thus far since it is known to be robust against cation substitution during crystal growth and there are stoichiometric dopant oxygen concentrations ($YBa_2Cu_3O_7$ and $Y_2Ba_4Cu_6O_{13}$) which can be coerced into ordered phases [32, 33].

The unit cell of fully oxygenated $YBa_2Cu_3O_7$ is shown in Fig.2.1. Note that this material has two $(CuO_2)^{2-}$ $\hat{ab}$-oriented planes separated by the Y^{3+} ion. Furthermore, there is a single layer of $\hat{b}$-oriented CuO chains per unit cell. Copper atoms in the latter layer are coordinated directly above the in-plane Cu^{2+} sites and they are bonded to a common oxygen atom in the $\hat{ab}$-oriented BaO layer. This last point is critical in any discussion of doping the $(CuO_2)^{2-}$ planes.

2.2 Hole Doping in $YBa_2Cu_3O_{6+x}$

A simple counting of formal valencies in $YBa_2Cu_3O_7$ points to an immediate problem - if one assumes that the ionized states are Y^{3+}, Ba^{2+}, Cu^{2+} and O^{2-}, then the unit cell depicted in Fig. 2.1 would appear to be charged. However, the system avoids this problem by generating mobile holes (electron vacancies) on Cu^{2+} sites; in the case of $YBa_2Cu_3O_7$ this produces a mean ionization state of $Cu^{(7/3)+}$. The additional $+1/3$ charge doping per copper atom is divided between both the CuO chains and $(CuO_2)^{2-}$ planes, thus rendering both of these components electrically conductive.

Away from full oxygenation ($0 < x < 1$) it is known that oxygen vacancies are found on the CuO chain layer, thus resulting in segments of CuO chain of finite length being terminated with copper atoms in the Cu^{1+} ionization state. By this means the

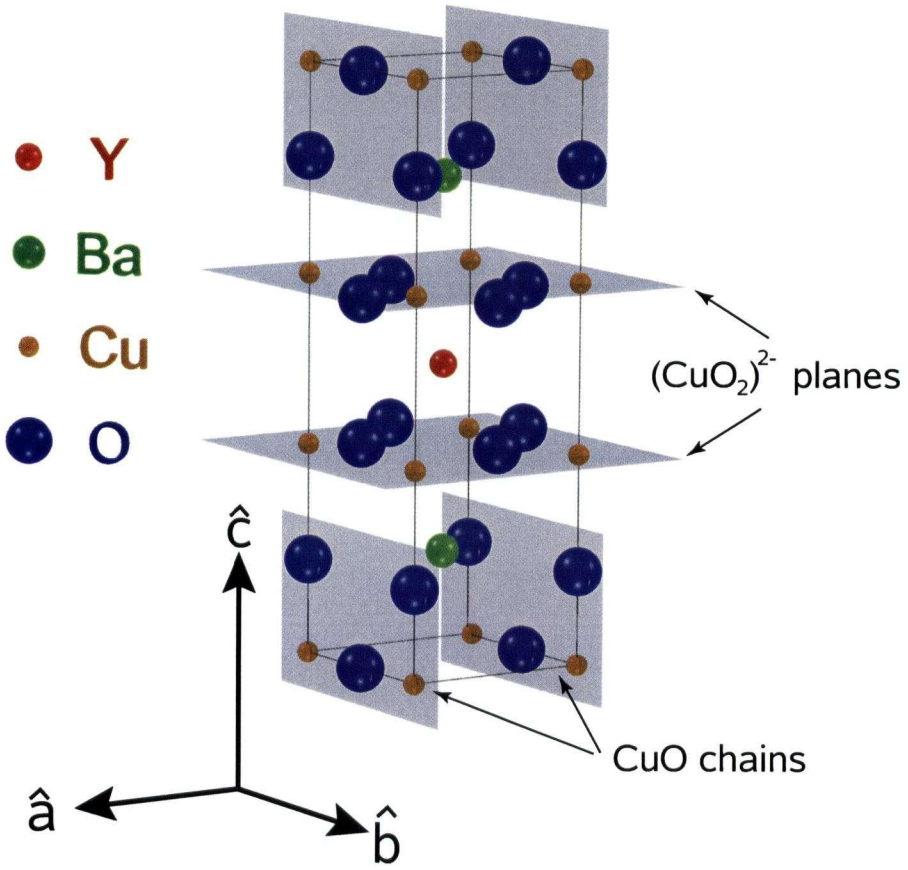

Figure 2.1: The unit cell of fully oxygenated $YBa_2Cu_3O_7$. Unit lattice vectors $(\hat{a}, \hat{b}, \hat{c})$ are oriented as indicated with dimensions $(a, b, c) = (3.8227, 3.8872, 11.68)$ Å. Image provided by D. Peets [34]

additional charge doping per Cu is eventually reduced to zero in the undoped parent compound $YBa_2Cu_3O_6$ ($x = 0$). Thus $YBa_2Cu_3O_{6+x}$ can be hole doped over a broad range *without introducing electronic disorder directly into the* $(CuO_2)^{2-}$ *planes.* However, the presence of the conductive $\hat{b}$-oriented CuO chains does complicate matters to some degree, for one cannot assume a monotonic correspondence between oxygen content x and hole doping per unit Cu on the planes δ. This has been known for quite some time, but was spectacularly demonstrated in recent experiments by Hosseini *et al.* in which T_c of a sample of $YBa_2Cu_3O_{6.3}$ evolved from 0 to approximately $20\,K$ as a function of sample annealing time [35]. These measurements were made by first randomizing the positions of chain oxygen such that there were very few segments of contiguous CuO chains. As the sample annealed, mobile oxygen atoms eventually self organized into longer chain segments that were able to mediate charge doping on the $(CuO_2)^{2-}$ planes. Figure 2.2 summarizes the important details of charge doping in $YBa_2Cu_3O_{6+x}$.

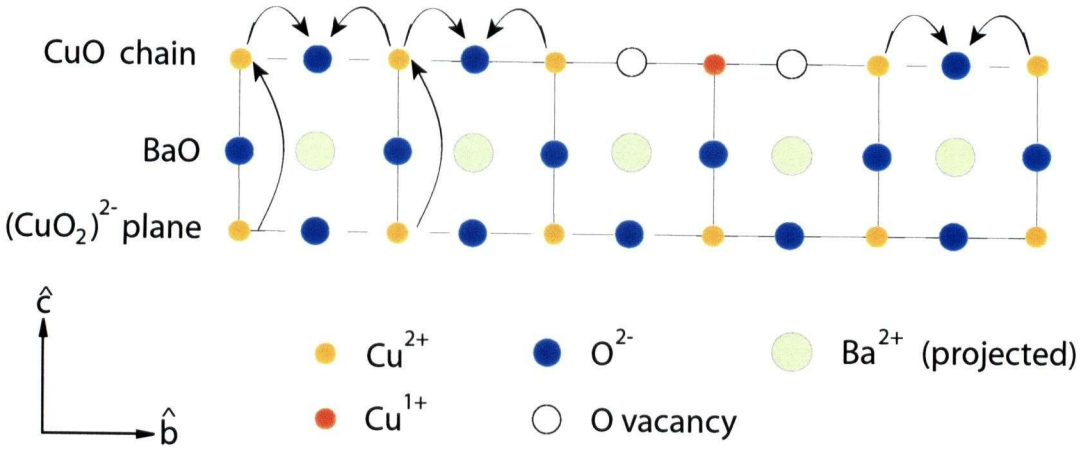

Figure 2.2: Hole doping mechanism in $YBa_2Cu_3O_{6+x}$. A cross section of a single $(CuO_2)^{2-}$ plane, BaO layer and CuO chain are shown. Contiguous chain segments (top left) require the extraction of excess negative charge from nearby Cu sites to doubly ionize every oxygen atom. An isolated oxygen in the chain layer (top right) is able to remove one electron from each of its neighbouring Cu atoms and has no need to dope the plane. Chain Cu with no neighbouring O are singly ionized.

2.3 Oxygen Ordering in $YBa_2Cu_3O_{6+x}$

While oxygenation of $YBa_2Cu_3O_{6+x}$ is a 'clean' mechanism for doping the $(CuO_2)^{2-}$ planes, it is inherently inhomogeneous. As depicted in Fig. 2.2, it is conceivable that there will be a higher probability of finding a dopant hole directly under contiguous CuO chain segments than elsewhere. Therefore, it is conceivable that mobile holes in plane layers may view chain ends as scattering potentials. One way to minimize this concern would be to order the oxygen vacancies in the chain layer into a periodic structure - this would at least make the hole doping of the planes uniform on a mesoscopic scale. Data from samples of two such ordered phases will be presented in this thesis: overdoped *Ortho-I* ordered (all chains full) $YBa_2Cu_3O_{6.993}$ and underdoped Ortho-II ordered (alternating chains full) $YBa_2Cu_3O_{6.5}$. Both of these compositions are (at least approximately) stoichiometric and can be coerced into a periodic array. Figure 2.3 depicts the above mentioned ordered oxygen phases in the CuO layer.

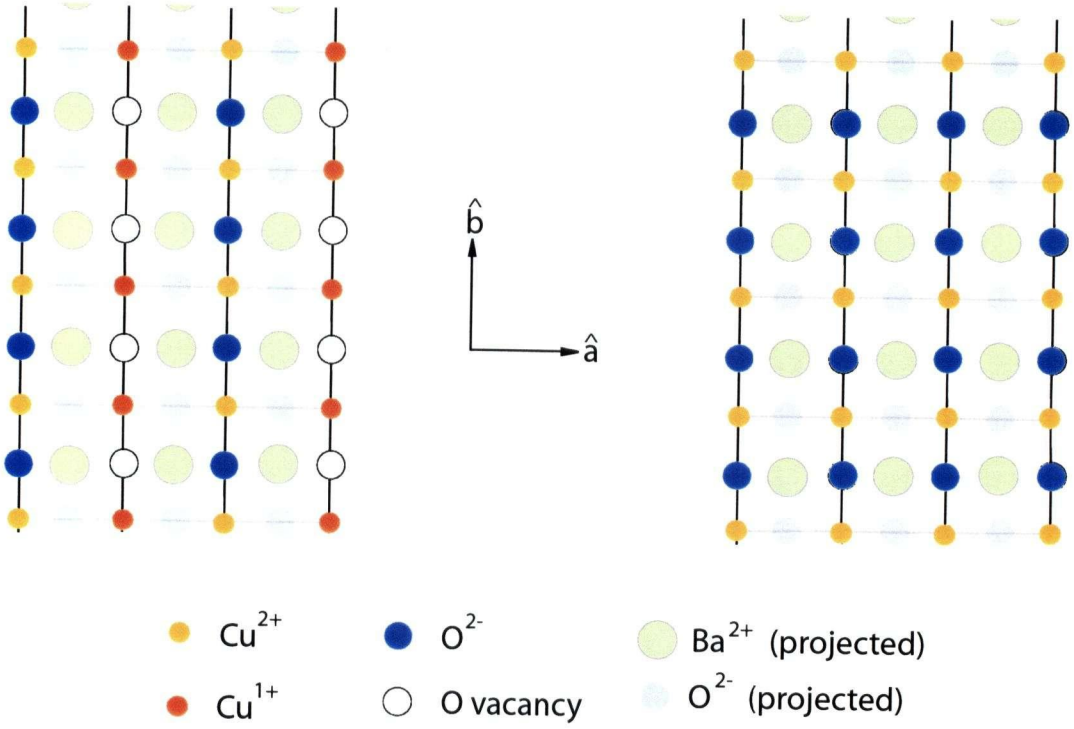

Figure 2.3: The *Ortho-II* (left) and *Ortho-I* (right) oxygen ordered phases of $YBa_2Cu_3O_{6+x}$, as viewed in the $\widehat{ab}$ oriented CuO chain layer.

2.4 Electronic Bandstructure

Since it will be assumed, at least initially, that the Fermi liquid picture is indeed absolutely correct deep in the superconducting state of the cuprates, then one ought to analyze the electronic properties of $YBa_2Cu_3O_{6+x}$ using that bastion of condensed matter theory known as bandstructure [3]. Within this theory one assumes that the strong electronic correlations imposed by the parameter U_{eff} can be incorporated into the kinetics of the electrons:

$$\mathcal{H}_{plane} = -t_{plane} \sum_{<i,j>,\sigma} (c_{i\sigma}{}^{\dagger} c_{j\sigma} + c^{\dagger}_{j\sigma} c_{i\sigma}) - \mu_{plane} \cdots \tag{2.1}$$

where μ_{plane} is a shift in the plane band energy relative to the Fermi energy. Upon Fourier transforming the above expression, one obtains a single particle dispersion relation for electrons in a $(CuO_2)^{2-}$ plane:

$$\mathcal{H}_{plane} = \sum_{\vec{k},\sigma} \xi^{plane}_{\vec{k}} c_{\vec{k}\sigma}{}^{\dagger} c_{\vec{k}\sigma} \tag{2.2}$$

$$\xi^{plane}_{\vec{k}} = -2t_{plane}\big(\cos(k_x a) + \cos(k_y b)\big) - \mu_{plane} \cdots$$

Here, $\vec{k} = (k_x, k_y)$ where the x and y components of the momentum are parallel to $\hat{a}$ and $\hat{b}$, respectively, and a and b are the in-plane unit cell dimensions.

If the electronic system is superconducting, then there are long range correlations between pairs of electrons (Cooper pairs) of opposing momenta $(+\vec{k},-\vec{k})$ bound with an energy $2\Delta_{\vec{k}}$ [36]. One must then rewrite Eq. 2.2 accordingly:

$$\begin{aligned} \mathcal{H}_{plane} &= \sum_{\vec{k},\sigma} \xi^{plane}_{\vec{k}} c^{\dagger}_{\vec{k}\sigma} c_{\vec{k}\sigma} + \sum_{\vec{k}} (\Delta_{\vec{k}} c_{-\vec{k}\downarrow} c_{\vec{k}\uparrow} + \Delta_{\vec{k}} c^{\dagger}_{-\vec{k}\downarrow} c^{\dagger}_{\vec{k}\uparrow}) \\ &= \sum_{\vec{k}} \begin{pmatrix} c^{\dagger}_{-\vec{k}\downarrow} & c_{\vec{k}\uparrow} \end{pmatrix} \begin{pmatrix} \xi^{plane}_{\vec{k}} & \Delta_{\vec{k}} \\ \Delta_{\vec{k}} & -\xi^{plane}_{\vec{k}} \end{pmatrix} \begin{pmatrix} c_{-\vec{k}\downarrow} \\ c^{\dagger}_{\vec{k}\uparrow} \end{pmatrix} \end{aligned} \tag{2.3}$$

Note that the Hamiltonian Eq. 2.3 is not diagonal with respect to electron creation/annihilation operators, rather the eigenstates must be a linear combination of particle and hole wavefunctions. These are, of course, the famous bogolons [37]. Nevertheless, the form of this expression suggests that it will always be convenient to write Hamiltonians (and their perturbations) in the superconducting state in terms of the so called Nambu spinors [37]:

$$C^{\dagger}_{\vec{k}} = \begin{pmatrix} c^{\dagger}_{-\vec{k}\downarrow} & c_{\vec{k}\uparrow} \end{pmatrix} \tag{2.4}$$

Nambu notation will be used heavily in Chapter 6 of this thesis, as it provides a convenient means of introducing scattering of quasiparticles into Eq. 2.3.

To model the low energy electrodynamics of $YBa_2Cu_3O_{6+x}$ one must introduce three electronic dispersions, thus accounting for the presence of two $(CuO_2)^{2-}$ plane

layers and one CuO chain layer. The Hamiltonian of each isolated plane can be represented using Eq. 2.3, while that of the one-dimensional chains can be written as follows:

$$\mathcal{H}_{chain} = \sum_{\vec{k}} \begin{pmatrix} c^{\dagger}_{-\vec{k}\downarrow} & c_{\vec{k}\uparrow} \end{pmatrix} \begin{pmatrix} \xi^{chain}_{\vec{k}} & 0 \\ 0 & -\xi^{chain}_{\vec{k}} \end{pmatrix} \begin{pmatrix} c_{-\vec{k}\downarrow} \\ c^{\dagger}_{\vec{k}\uparrow} \end{pmatrix} \tag{2.5}$$

$$\xi^{chain}_{\vec{k}} = -2t_{chain}\cos(k_y b) - \mu_{chain} \tag{2.6}$$

Here it has been assumed that the chains are incapable of generating superconducting correlations on their own. Furthermore, I will employ a planar dispersion relation which accounts for diagonal and next nearest neighbour hopping:

$$\begin{aligned} \xi^{plane}_{\vec{k}} \;=\; & -2t_{plane}\big(\cos(k_x a) + \cos(k_y b) + 2t'\cos(k_x a)\cos(k_y b) \\ & + t''(\cos(2k_x a) + \cos(2k_y b))\big) - \mu_{plane} \end{aligned} \tag{2.7}$$

where $t' = -0.3$ and $t'' = 0.1$. The values of these latter two parameters have been chosen to be roughly in agreement with those frequently encountered in the literature [14].

One can now write an all-encompassing Hamiltonian that includes mixing of three bands via plane-plane and plane-chain hopping (it will be assumed that chain-chain hopping is negligibly small). As shown by Atkinson [38], this can be accomplished by writing $\mathcal{H}$ in terms of a 6-component Nambu spinor $\mathbf{C}^{\dagger}_{\vec{k}}$:

$$\mathcal{H} = \sum_{\vec{k}} \mathbf{C}^{\dagger}_{\vec{k}} \begin{pmatrix} \xi^{plane}_{\vec{k}} & t_{pp} & t_{cp} & 0 & 0 & \Delta_{\vec{k}} \\ t_{pp} & \xi^{plane}_{\vec{k}} & t_{cp} & 0 & \Delta_{\vec{k}} & 0 \\ t_{cp} & t_{cp} & \xi^{chain}_{\vec{k}} & 0 & 0 & 0 \\ 0 & 0 & 0 & -\xi^{chain}_{\vec{k}} & t_{cp} & t_{cp} \\ 0 & \Delta_{\vec{k}} & 0 & t_{cp} & -\xi^{plane}_{\vec{k}} & t_{pp} \\ \Delta_{\vec{k}} & 0 & 0 & t_{cp} & t_{pp} & -\xi^{plane}_{\vec{k}} \end{pmatrix} \mathbf{C}_{\vec{k}} \tag{2.8}$$

$$\mathbf{C}^{\dagger}_{\vec{k}} = \begin{pmatrix} c^{\dagger}_{1-\vec{k}\downarrow} & c^{\dagger}_{2-\vec{k}\downarrow} & c^{\dagger}_{3-\vec{k}\downarrow} & c_{3\vec{k}\uparrow} & c_{2\vec{k}\uparrow} & c_{1\vec{k}\uparrow} \end{pmatrix}$$

where $c^{\dagger}_{i\vec{k}\sigma}$ ($c_{i\vec{k}\sigma}$) are creation (annihilation) operators on layer $i = 1$ ($(CuO_2)^{2-}$ plane), 2 ($(CuO_2)^{2-}$ plane) or 3 (CuO chain). The symbols t_{pp} and t_{cp} are the plane-plane and chain-plane hopping energies, respectively.

Ideally, one would be able to establish numerical values for all hopping energies and shifts from spectroscopic measurements such as angular resolved photoemission spectroscopy (ARPES). While this technique has provided a wealth of information pertaining to some of the cuprate superconductors (in particular the Bi containing compounds), measurements on $YBa_2Cu_3O_{6+x}$ have been complicated by the presence of the CuO chain layer and surface reconstruction upon cleaving [39, 40]. It is known that when $YBa_2Cu_3O_{6+x}$ is cleaved parallel to the $\widehat{ab}$ plane that the resultant surface is an admixture of BaO and CuO planes (the only charge neutral layers in the fully doped compound, see Fig. 2.1). Consequently, the dominant features found in ARPES

measurements are typically related to chain derived electronic surface states [41]. Therefore, the values of many of the parameters in Eq. 2.8 have not been measured.

For demonstration purposes, I will take the following parameters as being representative of $YBa_2Cu_3O_{6+x}$ over a nominal doping range:

$$(t_{plane}, t_{chain}, \mu_{plane}, \mu_{chain}) = (500, 800, -100, -1100)\ meV \tag{2.9}$$

Here the values of t_{plane} and t_{chain} have been motivated by detailed LMTO calculations of Andersen *et al.* [42] that suggest bandwidths ($\sim 4t_{plane}$ and $\sim 4t_{chain}$) on the order of $3 \rightarrow 4\ eV$ for the three bands that disperse across the Fermi energy. To make a reasonable guess for μ_{plane}, recall that the $(CuO_2)^{2-}$ planes in $YBa_2Cu_3O_{6+x}$ are presumed to be *lightly* hole doped away from half filling. Therefore, this energy shift must be subject to the constraints $\mu_{plane} < 0$ and $|\mu_{plane}|/4t_{plane} \ll 1$. Finally, the value of μ_{chain} has been motivated by the plausible identification of a chain-like band in the ARPES data of Lu *et al.* [41], where the bottom of this band appears to be $\sim -2t_{chain} - \mu_{chain} \approx -400 \rightarrow -500\ meV$ below the Fermi energy.

To begin, consider the case $\Delta_{\vec{k}} = 0$. Diagonalizing Eq. 2.8 yields new dispersion relations $\xi^1_{\vec{k}}$, $\xi^2_{\vec{k}}$ and $\xi^3_{\vec{k}}$ (eigenvalues) for new normal modes (eigenvectors) that are a mixture of plane and chain electronic states. If $t_{pp} = t_{cp} = 0$ then $\xi^1_{\vec{k}} = \xi^2_{\vec{k}} = \xi^{plane}_{\vec{k}}$ and $\xi^3_{\vec{k}} = \xi^{chain}_{\vec{k}}$. The two distinct electronic bands and their Fermi surfaces (defined as $\{\vec{k}|\xi^i_{\vec{k}} \equiv 0\}$) are shown in Fig. 2.4. Note that only a single quadrant of the First Brillouin zone will be shown in the following figures as the normal state Fermi surface and superconducting gap magnitude are both presumed to be four-fold symmetric about the $\Gamma = (0,0)$ point. Special points in momentum space $X = (\pi/a, 0)$, $Y = (0, \pi/b)$ and $S = (\pi/a, \pi/b)$ have been identified as well.

It has been noted that ARPES measurements on $YBa_2Cu_3O_{6.993}$ (overdoped) have indicated that $\Delta_{\vec{k}}$ may have orthorhombic (2-fold) rather than tetragonal (4-fold) symmetry about the Γ point [41]. However, as noted previously, these measurements are complicated by the presence of poorly understood surface states. This fact warrants significant consideration in regards to the above mentioned observations, for the purported superconducting peak in Ref. [41] shows negligible dispersion - much like the well characterized surface state. Furthermore, the interpretation of these data are highly dependent upon there being well defined electronic states near the momenta X and Y. Arguments pertaining to why this may very well not be the case in the cuprates will be presented in Chapter 5. On the other hand the low frequency electrodynamics in the superconducting state will primarily be dependent upon the behaviour of $\Delta_{\vec{k}}$ near the nodes ($|\Delta_{\vec{k}}| = 0$) and the ARPES data lack the resolution to suggest that the magnitude of the gap function is anisotropic about the nodal directions. Therefore, it will be assumed that $\Delta_{\vec{k}}$ has tetragonal symmetry.

There are two key points to be drawn from the top panel of Fig. 2.4: First, the plane bands are clearly 2-dimensional since their dispersion relations depend explicitly upon both k_x and k_y (Eq. 2.7), while the chain band is consequently one-dimensional (Eq. 2.6). Second, consider the Fermi velocity $\vec{v}_F$, defined as

$$\vec{v}_F \equiv \frac{1}{\hbar}\frac{d\xi}{d\vec{k}}\Big|_{\vec{k}=\vec{k}_F} \tag{2.10}$$

along the zone diagonal Γ-S. Note that $\vec{v}_F^{plane}$ is directed along the zone diagonal while $\vec{v}_F^{chain}$ points in the $\hat{b}$ direction (lower right panel, Fig. 2.4). The importance of these two points is made evident when one considers $\Delta_{\vec{k}} \neq 0$ in the superconducting state. For the sake of a demonstration, I once again invoke Atkinson's parameterization [38]:

$$\Delta_{\vec{k}} = \Delta_o \left(g(k_x) - g(k_y)\right) \tag{2.11}$$
$$g(k_i) = \cos(k_i a) - 0.3\cos(3k_i b)$$

with $\Delta_o = 11\, meV$. If one diagonalizes Eq. 2.8 in the superconducting state and then evaluates the quasiparticle energies, then the new dispersions will be

$$\xi_{\vec{k}}^1 = \xi_{\vec{k}}^2 = \sqrt{(\xi_{\vec{k}}^{plane})^2 + \Delta_{\vec{k}}^2} \tag{2.12}$$
$$\xi_{\vec{k}}^3 = \xi_{\vec{k}}^{chain}$$

It is now clear that the only low energy excitations in the plane band will be located at the nodes of the superconducting gap function ($\Delta_{\vec{k}} = 0$), which are located along the zone diagonal (lower left panel, Fig. 2.4). However, there is no gap on the chains (by assumption). Therefore, if one induces a charge current density $\vec{\mathcal{J}}$ with a potential $\vec{E}$ (ignoring the superfluid response momentarily), where

$$\vec{\mathcal{J}} \propto \sum_{bands} \vec{v}_F \cdot \vec{E}$$

then the plane band will contribute to $\vec{\mathcal{J}}$ in both the $\hat{a}$ and $\hat{b}$ directions. On the other hand, the chain band will make a substantial contribution to currents *only* in the $\hat{b}$ direction.

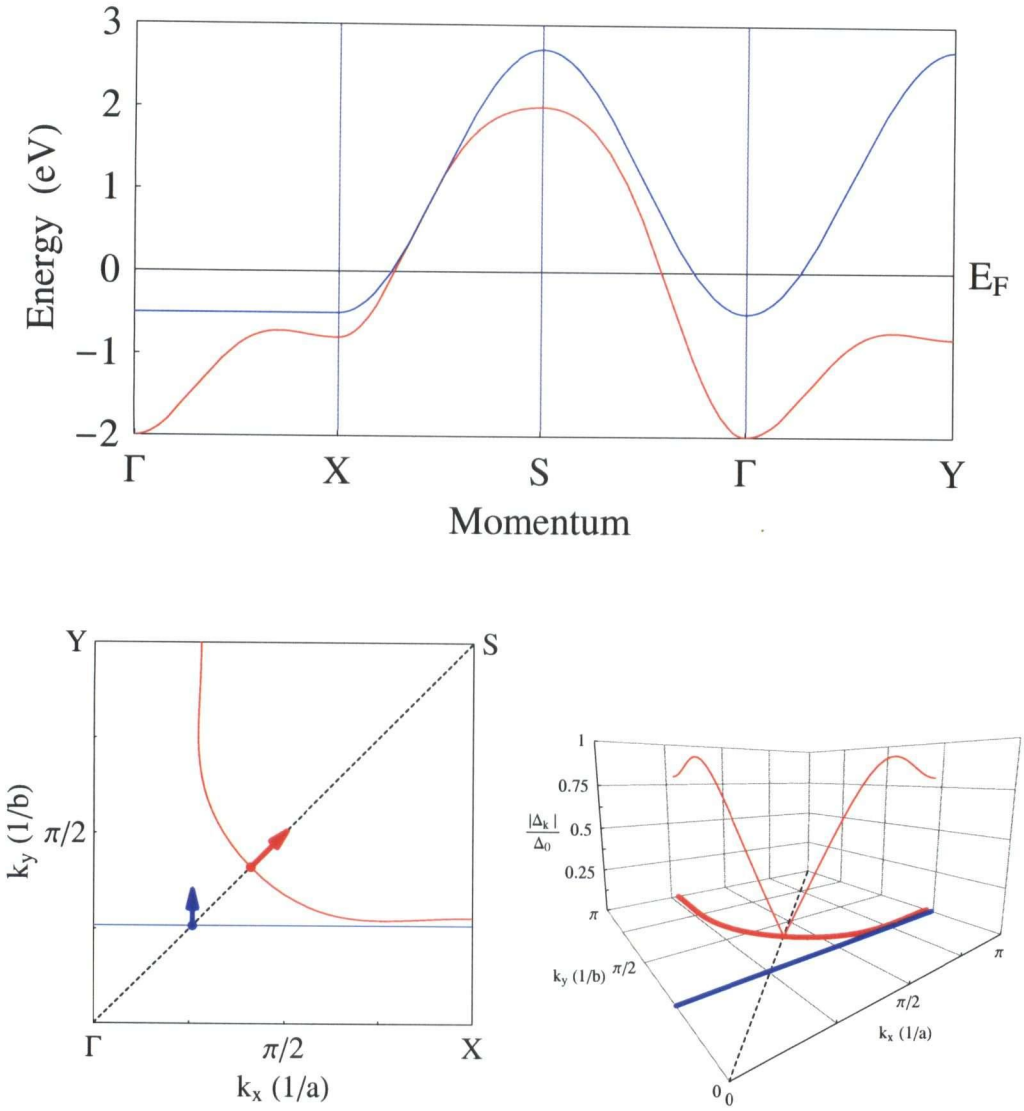

Figure 2.4: The bare low energy electronic bandstructure of $YBa_2Cu_3O_{6+x}$, assuming $t_{pp} = t_{cp} = 0$. Upper panel shows the two distinct dispersions $\xi^1_{\vec{k}} = \xi^2_{\vec{k}} = \xi^{plane}_{\vec{k}}$ (red) and $\xi^3_{\vec{k}} = \xi^{chain}_{\vec{k}}$ (blue). Fermi surfaces are shown in the lower left panel with the direction of the Fermi velocities at points on the zone diagonal indicated with arrows. Lower right panel displays the magnitude of the superconducting gap $|\Delta_{\vec{k}}|$ evaluated along each Fermi surface with the nodes located along the zone diagonal (dashed line).

The scenario does not change qualitatively when one considers weak coupling between planes and chains. Again, first consider $\Delta_{\vec{k}} = 0$, but now employing the following coupling parameters [38]:

$$(t_{pp}, t_{cp}) = (100, 100)\, meV \tag{2.13}$$

where these numerical values have been motivated solely by the presumption that the interlayer coupling energies must be much less than the bandwidths, $\{t_{pp}, t_{cp}\} \ll \{4t_{plane}, 4t_{chain}\}$. One now obtains the hybridized dispersion relations shown in the upper panel of Fig. 2.5. There are now two distinct 2-dimensional bands due to bonding and antibonding combinations of the plane wavefunctions. In addition, the formerly 1-dimensional chain band has hybridized primarily with the antibonding plane band to produce what can be described as a quasi-1-dimensional band. The lower left panel of Fig. 2.5 shows the resulting normal state Fermi surfaces and the new Fermi velocities on each band along the zone diagonal. If one now examines the superconducting state by using Eq. 2.11 and then diagonalizes Eq. 2.8, the new quasiparticle dispersions (for small t_{cp}) will be

$$\begin{aligned} \xi^1_{\vec{k}} &\approx \sqrt{(\xi^{plane}_{\vec{k}} - t_{pp})^2 + \Delta^2_{\vec{k}}} \\ \xi^2_{\vec{k}} &\approx \sqrt{(\xi^{plane}_{\vec{k}} + t_{pp})^2 + \Delta^2_{\vec{k}}} \\ \xi^3_{\vec{k}} &\approx \sqrt{(\xi^{chain}_{\vec{k}})^2 + (\Delta^{chain}_{\vec{k}})^2} \end{aligned} \tag{2.14}$$

for $\vec{k}$ near the zone diagonal. Note that $\Delta^{chain}_{\vec{k}}$ is the *induced* superconducting gap in the quasi-1-dimensional band. As shown in the lower right panel of Fig. 2.5, the induced gap need not resemble the distinct nodal structure with linear dispersion perpendicular to the zone diagonal. Rather, $\Delta^{chain}_{\vec{k}}$ is extremely small for $k_x < \pi/3$ but resembles $\Delta_{\vec{k}}$ for larger k_x. The key point to be drawn from a comparison of Figs. 2.4 and 2.5 is that the low energy excitations of the two dimensional bands still have $\vec{v}_F$ directed along the zone diagonal and will behave qualitatively similar to the excitations of a single uncoupled $(CuO_2)^{2-}$ plane. On the other hand, the node in $\Delta^{chain}_{\vec{k}}$ is located on a segment of the quasi-1-dimensional Fermi surface that is primarily chain-like ($\vec{v}_F \parallel k_y$) despite hybridization. Therefore, the conclusion that CuO chains only contribute to charge conduction in the $\hat{b}$ direction remains valid.

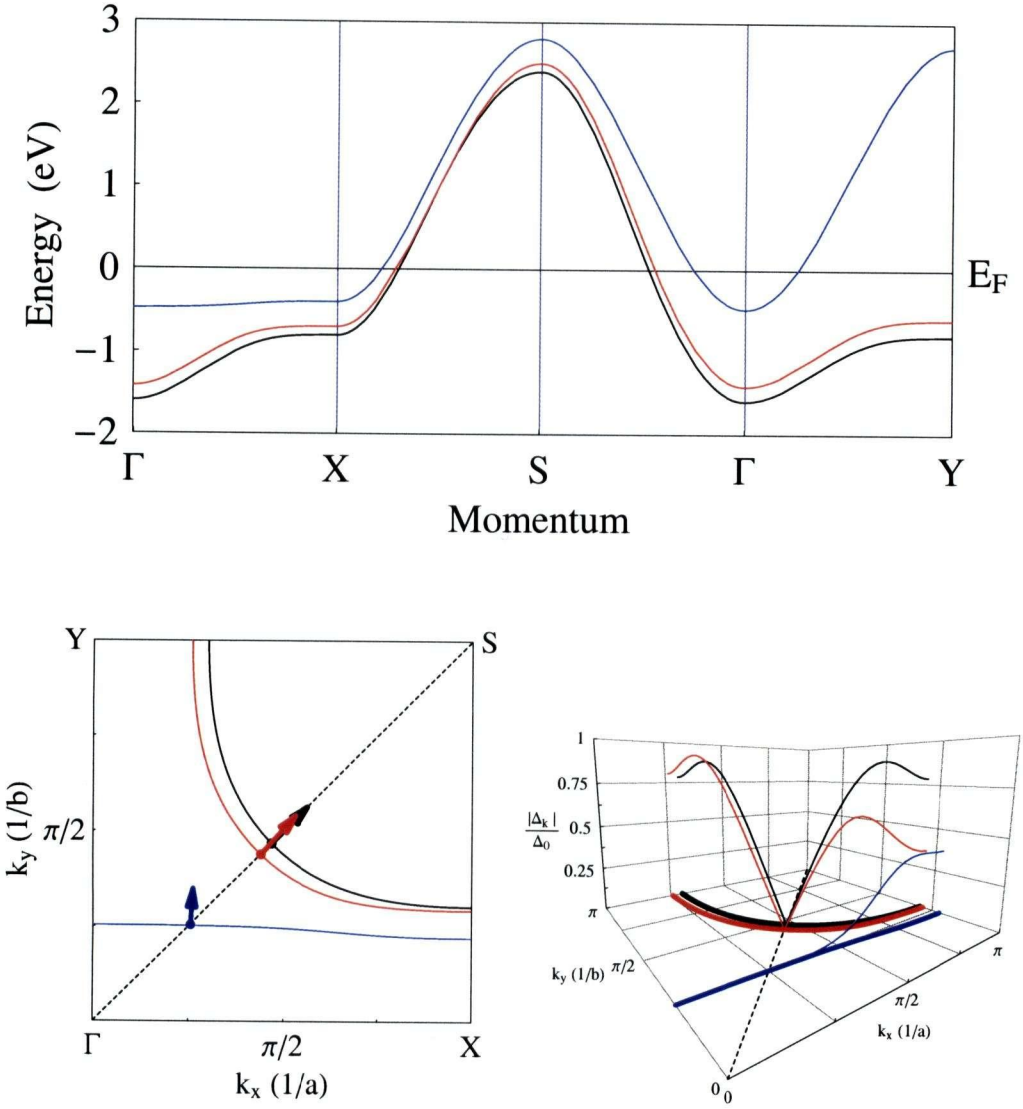

Figure 2.5: The bare low energy electronic bandstructure of $YBa_2Cu_3O_{6+x}$, assuming $(t_{pp}, t_{cp}) = (100, 100)\, meV$. Upper panel shows two 2-dimensional dispersions $\xi^1_{\vec{k}}$ (black) and $\xi^2_{\vec{k}}$ (red) and a quasi-1-dimensional band $\xi^3_{\vec{k}}$ (blue). Fermi surfaces are shown in the lower left panel with the direction of the Fermi velocities at points on the zone diagonal indicated with arrows. Lower right panel displays the magnitude of the superconducting gap $|\Delta_{\vec{k}}|$ evaluated along each Fermi surface with the node in each band located along the zone diagonal (dashed line).

2.5 Scattering Considerations

2.5.1 Elastic Scattering at Low Temperatures

To finish this discussion of the electronic structure of $YBa_2Cu_3O_{6+x}$, it is prudent to consider how the inclusion of real defects ought to manifest themselves in light of the bandstructure calculations presented above. Given the approximate forms of the dispersion relations in the superconducting state (Eq. 2.14), one should observe that the eigenstates of bands 1 and 2 are, for the most part, those of Eq.2.3. These quasiparticles will be primarily confined to the $(CuO_2)^{2-}$ planes and scatter from typical planar defects. However, the eigenstates of band 3 near the zone diagonal will be those of Eq. 2.5 with very weak off-diagonal components. These quasiparticles are primarily confined to the CuO chains and will likewise scatter from typical chain defects. The question is then what are these typical defects?

As argued by this author in a previous publication [43], one can at least offer heuristic answers by noting that the most ubiquitous defect on a metallic chain will be oxygen vacancies followed by a Cu^{1+} site, as shown in Fig.2.2. For example, if $x = 0.993$, then approximately 1 out of every 143 chain oxygen sites will be vacant - this corresponds to an astoundingly large defect density of $n_i = 0.007$ vacant sites/1 oxygen site per unit cell$\sim 7000\,ppm$ on the chains! The mean free path for a chain quasiparticle will then be $\ell \sim 143 \times b \rightarrow 572$ Å. Taking a reasonable estimate of $|\vec{v}_F^3|$ from the Γ-S cut of the first Brillouin zone of Fig. 2.5 as $\sim 10^5\, m/s$, the mean defect scattering rate will be $\tau^{-1} \sim 2 \times 10^{12}\, s^{-1}$.

In contrast to the chains, a typical planar defect will most likely be a cation substituted into a Cu^{2+} site. Chemical assays performed upon $YBa_2Cu_3O_{6+x}$ crystals similar to those studied in this thesis indicate that cation impurities are present at no more than the level of $n_i \sim 1 \rightarrow 10\,ppm$. Assuming a worst case scenario in which *all* of the defects are infinitely strong (Unitary scatterers), the mean free path ℓ in two dimensions can be defined as the diameter of a circle in the $(CuO_2)^{2-}$ plane that contains a single defect. One can then write an expression for ℓ as follows:

$$\frac{1}{n_i} = \frac{\pi(\ell/2)^2}{ab}$$

Taking the lower bound on n_i gives $\ell \sim 4000$ Å. Again, making a reasonable estimate for the Fermi velocities $|\vec{v}_F^1| \approx |\vec{v}_F^2| \sim 10^5\, m/s$ from Fig. 2.5, the mean defect scattering rate will be $\tau^{-1} \sim 2.5 \times 10^{11}\, s^{-1}$. Even with these very crude estimates, one can see that the scattering rate on the $(CuO_2)^{2-}$ planes will be *at the very least* an order of magnitude smaller than that on the CuO chains. Note that if the in-plane scatterers are not truly Unitary then the disparity between planar and chain scattering rates will be even larger. This final conclusion will have considerable bearing upon how microwave (charge) conductivity data will be interpreted in Chapter 4 of this thesis.

A key issue to be addressed in Chapter 5 of this thesis is the ability of a defect potential to elastically scatter an incident quasiparticle of energy ω with momentum $\vec{k}$ into another state with momentum $\vec{k}'$. This will give rise to the definition of the $\hat{T}$-matrix which is proportional to the Fourier transform of the real space defect

potential. This matrix will contain elements identified as $\hat{T}(\vec{k}, \vec{k}', \omega)$ that control the probability of scattering from any state $\vec{k}$ into another state $\vec{k}'$. At low temperatures the superconducting gap enforces very stringent phase space restrictions in that the low energy quasiparticles will all have momenta near the nodes of the gap (along the first Brillouin zone diagonals), as sketched in Fig. 2.6. If, for example, the system is carrying charge current $\vec{\mathcal{J}}$ in the $\hat{a}$-axis direction ($\hat{k_x}$), then only those scattering events ($\hat{T}$-matrix elements) which move excitations from the nodes at $\vec{k}_{++}$ and $\vec{k}_{-+}$ to the nodes at $\vec{k}_{+-}$ and $\vec{k}_{--}$ will be able to relax the quasiparticle current. These processes are known as *internode scattering*. On the other hand, scattering via small wavevectors $\vec{q} = \vec{k} - \vec{k}'$ cannot lead to significant relaxation of charge current because these events leave quasiparticles trapped within the locality of one node. These latter processes are known as *intranode scattering*.

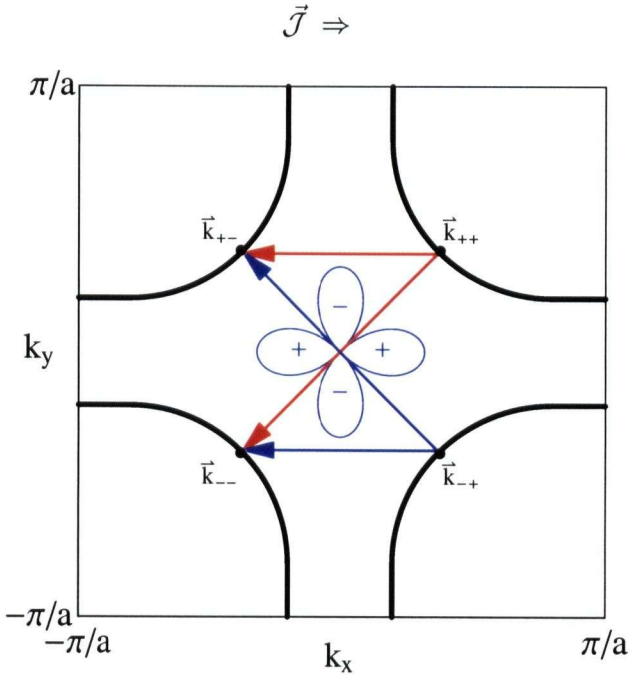

Figure 2.6: Elastic scattering of d-wave quasiparticles between the four Fermi points located at the nodes of the superconducting gap in a 2-dimensional band. Only those scattering events that move quasiparticles from $\vec{k}_{++}$ and $\vec{k}_{-+}$ across the normal state Fermi surface are able to relax a charge current $\vec{\mathcal{J}}$ flowing in the $\hat{a}$-axis direction ($\hat{k_x}$).

As a final point, it should be noted that point-like defects (δ-function potentials) will prove to be the most efficient scattering centres because their Fourier transforms are broad functions of $\vec{q} = \vec{k} - \vec{k}'$. On the other hand, finite sized defect potentials are not very effective scattering centres in a d-wave superconductor because their

Fourier transforms will vary as $|\vec{q}|^{\alpha}$ with $\alpha < 0$ for large $|\vec{q}|$. For example, if the defects are screened charges that can be described by a Yukawa potential [3], then the Fourier transform of such a potential is $V(\vec{q}) \propto 1/(1 + (q/q_o)^2)$ (with the wavevector q_o setting the screening lengthscale). Consequently, the elements of the $\hat{T}$-matrix $\hat{T}(\vec{q}, \omega) \propto 1/(1 + (q/q_o)^2)$ as well. If the internode scattering wavevectors are large compared to q_o, then the effective scattering rate will be reduced.

2.5.2 Inelastic Scattering at Finite Temperature

Away from $T = 0$ it is possible to relax charge currents via interactions between d-wave quasiparticles and other thermal excitations in the system. Quasiparticle-spin fluctuation scattering has featured prominently in the literature but, as demonstrated by Quinlan, Scalapino and Bulut [44], this mechanism alone does not explain what has been observed experimentally. Rather, it has been argued by Walker and Smith [45] that at low temperature the inelastic scattering in a d-wave superconductor can be described by second order quasiparticle-quasiparticle interactions involving an Umklapp process [3], as sketched in Fig. 2.7. Here, a nodal quasiparticle with momentum $\vec{k}_1$ is scattered from a second quasiparticle with momentum $\vec{k}_2$ located away from the node (where $|\Delta_{\vec{k}_2}| \equiv \Delta_U > 0$) such that $\vec{k}_1 + \vec{k}_2$ resides on the First Brillouin zone boundary. By conservation of crystal momentum the two quasiparticles can scatter across the normal state Fermi surface into the states $\vec{k}_3$ (a nodal state) and $\vec{k}_4$ where $\vec{k}_1 + \vec{k}_2 + \vec{G} = \vec{k}_3 + \vec{k}_4$ and $\vec{G}$ is a reciprocal lattice vector. One can calculate an inelastic scattering rate Λ_{inel}^{-1} for the nodal quasiparticle at $\vec{k}_1$ in a Born approximation from knowledge of the thermal occupation of the states $(\vec{k}_1, \vec{k}_3)$ (where $\xi_{\vec{k}}^1 \approx 0$) and $(\vec{k}_2, \vec{k}_4)$ (where $\xi_{\vec{k}}^1 \approx \Delta_U$):

$$\begin{aligned} \Lambda_{inel}^{-1}(T) &\propto \sum_{\vec{k}_2,\vec{k}_3,\vec{k}_4} |M|^2 f(\xi_{\vec{k}_2}^1) \left(1 - f(\xi_{\vec{k}_3}^1)\right) \left(1 - f(\xi_{\vec{k}_4}^1)\right) \delta(\xi_{\vec{k}_1}^1 + \xi_{\vec{k}_2}^1 - \xi_{\vec{k}_3}^1 - \xi_{\vec{k}_4}^1) \\ &\approx CT^2 f(\Delta_U)\left(1 - f(\Delta_U)\right) \end{aligned} \tag{2.15}$$

Here, C is a numerical prefactor, $f(\epsilon) \equiv 1/(e^{\epsilon/T} + 1)$ is the Fermi function and the factor of T^2 accounts for the available phase space into which one can scatter the nodal quasiparticle $(\vec{k}_3)$. Note that this is by no means a detailed theory, but nonetheless allows one to parameterize a 'thermal averaged' inelastic scattering rate for nodal quasiparticles in the limit $T \ll \Delta_o$.

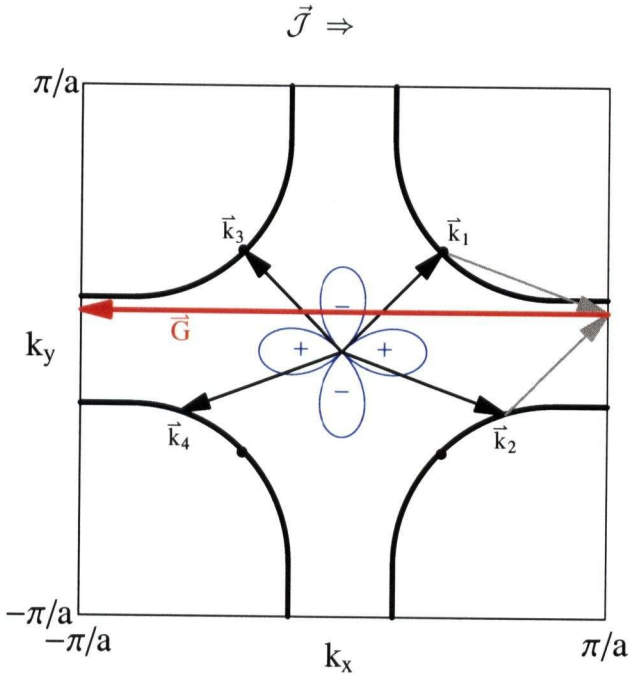

Figure 2.7: Inelastic scattering of a nodal d-wave quasiparticles via an Umklapp process. A charge current $\vec{\mathcal{J}}$ flowing in the $\hat{a}$-axis direction is relaxed by scattering the quasiparticles at $\vec{k}_1$ and $\vec{k}_2$ into the states $\vec{k}_3$ and $\vec{k}_4$.

Chapter 3

The Experiments

The following is a survey of the experimental techniques that have provided the data presented at the end of this chapter. The story will begin with the growth, detwinning and oxygen doping of ultrahigh purity single crystals of $YBa_2Cu_3O_{6+x}$. Next, the reader is introduced to the concept of surface impedance, which is an experimentally accessible quantity related to the electrical conductivity of a metallic system. Two methods used in the UBC Superconductivity Laboratory for measuring the real part of the surface impedance will be described: the broadband bolometric apparatus and microwave cavity perturbation. This will be followed by a brief discussion on the measurement of the imaginary part of the surface impedance using the $1.14\,GHz$ cavity perturbation apparatus. Calibrated data obtained from samples of overdoped $YBa_2Cu_3O_{6.993}$ and underdoped *Ortho-II* ordered $YBa_2Cu_3O_{6.5}$ will be presented along with the discussion of each experimental method.

3.1 Sample Growth and Preparation

3.1.1 Growth of Single Crystals Via Self-Flux Method

The single crystals of $YBa_2Cu_3O_{6+x}$ which were used for the measurements presented herein were grown by a self-flux method by Dr. Ruixing Liang [46]. The starting materials were $99.995 \rightarrow 99.999\%$ atomic purity powders of Y_2O_3, CuO and $BaCO_3$ which were repeatedly ground and annealed in an inert gas at 890^oC to reduce volume and liberate CO_2. The resulting mixture of powders contained CuO:BaO (28:72) in excess such that the quantity of Y_2O_3 controlled the trajectory in the eutectic phase diagram and the ultimate yield during crystal growth (see Fig. 3.1). The powders were then melted in high density $BaZrO_3$ ceramic crucibles (which are inert to the CuO:BaO flux) inside a box furnace held at 1020^oC for 15 hours and then the temperature was lowered to 1000^oC. At this point one end of a quartz rod, which terminated outside of the box furnace, was moved proximal to the crucible (Fig. 3.1). This resulted in a 10 to 20^oC thermal gradient across the crucible with the coldest spot located nearest the quartz rod. The cold spot served as the nucleation point for crystallization of supercooled $YBa_2Cu_3O_{6+x}$ as the temperature was lowered further at a rate of 0.3 to 1^oC/hour to a final temperature of 960^oC. At this final temperature the crucible contained solid $YBa_2Cu_3O_{6+x}$ and liquid CuO:BaO which was then decanted in situ. Finally, the crucible was cooled to room temperature and the single crystals were removed using plastic forceps.

Due to asymmetries in the growth rate of $YBa_2Cu_3O_{6+x}$, as-grown single crystals are typically thin ($< 100\,\mu m$) platelets with broad ($\sim 1\,mm^2$) $\widehat{ab}$ oriented faces. Fur-

thermore, they typically suffer from twinning (nonuniform mixture of crystal domains whose in-plane unit cell vectors have one of two possible orthogonal orientations) since the $\hat{a}$ and $\hat{b}$ unit cell dimensions are particularly close below the orthorhombic-tetragonal transition at $460°C$, as demonstrated in Fig. 3.2. Thin crystals can be homogenized by squeezing them (uniaxially) in a custom built vice held at temperatures on the order of $200 \rightarrow 300\,°C$ in an environment of flowing oxygen or nitrogen.

3.1.2 Oxygen Doping and Ordering

An as-grown single crystal of $YBa_2Cu_3O_{6+x}$ typically has an oxygen doping $x \sim 0.1 \rightarrow 0.2$. To obtain a superconductor, one augments this to $x \geq 0.3$ by annealing at high temperatures in flowing prepurified oxygen gas. The pressure-temperature doping diagram has been mapped out in great detail by Schleger *et al.* [47], but the general rule is that larger values of x require lower annealing temperatures and consequently longer annealing times to reach equilibrium.

For the overdoped $YBa_2Cu_3O_{6.993}$ samples, as-grown crystals were first detwinned by applying approximately $100\,atm$ uniaxial pressure at $250°C$ under flowing oxygen gas. Next, the crystals were annealed at $350°C$ in flowing oxygen inside a tube furnace for 50 days. A large volume of $YBa_2Cu_3O_{6+x}$ sintered ceramic was also annealed simultaneously for test purposes, as will be explained below.

To produce the underdoped *Ortho-II* ordered $YBa_2Cu_3O_{6.5}$ samples the sequence of events had to be modified slightly to avoid reintroducing twinning during oxygenation at temperatures exceeding the orthorhombic-tetragonal transition. First the oxygen concentration was set by annealing crystals and a much larger volume ($\times 100$) of $YBa_2Cu_3O_{6+x}$ sintered ceramic pellets at $760°C$ in flowing oxygen inside a tube furnace for two weeks, followed by a rapid quench to room temperature under a protective flow of nitrogen gas. The crystals and pellets were then sealed together in an evacuated quartz tube and annealed at $390°C$ to remove any inhomogeneity associated with the quench. Detwinning was then performed at temperatures below $200°C$. Finally, the crystals and pellets were sealed once again in an evacuated quartz tube and annealed at $84°C$ for 2 days and $60°C$ for 5 days. This latter step established the *Ortho-II* ordering of the chain layer oxygen (see Fig. 2.3) which was verified by X-ray diffraction [33].

The final check for all annealing procedures was verification of oxygen content. This was accomplished via iodometric titration in which $YBa_2Cu_3O_{6+x}$ ceramic pellets were dissolved in HCl into their ionic components Y^{3+}, Ba^{2+}, $Cu^{\bar{n}+}$ and O^{2-}, where $\bar{n}$ is the mean ionization of the copper. Upon addition of KI, copper precipitates out via

$$Cu^{\bar{n}+} + I^- \rightarrow CuI_{(s)} + \frac{\bar{n}-1}{2} I_2$$

The iodine is then titrated using a sodium thiosulfate ($Na_2S_2O_3$) solution which is calibrated by repeating the above procedure with CuO ($\bar{n} = 2$) substituted for $YBa_2Cu_3O_{6+x}$. One can then relate the oxygen content to the mean ionization of copper: $x = (3\bar{n} - 5)/2$.

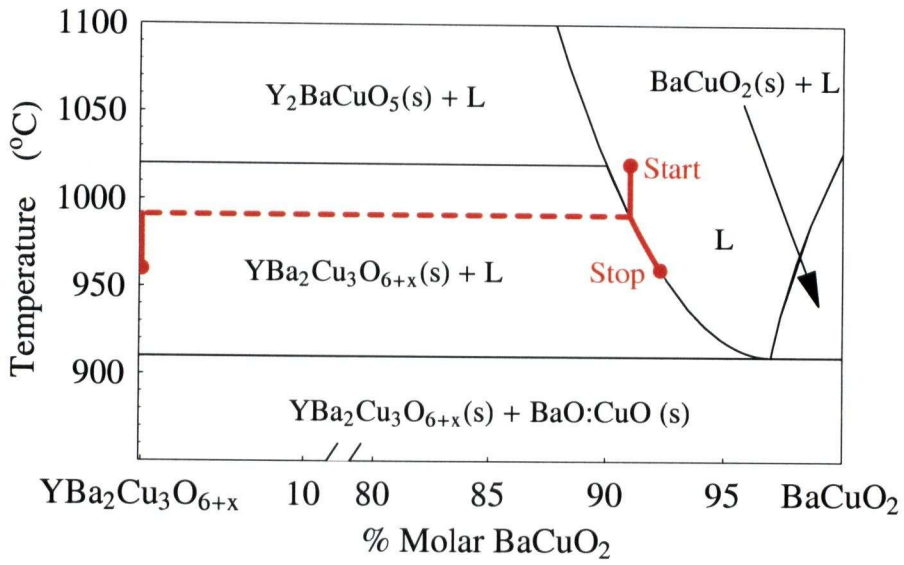

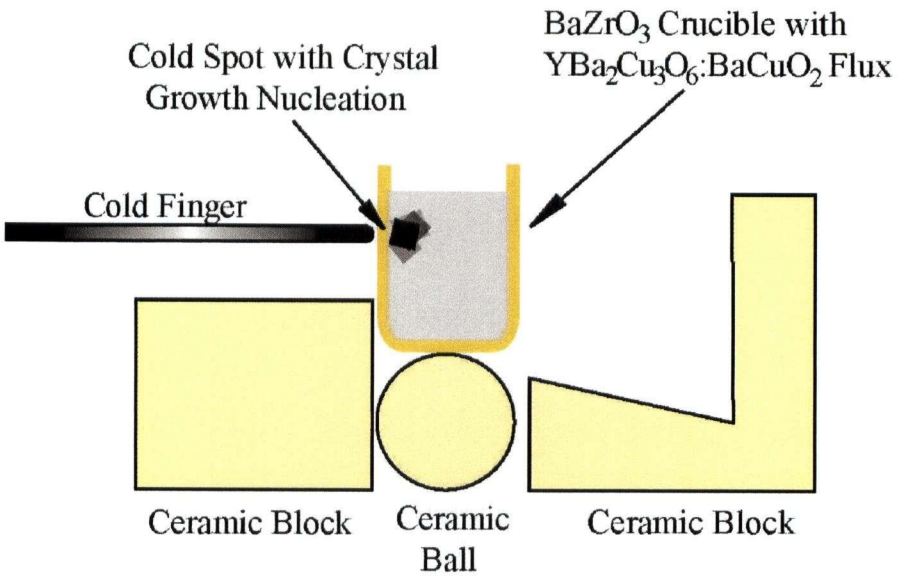

Figure 3.1: Growth of $YBa_2Cu_3O_{6+x}$ single crystals via the self-flux method. The trajectory of a typical growth procedure is shown in the $YBa_2Cu_3O_{6+x}$-CuO:BaO eutectic phase diagram (top panel). A caricature of the cold finger method for nucleating crystal growth is shown as well (lower panel).

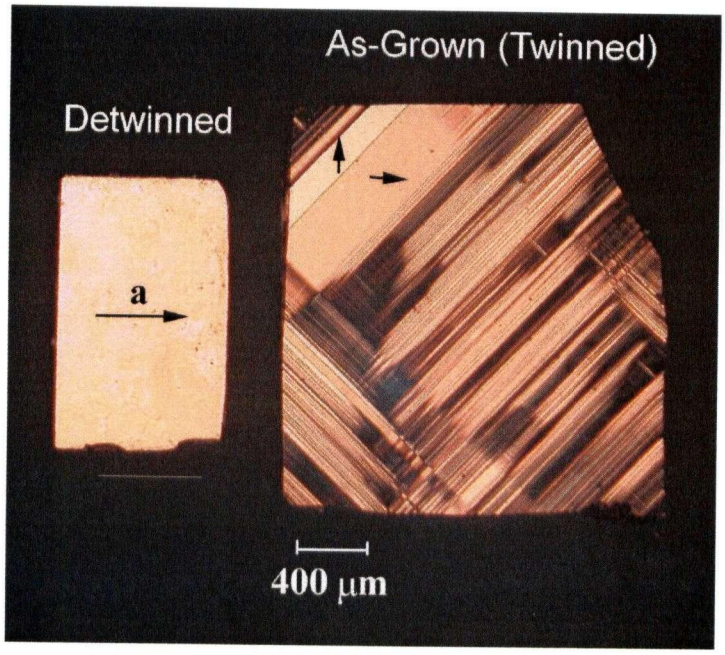

Figure 3.2: An as-grown (right) and a detwinned (left) single crystal of $YBa_2Cu_3O_{6+x}$. Image taken with incident light polarized at 45^o to the $\hat{a}$ axis in the $\widehat{ab}$ plane and a polarizer rotated at 45^o with respect to the incident light's polarization placed before the microscope ocular. Dark arrows indicate $\hat{a}$-axis direction in the detwinned crystal and in two domains of the as-grown crystal. Subtle differences in index of refraction for incident polarization along the $\hat{a}$ and $\hat{b}$ orientations provides contrast between domains. Dark regions indicate areas containing a high density of twin boundaries. Note that the detwinning procedure can essentially remove all of the twin boundaries.

3.2 The Surface Impedance of Superconducting Materials

One of the objectives of the microwave spectroscopy programme at UBC is to measure the electrical conductivity $\sigma(\Omega, T)$ of $YBa_2Cu_3O_{6+x}$ as a function of microwave angular frequency Ω and temperature T. This quantity is a linear response tensor defined in terms of the current density $\vec{\mathcal{J}}$ (with component $\mathcal{J}_i$ in the $i \in \{x, y, z\}$ direction) generated by applying an oscillatory magnetic field $\vec{H}_{rf} = (\vec{\nabla} \times \vec{A})/\mu_o$ to an electronic system:

$$\mathcal{J}_i \equiv \sum_{j=x,y,z} \Omega \sigma_{ij}(\Omega, T) A_j(\Omega) \tag{3.1}$$

This thesis will concentrate solely upon two of the diagonal components $(\sigma_{xx}, \sigma_{yy})$ of the tensor, with currents being driven in the $\widehat{ab}$ oriented $(CuO_2)^{2-}$ planes by microwave magnetic fields polarized parallel to these planes. Conduction in the $\hat{c}$ direction will not be discussed here, however it is an interesting problem in its own right that will be governed by the hopping of charge between Josephson coupled 2-dimensional superconductors [35]. For simplicity, the subscripts (xx,yy) will be dropped henceforth on all conductivity expressions.

Within the superconducting state for $T > 0$, one can naively expect that there will be two contributions to $\sigma(\Omega, T)$: one from those electrons in the superconducting condensate (superfluid) and the thermally excited quasiparticles (the perhaps inappropriately named normal fluid).

$$\sigma(\Omega, T) \equiv \sigma_1 - i\sigma_2 = \sigma_{qp}(\Omega, T) + \sigma_{sf}(\Omega, T) \tag{3.2}$$

The superfluid is a perfect conductor at $\Omega = 0$ whose total strength is controlled by the superfluid spectral weight $(n_s e^2/m^*)(T)$. This contribution to Eq. 3.2 can be written as

$$\sigma_{sf}(\Omega, T) = \frac{n_s e^2}{m^*}(T) \left(\pi \delta(\Omega) - \frac{i}{\Omega} \right) \tag{3.3}$$

where the δ-function represents the perfect DC conductivity and the imaginary part is required by causality through the Kramers-Kronig relations [1]. It is this latter part which accounts for the screening of the interior of the material over a lengthscale $\lambda_L(T)$, known as the London penetration depth. It can be shown via the London equations [1] that this lengthscale is related to the superfluid spectral weight via

$$\frac{n_s e^2}{m^*}(T) = \frac{1}{\mu_o \lambda_L^2(T)} \tag{3.4}$$

As often happens in experimental physics, one does not obtain intrinsic quantities such as $\sigma(\Omega, T)$ by direct observation. Rather, the experimentally accessible quantities are the energy losses (power absorption) and diamagnetic moment due to the flow of charge currents in a superconductor subjected to an external field. For the

experiments of concern here, these quantities can be phrased in terms of the surface impedance, defined as

$$Z_s(\Omega,T) \equiv \frac{E_\perp}{H_{rf}} = R_s(\Omega,T) + iX_s(\Omega,T) \tag{3.5}$$

where H_{rf} is the magnitude of a uniform applied microwave magnetic field at the surface of a metal and $E_\perp$ is the resulting transverse electric field (due to the flow of screening currents) at the surface. In the limit of local electrodynamics [1] this quantity can be related to the electrical conductivity as follows:

$$Z_s(\Omega,T) = \left(\frac{i\mu_o\Omega}{\sigma(\Omega,T)}\right)^{1/2} \tag{3.6}$$

Within the superconducting state at sufficiently low microwave frequency one expects the imaginary part of the conductivity to be dominated by the superconducting condensate (Eq. 3.3), therefore $\sigma_2 \approx \mathrm{Im}|\sigma_{sf}|$. Using Eqns. 3.2 and 3.3, one can separate out the real and imaginary components of Eq. 3.5:

$$\begin{aligned} R_s(\Omega,T) &\approx \tfrac{1}{2}\mu_o^2\Omega^2\lambda_L^3(T)\sigma_1(\Omega,T) \\ X_s(\Omega,T) &\approx \mu_o\Omega\lambda_L(T) \end{aligned} \tag{3.7}$$

Of course, for $\Omega \neq 0$, $\sigma_1(\Omega,T) = \mathrm{Re}|\sigma_{qp}(\Omega,T)|$ (no superfluid contribution). Strictly speaking there will be a quasiparticle contribution to $\sigma_2(\Omega,T)$ as well and it will be addressed in Chapter 4.

3.3 Measurement Principle

In all of the experiments discussed herein the samples were thin superconducting platelets (with broad $\widehat{ab}$ oriented faces) that were placed in very weak ($\ll H_{c1}$) uniform microwave magnetic fields polarized parallel to either the $\hat{a}$ or $\hat{b}$ axis, as shown in Fig. 3.3. For samples with very high aspect ratios ($x_a, x_b \gg x_c$), demagnetization factors are negligible for the chosen geometry, so the applied field can be equated to the actual field at the superconductor-vacuum interfaces [48]. Diamagnetic screening currents flow across the broad $\widehat{ab}$ oriented surfaces perpendicular to $\vec{H}_{rf}$ and then along the $\hat{c}$ direction on the thin $\widehat{ac}$ or $\widehat{bc}$ faces, depending upon orientation of the crystal. Along these directions the superconducting coherence length ξ is small so one avoids the nonlocal superfluid electrodynamics of Kostzin and Leggett [49] in which a Cooper pair would experience a nonuniform magnetic field over the extent of its wavefunction. Furthermore, if one ignores the edges, then each $(CuO_2)^{2-}$ plane experiences a uniform magnetic field that decays exponentially in magnitude (on a lengthscale λ_a or λ_b) away from the broad $\widehat{ab}$ oriented surfaces. In this scenario the field should be uniform in each $(CuO_2)^{2-}$ plane over lengthscales much greater than the in-plane quasiparticle mean free path ℓ_{ab} and the out of plane quasiparticle mean

free path ℓ_c will be much shorter than λ_a, λ_b (because of the substantial in-plane:out of plane anisotropy in charge conductivity in the cuprates). The conclusion is that charge transport in $YBa_2Cu_3O_{6+x}$ will not be subject to the nonlocal electrodynamics of Pippard [1, 50] in which a quasiparticle would experience a nonuniform magnetic field over its trajectory.

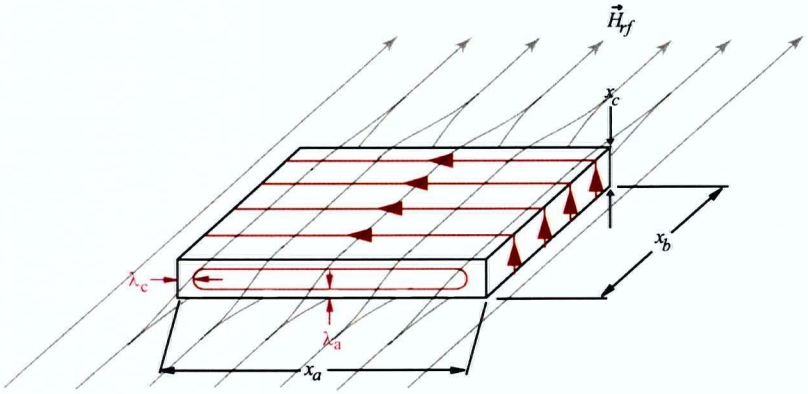

Figure 3.3: Canonical measurement geometry in the UBC superconductivity laboratory. A thin superconducting platelet is immersed in a weak uniform microwave magnetic field $\vec{H}_{rf}$ polarized parallel to the $\widehat{ab}$ plane. In this example, $\vec{H}_{rf} \parallel \hat{b}$ so screening currents run in the $\hat{a}$ direction across the broad faces and along the $\hat{c}$ direction on the thin edges. Fields penetrate into the broad surfaces on a lengthscale λ_a. Rotating the crystal 90° about the $\hat{c}$-axis forces screening currents to run in the $\hat{b}$ direction on the broad surfaces and the penetration depth with then be λ_b.

The flow of diamagnetic screening currents in the geometry of Fig. 3.3 generates two observable consequences. First and foremost, the interior of the sample is screened from the applied field. For simplicity, if one considers an infinite slab of thickness x_c with applied field $\vec{H}_{rf}$ on both sides, then solving London's and Maxwell's equations reveals that the sample has a magnetic moment $\vec{m}$ aligned antiparallel to the applied field [48]:

$$|\vec{m}| \approx V_{sample}\left(1 - \frac{2\lambda}{x_c}\right)|\vec{H}_{rf}| \tag{3.8}$$

where $V_{sample} = x_a \times x_b \times x_c$ is the volume of the sample. The second consequence is power dissipation due to the flow of thermally excited quasiparticles. Using the definition of surface resistance R_s, the total power dissipated will vary proportional to the amount of surface area exposed to the applied field:

$$P = \mu_o^2 \int_S dS R_s H_{rf}^2 \propto \frac{V_{sample}}{x_c} R_s \tag{3.9}$$

3.4 Measuring Surface Impedance

3.4.1 Broadband Bolometry Apparatus

The broadband bolometry apparatus is primarily the domain of Patrick Turner and the reader is referred to his writings for specific details [51, 52]. However, as it is important to view experimental data in context, this author will briefly describe the apparatus herein.

The core of the broadband bolometry apparatus is a short section of coaxial transmission line of rectangular cross section whose interior is coated with PbSn solder ($T_c \sim 7\,K$). One end of this line is shorted by a flat wall and the other is connected to standard 0.141" outer diameter stainless steel cylindrical coaxial line. The rectangular section is held at a base temperature of $1.3\,K$ by contacting it with a pumped liquid helium bath inside a glass walled cryostat. The stainless steel line connects the rectangular segment to a broadband ($0.01 \rightarrow 26.5\,GHz$) microwave synthesizer and amplifier at room temperature. When microwave power is transmitted from the source, a TEM standing mode is established with a magnetic field maximum and electric field minimum located at the short [53]. Due to the rectangular geometry the microwave magnetic fields are symmetric and relatively uniform on lengthscales of $1\,mm$ on either side of the broad faces of the centre conductor near the short (see Fig. 3.4). A $YBa_2Cu_3O_{6+x}$ sample and a reference Ag:Au alloy (70:30) are placed in the uniform field on either side of the centre conductor supported by thin ($2\,mm \times 0.004''$ cross section) high purity sapphire plates that are thermally isolated from the rectangular coaxial structure. The sapphire plates protrude outside of the microwave structure through $4\,mm$ diameter holes (cutoff frequency $\gg 20\,GHz$) and have weak thermal links to the helium bath through a quartz tube (for superconductor sample) or a thin walled stainless steel tube (for the Ag:Au reference sample). A chip heater and Cernox [54] RuO thin film resistor are mounted on each sapphire plate near the thermal weak link.

During the course of an experiment the microwave power is modulated at a low frequency of $1\,Hz$ (a frequency limited by the thermal response time of the sample stages) and the temperature rises due to power dissipation in the samples are monitored via 4-probe resistance measurements of the Cernox sensors. Lock-in amplifiers are used to monitor the periodic temperature variations that are typically on the order of $\mu Kelvin$'s. The ratio of the signals from each sample is then proportional to the ratio of the samples' surface resistances if they experience identical microwave fields, as per Eq. 3.9. This procedure normalizes out the variations in microwave power as a function of frequency. The thermal sensitivity of each sample stage is calibrated absolutely by turning off the microwave power and applying a known amount of heat via the chip heaters. Thus the absolute power dissipated in each sample is known and their ratio yields

$$\frac{P_{sc}}{P_{ref}} = \frac{R_s^{sc} A_{sc}}{R_s^{ref} A_{ref}} \tag{3.10}$$

where P_i, R_s^i and A_i are the power dissipation, surface resistance and broad surface area of either the superconductor (sc) or reference sample (ref). One can then isolate

R_s^{sc} by a measurement of the surface areas of both samples and by a calculation of the surface resistance of the reference alloy from the DC conductivity, σ_o, via the skin depth formula [55]:

$$R_s^{ref}(\Omega) = \sqrt{\frac{\mu_o \Omega}{2\sigma_o}} \tag{3.11}$$

The value of σ_o at low temperatures is obtained from a 4-point resistivity measurement in a separate apparatus.

The bolometry apparatus is able to measure continuously between $\sim 0.3 \rightarrow 22.5\,GHz$, being limited at low frequencies by small signals from $YBa_2Cu_3O_{6+x}$ and at high frequencies by asymmetric microwave resonances inside the rectangular coaxial line. One can also perform measurements at higher temperatures by regulating the sample stage using the chip heater. However, measurements for superconducting samples are currently limited to a base temperature of $1.3\,K$ and an upper temperature of about $10\,K$ due to the loss of sensitivity of the Cernox sensors. The ultimate accuracy of all measurements with this apparatus is limited by the systemic error of $\pm 10\%$ in the measurement of σ_o for the Ag:Au reference alloy. Measurements of R_s^{sc} typically have 10% stochastic error at $\Omega/2\pi < 1\,GHz$ and less than 5% at higher frequencies. The reader is referred to Ref. [51] for further details.

Measurements of the in-plane surface resistance of *Ortho-II* ordered $YBa_2Cu_3O_{6.5}$ (underdoped) and $YBa_2Cu_3O_{6.993}$ (overdoped) are shown in Figs. 3.5 and 3.6, respectively. The $\hat{a}$ axis data have been published previously in Refs. [26, 51].

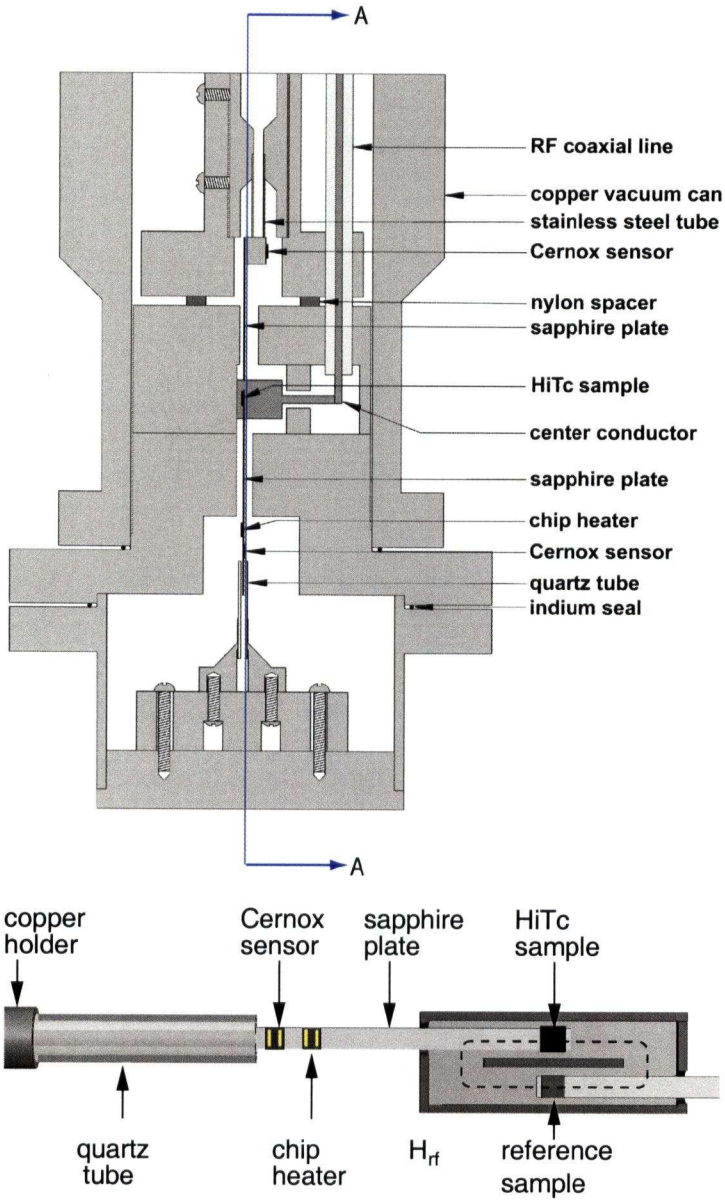

Figure 3.4: The core of the broadband microwave bolometry apparatus. Upper panel shows a cross section through the copper vacuum can of the bolometry probe. The Ag:Au alloy sample stage feeds into the rectangular coaxial line from above while the superconducting sample stage does so from below. The entire can is immersed in a pumped liquid He bath during operation. Lower panel shows the central portion of the Section A-A through the upper panel. The dashed line indicates a contour of constant magnetic field strength around the broad centre conductor. Figures provided courtesy of P. Turner [56].

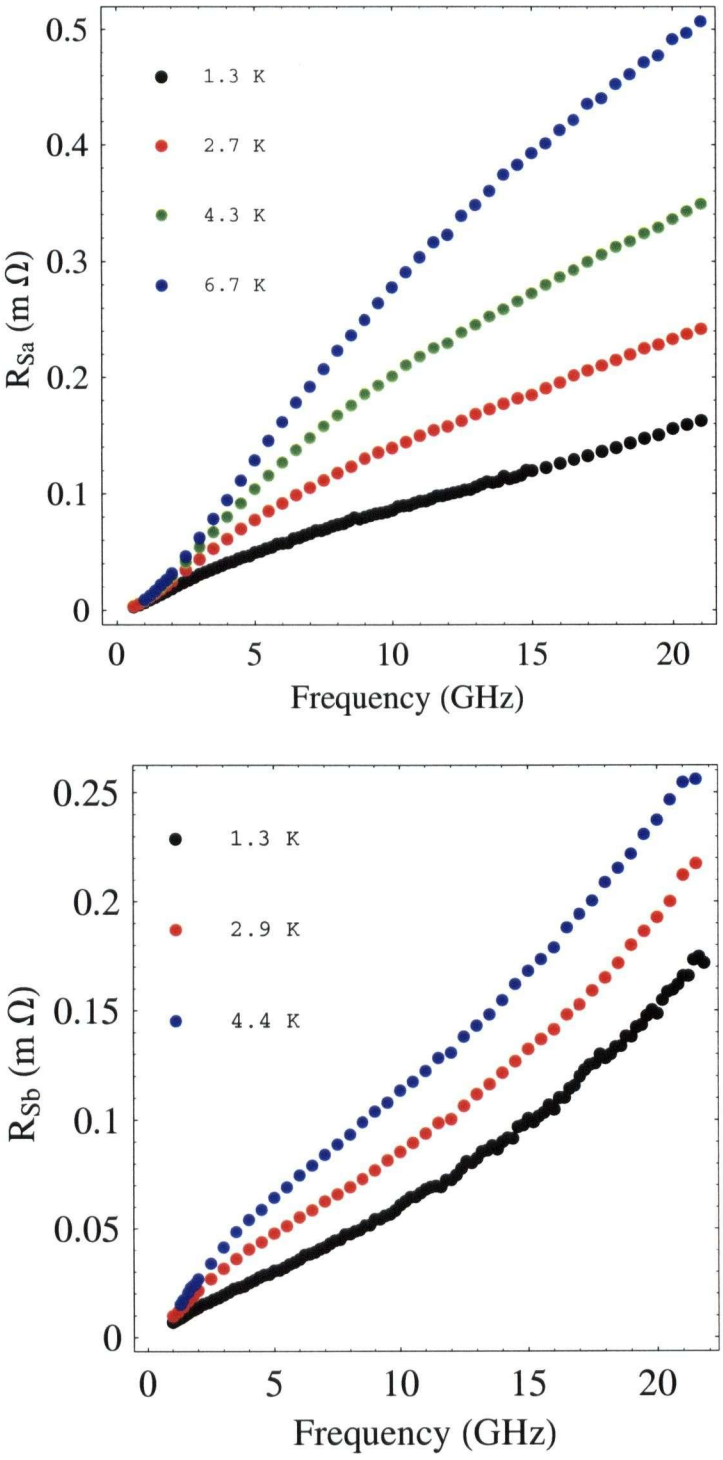

Figure 3.5: The in-plane surface resistance of *Ortho-II* ordered $YBa_2Cu_3O_{6.5}$ (underdoped) measured via broadband bolometry: R_{sa} (upper panel) and R_{sb} (lower panel).

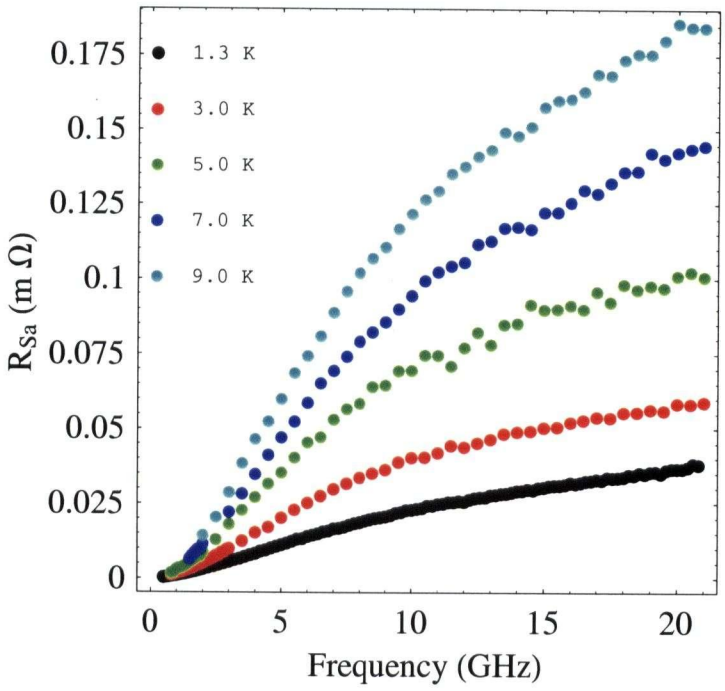

Figure 3.6: The $\hat{a}$-axis surface resistance of $YBa_2Cu_3O_{6.993}$ (overdoped) measured via broadband bolometry.

3.4.2 Microwave Cavity Perturbation

A forte of the UBC superconductivity programme is the design of high Q superconducting resonators for performing cavity perturbation experiments at discrete frequencies. The laboratory has a suite of such experiments that have been constructed and operated by a number of students; 1.14 *GHz* (Dr. Saeid Kamal and Geoff Mullins), 2.25 and 2.99 *GHz* (Pinder Dosanjh), 13.4 and 22.7 *GHz* (Dr. Ahmad Hosseini) and 75.4 *GHz* (this author).

Consider an enclosed metallic cavity that supports a well defined electromagnetic resonant mode [57] at a frequency f_o, as depicted in Fig. 3.7. The electromagnetic energy stored in this mode is given by

$$E_{stored} = \int_{V_o} dV \left(\vec{E}_o \cdot \vec{D}_o - \vec{H}_o \cdot \vec{B}_o \right) \tag{3.12}$$

where $\vec{E}_o = \epsilon_o \vec{D}_o$ and $\vec{B}_o = \mu_o \vec{H}_o$ are the electric and magnetic fields of the resonance mode and V_o is the volume of the unperturbed cavity. Now consider a thin superconducting platelet inserted into a region of the resonator where there is a uniform microwave magnetic field, as depicted in Figs. 3.3 and 3.7. The diamagnetic moment of the sample results in the reduction of the stored magnetic energy within the resonator, which then shifts the resonant frequency by an amount δf. For an infinite superconducting slab of thickness x_c, $\delta f / f_o$ is proportional to the magnetic moment (Eq. 3.8) divided by the energy stored in the unperturbed mode:

$$\frac{\delta f}{f_o} = \mathbf{C} \frac{V_{sample}}{V_o} \left(1 - \frac{\tanh(x_c/2\lambda)}{x_c/2\lambda} \right) \tag{3.13}$$

where λ is either $\lambda_a(T)$ or $\lambda_b(T)$, depending upon the orientation of the slab with respect to $\vec{H}_{rf}$. $\mathbf{C}$ is a geometric factor which can be obtained by calibrating with a well characterized metallic sample (see below). In the limit $\lambda \ll x_c$ the above expression reduces to

$$\frac{\delta f}{f_o} = \mathbf{C} \frac{V_{sample}}{V_o} \left(1 - \frac{2\lambda}{x_c} \right) \tag{3.14}$$

At low temperatures one can relate the shift in frequency to the surface reactance via Eq. 3.7. However, it is more customary in the field of superconductivity to present data in terms of $\lambda(T)$ or $1/\mu_o \lambda^2(T)$ rather than $X_s(\Omega \to 0, T)$.

The surface resistance of the superconducting sample dissipates energy from the resonant mode. This results in a reduction of the quality factor Q of the resonance [53], defined via

$$\delta \left(\frac{1}{Q} \right)_{sc} \equiv \frac{\text{energy dissipated by superconductor per period}}{2\pi E_{stored}} = \mathbf{C} \frac{\mu_o \Omega V_{sample}}{V_o x_c} R_s^{sc} \tag{3.15}$$

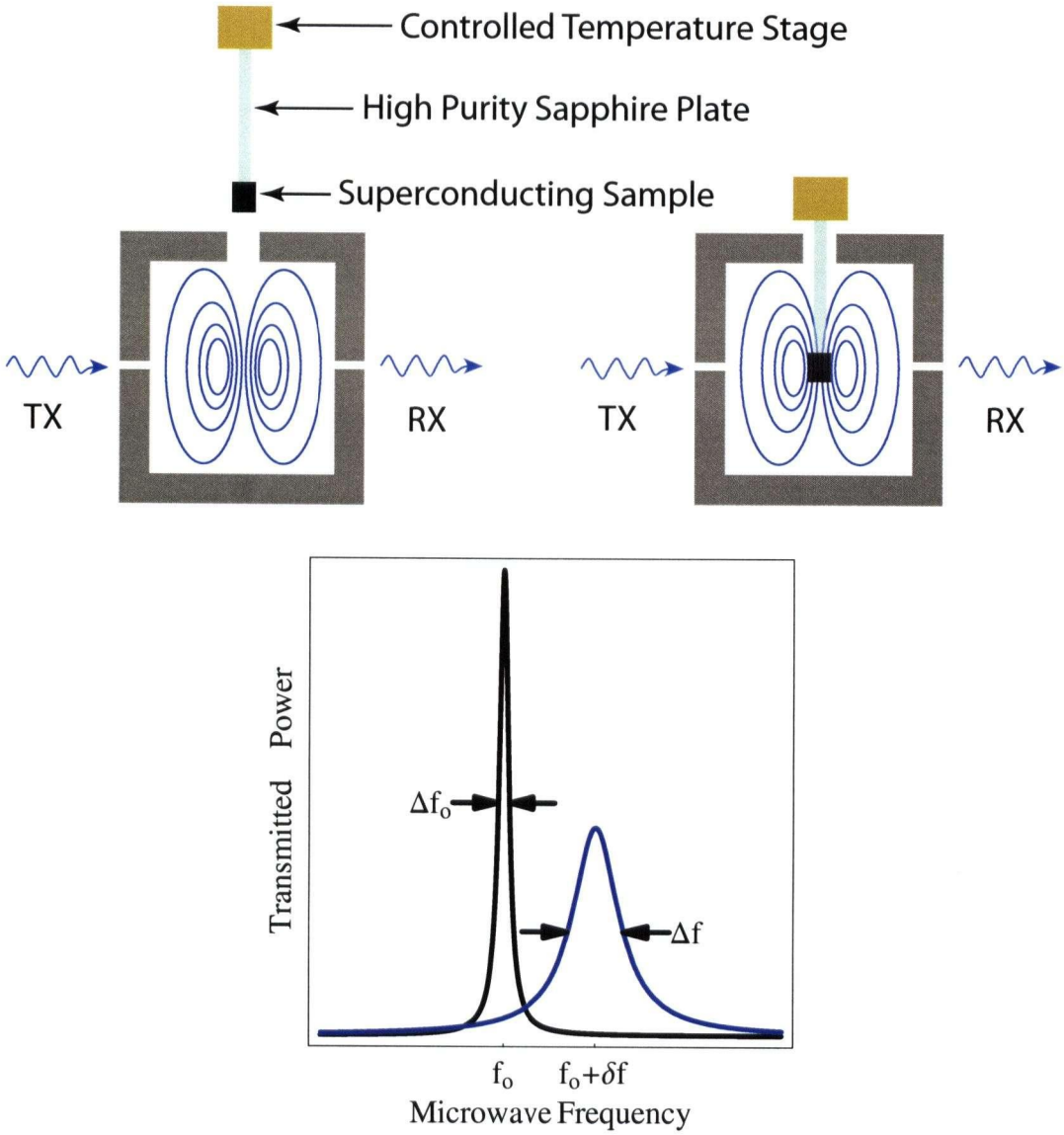

Figure 3.7: The principles of cavity perturbation. An unloaded cavity (top right panel) is coupled into a microwave transmission line via transmitter input (TX) and receiver output (RX) ports. Magnetic field lines (sketched in blue) for a high $Q_o \equiv \Delta f_o / f_o$ resonance mode at frequency f_o generate a uniform field at the centre of the resonance structure. A superconducting sample secured to a high purity sapphire plate that is isothermal with a controlled temperature stage outside of the resonator. Upon inserting the superconducting sample into the uniform field (top left panel), the resonance frequency shifts by an amount δf and the new quality factor becomes $Q = \Delta f / f_o < Q_o$. Note that the thermal stage is kept outside of and thermally isolated from the resonator.

Surface Resistance

Each cavity perturbation experiment in the UBC Superconductivity Laboratory is unique and has been the topic of at least one thesis ($1.14\,GHz$ [58, 59];$2.25, 2.99\,GHz$ [60]; $13.4\,GHz$ [61]; $22.7\,GHz$ [62]; $75.4, GHz$ [63]). While all of these experiments operate upon the same general principles, they differ significantly in their implementation. For this reason, only the $75.4\,GHz$ apparatus (which was the assembled and operated by this author) will be discussed in detail in this thesis.

As stated above, a convienient means of producing a relatively homogeneous microwave magnetic field is to employ an appropriate resonance mode inside a resonant cavity. There are many possible geometries capable of producing potentially useful resonances at any given frequency, but the TE_{011} resonance mode in a right cylindrical cavity has proven to be quite practical at frequencies greater than $\approx 10\,GHz$. The field profiles can be found in any standard microwave circuitry textbook [64], and the key features of the $75\,GHz$ TE_{011} resonator are sketched in Fig. 3.8.

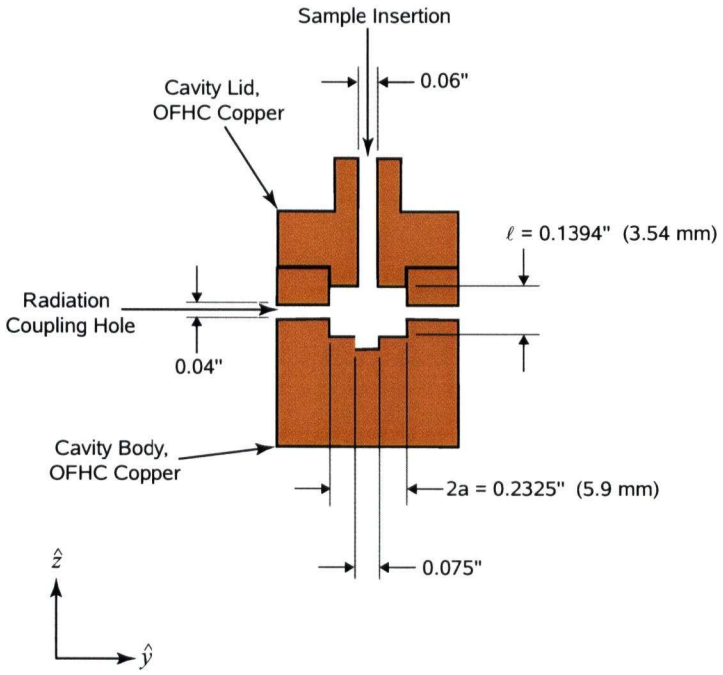

Figure 3.8: A cross section of the $75\,GHz$ TE_{011} mode right cylindrical resonator. ℓ represents the length and a the radius of the cylindrical structure. The field $\vec{H}_{rf}$ is maximized in the vertical direction at the centre of the resonator. Two holes were created for coupling radiation into and out of the resonance structure, and a third hole along the axis of the resonator allows a sample to be inserted.

The TE_{011} resonance can be characterized by the following set of equations for $\vec{E}$ and $\vec{H}$.

$$E_r = 0 \tag{3.16}$$

$$E_\theta = \frac{i\Omega_o}{k}\mu_o B J_0'(kr)\sin(\pi z/\ell) \tag{3.17}$$

$$E_z = 0 \tag{3.18}$$

$$H_r = \frac{\pi}{kl} B J_0'(kr)\cos(\pi z/\ell) \tag{3.19}$$

$$H_z = B J_0(kr)\sin(\pi z/\ell) \tag{3.20}$$

$$H_\theta = 0 \tag{3.21}$$

$$k^2 = \Omega_o^2 \epsilon_o \mu_o - \pi^2/\ell^2 = \chi^2/a^2$$

$$\chi \equiv \text{first root of } J_0' = 3.832$$

Note that near the centre of the resonator, $\vec{H}_{rf} \approx H_z\vec{z}$ and $\vec{E} \approx 0$. By employing an appropriate aspect ratio of $\ell/2a \sim 1.7$, one can locate the TE_{011} resonant frequency Ω_o well away from other resonant modes, an exception being the TM_{111} mode [65]. However, the small indentation in the bottom of the resonator, as indicated in Fig. 3.8 serves to remove this degeneracy. The TM_{111} mode has a magnetic field maximum at the centre of the top and bottom faces of the resonator. The indentation effectively increases the volume of the resonator for the mode, thus moving its resonance to a lower frequency. This alteration should have a negligible effect upon $\vec{H}$ in the TE_{011} mode.

Nearly lossless resonator walls are essential to obtain the required sensitivity. By electrochemically coating the interior of the resonator with a sufficiently thick superconducting $Pb_{0.95}Sn_{0.05}$ alloy ($T_c \sim 7\,K$) and cooling the resonator structure with a liquid ^4He bath regulated at $1.3\,K$, one can obtain relatively high values of the unperturbed quality factor Q_o. It has been determined from experience within the UBC superconductivity laboratory that a $Pb_{0.95}Sn_{0.05}$ coating approximately $1\,\mu m$ thick effectively shields the copper walls of the resonator from the impinging fields.

The superconducting sample is thermally isolated from the resonator using a sapphire hotfinger [66] similar to those used in the bolometry apparatus. However, in this case the heater and Cernox thermometer are used solely as elements in a feedback circuit to regulate the sample temperature. The $75.4\,GHz$ hotfinger assembly is shown in Fig. 3.9. A 0.004" thick and $0.5\,mm$ wide sapphire (Al_2O_3) plate is secured to an oxygen free high conductivity (OFHC) copper block using #2303 Stycast epoxy and the sample is mounted on the opposite end with a minute drop of NonAq stopcock grease. Sapphire was chosen for its high thermal conductivity and its very low losses when subjected to an rf magnetic field [67]. The thermometer and heater are secured to the copper block and a weak thermal link to the ^4He bath is established through the thin walled stainless steel tube. The entire hotfinger assembly is then held in a vertical translation stage referred to as the sample gantry, which is shown in Fig. 3.10.

The gantry allows for the sample to be loaded and unloaded from the microwave cavity during the course of an experiment (motion in the $\vec{z}$ direction of Fig. 3.10), thereby facilitating in situ measurements of Q_o. The design presented herein provides minimal intrusion of components into the resonator and almost complete thermal isolation of the sample from the resonator. However, it must be recognized that the sapphire and grease will introduce dielectric losses due to the field E_θ in the TE_{011} resonance mode. This rightfully introduces another loss term into the numerator of Eq. 3.15 and will be discussed further below.

The practical issues surrounding the propagation and coupling of signals at frequencies near $75\,GHz$ required that this experiment's microwave circuitry be rather different as compared to the other microwave devices presently being used at UBC. At such high microwave frequencies, hollow metallic waveguides are preferable over coaxial cables for propagation due to high losses in the latter, however even the waveguides will attenuate signals very rapidly since the surface resistance of the the waveguide walls $R_{S(metal)} \propto \sqrt{f}$. Furthermore, the problem of standing modes in long lengths of waveguide is a serious concern at high frequencies as they could complicate coupling into and out of the resonator.

The solution to the propagation loss problem involved placing the radiation source and detector as close as possible to the resonator, thus minimizing the length of waveguide required. This in turn prompted the need for alternative cryogenics since the conventional glass immersion dewar and modular probe design used for the 1.14, 2.25, 2.99, 13.4 and $22.7\,GHz$ apparatus require microwave propagation paths approximately $2\,m$ long [58, 60–62]. An Infrared Laboratories HDL-8 dewar with a ^4He cold plate was chosen for the task, and the layout of the dewar contents is shown in Fig. 3.11. In this design the total high frequency path length is only approximately $30\,cm$, as one can access the cold plate via ports in the sides of the dewar. However, an obvious concern is the inevitable heat leakage through the waveguides, as they support large thermal gradients from room temperature to $1.3\,K$ over a distance of only $10\,cm$. To minimize the thermal load on the He bath, the critical parts of the waveguide were manufactured from 0.015" thick stainless steel. Since the microwave circuit elements are not immersed in the coolant, it was necessary to take extra precautions when heat sinking components to the cold plate. Wakefield Engineering thermal compound and a grease loaded with OFHC copper, known as Cry-Con grease, were employed.

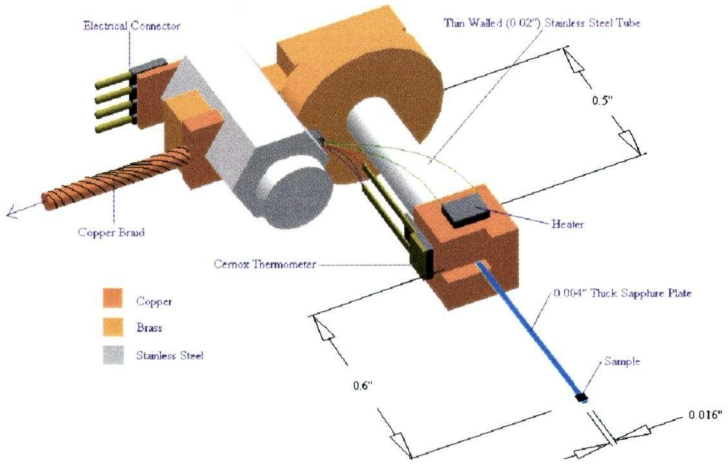

Figure 3.9: The 75.4 *GHz* apparatus hotfinger assembly. A superconducting sample is mounted on one end of a high purity sapphire plate. The opposing end is glued to a controlled temperature stage with a thin walled stainless steel tube serving as a thermal break between the stage and the 1.3 K He bath. One end of the copper braid (not shown) is bolted to a cold stage which is in contact with the 1.3 K He bath.

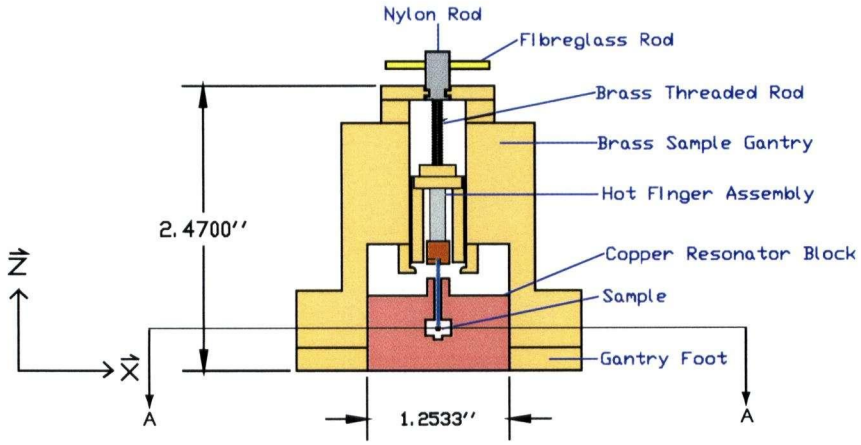

Figure 3.10: The 75.4 *GHz* apparatus sample gantry. The hotfinger assembly of Fig. 3.9 is held vertically inside the mechanical gantry. The superconducting sample can be completely removed from the cylindrical TE_{011} resonance cavity.

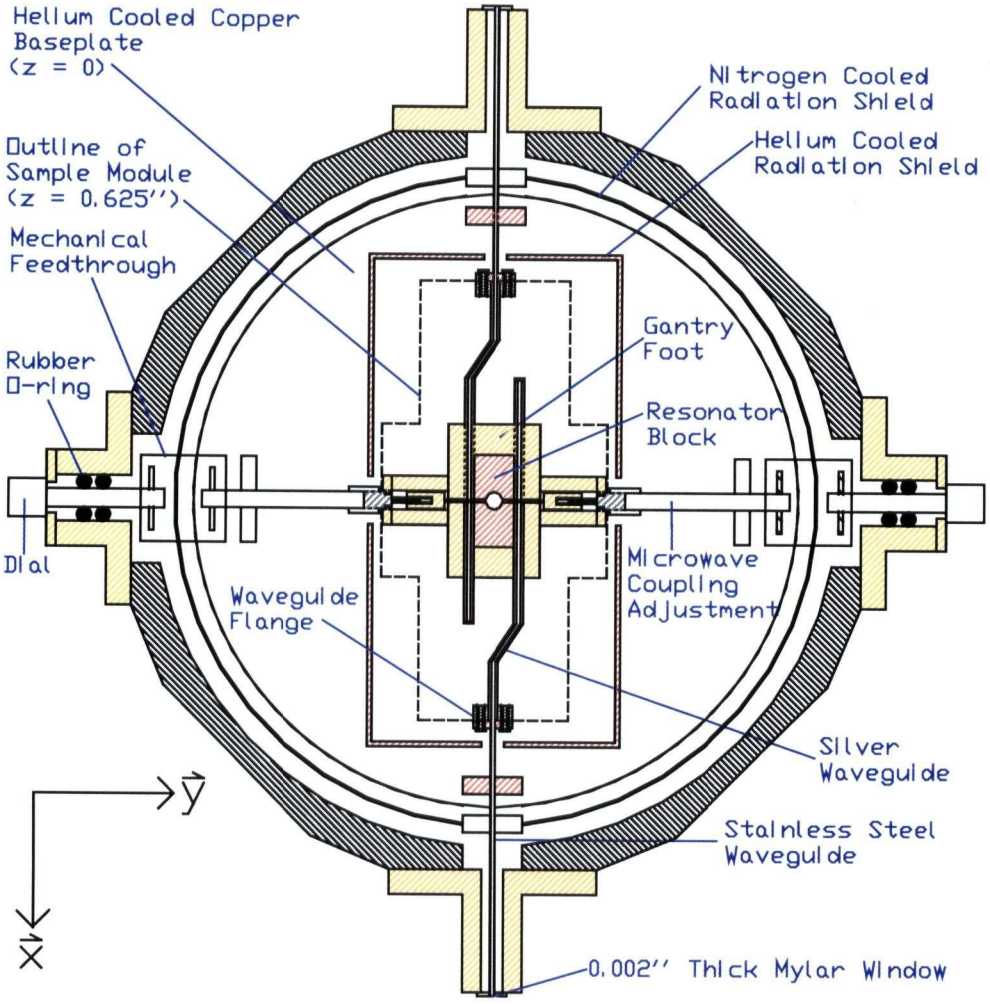

Figure 3.11: A cross section of the microwave circuitry inside the dewar, at $z = 1$" below the helium cooled baseplate (the dewar is inverted during operation, refer to Fig. 3.14). Shown in this diagram are the sections of waveguide, microwave coupling adjustment mechanisms and the resonator in the centre. The resonator block, sample gantry, microwave couplings and those section of waveguide near the resonator all reside on a 0.625" thick copper plate that can be easily removed from the dewar. This figure corresponds to cross section A-A through Fig. 3.10.

Coupling was accomplished via antennae fabricated from thin superconducting wires that coupled to electric fields in the waveguides and magnetic fields in the coupling holes on either side of the cylindrical TE_{011} resonator (see Fig. 3.12). Both the input and output coupling to the resonator can be adjusted in situ via mechanical feedthroughs which allow for motion of the antennae in the $\vec{y}$ direction of Fig. 3.12. Additional heat leaks through the feedthroughs were minimized by employing mechanisms that allow for complete thermal isolation of these components when they are not being adjusted, as shown in Figure 3.13. The experimenter can engage the mechanical feedthrough by rotating the dials on the outside of the dewar (see Fig. 3.11) such that both fibreglass rods in Fig. 3.13 contact the rotating aluminum part on the N_2 cooled shield, and then disengage it by an appropriate sequence of partial rotations of the external dial.

A schematic diagram of the complete apparatus is shown in Fig. 3.14. The reader should note that there are four subsystems associated with this experiment: the microwave circuit, thermometry circuit, cryogenics and a computer to coordinate the data acquisition and thermometry.

The critical components of the microwave circuit are the 75 GHz resonator, Schottky diodes for generating and detecting the $75\,GHz$ signal, an HP 83620A microwave synthesizer and HP 83498 microwave amplifier for generating a $15\,GHz$ signal and an ABmm millimeter vector network analyzer (MVNA) for signal processing [68]. Isolators were used to improve signal quality and a directional coupler was needed to feed a sample of the $15\,GHz$ signal into the MVNA. The diode for generating the input signal, known as the harmonic generator (HG), and the diode for detecting the signal transmitted through the cavity, known as the harmonic mixer (HM),were tuned to optimize the response to the 5^{th} harmonic, with the $15\,GHz$ fundamental frequency supplied by the HP synthesizer. Though the MVNA was provided with an internal synthesizer (resolution of 50 kHz), it proved necessary to use an external synthesizer (resolution of 1 Hz) in order to resolve the high Q resonances encountered in this experiment. All measurements of Q were made in the frequency domain, with the key advantage that the MVNA provides one with a measure of both amplitude and phase of the transmitted signal.

Both the sample and resonator temperature were monitored using a 4-probe measurement of Cernox 1050 resistors, calibrated to an accuracy of $\pm 0.1\,K$. The sample temperature was regulated through a feedback circuit consisting of the sample thermometer, a metal film heater ($R \sim 300\,\Omega$) and a Conductus LTC-21 PID controller. A similar feedback circuit was available for regulation of the resonator temperature, however it proved to be unnecessary. All heaters and thermometers were secured to their respective surfaces with GE varnish.

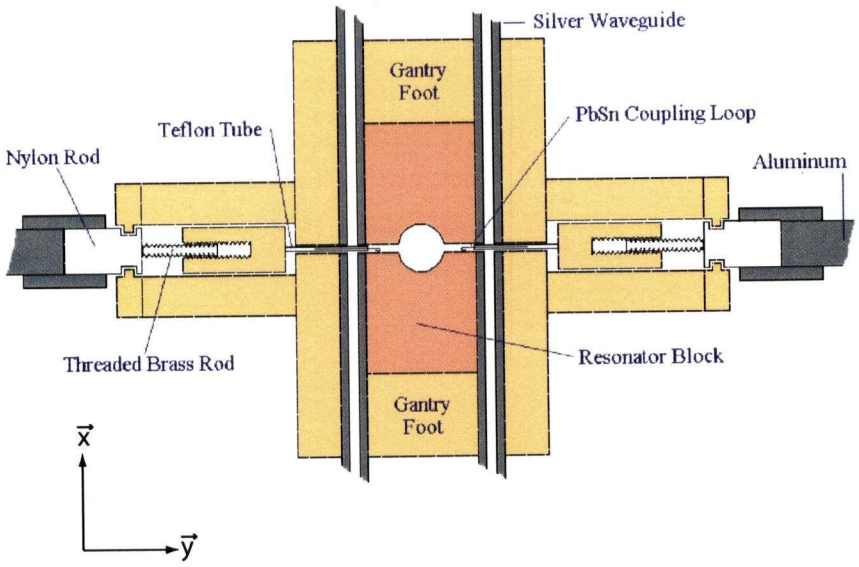

Figure 3.12: The 75.4 *GHz* apparatus coupling mechanism. Input and output microwave waveguides are coupled to the resonator via antennae that pass through the waveguides and into small coupling holes on either side of the resonance cavity. This figure corresponds to cross section A-A through Fig. 3.10.

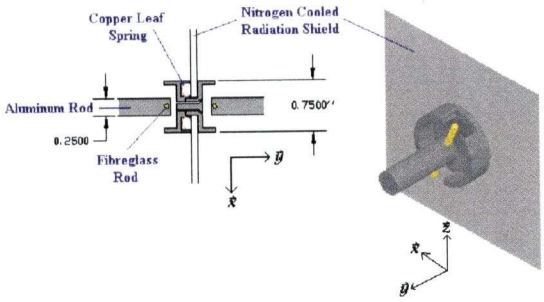

Figure 3.13: The 75.4 *GHz* apparatus mechanical feedthrough design. A rotating aluminum part passing through the N_2 cooled heat shield provides a physical connection between two aluminum shafts terminated with fibreglass rods; one at room temperature and the other in contact with the He cooled base plate. The rotating aluminum part can be completely disengaged from both fibreglass rods through a sequence of partial rotations of the room temperature shaft.

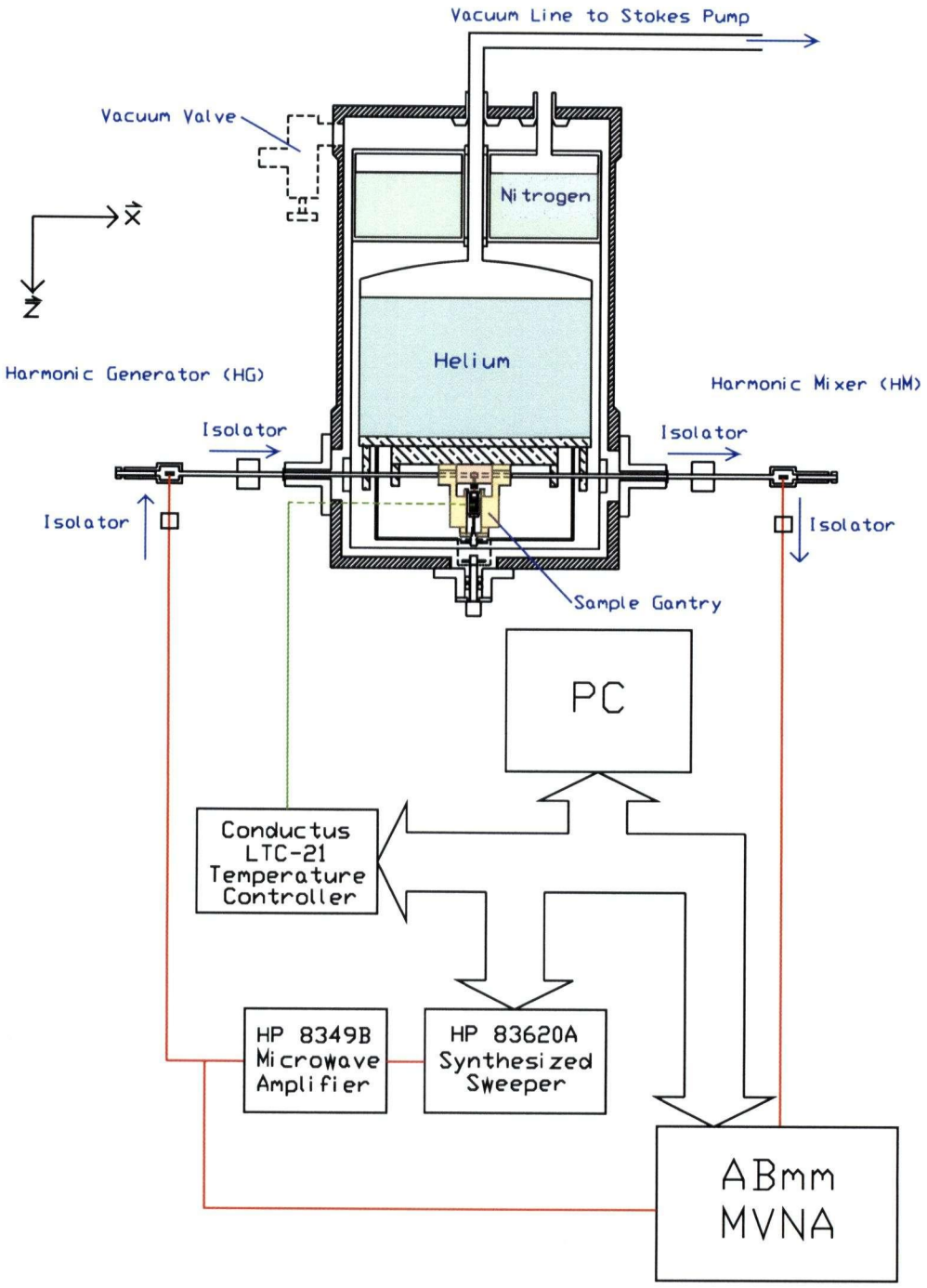

Figure 3.14: Overall schematic diagram of the 75.4 *GHz* apparatus. Microwave circuitry is denoted in red with MVNA representing a millimeter-wave vector network analyzer connected to Schottky diodes (HG and HM) for launching and detecting millimeter wave radiation into and out of the resonator circuit. Thermometry circuitry is noted schematically in green. Both the microwave and thermometry are controlled via a computer (PC) during an experiment.

In order to determine surface resistance via Eq. 3.15 one must separate out changes in $1/Q$ due to the insertion of superconducting sample alone into the microwave cavity. Rightfully an expression for Q for such a system must contain *at least* four distinct terms, with each term accounting for various energy loss mechanisms acting in series:

$$\frac{1}{Q} = \delta\left(\frac{1}{Q}\right)_{sc} + \delta\left(\frac{1}{Q}\right)_{bkgd} + \delta\left(\frac{1}{Q}\right)_{c} + \frac{1}{Q_o} \tag{3.22}$$

Here Q_o is the optimal Q of the unperturbed cavity, $\delta(1/Q)_c$ accounts for coupling losses and $\delta(1/Q)_{bkgd}$ accounts for background losses associated with the sample stage used to introduce the superconducting sample into the cavity. The former two terms can be isolated by first measuring Q with neither sample nor sample stage present. $\delta(1/Q)_{bkgd}$ can then be measured by inserting the sample stage (with no sample) into the resonator and measuring Q again. Finally, $\delta(1/Q)_{sc}$ can be determined by subtracting the three rightmost terms of Eq. 3.22 from the measured $1/Q$ with the sample present.

There are many ways to experimentally measure Q [61, 63]. The method of choice for the $75.4\,GHz$ apparatus is to weakly couple the cavity to input and output transmission lines and then observe the transmitted power $P(f) \equiv |A(f)|^2$ as a function of frequency f at constant input power, where $A(f)$ is the complex amplitude of the transmitted wave. The observed resonance can be fit to a Lorentzian lineshape parameterized as a circle in the complex amplitude plane:

$$A(f) = \frac{|A(f_o)|}{1 + \imath(\frac{f}{f_o} - \frac{f_o}{f}) \cdot \frac{f_o}{\Delta f}} e^{\imath(\phi(f_o) + (f - f_o)\frac{d\phi}{df}|_{f_o})} + x_{leak} + \imath y_{leak}$$

The free parameters $|A(f_o)|$ and $\phi(f_o)$ correspond to the amplitude and phase of the transmitted wave at the resonance frequency f_o, while Δf represents the full width at half maximum (FWHM) of the transmitted power spectrum. Thus $Q \equiv f_o/\Delta f$ is an implicit fitting parameter [53]. Any slowly varying background signals are accounted for by the free parameters x_{leak}, y_{leak} and $d\phi(f_o)/df$.

As with the bolometry apparatus, calibration is accomplished by measuring the surface resistance of a metallic sample similar in size to a typical $YBa_2Cu_3O_{6+x}$ sample. The choice material for calibrating resonators has been a $Pb_{0.95}Sn_{0.05}$ alloy (superconducting transition $T_c \sim 7\,K$) which obeys the skin depth relation (Eq. 3.11) for $T > T_c$. Measurements performed at the base temperature of $1.3\,K$ (where the calibration sample is superconducting) can be used to infer nonperturbative corrections due to distortions of the resonant fields caused by strongly diamagnetic samples, assuming $R_s^{ref} \ll R_s^{sc}$ at this temperature. Although the resonators are only capable of measuring R_s at a single frequency, they can measure over a much broader temperature range than the bolometry apparatus. The sensitivity of a cavity perturbation is ultimately limited by the filling factor V_{sample}/V_o and by large values of R_s (encountered at temperatures well above T_c of $YBa_2Cu_3O_{6+x}$) which can reduce Q to nearly zero.

The reader is referred to Appendix A for a detailed description of how R_{sa} and R_{sb} were obtained from measurements on a sample of $YBa_2Cu_3O_{6.993}$ (overdoped) at $75.4\,GHz$. Appendix A also contains measurements on a sample of *Ortho-II* ordered $YBa_2Cu_3O_{6.5}$ (underdoped) and explains why the $75.4\,GHz$ apparatus could not yield reliable results for this doping.

Measurements of R_{sa} and R_{sb} from cavity perturbation experiments on underdoped *Ortho-II* ordered $YBa_2Cu_3O_{6.5}$ and overdoped $YBa_2Cu_3O_{6.993}$ are shown in Figs. 3.15 and 3.16, respectively. Only the data in the latter have been published previously in Ref. [69] ($\hat{a}$-axis) and Ref. [43] ($\hat{b}$-axis). The data from each resonator experiment have been calibrated independently and there can exist up to a 10% systematic error due to uncertainty in measuring σ_o of the PbSn alloy used for calibration. Stochastic noise is typically less than 5% for measurements well below T_c. Uncertainty in the nonperturbative corrections have been estimated to be ± 0.2, 10, 10, 20 and $360\,\mu\Omega$ at 2.25, 2.99, 13.4, 22.7 and $75.4\,GHz$, respectively. A relatively large uncertainty of $\pm 0.7\,\mu\Omega$ is quoted for measurements at $1.14\,GHz$ for reasons that will be explained in short order.

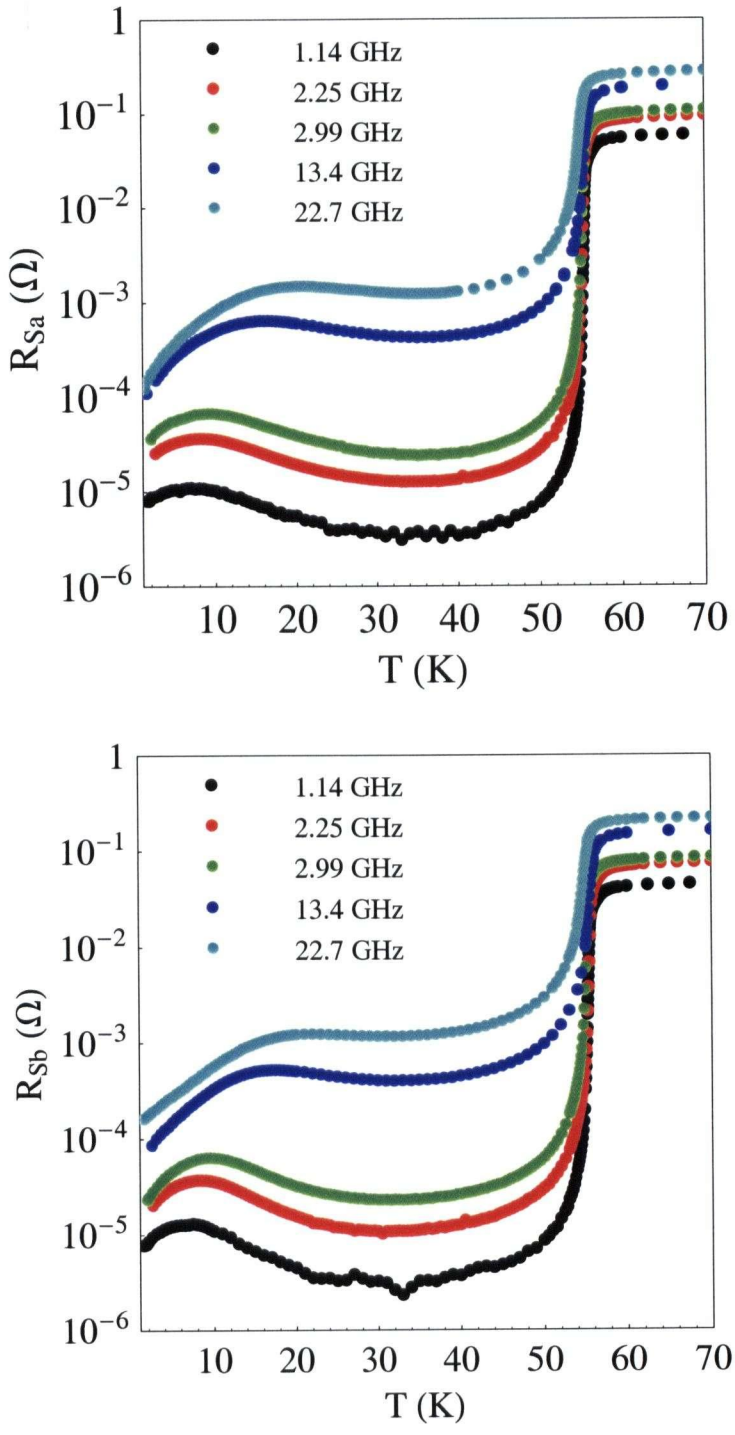

Figure 3.15: The in-plane surface resistance of *Ortho-II* ordered $YBa_2Cu_3O_{6.5}$ (underdoped) measured via cavity perturbation: R_{sa} (upper panel) and R_{sb} (lower panel).

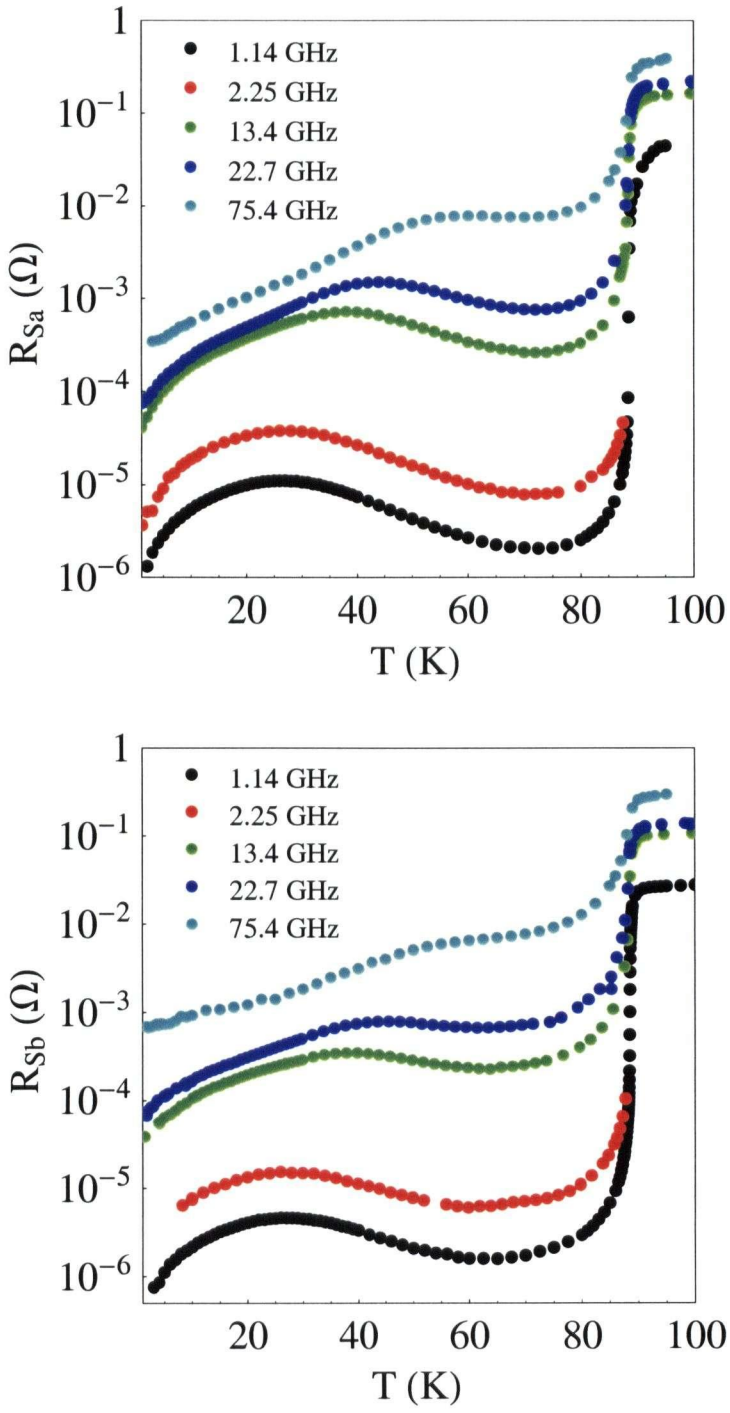

Figure 3.16: The in-plane surface resistance of $YBa_2Cu_3O_{6.993}$ (overdoped) measured via cavity perturbation: R_{sa} (upper panel) and R_{sb} (lower panel).

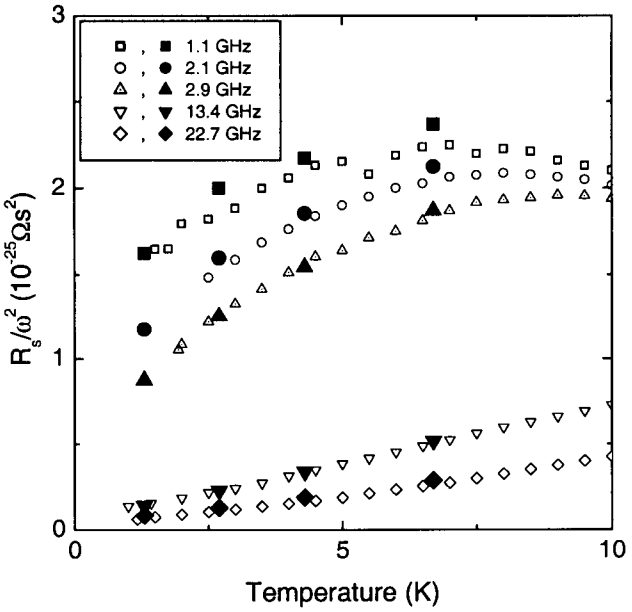

Figure 3.17: A demonstration of the agreement between measurements performed with the broadband bolometry apparatus (solid points) and cavity perturbation experiments (hollow points) on $YBa_2Cu_3O_{6.5}$. Figure provided courtesy of P. Turner [56].

It is worthwhile concluding this description of experimental approaches to measuring surface resistance with a demonstration of consistency between probes. As an example, the low temperature R_{sa} of the underdoped material, as measured by both the broadband bolometry apparatus and five different cavity perturbation experiments, is shown in Fig. 3.17. As one can see, with the exception of the 1.14 *GHz* cavity perturbation measurements, the level of agreement is quite exceptional. Recall that each experiment has been *independently* calibrated.

Surface Reactance

As stated in Eq. 3.14, one must measure shifts in resonance frequency due to the diamagnetic moment of a superconducting sample in order to determine X_s or equivalently λ. This quantity has particular relevance at low frequencies $\Omega \rightarrow 0$ because one can then claim $\lambda \approx \lambda_L$ and determine superfluid density via Eq. 3.3. The 1.14 *GHz* apparatus is dedicated to performing this task and the reader is referred to Refs. [58] and [59] for specific details. However, it is important to note that this cavity perturbation experiment differs from the others in that the sample is held *rigidly* inside the resonator and cannot be loaded/unloaded during the course of an experiment. This experimental approach helps to minimize microphonics which will contribute to noise in the measurement of f_o. Furthermore, it is very difficult to load/unload a sample with sufficient mechanical precision to reliably measure temperature dependent

shifts in f_o due to changes in $\lambda(T)$ alone at low temperatures. As such, the $1.14\,GHz$ apparatus provides high precision measurements of $\Delta\lambda(T) \equiv \lambda(T) - \lambda(T_{base})$ with $T_{base} \approx 1.3\,K$. However, one can obtain neither $\lambda(T_{base})$ nor the unloaded Q_o of the resonator (hence the uncertainty in R_s) during the course of an experiment.

In order to determine $\lambda(T_{base})$ absolutely one must turn to a completely different experimental procedure that will not be elaborated upon in this thesis - this story will be left for others to tell [70, 71]. All that will be mentioned is that one can measure the absolute intensity of the zero field electron spin resonance (ESR) absorption lines of Gd^{3+} ions doped into the Y sites of $YBa_2Cu_3O_{6+x}$. This is accomplished using the broadband bolometry apparatus discussed previously. Within the superconducting state the intensity of the absorption lines is proportional to $\mu_o\Omega\lambda(T)\chi''(\Omega,T)$, where the imaginary part of the Gd^{3+} spin susceptibility $\chi''(\Omega,T)$ can be calculated from first principles. Comparing with the observed power absorption as a function of frequency Ω then yields $\lambda(T)$ *absolutely*. Preliminary values of $\lambda_a(T_{base})$ and $\lambda_b(T_{base})$ for $YBa_2Cu_3O_{6.5}$ and $YBa_2Cu_3O_{6.993}$ are presented in Table 3.1.

The normalized $\hat{a}$-axis and $\hat{b}$-axis superfluid density (Eq. 3.4) for *Ortho-II* ordered $YBa_2Cu_3O_{6.5}$ and $YBa_2Cu_3O_{6.993}$ are presented in Fig. 3.18. Again, only the overdoped data have been published previously in Refs. [43, 69, 72], however these authors used very different absolute values of the low temperature penetration depth ($\lambda_a(T_{base} = 1600\,\text{Å})$ and $\lambda_b(T_{base}) = 1000\,\text{Å}$). While the choice of $\lambda(T_{base})$ has negligible impact upon the qualitative features that one can extract from surface impedance data, it does have a significant role when making quantitative comparisons between dopings and between in-plane crystal orientations. As it will be demonstrated in Chapter 4, several of the key outstanding issues noted in Ref. [43] can be resolved given the new measurements in Table 3.1.

At low temperatures all four plots of superfluid density versus temperature become linear, which is one of the hallmark signatures of a superconductor with lines of nodes in the gap function $\Delta_{\vec{k}}$ [73]. These slopes (multiplied by $\hbar/k_B$) have been noted in Table 3.1 and will play an essential role in the following two chapters.

x	$\lambda_a(T_{base})$ (Å)	$\frac{\hbar}{k_B}\frac{d(1/\mu_o\lambda_a^2)}{dT}$ $(\Omega^{-1}m^{-1})$	$\lambda_b(T_{base})$ (Å)	$\frac{\hbar}{k_B}\frac{d(1/\mu_o\lambda_b^2)}{dT}$ $(\Omega^{-1}m^{-1})$
0.5	2020 ± 200	$-(1.54 \pm 0.15) \times 10^6$	1400 ± 140	$-(3.57 \pm 0.36) \times 10^6$
0.993	1010 ± 100	$-(4.15 \pm 0.42) \times 10^6$	780 ± 78	$-(5.96 \pm 0.60) \times 10^6$

Table 3.1: Summary of $T \rightarrow 0$ limits of the in-plane penetration depth and slope of the superfluid density. Values of $\lambda_a(T_{base})$ and $\lambda_b(T_{base})$ are results from the Gd^{3+} ESR experiment and were current as of October 15, 2003. Conservative errors of $\pm 10\%$ have been placed on these values for the time being. [74]

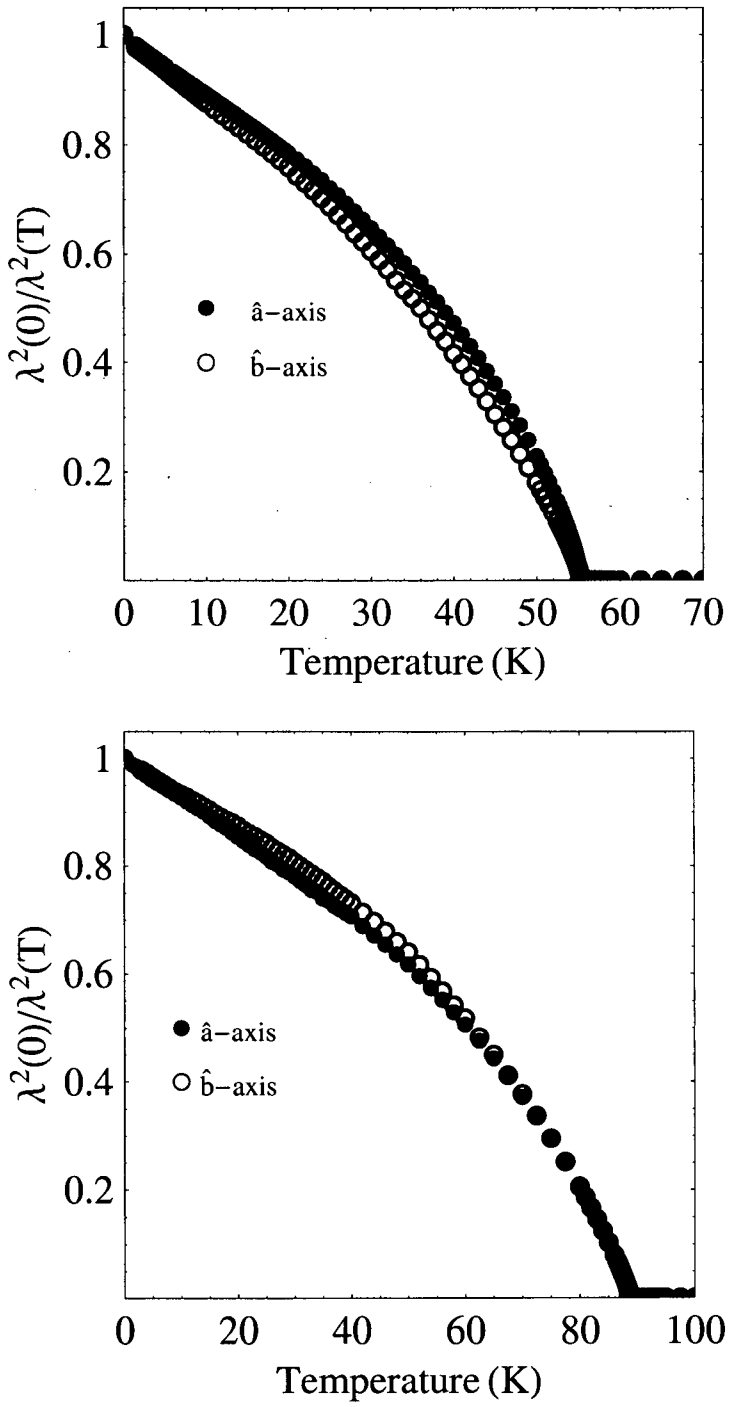

Figure 3.18: The in-plane superfluid density of *Ortho-II* ordered $YBa_2Cu_3O_{6.5}$ (underdoped, top panel) and $YBa_2Cu_3O_{6.993}$ (overdoped, lower panel), normalized to values at $T = 0$.

Chapter 4

Extracting Quasiparticle Charge Conductivity

Given the surface resistance $R_s(\Omega, T)$ and low frequency limit of the surface reactance $X_s(\Omega \rightarrow 0, T)$ data in Chapter 3, the challenge is to extract the charge conductivity via Equation 3.6. While this would be a straightforward chore if one had both R_s and X_s at each frequency of interest, it has proven very difficult to acquire both of these quantities from the same experiment. Rather, the approach taken by our laboratory has been to design apparatus that are intentionally optimized for the measurement of either R_s or X_s. Therefore, one must find a self consistent means of filling in the gaps. At low frequencies and temperatures, one can separate the real and imaginary components of $Z_s(\Omega, T)$ if one assumes $\sigma_2(\Omega, T) \approx 1/(\mu_o \Omega \lambda_L^2(T))$ as given by Eq. 3.7. However, it is desirable to go one step further by accounting for the quasiparticle contribution to $\sigma_2(\Omega, T)$ as well. To do so will require some modelling of $\sigma_1(\omega, T)$, at least at a phenomenological level.

4.1 $\hat{a}$-Axis Conductivity

As argued in Chapter 2, charge transport in the $\hat{a}$-axis direction in $YBa_2Cu_3O_{6+x}$ will be governed by the two 2-dimensional plane-like bands sketched in Fig. 2.5. Provided the plane-chain coupling is weak, then these two bands will behave in a qualitatively similar manner and the problem can be treated, at least approximately, as that of two identical bands. In a metal, the physics of electron charge transport can be modelled for many applications by the classical Drude model in which the conductivity is expressed in terms of the total oscillator strength in the band ne^2/m^* and an electron scattering rate τ^{-1} [3]:

$$\sigma(\Omega) = \frac{ne^2}{m^*} \frac{-i}{\Omega - i/\tau} = \frac{ne^2}{m^*} \left(\frac{\tau}{1 + \Omega^2\tau^2} - \frac{i\Omega\tau^2}{1 + \Omega^2\tau^2} \right) \tag{4.1}$$

As one can see, the Drude conductivity spectrum is characterized by a constant oscillator strength ne^2/m^* and high frequency behaviour that varies as $1/\Omega^2$. Furthermore there is an imaginary part that varies linearly with Ω at low frequencies, peaks at $\Omega\tau \sim 1$ and then drops as $1/\Omega$ at high frequency. This latter term gives rise to diamagnetic screening of AC magnetic fields in metals.

In the case of a *d*-wave superconductor it seems highly improbable that one can use a Drude-like form to describe $\sigma(\Omega, T)$. Nonetheless, such analysis has been used extensively in the literature [31, 75, 76] and does allow the experimentalist to obtain

a phenomenological handle on their data. In this case once replaces ne^2/m^* and τ in Eq. 4.1 by a temperature dependent quasiparticle oscillator strength $(n_n e^2/m^*)(T)$ and a temperature dependent quasiparticle scattering rate, respectively:

$$\sigma_1(\Omega, T) = \frac{n_n e^2}{m^*}(T)\frac{\tau(T)}{1+\Omega^2\tau^2(T)} \equiv \frac{\sigma_o(T)}{1+\Omega^2\tau^2(T)} \tag{4.2}$$

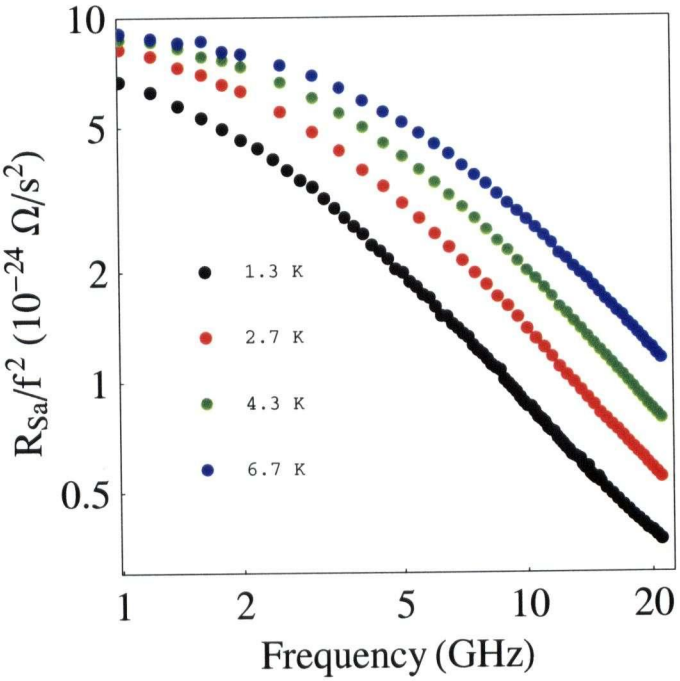

Figure 4.1: A log-log plot of R_{sa}/f^2 versus f data from underdoped *Ortho-II* ordered $YBa_2Cu_3O_{6.5}$. To within a few constants, this is essentially $\sigma_{1a}(f, T)$. The high frequency tails show exponents ranging from -1.4 to -1.5 which deviate significantly from -2 (Drude model).

However, there is no a priori reason to assume that τ^{-1} is frequency independent for a *d*-wave quasiparticle. This assumption holds for elastic scattering in metals where the electronic energy dispersion near the Fermi surface is relatively weak (on the scale of any temperature $T \ll E_F$), but it need not be the case in a *d*-wave superconductor where the superconducting gap introduces strong energy dependence in $\xi^i_{\vec{k}}$ near E_F, as given by Eq. 2.14. Therefore, $\sigma_1(\Omega, T)$ need not adhere to the form of Eq. 4.2. To demonstrate, the $\hat{a}$-axis surface resistance data of Fig. 3.5 have been replotted as R_s/f^2 versus f in Fig. 4.1 on a log-log plot - this gives an approximate form for $\sigma_1(\Omega, T)$ as given by Eq. 3.7. Note that at high frequencies $R_s/f^2 \propto 1/f^y$ with $y \approx 1.5$.

To at least capture the spirit of the data, this author has suggested a more flexible phenomenological form for modelling the total quasiparticle conductivity attributed

to the two approximately identical 2-dimensional bands in $YBa_2Cu_3O_{6+x}$:

$$\sigma_{1a}(\Omega,T) = \sigma_1^{2D}(\Omega,T) = \frac{\sigma_o(T)}{1+(\Omega\Lambda(T))^{y(T)}} \tag{4.3}$$

Furthermore, the above form can also be used to generate the quasiparticle contribution to $\sigma_2(\Omega,T)$ via a Kramers-Kronig relation [3].

$$\sigma_{2a}(\Omega,T) = -\frac{2\Omega}{\pi}\mathcal{P}\int_{-\infty}^{\infty} d\omega \frac{\sigma_{1a}(\omega,T)}{\omega^2-\Omega^2} \tag{4.4}$$

As with the metallic expression, one expects $\sigma_{2a}(\Omega,T) \to 0$ at both $\Omega = 0$ and $\Omega \to \infty$ and it will be peaked at $\Omega\Lambda(T) \approx 1$. One then has a complete expression for $\sigma_2(\Omega,T)$ in terms of a modelled quasiparticle contribution and the experimentally measured superfluid response:

$$\sigma_2(\Omega,T) = \sigma_{2a}(\Omega,T) + \frac{1}{\mu_o\Omega\lambda_L^2(T)} \tag{4.5}$$

Provided one has sufficient experimental bandwidth ($\Omega_{max} > \Lambda^{-1}(T)$), then one can fit the model directly to R_s via

$$R_s(\Omega,T) = Re\left(\frac{i\mu_o\Omega}{\sigma(\Omega,T)}\right)^{1/2} \tag{4.6}$$

with the model σ_1 (Eq. 4.3) and hybrid σ_2 (Eq. 4.5). If the model expression fits the $R_s(\Omega,T)$ data to sufficient accuracy, then one can take the model of $\sigma_{2a}(\Omega,T)$ as being a reasonable substitute for experimental data. Returning to Eq. 4.6 one more time, one can now extract 'experimental' values of $\sigma_{1a}(\Omega,T)$ by inserting R_s measurements, λ_L measurements and the (presumably) successfully modelled $\sigma_{2a}(\omega,T)$ into this expression and then solve for $\sigma_1(\Omega,T)$. Even if the model does not fit $R_s(\Omega,T)$ exactly, this procedure at least acknowledges the existence of quasiparticle contributions to $\sigma_2(\Omega,T)$ and provides one with a reasonable means of accounting for its presence. As stated above, this approach will work if one can experimentally observe enough curvature in R_s to which one can reliably fit a model containing three parameters: σ_o, Λ and y. One can anticipate that this method will work best at low temperature where the half width at half maximum Λ^{-1} will be governed by elastic scattering of d-wave quasiparticles from static defects in the crystal. As shown in Fig. 4.1, it can be estimated that Λ^{-1} of the low energy conductivity spectra in $YBa_2Cu_3O_{6.5}$ can be as small as a few *GHz*. With increasing temperature one anticipates that the rise of inelastic scattering processes (from magnons, phonons, other quasiparticles ...) will augment Λ^{-1} to well beyond the experimental bandwidth ($22\,GHz$ for underdoped $YBa_2Cu_3O_{6.5}$, $75\,GHz$ for overdoped $YBa_2Cu_3O_{6.993}$). However, as $\sigma_{1a}(\Omega,T)$ broadens then $\sigma_{2a}(\Omega,T)$ will become small at frequencies $\Omega < \Lambda^{-1}$, therefore the quasiparticle screening corrections to $\sigma_2(\Omega,T)$ (Eq.4.5) can be neglected at the higher temperatures.

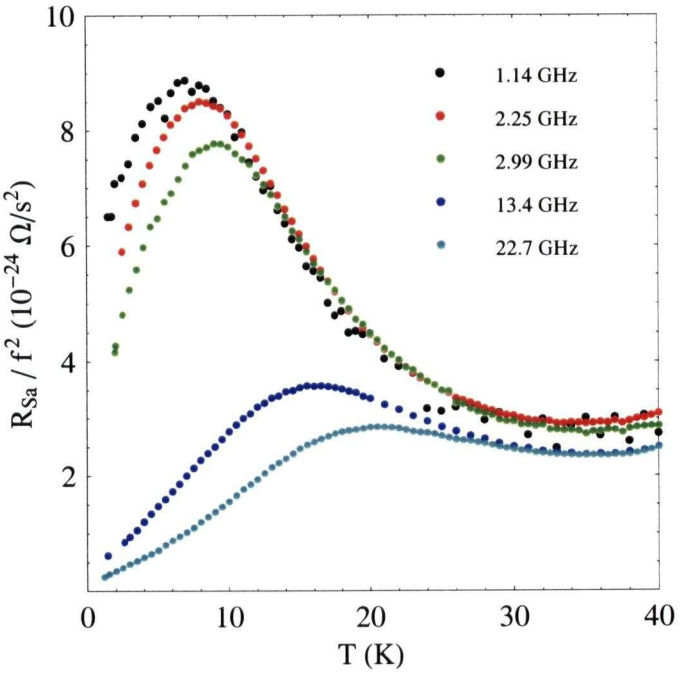

Figure 4.2: A plot of R_{sa}/f^2 versus T data from underdoped *Ortho-II* ordered $YBa_2Cu_3O_{6.5}$. To within a few constants, this is essentially $\sigma_{1a}(f,T)$. The five resonator data sets roughly converge above $20\,K$, thus indicating that σ_{1a} becomes frequency independent in the microwave regime above this temperature.

As a demonstration, the surface resistance data of Fig. 3.15 have been replotted as R_s/f^2 versus T in Fig. 4.2. The broad peak centred at $\sim 8\,K$ is attributed to a competition between decreasing normal fluid oscillator strength $n_n e^2/m^*$ and increasing quasiparticle lifetime ($\sim \Lambda$) as T decreases. Immediately below T_c Λ increases faster than $n_n e^2/m^*$ decreases, thus augmenting the charge conductivity at low frequencies. Eventually Λ saturates at some level governed by elastic scattering alone while $n_n e^2/m^*$ decreases linearly as $T \to 0$, hence σ_1 decreases as well.

In the case of *Ortho-II* ordered $YBa_2Cu_3O_{6.5}$, it can be surmised that Λ^{-1} will exceed the experimental bandwidth at $\sim 20\,K$, beyond which σ_1 will appear frequency independent in the microwave regime. At these higher temperatures, one can set $\sigma_{2a} \approx 0$ and extract σ_{1a} from R_s and λ_L without any of the corrections discussed above. As $T \to T_c^-$ the London penetration depth λ_L will approach sample dimensions and additional procedures may be needed to successfully extract $\sigma_1(\Omega,T)$ from $R_s(\Omega,T)$. However, this thesis will concentrate on low temperature behaviour and the so called thin limit problem will not be addressed here [73].

4.2 $\hat{b}$-Axis Conductivity

Figure 4.3 shows the $\hat{b}$-axis surface resistance data of Fig. 3.15 plotted as R_s/f^2 versus f. While the $\hat{a}$-axis data showed high frequency power law behavior $\propto 1/\Omega^{1.5}$, one can see the $\hat{b}$-axis data appear to be concave-up beyond $\sim 10\,GHz$. Indeed, a comparison of the $\hat{a}$ and $\hat{b}$-axis surface resistance data in Fig. 3.5 should be all that is needed to convince the reader that $\hat{b}$-axis charge conductivity appears to be qualitatively different than that in the $\hat{a}$-axis direction.

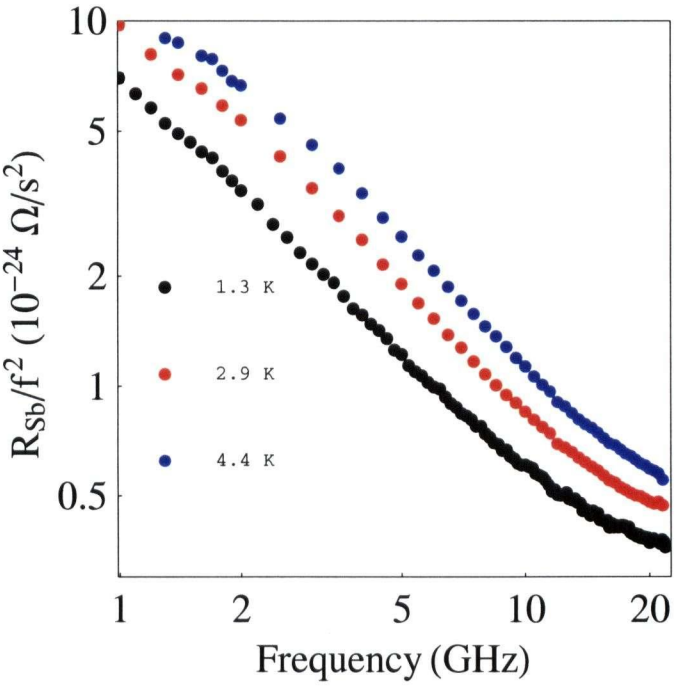

Figure 4.3: A log-log plot of R_{sb}/f^2 versus f data from *Ortho-II* ordered $YBa_2Cu_3O_{6.5}$. To within a few constants, this is essentially $\sigma_{1b}(f,T)$.

It is hypothesized that this change in curvature can be attributed to a very broad spectral feature that arises because of the presence of metallic 1-dimensional CuO chains in $YBa_2Cu_3O_{6+x}$. In Chapter 2 it was argued that $YBa_2Cu_3O_{6+x}$ should have a quasi-1-dimensional band whose low energy excitations in the superconducting state are primarily chain-like and will therefore only contribute to charge conduction in the $\hat{b}$-axis direction. The chain scattering rate is expected to be much larger than that in the $(CuO_2)^{2-}$ planes, and should give rise to a very broad contribution to $\sigma_1(\Omega,T)$ which will be approximated as a T-dependent constant over the experimental bandwidth. The microwave conductivity can then be expressed as a sum of contributions from the 2-dimensional bands (a term identical in form to Eq. 4.3) plus a constant attributed to the quasi-1-dimensional band:

$$\sigma_{1b}(\Omega,T) = \sigma_1^{2D}(\Omega,T) + \sigma_1^{1D}(\Omega,T) = \frac{\sigma_o(T)}{1+(\Omega\Lambda(T))^{y(T)}} + \sigma_1^{1D}(\Omega \to 0,T) \qquad (4.7)$$

For the purpose of describing $\hat{b}$-axis data the parameters σ_o, Λ and y will not be required to match those used to fit $\hat{a}$-axis data. One can then extract $\sigma_1(\Omega,T)$ from R_s, λ_L and a modelled $\sigma_{2b}(\Omega,T)$ as described in the previous section (a constant in Eq. 4.7 will give no contribution to σ_{2b}). The procedure will have limitations similar to those for the $\hat{a}$-axis direction, but the addition of a fourth parameter σ_1^{1D} will make the analysis less reliable as Λ^{-1} approaches the experimental bandwidth.

4.3 Ortho-II Ordered $YBa_2Cu_3O_{6.5}$ (Underdoped)

The real part of the microwave conductivity of *Ortho-II* ordered $YBa_2Cu_3O_{6.5}$, as obtained from the bolometry experiment, is shown in Fig. 4.4. The points are 'experimental' values obtained from measurements of R_s, as described previously, and the lines are Eq. 4.3 ($\hat{a}$-axis) and Eq. 4.7 ($\hat{b}$-axis) with the fit parameters used to model the surface resistance data. Fits were obtained by minimizing the quantity χ^2 defined as

$$\chi^2 = \sum_{i=1}^{m} \frac{R_s^i - R_s^{model}(\sigma(\Omega_i, T))^2}{2(\Delta R_s^i)^2} \tag{4.8}$$

where R_s^i is the i^{th} measurement at angular frequency Ω_i and R_s^{model} is the modelled surface resistance function, Eq. 4.6, with the appropriate $\hat{a}$-axis or $\hat{b}$-axis expression substituted for $\sigma(\omega, T)$. Since the broadband bolometry data at any given temperature were obtained in a single experiment, the errors ΔR_s^i were taken to be $\pm 5\%$ relative errors at each frequency due to statistical fluctuations. As one can see, the model lineshape serves its intended purpose very well in that it fits the observed high frequency behavior. The fits appear cusp-like with T-independent zero frequency intercepts of $\sigma_{1a}(\Omega \to 0, T) \approx 3.5 \times 10^7\, \Omega^{-1} m^{-1}$ and $\sigma_{1b}(\Omega \to 0, T) \approx 2.0 \times 10^8\, \Omega^{-1} m^{-1}$ (latter intercept is not shown in Figure).

Error bars on fit parameters were obtained by calculating the covariance matrix $[C]$ for either a 3-parameter ($\hat{a}$-axis) or 4-parameter ($\hat{b}$-axis) fit whose eigenvalues and eigenvectors describe the aspect ratio and orientations of ellipses of constant χ^2 in parameter space [77]. The dimensionality of the fit then dictates the value of χ^2 which defines 1 standard deviation away from optimal fitting ($\Delta\chi^2 = 3.53$ or 4.72 for 3 or 4 parameters, respectively). Projecting this ellipsoid onto the original fit parameter axes thus gives error bars on fit parameters that can account for covariance of fit parameters.

The fit parameter $y(T)$ is shown in Fig. 4.5. The plot has been scaled from $y = 1$ (where the 2-dimensional band conductivity term becomes nonintegrable with respect to Ω) and $y = 2$ (Drude Model, Eq. 4.2). It is obvious that the conductivity spectra in Fig. 4.4 deviate significantly from the Drude Model. Rather, the data suggest a high frequency power of -1.46 ± 0.02. Interestingly, if one neglects the quasiparticle contributions to $\sigma_2(\Omega, T)$ and simply employs Eq. 3.7 to obtain $\sigma_1(\Omega, T)$, then the high frequency power is observed to be roughly -1.5. Thus the conclusion that these spectra deviate significantly from Drude lineshapes is robust and the details of the scheme accounting for quasiparticle screening do not affect this key feature.

The processing of data from cavity perturbation experiments was performed in a manner similar to what has been described above. χ^2 was defined according to Eq. 4.8 but with two key differences: First, since there are measurements at only five distinct frequencies ($m = 5$ in Eq. 4.8) then it would be highly desirable to reduce the number of fit parameters given knowledge obtained from fits to bolometry data. In particular, the exponent y was noted to settle into a constant value of 1.46 in Fig. 4.5, so this parameter was fixed accordingly in the processing of all resonator data from underdoped $YBa_2Cu_3O_{6.5}$ samples.

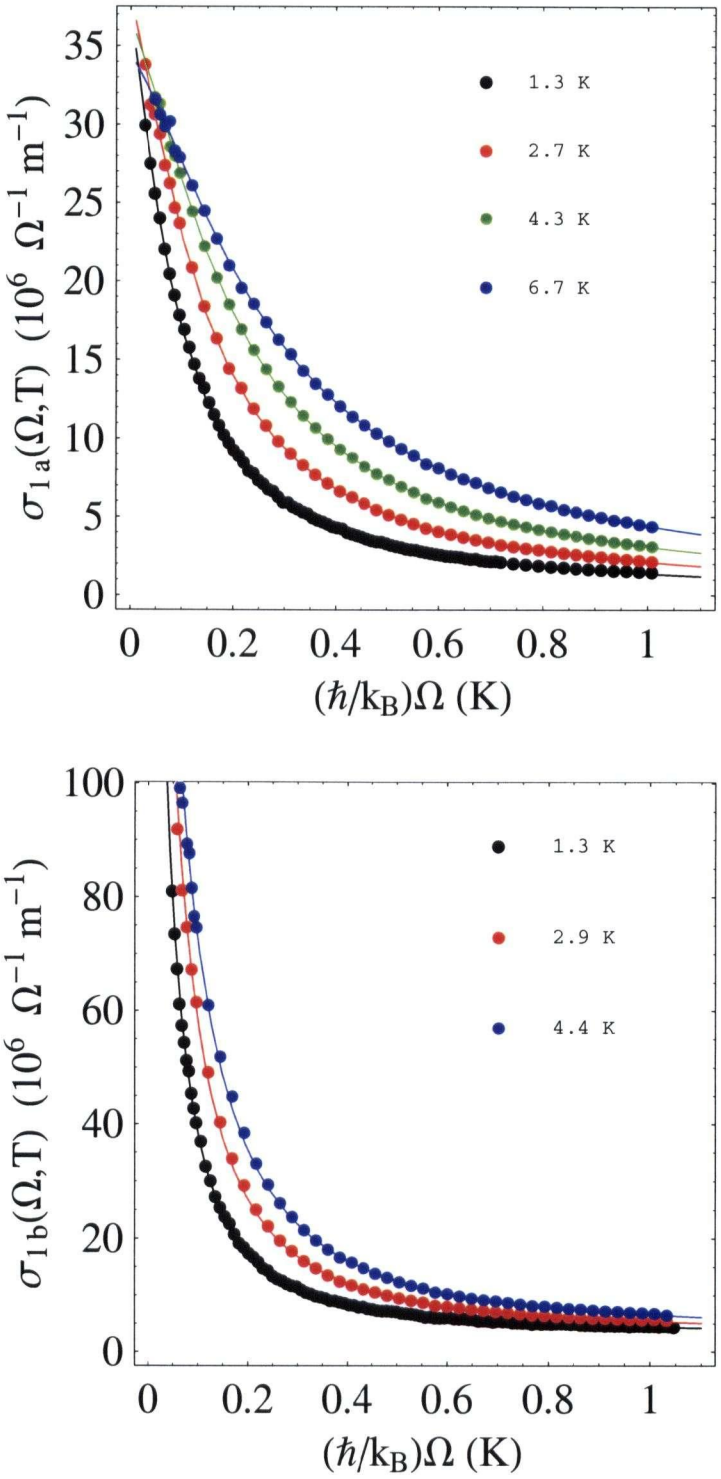

Figure 4.4: The real part of the in-plane microwave conductivity $\sigma_1(\Omega, T)$ of *Ortho-II* ordered $YBa_2Cu_3O_{6.5}$, as obtained from the bolometry experiment: $\hat{a}$-axis (upper panel) and $\hat{b}$-axis (lower panel).

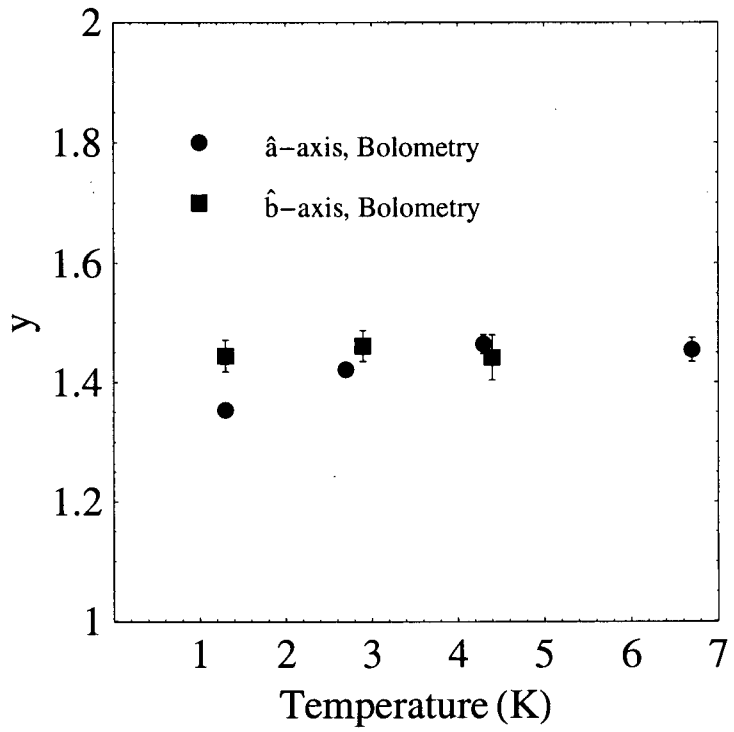

Figure 4.5: The high frequency exponent y from fitting the in-plane surface resistance data from *Ortho-II* ordered $YBa_2Cu_3O_{6.5}$ obtained from the bolometry experiment.

Second, since the fits as a function of frequency involve 5 independently calibrated experiments, the weights ΔR_s^i must rightfully include both the systematic errors of $(0.7, 0.2, 0, 2, 10, 20)\,\mu\Omega$ at $(1.14, 2.25, 2.99, 13.34, 22.71)$ *GHz* and any statistical scatter in each measurement as well. The fitting procedure was observed to work up to $\sim 17\,K$, beyond which σ_1 becomes roughly frequency independent over the experimental bandwidth.

The real part of the microwave conductivity of *Ortho-II* ordered $YBa_2Cu_3O_{6.5}$, as obtained from cavity perturbation (resonator) experiments, is shown in Fig. 4.6. The values plotted versus T were obtained from a combination of procedures; below $17.5\,K$ via the fitting procedure presented herein and above $17.5\,K$ by neglecting the quasiparticle contribution to $\sigma_2(\Omega, T)$. Sample plots versus Ω for $T < 17.5K$ are shown as well. The error bars in the conductivity points reflect the combination of systematic and statistical errors in the corresponding surface resistance measurement.

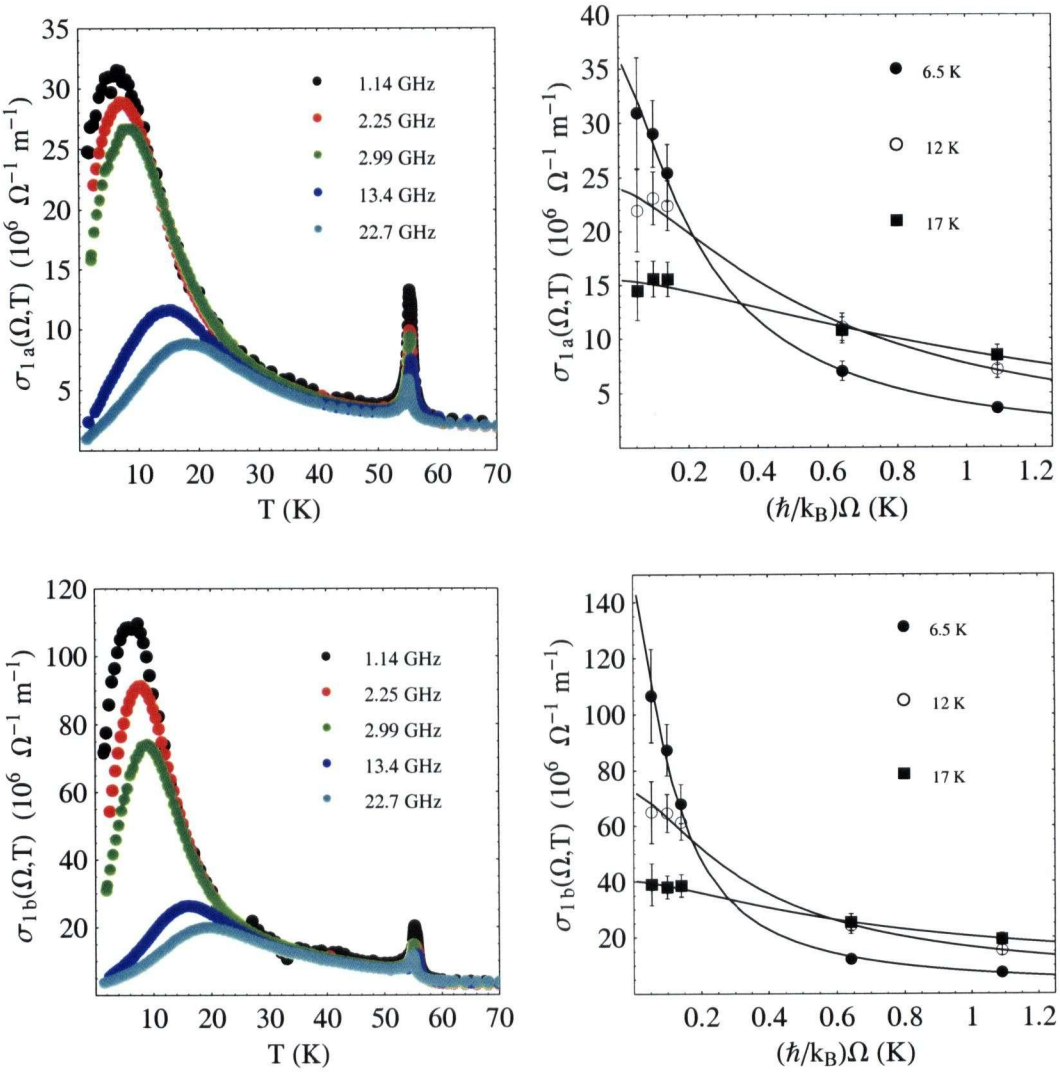

Figure 4.6: The real part of the in-plane microwave conductivity $\sigma_1(\Omega, T)$ of *Ortho-II* ordered $YBa_2Cu_3O_{6.5}$, as obtained from cavity perturbation experiments. Full temperature sweeps and sample spectra as a function of frequency are shown: $\hat{a}$-axis (upper panels) and $\hat{b}$-axis (lower panels).

Given the fits to both the bolometry and resonator data in Figs. 4.4 and 4.6 one can now create combined plots of the scattering parameter $\Lambda^{-1}(T)$ over a broad temperature range, as shown in Fig. 4.7. These numbers are accompanied by representative error bars at a few select temperatures. In both the $\hat{a}$ and $\hat{b}$-axis directions it appears that $\Lambda^{-1} \propto T$ below $8\,K$ and then increases rapidly. The bolometry and low temperature resonator points can be fit to straight lines of the form $\Lambda_{el}^{-1}(T) = a + bT$ and the results are noted in Table 4.1.

Orientation	Probe	$a\,(K)$	b
$\hat{a}$	Bolometry	$(5.0 \pm 0.4) \times 10^{-2}$	$(3.3 \pm 0.1) \times 10^{-2}$
$\hat{b}$	Bolometry	$(1.9 \pm 0.1) \times 10^{-2}$	$(1.0 \pm 0.1) \times 10^{-2}$
$\hat{a}$	Resonators	$(5.0 \pm 1.0) \times 10^{-2}$	$(3.0 \pm 0.5) \times 10^{-2}$
$\hat{b}$	Resonators	$(2.0 \pm 1.0) \times 10^{-2}$	$(1.4 \pm 0.5) \times 10^{-2}$

Table 4.1: Linear fits to the low temperature scattering parameter $\Lambda_{el}^{-1}(T) = a + bT$ for *Ortho-II* ordered $YBa_2Cu_3O_{6.5}$.

It is conceivable that the linear behaviour of $\Lambda^{-1}(T)$ at low T is due to elastic scattering of quasiparticles from weak crystalline defects, as suggested by the microwave conductivity calculations of Hirschfeld *et al.* for *d*-wave quasiparticles in the presence of Born scatterers [78, 79]. Therefore, subtracting the linear behaviour from the experimental points will yield the inelastic scattering; $\Lambda_{inel}^{-1}(T) = \Lambda^{-1}(T) - (a + bT)$. The results are shown in the lower panel of Fig. 4.7. While the in-plane elastic scattering rate appears to be $\hat{a} : \hat{b}$ anisotropic, it seems that the inelastic scattering rate is roughly $\hat{a} : \hat{b}$ isotropic. In the absence of a detailed model for the bandstructure of *Ortho-II* ordered $YBa_2Cu_3O_{6.5}$ it is not clear why the elastic and inelastic scattering rates should behave in this manner. Nonetheless, one can forge ahead and fit $\Lambda_{inel}^{-1}(T)$ to the Umklapp expression of Walker and Smith [45], Eq. 2.15. Admittedly, one must do this with some caution as the simple theory presented in Section 2.5.2 of this thesis does not account for the additional energy $\hbar\Omega$ absorbed by quasiparticles when probed by microwaves, nor does it contain detailed information regarding the lineshape of $\sigma_1(\Omega, T)$. However, this author contends that it does provide a fair estimate of the half width of the lineshape (the frequency Ω at which $\sigma_1(\Omega, T)/\sigma_1(\Omega \to 0, T) \sim 1/2$) in the limit $\hbar\Omega \ll k_B T$. The best fit parameters were determined to be $C = (2.7 \pm 0.9) \times 10^{-2}\,K^{-1}$ and $\Delta_U = (39 \pm 8)\,K$ for the $\hat{a}$-axis points and $C = (1.2 \pm 0.5) \times 10^{-2}\,K^{-1}$ and $\Delta_U = (26 \pm 7)\,K$ for the $\hat{b}$-axis points. Given these error estimates, one can only conclude that the presumed inelastic scattering rate is crudely $\hat{a} : \hat{b}$ isotropic.

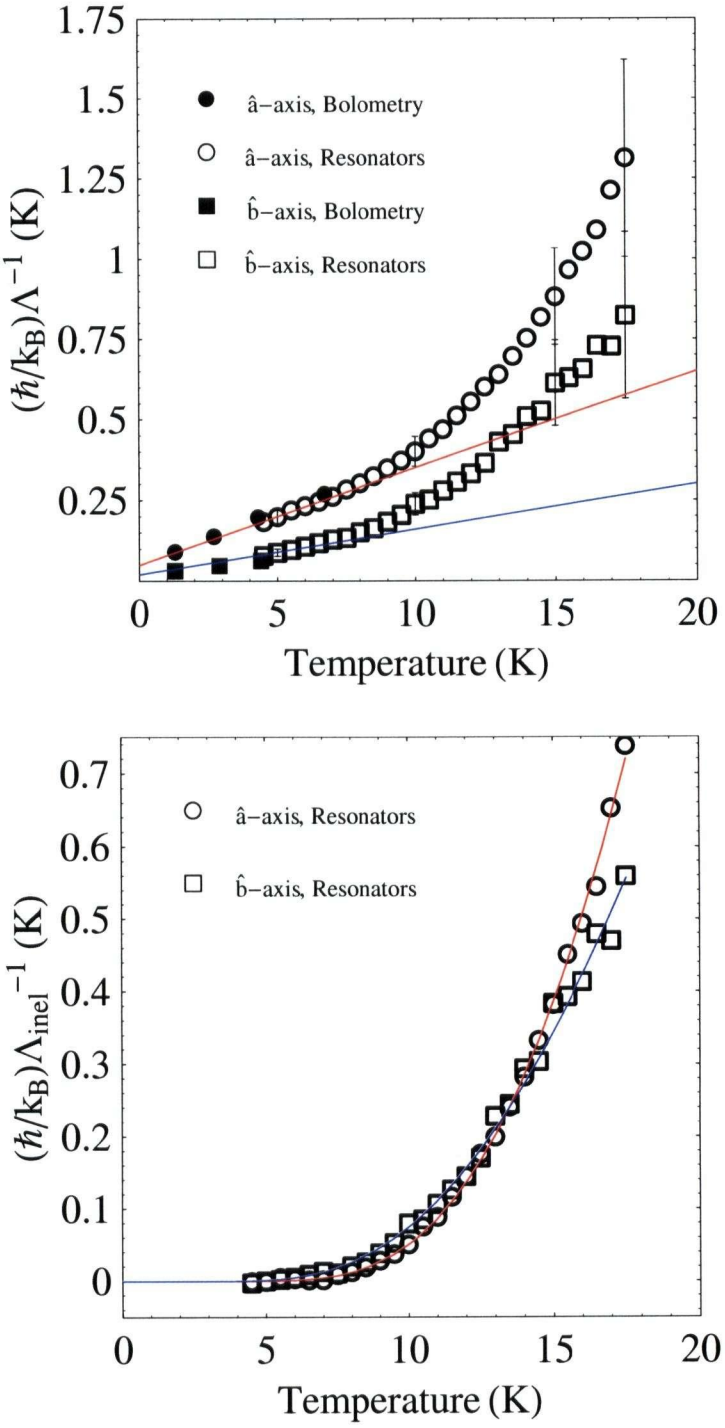

Figure 4.7: The in-plane scattering parameter $\Lambda^{-1}(T)$ of *Ortho-II* ordered $YBa_2Cu_3O_{6.5}$(upper panel). Solid lines capture the asymptotic behaviour of the resonator points at low T. The presumed inelastic scattering rate obtained by subtracting the asymptotic linear behaviour from $\Lambda^{-1}(T)$ (lower panel). Solid curves are fits to the Walker-Smith Umklapp model.

Rather than plotting the fit parameter $\sigma_o(T)$, it will prove more useful to plot the integrated quasiparticle oscillator strength in the 2-dimensional band, which will be defined as

$$\left(\frac{n_n e^2}{m^*}\right)_{2D}(T) = \frac{2}{\pi}\int d\Omega\, \sigma_1^{2D}(\Omega, T) = \frac{\sigma_o(T)}{y(T)\Lambda(T)}\csc(\pi/y(T)) \tag{4.9}$$

Note that the quasi-1-dimensional contribution to $\sigma_{1b}(\Omega, T)$ (Eq. 4.7) cannot be integrated as it is presumably much broader than the experimental bandwidth. As such, the evolution of quasiparticle oscillator strength in this band,

$$\left(\frac{n_n e^2}{m^*}\right)_{1D}(T) \equiv \frac{2}{\pi}\int d\Omega\, \sigma_1^{1D}(\Omega, T)$$

cannot be extracted from these data.

One of the tenets of superconductivity is the Ferrel-Tinkham-Glover sum rule [1] which states that the sum of the quasiparticle and superfluid oscillator strength must equal a constant governed by the total electron density in the system:

$$\sum_{\text{Bands } i}\left[\left(\frac{n_n e^2}{m^*}\right)_i(T) + \left(\frac{n_s e^2}{m^*}\right)_i(T)\right] = \sum_{\text{Bands } i}\left(\frac{n e^2}{m^*}\right)_i \tag{4.10}$$

where the *total* superfluid oscillator strength in all bands will be written as

$$\frac{n_s e^2}{m^*}(T) \equiv \sum_{\text{Bands } i}\left(\frac{n_s e^2}{m^*}\right)_i(T) \tag{4.11}$$

and can be determined experimentally from measurements of the London penetration depth via Eq. 3.4. The *total* electronic spectral weight will be written as

$$\frac{n e^2}{m^*} \equiv \sum_{\text{Bands } i}\left(\frac{n e^2}{m^*}\right)_i \tag{4.12}$$

As a corollary to the sum rule, many in the field of superconductivity assume that $n_s e^2/m^*(T = 0) \approx n e^2/m^*$ and therefore $n_n e^2/m^*(T = 0) \approx 0$, where the *total* quasiparticle oscillator strength at any given T is defined as

$$\frac{n_n e^2}{m^*}(T) \equiv \sum_{\text{Bands } i}\left(\frac{n_n e^2}{m^*}\right)_i(T)\,. \tag{4.13}$$

However, this is not a requirement to fulfill Eq. 4.10 nor is it necessarily supported by experiments [75]. All that can be concluded from Eq. 4.10 is that any oscillator strength lost from the superfluid must necessarily show up in the quasiparticle oscillator strength:

$$\frac{n_n e^2}{m^*}(T) - \frac{n_n e^2}{m^*}(T = 0) = \frac{n_s e^2}{m^*}(T = 0) - \frac{n_s e^2}{m^*}(T) = \frac{1}{\mu_o \lambda_L^2(T = 0)} - \frac{1}{\mu_o \lambda_L^2(T)} \tag{4.14}$$

Thus one should be able to compare the quasiparticle spectral weight attributed to the 2-dimensional bands (Eq. 4.9) to the loss of superfluid spectral weight from penetration depth measurements (Eq. 4.14). The results for underdoped *Ortho-II* ordered $YBa_2Cu_3O_{6.5}$ are shown in Fig. 4.8. Error bars from integrating conductivity spectra were obtained by adding the error due to each fit parameter in quadrature

$$\delta\frac{n_n e^2}{m^*}(T) = \sqrt{\sum_{i=1}^{m}(\frac{\partial\sigma_1}{\partial p_i}\delta p_i)^2}$$

where $p_i \pm \delta p_i = (\sigma_o \pm \delta\sigma_o, \Lambda \pm \delta\Lambda, y \pm \delta y)$. In both cases it can be seen that the integrated spectral weight varies linearly over the range $0 < T < 10\,K$. At higher temperatures, $\sigma_1(\Omega, T)$ broadens rapidly as $\Lambda^{-1}(T)$ increases, thus reducing the reliability of the fit which then increases the uncertainty $\delta(m_n e^2/m^*)$. This is particularly true for the $\hat{b}$-axis fits in which there is a strong covariance between the parameters $(\sigma_1^{1D}, \sigma_o)$ and (σ_1^{1D}, Λ). Nonetheless, one can indeed parameterize the experimental points as straight lines and make some useful observations. The $T = 0$ intercepts and slopes (multiplied by $\hbar/k_B$) from the 2-dimensional bands and the change in *total* quasiparticle oscillator strength from penetration depth measurements are noted in Table 4.2.

Bands	Probe	$\frac{n_n e^2}{m^*}(T=0)(\Omega^{-1}m^{-1}s^{-1})$	$\frac{\hbar}{k_B}\frac{\partial(n_n e^2/m^*)}{\partial T}(\Omega^{-1}m^{-1})$
$\hat{a}, 2D$	Bolometry	$(6.3 \pm 0.8) \times 10^{17}$	$(1.5 \pm 0.2) \times 10^6$
$\hat{b}, 2D$	Bolometry	$(1.0 \pm 0.5) \times 10^{18}$	$(3.1 \pm 1.5) \times 10^6$
$\hat{a}, 2D$	Resonators	$(5.7 \pm 3.0) \times 10^{17}$	$(1.5 \pm 0.4) \times 10^6$
$\hat{b}, 2D$	Resonators	$(1.1 \pm 1.0) \times 10^{18}$	$(3.0 \pm 1.5) \times 10^6$
$\hat{a}$, All	$\Delta\lambda(T)$	0 (assumed)	1.5×10^6
$\hat{b}$, All	$\Delta\lambda(T)$	0 (assumed)	3.6×10^5

Table 4.2: Linear fits to the low temperature quasiparticle oscillator strength $(n_n e^2/m^*)(T)$ for *Ortho-II* ordered $YBa_2Cu_3O_{6.5}$.

In the $\hat{a}$-axis direction, the loss of superfluid spectral weight is tracked by the gain in normal fluid spectral weight extremely well. Furthermore, the bolometry points in Fig. 4.8 clearly extrapolate back to a nonzero value of $(n_n e^2/m^*)_{2D}(T = 0)$, which will henceforth be called residual oscillator strength (ROS). Taking a low temperature limit of $\lambda_L^a(T = 0) = 2020\,\text{Å}$, one can calculate the zero temperature total superfluid oscillator strength $(n_s e^2/m^*)(T = 0) = 1.95 \times 10^{19}\,\Omega^{-1}m^{-1}s^{-1}$. Summing the two zero temperature values gives the total oscillator strength $ne^2/m^* = 2.01 \times 10^{19}\,\Omega^{-1}m^{-1}s^{-1}$. The ROS in the $\hat{a}$-axis quasiparticle conductivity is then estimated to be $\sim 3\%$ of the total low frequency oscillator strength. As an aside, note that the above mentioned value of ne^2/m^* implies a relatively large effective mass $m^* \sim 30m_e$, where m_e is the bare mass of an electron. This number has been obtained by assuming roughly 1 electron per planar Cu^{2+} site and two such sites per

unit cell, thus giving a conduction electron density of $n \sim 2 \times 10^{28}\ m^{-3}$. This issue will be discussed further in Chapter 5 of this thesis in the context of Fermi liquid corrections.

The story is qualitatively similar in the $\hat{b}$ direction, although the quantitative analysis suffers from much larger uncertainties in all fit parameters. Nonetheless it is important to note that the slope obtained from the bolometry points is *less* than that obtained from the loss of superfluid oscillator strength. This is a reasonable result for charge conductivity in the $\hat{b}$-axis direction since any gains in the quasiparticle oscillator strength must be partitioned between the 2-dimensional and the quasi-1-dimensional bands described in Chapter 2. Given the ratio of the $\hat{b}$-axis bolometry to the penetration depth slopes in Table 4.2 it would appear that roughly 86% of the oscillator strength lost from the superfluid ends up in the 2 dimensional bands.

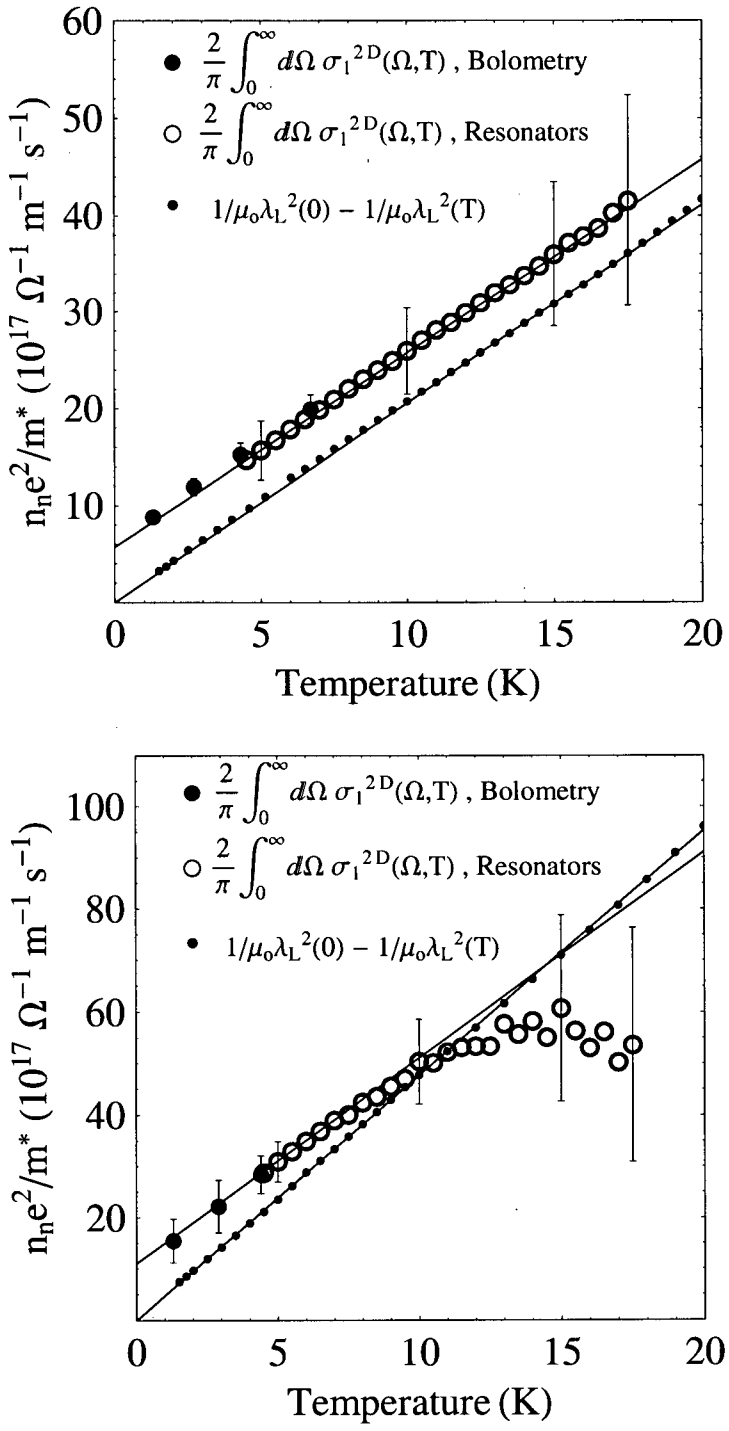

Figure 4.8: The in-plane quasiparticle oscillator strength $(n_n e^2/m^*)(T)$ of *Ortho-II* ordered $YBa_2Cu_3O_{6.5}$: $\hat{a}$-axis (upper panel) and $\hat{b}$-axis (lower panel).

It is useful to compare the absolute values of the quasiparticle oscillator strength in the 2-dimensional bands, as inferred from the $\hat{a}$ and $\hat{b}$-axis data. However, before proceeding with this analysis, the reader is cautioned that any comparison of the absolute magnitude of the oscillator strength between $\hat{a}$ and $\hat{b}$-axis directions could be fraught with peril due to uncertainties in the absolute value of the London penetration depth $\lambda_L(T = 0)$. Recall from Eq. 3.7 that at low temperatures $\sigma_1 \propto 1/\lambda_L^3(T) \approx 1/\lambda_L^3(T = 0)$. Therefore, $\int d\Omega\, \sigma_1(\Omega) \propto 1/\lambda_L^3(T = 0)$ as well. Thus a 20% change in $\lambda_L(T = 0)$ can alter the integrated spectral weight by almost a factor of 2! Fortunately, comparisons between integrated quasiparticle oscillator strength and variations in the superfluid spectral weight in the same direction (for the same sample) are independent of the choice of $\lambda_L(T = 0)$ to first order. From Eq. 4.14,

$$\frac{n_n e^2}{m^*}(T) - \frac{n_n e^2}{m^*}(T = 0) \approx \frac{2\Delta\lambda_L(T)}{\lambda_L^3(T = 0)}$$

where $\Delta\lambda_L(T) = \lambda_L(T) - \lambda_L(T = 0)$. Therefore, any comparison of slopes in Table 4.2 for the same crystal orientation is meaningful. However, any comparison between $\hat{a}$ and $\hat{b}$ axis results within either of these tables should be interpreted with care, as should any comparisons between dopings. Nonetheless, if the values of $\lambda_a(T_{base})$ and $\lambda_b(T_{base})$ are reliable, then one make a very important observation; the quasiparticle spectral weight attributed to the 2-dimensional bands is $\hat{a} : \hat{b}$ anisotropic. In fact, the ratio of either the bolometry or resonator data reveals

$$\frac{(n_n e^2/m^*)^a_{2D}}{(n_n e^2/m^*)^b_{2D}} \sim \frac{1}{2}.$$

This is indeed surprising, for if the Fermi velocities of the 2-dimensional bands were directed along the first Brillouin zone diagonals, then these bands should contribute equivalent amounts of spectral weight to $\hat{a}$ and $\hat{b}$-axis conductivity. Given the observation of an $\hat{a} : \hat{b}$ anisotropic elastic scattering rate as well, this author has reached the conclusion that the bandstructure model of Chapter 2 may not be appropriate for *Ortho-II* ordered $YBa_2Cu_3O_{6.5}$. This issue will be discussed more thoroughly at the end of this chapter.

A plot of the fit parameter σ_1^{1D} versus T (Fig. 4.9) shows that this fit parameter is constant ($3 \times 10^6\, \Omega^{-1}m^{-1}$) to within error over the range of temperatures studied in the bolometry experiment. The results from fitting resonator data also suggest that σ_1^{1D} is constant ($2 \times 10^6\, \Omega^{-1}m^{-1}$) up to approximately $10\, K$, but there is an evident mismatch between the two experimental techniques. If the physical origin of this term has been explained correctly, then it is entirely possible that the mean length of contiguous CuO chains was larger in the bolometry sample than in the resonator samples of $YBa_2Cu_3O_{6.5}$. This would lead to an increase in the quasiparticle lifetime in the former sample and therefore augment the low frequency limit of the quasi-1-dimensional band conductivity.

Finally, note that σ_1^{1D} shows no intention of collapsing as $T \rightarrow 0$, thus implying substantial ROS in the quasi-1-dimensional band. This effect was predicted by Atkinson [38] due to the strong Cooper pair breaking effect of CuO chain ends and localization of charge on finite length chains.

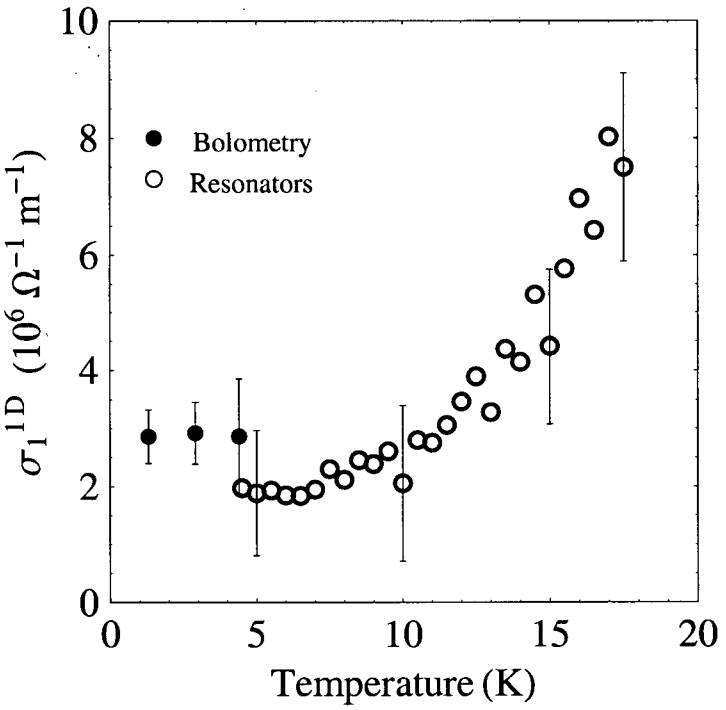

Figure 4.9: The broad quasi-1-dimensional component $\sigma_1^{1D}(\Omega \rightarrow 0, T)$ of the microwave conductivity of *Ortho-II* ordered $YBa_2Cu_3O_{6.5}$.

To summarize the analysis of the underdoped *Ortho-II* $YBa_2Cu_3O_{6.5}$ microwave conductivity data, one can draw four key conclusions:

1. The data support the picture of a quasi-1-dimensional band that contributes solely to $\hat{b}$-axis quasiparticle conductivity.

2. The 2-dimensional band contribution to quasiparticle conductivity appears to be $\hat{a} : \hat{b}$ *anisotropic* with respect to the *elastic scattering rate* and possibly the *spectral weight* as well (provided one trusts the ratio of the in-plane London penetration depths). However, the *inelastic scattering rate* seems to be roughly $\hat{a} : \hat{b}$ *isotropic.*

3. The $T \rightarrow 0$ scattering rate (presumably elastic scattering) varies as $\Lambda^{-1}(T) = a + bT$.

4. There is ROS in the 2-dimensional bands which indicates that not all of the available spectral weight ends up in the superconducting condensate at $T = 0$.

4.4 $YBa_2Cu_3O_{6.993}$ (Overdoped)

For the sake of completeness, the analysis performed upon the underdoped *Ortho-II* ordered $YBa_2Cu_3O_{6.5}$ data will likewise be performed upon the $YBa_2Cu_3O_{6.993}$ data. The discussion will be kept as brief as possible since the $\hat{a}$-axis and $\hat{b}$-axis quasiparticle conductivity have been the topics of previous publications ([69] and [43], respectively). However, the analysis presented herein differs from these publications in the use of the more flexible phenomenological model for $\sigma_1(\Omega, T)$ than the Drude-like model. In particular, the choice of the exponent y will prove critical in accounting for spectral weight at higher temperatures.

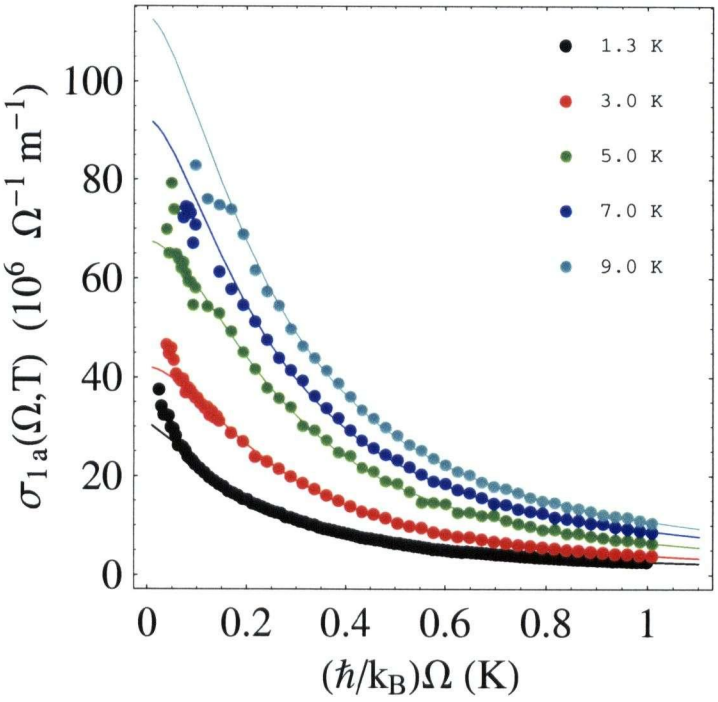

Figure 4.10: The real part of the $\hat{a}$-axis microwave conductivity $\sigma_{1a}(\Omega, T)$ of $YBa_2Cu_3O_{6.993}$ (overdoped), as obtained from the bolometry experiment.

The real part of the $\hat{a}$-axis microwave conductivity of $YBa_2Cu_3O_{6.993}$, as determined from bolometry data, is shown in Fig. 4.10 along with the fitted curves using the form Eq. 4.3. One should note that these spectra differ significantly from those in the top panel of Fig. 4.4. Most striking is the fact that the spectra appear very sharp at $1.3\,K$ and broaden quickly to a half width $\sim 0.35\,K$ at the higher temperatures. Furthermore, there is no temperature independent zero frequency intercept, rather the extrapolated values of $\sigma_1(\Omega \to 0, T)$ increase almost linearly with T from $3.0\,K$ to $9.0\,K$. Finally, one should note that the fit to the $1.3\,K$ points is not particularly reliable as it could not satisfy the almost divergent behavior at small Ω and the high

frequency tail simultaneously.

One can see that the lineshape changes as a function of temperature by plotting the fit parameter y versus T, as shown in Fig. 4.11. At the lowest temperature $y \approx 1.48 \pm 0.01$, which is remarkably close to the value obtained from fits to the *Ortho-II* data in the previous section. This parameter then rises to 1.75 and drops to 1.65 ± 0.01 beyond $7K$. The exponent was then fixed at $y = 1.65$ in the simultaneous fits to the five sets of resonator data shown in Fig. 3.16.

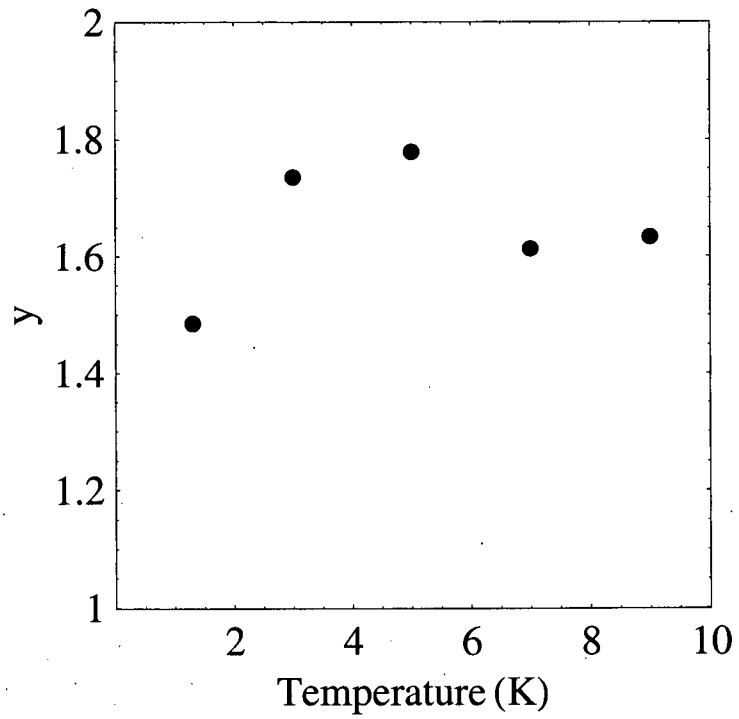

Figure 4.11: The high frequency exponent y from fitting the $\hat{a}$-axis surface resistance data from $YBa_2Cu_3O_{6.993}$ obtained from the bolometry experiment.

The real part of the microwave conductivity of $YBa_2Cu_3O_{6.993}$, as determined from resonator data, is shown in Fig. 4.12 along with some sample fits at selected temperatures. The $\sigma_2(\Omega, T)$ correction scheme was applied up to a highest temperature of $40.5K$, beyond which $\sigma_2(\Omega, T) \approx \sigma_2^{sf}(\Omega, T)$ as explained previously. Note that the peaks in σ_1 versus T have shifted up in temperature as compared to the *Ortho-II* data (Fig. 4.6), thus indicating a significant difference in quasiparticle scattering rates between the two dopings.

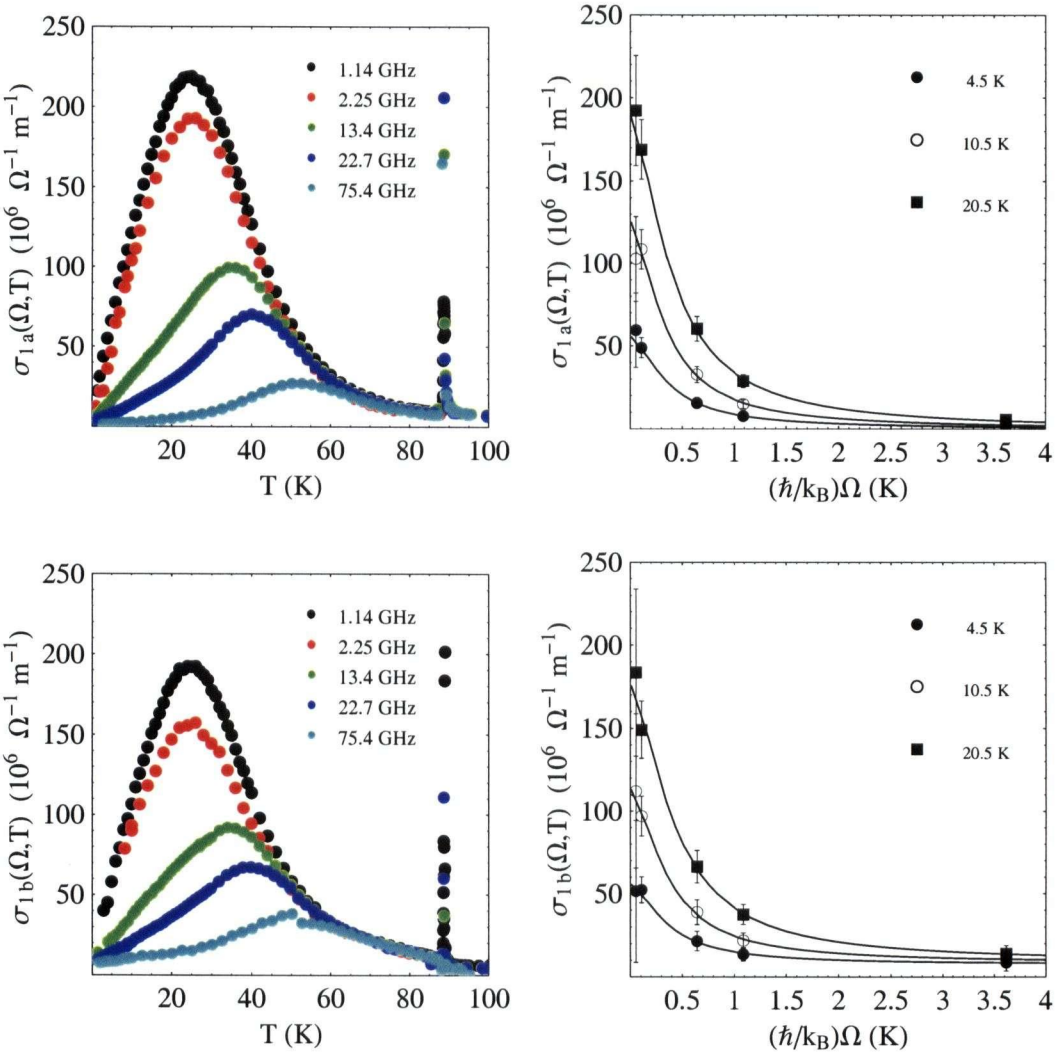

Figure 4.12: The real part of the in-plane microwave conductivity $\sigma_1(\Omega, T)$ of $YBa_2Cu_3O_{6.993}$, as obtained from cavity perturbation experiments. Full temperature sweeps and sample spectra as a function of frequency are shown: $\hat{a}$-axis (upper panels) and $\hat{b}$-axis (lower panels).

A summary of the scattering rate parameter $\Lambda^{-1}(T)$ for both $\hat{a}$ and $\hat{b}$-axis quasiparticle charge transport is shown in Fig. 4.13. As mentioned in Refs. [69] and [43], the in-plane scattering rate appears to be $\hat{a} : \hat{b}$ isotropic with a (presumably elastic scattering) low temperature limit of $0.35 \pm 0.05\,K$. Assuming that this constant accounts for elastic scattering of quasiparticles from crystalline defects, then the temperature dependence of $\Lambda^{-1}(T)$ can be fit with the Umklapp model of Walker and Smith [45]. The resulting fit is shown in Fig. 4.13 with the best fit parameters $C = (1.0 \pm 0.1) \times 10^{-2}\,K^{-1}$ and $\Delta_U = (105 \pm 20)\,K$. Note that this value of Δ_U is roughly a factor of 3 larger than that used to describe the $YBa_2Cu_3O_{6.5}$ (underdoped) data. This is somewhat surprising given the general trend in the cuprates that the superconducting gap maximum Δ_o (see Eq. 2.11) increases with decreasing doping [80]. However, the reader is reminded that the Umklapp construction of Fig. 2.7 is very sensitive to Fermi surface geometry which changes with doping. In particular, as doping δ decreases the Fermi point $\vec{k}_1$ in Fig. 2.7 approaches $(k_x/a, k_y/b) = (\pi/2, \pi/2)$ and the required $\vec{k}_2$ for the Umklapp construction approaches $(k_x/a, k_y/b) = (\pi/2, -\pi/2)$, which is also a node in the superconducting gap ($\Delta_{\vec{k}} = 0$). Thus the smaller value of Δ_U for the underdoped sample can still be considered consistent with expectations, despite the increase of Δ_o with decreasing doping.

There is a slight mismatch between the values of $\Lambda^{-1}(T)$ from the two experimental approaches. However, it should be noted that the samples studied via the five cavity perturbation experiments were produced in 1998 while the sample studied via bolometry was produced in 2002. It is conceivable that the reduction of $\Lambda^{-1}(T)$ in the newer sample is due to recent improvements in $YBa_2Cu_3O_{6+x}$ crystal purity, thus resulting in a lower elastic scattering rate as compared to the older sample.

To see the benefits of the more flexible data analysis presented herein as compared to the Drude analysis of Refs. [69] and [43], note that the integrated quasiparticle weight in those references appeared slightly sublinear as a function of temperature. This was due to the fact that the Drude-like model (Eq. 4.2) correctly captures the width of the conductivity spectra at each temperature but the lineshape lacks spectral weight ($\sigma_1(\Omega) \propto 1/\Omega^2$ at high frequencies); this was particularly noticeable above $20\,K$. However, the more flexible conductivity model (Eq. 4.3 with $y = 1.65$) appears to capture both the width and spectral weight correctly, as demonstrated in Fig. 4.14. This is particularly true in the $\hat{a}$-axis direction where the spectral weight lost from the superfluid is tracked astoundingly well up to $40K$.

There appears to be a small but finite ROS at $T = 0$ according to both the bolometry and resonator points. Taking $\lambda_L^a(T = 0) = 1010\,\text{Å}$, one can calculate the zero temperature total superfluid oscillator strength $(n_s e^2/m^*)(T = 0) = 7.80 \times 10^{19}\,\Omega^{-1}m^{-1}s^{-1}$. Summing the superfluid and resonator ROS in the $\hat{a}$-axis direction gives the total oscillator strength $ne^2/m^* = 7.89 \times 10^{19}\,\Omega^{-1}m^{-1}s^{-1}$. The ROS in the $\hat{a}$-axis quasiparticle conductivity is then estimated to be $\sim 1\%$ of the total low frequency oscillator strength. Similarly, the bolometry ROS suggests that $\sim 0.5\%$ of the total low frequency oscillator strength does not condense. Interestingly, the *absolute values* of the ROS reported for the underdoped (Table 4.2) and overdoped (Table 4.3) compounds are comparable, ranging between $(0.5 \rightarrow 1.0) \times 10^{18}\,\Omega^{-1}m^{-1}s^{-1}$.

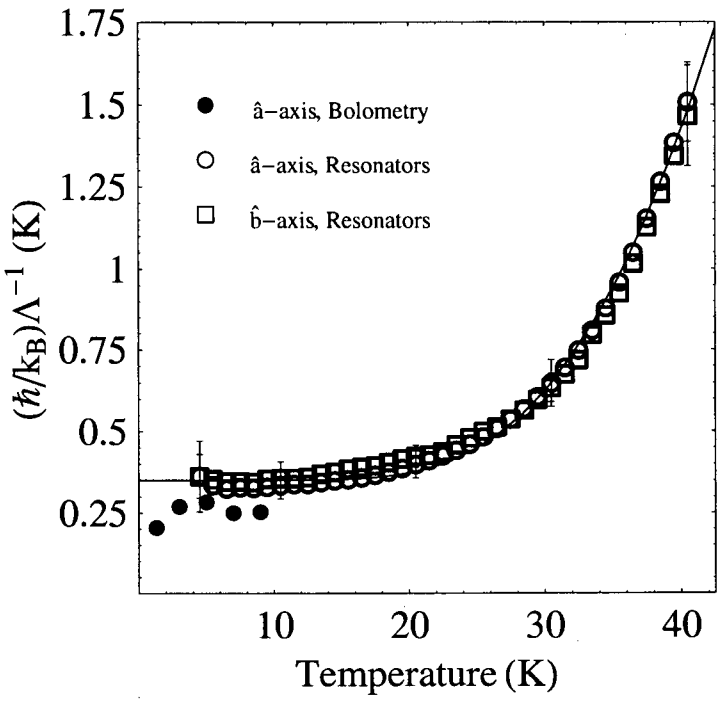

Figure 4.13: The in-plane scattering parameter $\Lambda^{-1}(T)$ of $YBa_2Cu_3O_{6.5}$. The values obtained from fitting both bolometry and resonator surface resistance spectra are shown. Low temperature values from fitting resonator data (below $20\,K$) approach a temperature independent constant of $(0.35 \pm 0.05)\,K$. The presumed inelastic scattering rate has been fit to Eq. 2.15.

The mismatch between the experimental probes is yet more evidence indicating that the sample studied in the bolometry experiments merely had fewer defects than those studied via the cavity perturbation experiments. In general, defects introduce low energy states in the quasiparticle density of states at the Fermi energy because they break Cooper pairs, thus giving rise to finite ROS at $T = 0$. Consequently, lower ROS is indicative of fewer defects in a material. A summary of linear fits to the integrated quasiparticle oscillator strength $(n_n e^2/m^*)_{2D}(T)$ and the change in total quasiparticle oscillator strength is shown in Table 4.3. Upon comparing to the low temperature slopes of the superfluid oscillator strength, one can see that the slope of the $\hat{a}$-axis quasiparticle spectral weight compares favorably while in the $\hat{b}$-axis direction roughly 70% of the spectral weight lost from the superfluid density ends up in the 2-dimensional bands. As an aside, note that the effective mass obtained from the above mentioned value of ne^2/m^* is roughly $m^* \sim 7.5m_e$, where $n \sim 2 \times 10^{28}\ m^{-3}$ as argued previously. While this effective mass is still relatively large, it must be noted that it is roughly a factor of 4 less than what was obtained from measurements on $YBa_2Cu_3O_{6.5}$ (underdoped).

The last important point to note regarding the temperature evolution of the quasiparticle oscillator strength in the 2-dimensional bands is that it appears to be $\hat{a} : \hat{b}$ *isotropic* to within experimental error, modulo any concerns about the values of $\lambda_a(T_{base})$ and $\lambda_b(T_{base})$. Given this observation and the apparent $\hat{a} : \hat{b}$ isotropy of the quasiparticle scattering rate, this author is led to conclude that the band structure picture presented in Chapter 2 does agree with experiments on $YBa_2Cu_3O_{6.993}$.

Orientation	Probe	$\frac{n_n e^2}{m^*}(T=0)(\Omega^{-1}m^{-1}s^{-1})$	$\frac{\hbar}{k_B}\frac{\partial(n_n e^2/m^*)}{\partial T}(\Omega^{-1}m^{-1})$
$\hat{a}$	Bolometry	$(4.9 \pm 1.0) \times 10^{17}$	$(3.7 \pm 0.4) \times 10^6$
$\hat{a}$	Resonators	$(9.4 \pm 3.0) \times 10^{17}$	$(4.3 \pm 0.8) \times 10^6$
$\hat{b}$	Resonators	$(7.0 \pm 5.0) \times 10^{17}$	$(4.1 \pm 1.0) \times 10^6$
$\hat{a}$	$\Delta\lambda(T)$	0 (assumed)	4.2×10^6
$\hat{b}$	$\Delta\lambda(T)$	0 (assumed)	6.0×10^6

Table 4.3: Linear fits to the low temperature quasiparticle oscillator strength $(n_n e^2/m^*)(T)$ for $YBa_2Cu_3O_{6.993}$.

Finally, the fit parameter σ_1^{ID} is shown in Fig. 4.15. The parameter extrapolates to a zero temperature intercept of roughly $7 \times 10^6\ \Omega^{-1}m^{-1}$.

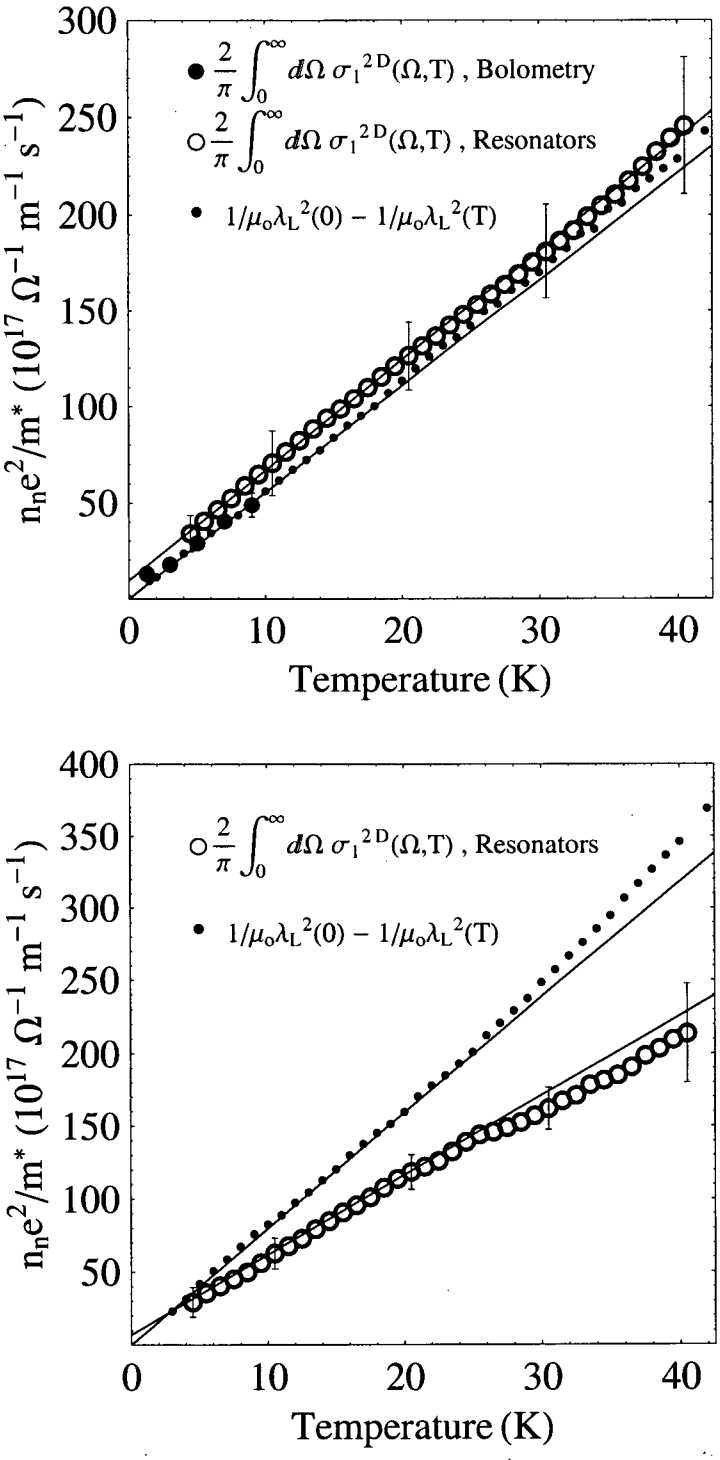

Figure 4.14: The in-plane quasiparticle oscillator strength $(n_n e^2/m^*)(T)$ of $YBa_2Cu_3O_{6.993}$: $\hat{a}$-axis (upper panel) and $\hat{b}$-axis (lower panel).

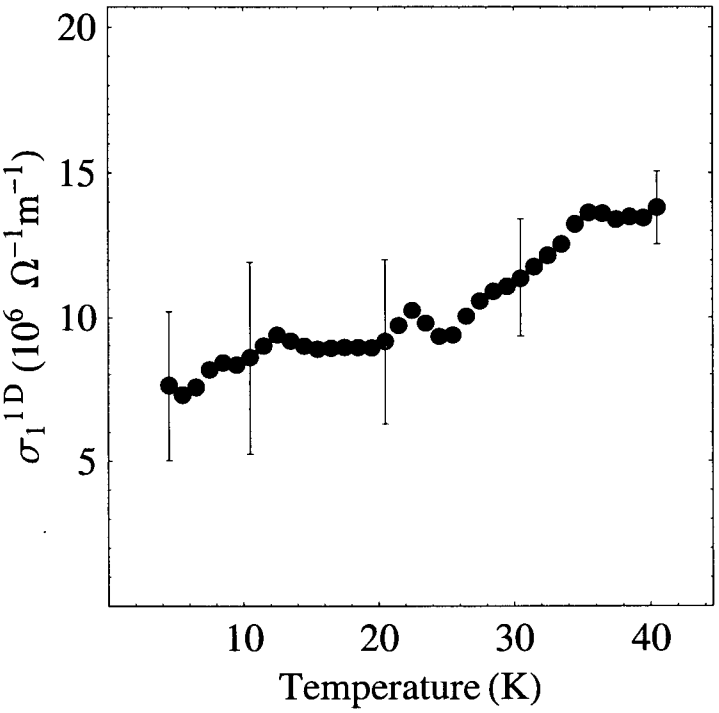

Figure 4.15: The broad quasi-1-dimensional component $\sigma_1^{1D}(\Omega \rightarrow 0, T)$ of the microwave conductivity of $YBa_2Cu_3O_{6.993}$.

To summarize the analysis of $YBa_2Cu_3O_{6.993}$ (overdoped) microwave conductivity data, one can draw 4 key conclusions:

1. The data clearly supports the picture of 2-dimensional bands that contribute equally to $\hat{a}$ and $\hat{b}$-axis charge conductivity and a quasi-1-dimensional band that contributes solely to conductivity in the $\hat{b}$-axis direction.

2. The 2-dimensional band quasiparticle conductivity appears to have an $\hat{a} : \hat{b}$ *isotropic scattering rate* and $\hat{a} : \hat{b}$ *isotropic spectral weight* (provided one trusts the ratio of the in-plane London penetration depths).

3. The $T \rightarrow 0$ scattering rate approaches a constant.

4. There is ROS strength in the 2-dimensional band which is most likely linked to the density of impurities in a given sample.

4.5 Wherefore the Anisotropy in *Ortho-II*?

The only inconsistency with the band structure picture presented in Chapter 2 is the apparent $\hat{a} : \hat{b}$ anisotropic contribution of the 2-dimensional bands to charge conductivity in the $\hat{a}$ and $\hat{b}$ directions of *Ortho-II* ordered $YBa_2Cu_3O_{6.5}$. As stated previously, if the Fermi velocity $\vec{v}_F$ at each of the nodes of the superconducting gap is indeed directed along the first Brillouin zone diagonals, as depicted in Fig. 2.5, then the total spectral weight available for transport $ne^2/m^* \propto (\vec{v}_F \cdot \hat{\imath})^2$ in either the $\hat{\imath} = \hat{a}$ or $\hat{\imath} = \hat{b}$ axis direction ought to be $\hat{a} : \hat{b}$ isotropic. Furthermore, the $\hat{a} : \hat{b}$ anisotropic elastic scattering rate and roughly $\hat{a} : \hat{b}$ isotropic inelastic scattering rate should also be recognized as outstanding issues. This author has hypothesized that this may be a band structure effect due to the *Ortho-II* ordering in the CuO chain layer (See Fig. 4.16). This could have substantial implications for in-plane charge dynamics in *Ortho-II* ordered $YBa_2Cu_3O_{6.5}$.

Before proceeding with any detailed arguments concerning electronic bandstructure, it would be prudent to review the experimental evidence for the existence of *Ortho-II* ordering in the $YBa_2Cu_3O_{6.5}$ samples produced at UBC. Samples similar to those used in the microwave studies were subjected to X-ray diffraction by the crystal grower, Dr. Ruixing Liang, as described in Ref. [33]. (hkl) rocking curves of the $\vec{q} = (5\pi/a, 0, 0)$ superlattice peak indicated that there were *Ortho-II* ordered domains with mean dimensions $(x, y, z) \approx (150, 430, 60)$ Å. Thus the *existence* of the ordering of oxygen in the CuO chain layers of $YBa_2Cu_3O_{6.5}$ produced at UBC has been verified experimentally.

However, the more serious question at hand is whether the ordering in the CuO layers has any measurable effect upon charge dynamics in the adjacent $(CuO_2)^{2-}$ planes. Recent soft resonant X-ray scattering (RSXS) experiments by Feng *et al.* [81] on *Ortho-II* ordered $YBa_2Cu_3O_{6.5}$ produced at UBC have yielded evidence for charge modulation at wavevector $\vec{q} = (\pi/a, 0, 0)$ on planar Cu^{2+} sites with an amplitude of ~ 0.1 hole. Furthermore, an anomalous peak in the $\hat{b}$-axis optical conductivity of other samples produced at UBC has been observed in the superconducting state which is consistent with the model calculations of Bascones [82]. These latter calculations are based upon the premise that *Ortho-II* ordering in the CuO chains leads to a modulation of the electronic state of plane Cu^{2+} sites. The magnitude and details of the modulation is currently the subject of microscopic calculations [81, 82]. Thus the experimental evidence for the oxygen ordering having a measurable effect upon in-plane charge dynamics looks promising at present. As such, it is worthwhile conjecturing how this effect ought to manifest itself in the microwave conductivity of *Ortho-II* ordered $YBa_2Cu_3O_{6.5}$ and then ascertain whether these ideas are consistent with observations.

The effects of doubling the unit cell in the $\hat{a}$-axis direction depend critically upon how one describes the perturbation on the $(CuO_2)^{2-}$ plane layers due to *Ortho-II* ordering in the CuO chain layers. This author has identified two hypotheses that deserve consideration: First, what if the *Ortho-II* ordering simply leads to a slight *modulation of the Coulomb potential* on planar Cu^{2+} sites? Second, what if the *Ortho-II* ordering leads to a *modulation of the ionization state* (through a variation in orbital

occupation) on planar Cu^{2+} sites? It will be demonstrated that these two hypotheses lead to very different conclusions, of which only that of the latter hypothesis can be reconciled with observations.

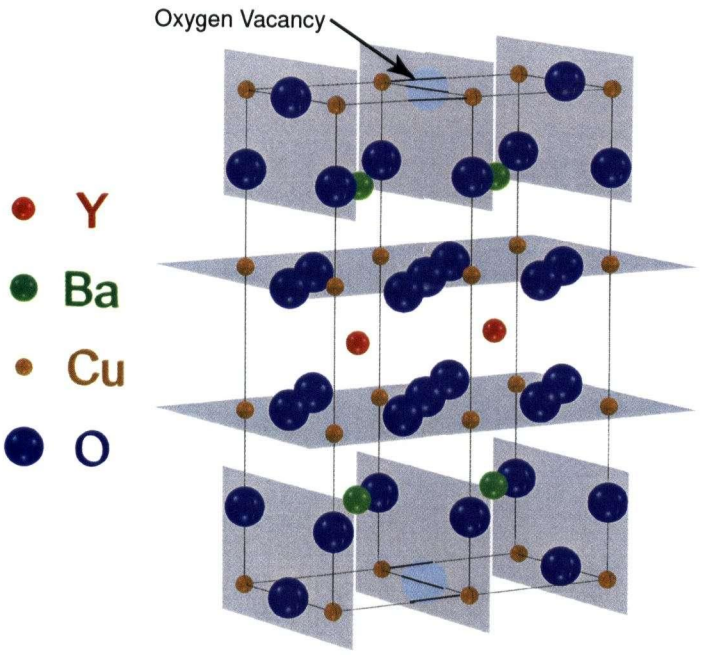

Figure 4.16: The unit cell of *Ortho-II* ordered $YBa_2Cu_3O_{6.5}$. Doubling of the $YBa_2Cu_3O_{6+x}$ unit cell in the $\hat{a}$-axis direction changes the dimensions to $(a, b, c) = (7.6454, 3.8872, 11.68)$ Å. Image provided by D. Peets [34]

4.5.1 Modulation of the Coulomb Potential

In this scenario, the modulation of the Coulomb potential presumably leads to a modulation of nearest neighbour hopping energies t_{plane} in the $\hat{a}$-axis direction. To be definite, make the replacement $t_{plane} \rightarrow t_{plane} \pm \delta t$ where the positive sign applies to sites under full CuO chains and the minus sign applies to sites under vacant chains. If one writes out the real space Hamiltonian for a single $(CuO_2)^{2-}$ plane and then takes its Fourier transform, the result will take on the following form:

$$\mathcal{H}_{plane} = \sum_{\vec{k},\sigma} \xi_{\vec{k}}^{plane} {c_{\vec{k}\sigma}}^{\dagger} c_{\vec{k}\sigma} \tag{4.15}$$

$$\xi_{\vec{k}}^{plane} = -2t_{plane}\big(\cos(k_x a) + \cos(k_y b) + (\delta t/t_{plane})\cos(k_x a - \pi)\big) - \mu_{plane} \ldots$$

Thus the effect of a modulation in the Coulomb potential is made manifest via a new 1-dimensional component in the planar electronic dispersion that is proportional

to $\delta t/t_{plane}$. Note that the perturbation can be tuned continuously and has no effect in the limit $\delta t \rightarrow 0$. However, what is most important is the fact that the Hamiltonian given by Eq. 4.15 has been written as a function of only a single species of fermion, therefore there will be only a single electronic band that crosses the Fermi energy for all values of δt. All that can happen is that the perturbation can break the mirror symmetry across the ΓS cut of the first Brillouin zone (FBZ), thus leading to a canting of the Fermi velocity at the nodal point away from the zone diagonal. Since the spectral weight available for transport $ne^2/m^* \propto (\vec{v}_F \cdot \hat{\imath})^2$ (where $\hat{\imath} = \hat{a}$ or $\hat{\imath} = \hat{b}$), then this model can generate $\hat{a} : \hat{b}$ anisotropic spectral weight from a 2-dimensional $(CuO_2)^{2-}$ plane band. On the other hand, since there must be a unique thermalization or scattering rate for any given band, then this model *cannot* produce $\hat{a} : \hat{b}$ anisotropic scattering. Therefore, the hypothesis that *Ortho-II* ordering simply leads to a modulation of the Coulomb potential on the adjacent $(CuO_2)^{2-}$ planes is inconsistent with observations.

4.5.2 Modulation of the Ionization State

Given that contiguous segments of CuO chain lead to hole doping of the adjacent $(CuO_2)^{2-}$ planes, it is entirely possible that there will be a higher probability of finding holes near these chains. Consequently, one expects that the electronic state of a Cu^{2+} under a full chain will differ from that under an empty chain. Feng *et al.* [81] have suggested that the hole density in planar Cu3*d* orbitals ρ_{3d} can be crudely expressed as

$$| \, (\rho_{3d})^{1/2} \, \Phi_{3d} \rangle_{F(E)} = \alpha_{F(E)} |3d_{x^2-y^2}\rangle + \beta_{F(E)} |3d_{3z^2-r^2}\rangle$$

where $F(E)$ denotes a planar Cu^{2+} adjacent to a full (empty) chain. The parameters α and β control the hole concentration in the $3d_{x^2-y^2}$ and $3d_{3z^2-r^2}$ orbitals, respectively. The reader is reminded that while the former orbital has figured prominently in much of the discussion thusfar, it is the latter which mediates hole doping of the $(CuO_2)^{2-}$ via bonding to an $O2p_z$ orbital in the BaO layer which then bonds to a $Cu3d_{y^2-z^2}$ orbital in the CuO layer. If the F state truly differs from the E state, then there will necessarily be two *distinct* electronic sublattices on the $(CuO_2)^{2-}$ plane with periodicity $2a$ in the $\hat{a}$-axis direction. One must then write the real space Hamiltonian in terms of two species of fermions which will then give rise to two distinct electronic bands in momentum space.

A solution to the above problem can be obtained by plotting the original plane and chain dispersions in a reduced FBZ, on account of the doubling of the unit cell dimension in the $\hat{a}$-axis direction which then halves the size of the FBZ in the $\hat{k}_x$ direction. As a result, all of the segments of Fermi surface between $\pi/2a \leq k_x \leq \pi/a$ in Fig. 2.5 should be folded back into the FBZ to produce three new bands. However, to keep the story simple I will choose to concentrate solely upon one of the 2-dimensional bands, as sketched in Fig. 4.17. The new band that is produced by zone folding will have a dispersion similar to that of the original $(CuO_2)^{2-}$ plane

band (Eq. 2.7), but with the substitution $k_x \rightarrow k_x - \pi/a$:

$$\begin{aligned} \xi_{\vec{k}}^{fold} &= -2t_{plane}\big(\cos(k_x a - \pi) + \cos(k_y b) + 2t' \cos(k_x a - \pi)\cos(k_y b) \\ &\quad + t''(\cos(2k_x a - \pi) + \cos(2k_y b))\big) - \mu_{plane} \end{aligned} \tag{4.16}$$

To lift the degeneracy between the bands given be Eqns. 2.7 and 4.16 at the new zone boundary $k_x = \pi/2a$, one must account for the kinetic energy difference between hopping an electron onto a Cu^{2+} site under either an empty or full CuO chain. Let this energy difference be denoted by t_{fold} (the choice of sign will not be important). The resulting Hamiltonian for this two band system will then be

$$\mathcal{H} = \sum_{\vec{k}} \mathbf{C}_{\vec{k}}^{\dagger} \begin{pmatrix} \xi_{\vec{k}}^{plane} & t_{fold} & 0 & \Delta_{\vec{k}} \\ t_{fold} & \xi_{\vec{k}}^{fold} & \Delta_{\vec{k}} & 0 \\ 0 & \Delta_{\vec{k}} & -\xi_{\vec{k}}^{fold} & t_{fold} \\ \Delta_{\vec{k}} & 0 & t_{fold} & -\xi_{\vec{k}}^{plane} \end{pmatrix} \mathbf{C}_{\vec{k}} \tag{4.17}$$

$$\mathbf{C}_{\vec{k}}^{\dagger} = \begin{pmatrix} c_{p-\vec{k}\downarrow}^{\dagger} & c_{f-\vec{k}\downarrow}^{\dagger} & c_{f\vec{k}\uparrow} & c_{p\vec{k}\uparrow} \end{pmatrix}$$

where $c_{p\vec{k}\sigma}^{\dagger}$ ($c_{p\vec{k}\sigma}$) and $c_{f\vec{k}\sigma}^{\dagger}$ ($c_{f\vec{k}\sigma}$) are creation (annihilation) operators for electrons in the original plane band (Eq. 2.7) and folded band (Eq. 4.16), respectively. This system can be diagonalized and in the limit $t_{fold} \ll t_{plane}$ yields two new dispersions of the form

$$\begin{aligned} \xi_{\vec{k}}^{1} &\approx \sqrt{(\xi_{\vec{k}}^{plane} - t_{fold})^2 + \Delta_{\vec{k}}^2} \\ \xi_{\vec{k}}^{2} &\approx \sqrt{(\xi_{\vec{k}}^{fold} + t_{fold})^2 + \Delta_{\vec{k}}^2} \end{aligned} \tag{4.18}$$

A visual demonstration of the zone folding procedure is shown in Fig. 4.17. The normal state dispersions ($\Delta_{\vec{k}} = 0$), normal state Fermi surfaces and superconducting gap along each Fermi surface are shown in Fig. 4.18 for the choice of parameters $(t_{plane}, t_{fold}, \mu_{plane}) = (500, 100, -100)\, meV$ with $t' = -0.3$ and $t'' = 0.1$. Note that the values of t_{plane}, μ_{plane}, t' and t'' chosen for this demonstration are identical to those used in Chapter 2. Arguably one should choose a value of μ_{plane} closer to zero (half filling) to model an underdoped cuprate such as $YBa_2Cu_3O_{6.5}$, but the arguments presented herein will not depend critically upon the exact value of μ_{plane}. The result provided from zone folding is a new 1-dimensional band that will contribute solely to charge transport in the $\hat{b}$-axis direction. Note that this new band is in no way related to the quasi-1-dimensional band discussed in Chapter 2 that primarily consisted of chain-like electronic states.

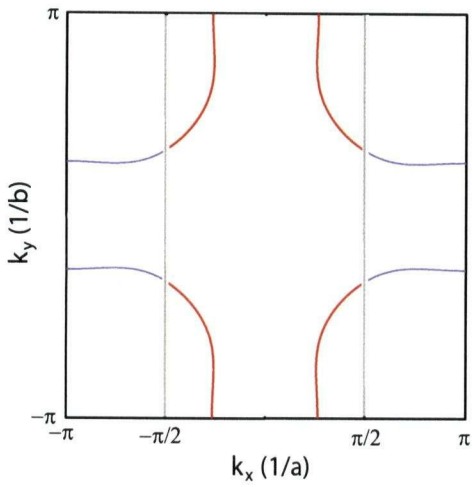

1. Original 2-dimensional Band FS

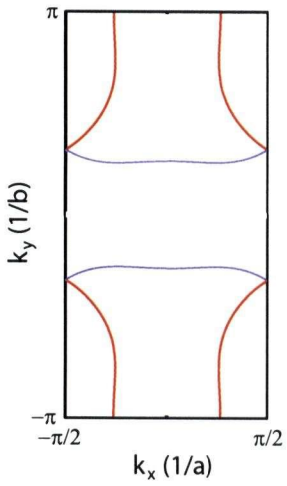

2. Folding into new first BZ

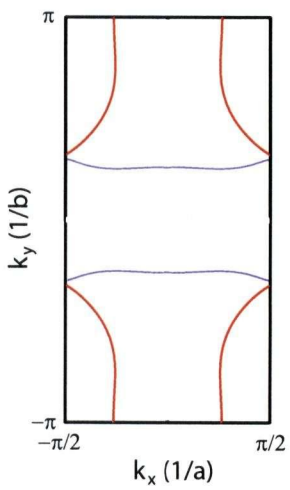

3. Level repulsion at boundary

Figure 4.17: The generation of a 1-dimensional band composed of plane states via zone folding in *Ortho-II* ordered $YBa_2Cu_3O_{6.5}$. A single $(CuO_2)^{2-}$ plane band (1) is subjected to a doubling of the unit cell dimension in the $\hat{x}$ direction. The first Brillouin zone is reduced to half of its original size and the wings of the original band are folded back into the new zone (2). The potential at the boundaries of the new unit cell provide a means of lifting the degeneracy at the first Brillouin zone boundary (3).

The new 1-dimensional band is constructed entirely of plane electronic states, therefore electrons occupying these states will scatter from the same in-plane crystalline defects as those electrons in the 2-dimensional band. Nonetheless, it is possible that the elastic scattering rates for these two bands will differ. As shown in Fig. 4.19, the four Fermi points of the 2-dimensional band are now located very close to the zone boundary and one can very effectively scatter into the second Brillouin zone (SBZ) via a very small wavevector $\vec{q}_{2D}^{\,min}$. On the other hand, the magnitude of the smallest wavevector connecting nodes in the 1-dimensional band, denoted by $\vec{q}_{1D}^{\,min}$ will be significantly larger; $|\vec{q}_{1D}^{\,min}| > |\vec{q}_{2D}^{\,min}|$. As argued in Chapter 2, if the in-plane defects generate $\hat{T}$-matrix components with non-negligible momentum dependence, then the elastic scattering rates for these bands will not be identical. As a crude estimate, assume that the defects are indeed Yukawa potentials with the screening wavevector $q_o \sim |\vec{k}_{F,1D}| = |\vec{q}_{1D}^{\,min}/\sqrt{2}|$, where $\vec{k}_{F,1D}$ is the Fermi wavevector of the 1-dimensional band. Using the simple Fourier transform formula discussed in Chapter 2,

$$\hat{T}(\vec{q},\omega) \approx V(\vec{q}) \propto \frac{1}{1+(q/q_o)^2},$$

one can then estimate that $\hat{T}(\vec{q}_{2D}^{\,min} \approx 0,\omega)/\hat{T}(\vec{q}_{1D}^{\,min},\omega) \sim (1+(|\vec{q}_{1D}^{\,min}|/q_o)^2) \sim 3$. If these two components of the $\hat{T}$-matrix dominate the internode scattering, then one can state that the elastic scattering rate will be approximately 3 times larger in the 2-dimensional band than in the 1-dimensional band.

Within the picture presented herein, the $\hat{b}$-axis quasiparticle conductivity of *Ortho-II* ordered $YBa_2Cu_3O_{6.5}$ should rightfully include contributions from six bands; two 2-dimensional bands, two 1-dimensional bands from zone folding and two quasi-1-dimensional bands from the folding of the primarily chain-like band of Chapter 2. Assuming that level repulsion does not drastically alter any of their Fermi surfaces, then an *effective* conductivity expression can be written as a sum of only three terms: a very broad contribution from the chain-derived quasi-1-dimensional bands (σ_1^{1D}), a narrower contribution from the 2-dimensional bands (σ_1^{2D}) and an even narrower contribution from the new 1-dimensional bands derived from zone folding (σ_1^{fold}):

$$\sigma_{1b}(\Omega,T) = \sigma_1^{1D}(\Omega,T) + \sigma_1^{2D}(\Omega,T) + \sigma_1^{fold}(\Omega,T) \tag{4.19}$$

Here it is anticipated that $\sigma_1^{1D}(\Omega,T) \approx \sigma_1^{1D}(\Omega \rightarrow 0,T)$ over the bandwidth of interest and that $\sigma_1^{2D}(\Omega,T) = \sigma_{1a}(\Omega,T)$ can be modelled by the form Eq. 4.3. The only new term is then $\sigma_1^{fold}(\Omega,T)$ whose spectrum can presumably be captured using the flexible form

$$\sigma_1^{fold}(\Omega,T) = \frac{\sigma_o^{fold}(T)}{1+(\Omega\Lambda_{fold}(T))^{y_{fold}(T)}} \tag{4.20}$$

with temperature dependent unknown parameters σ_o^{fold}, Λ_{fold} and y_{fold}.

A key question that must be addressed is whether $\sigma_{1b}(\Omega,T)$ (Fig. 4.4) has been successfully extracted from $R_{sb}(\Omega,T)$, despite having used a model conductivity expression in Section 4.3 that does not contain a presumably narrow component $\sigma_1^{fold}(\Omega,T)$. This author argues that the extraction procedure has worked properly because the form of the 2-dimensional term in Eq. 4.7 is sufficiently flexible to model the sum

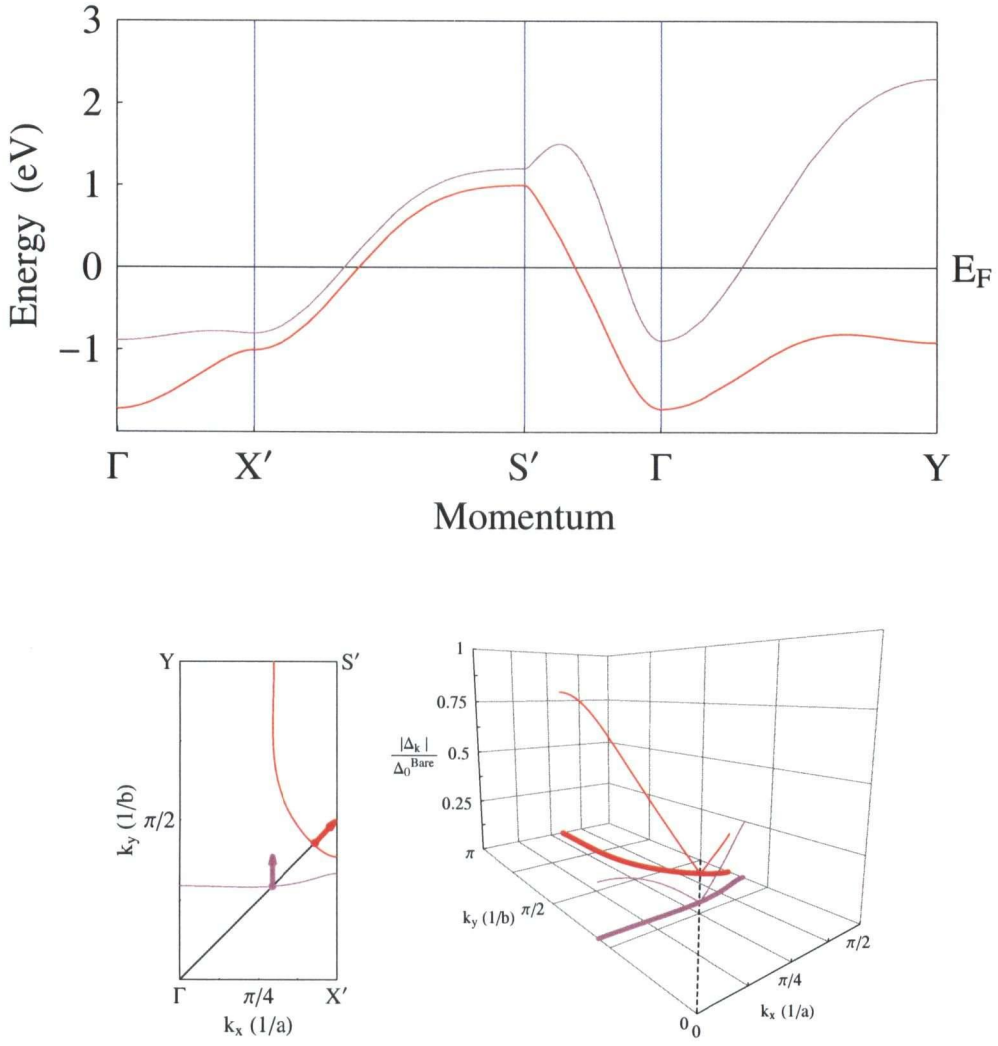

Figure 4.18: The effect of *Ortho-II* ordering on a 2-dimensional plane band. Upper panel displays the 2-dimensional dispersion $\xi^1_{\vec{k}}$ (red) and the new 1-dimensional dispersion $\xi^2_{\vec{k}}$ (mauve). Fermi surfaces are shown in the lower left panel with the direction of the Fermi velocities at points on the zone diagonal indicated with arrows. Lower right panel displays the magnitude of the superconducting gap $|\Delta_{\vec{k}}|$ evaluated along each Fermi surface with the node in each band located along the zone diagonal (dashed line).

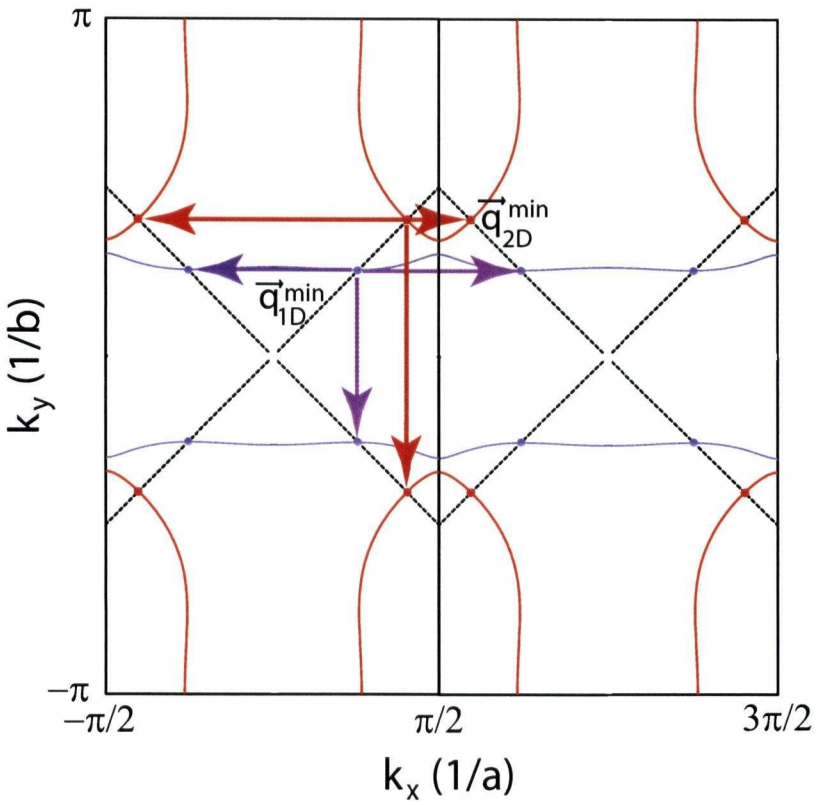

Figure 4.19: Elastic scattering in the plane derived bands of *Ortho-II* ordered $YBa_2Cu_3O_{6.5}$. The FBZ and one SBZ are shown. The 2-dimensional band Fermi surface is shown in red and the 1- dimensional band in mauve. The three shortest internode scattering wavevectors for each band are shown, with the smallest of these denoted as $\vec{q}_{1D}^{\,min}$ and $\vec{q}_{2D}^{\,min}$. Nodal directions ($\Delta_{\vec{k}} = 0$) are indicated by dashed lines.

$\sigma_1^{2D} + \sigma_1^{fold}$. Thus the $\hat{b}$-axis fit parameters y and Λ reported in Section 4.3 (Figs. 4.5 and 4.7, respectively) are then to be interpreted as weighted means of the exponents and scattering parameters for the 2-dimensional bands and the 1-dimensional bands. Therefore, the presumed anisotropy of the 2-dimensional band quasiparticle scattering rate in Fig. 4.7 is conceivably an artifact from misinterpreting the conductivity spectra.

As a demonstration, the $\hat{b}$-axis surface resistance data from the bolometry experiment have been fit with the new conductivity expression, Eq. 4.19, with $\sigma_1^{2D}(\Omega, T)$ parameterized by the fits to the $\hat{a}$-axis data (Eq. 4.3 with $y(T)$, $\Lambda(T)$ and $\sigma_o(T) \propto (n_n e^2/m^*)_{2D}(T)$ fixed to their best fit values for $\hat{a}$-axis conductivity), $\sigma_1^{fold}(\Omega, T)$ parameterized as in Eq. 4.20 (with $\sigma_o^{fold}(T)$, $\Lambda_{fold}(T)$ and $y_{fold}(T)$ as free parameters) and $\sigma_1^{1D}(\Omega, T) = \sigma_1^{1D}(\Omega \rightarrow 0, T)$ (a free parameter). 'Experimental' values of $\sigma_{1b}(\Omega, T)$ were then extracted as described previously. Note that this procedure *assumes* that σ_1^{2D} provides an isotropic contribution to in-plane quasiparticle charge conductivity. Furthermore, the validity of this procedure is highly dependent upon having the ratio of the absolute values of the $\hat{a}$ and $\hat{b}$-axis spectral weights correct (via the choice of $\lambda_a(T_{base})/\lambda_b(T_{base})$). The resulting values of $\sigma_{1b}(\Omega, T)$ and the best fits are shown in Fig. 4.20. Note that the points in this figure are virtually identical to those in the lower panel of Fig. 4.4, thus reinforcing this author's claim that the numerical procedures used herein to obtain $\sigma_1(\Omega, T)$ from $R_s(\Omega, T)$ are relatively model independent.

A summary of the best fit parameters is shown in Fig. 4.21. The behaviour of the exponent $y_{fold}(T)$ is noticeably different than those used to fit σ_1^{2D} ($\hat{a}$-axis values in Fig. 4.5), thus indicating that the 1-dimensional bands produce qualitatively different spectra than the 2-dimensional bands. The scattering parameter $(\hbar/k_B)\Lambda_{fold}^{-1}(T)$ displays a linear temperature dependence with a $T = 0$ intercept of $2.3 \times 10^{-2}\, K$ and slope 4.5×10^{-3}. This indicates that the $T = 0$ scattering rate for the 1-dimensional bands is roughly a factor of 2 less than that for the 2-dimensional bands (compare to $\hat{a}$-axis bolometry results in Table 4.1). Furthermore, the former scattering rate evolves much slower with temperature. The integrated quasiparticle spectral weight attributed to the 1-dimensional bands,

$$\left(\frac{n_n e^2}{m^*}\right)_{fold}(T) = \frac{2}{\pi}\int d\Omega\, \sigma_1^{fold}(\Omega, T) = \frac{\sigma_o^{fold}(T)}{y_{fold}(T)\Lambda_{fold}(T)}\csc(\pi/y_{fold}(T))$$

also shows linear behaviour with respect to temperature with $T = 0$ ROS of $5.3 \times 10^{17}\, \Omega^{-1}m^{-1}s^{-1}$ and slope (multiplied by $\hbar/k_B$) of $1.7 \times 10^6\, \Omega^{-1}m^{-1}$. Comparing these numbers to the $\hat{a}$-axis results in Table 4.2, one can conclude that the quasiparticle spectral weight attributed to the 1 and 2-dimensional bands are roughly equivalent. Finally, the parameter $\sigma_1^{1D}(\Omega \rightarrow 0, T)$ is shown to be roughly constant $\sim 2.6 \times 10^6\, \Omega^{-1}m^{-1}$, which is identical to the results shown in Fig. 4.9.

Based upon these observations, one must conclude that the zone folding picture developed herein is, *at the very least*, consistent with observations since nothing untoward comes out of fitting the $\hat{b}$-axis surface resistance data to the model conductivity expression Eq. 4.19. However, this is by no means a definitive proof that this picture is the correct explanation for the $\hat{a} : \hat{b}$ anisotropy of the in-plane electrodynamics of *Ortho-II* ordered $YBa_2Cu_3O_{6.5}$.

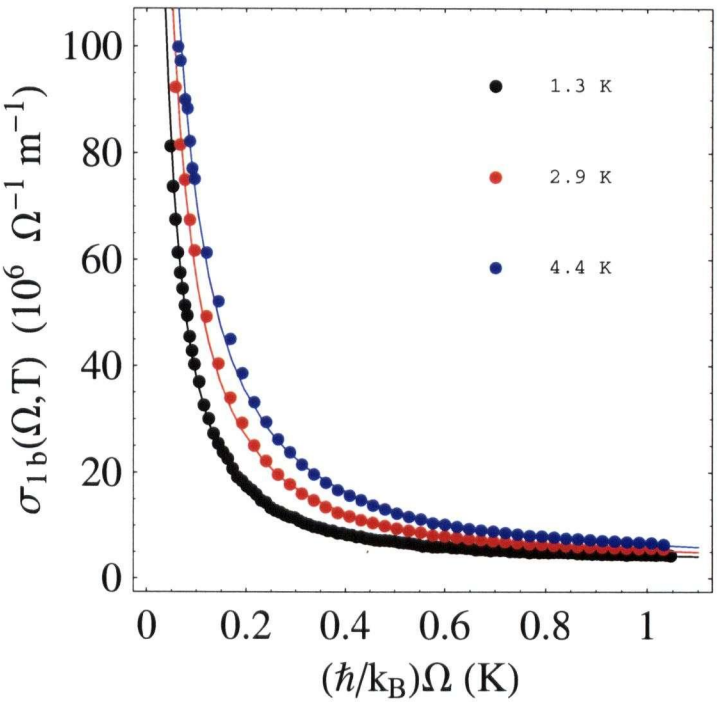

Figure 4.20: The real part of the $\hat{b}$-axis microwave conductivity of *Ortho-II* ordered $YBa_2Cu_3O_{6+x}$, as obtained by fitting to a model that includes the effects of doubling the unit cell in the $\hat{a}$-axis direction. Note that the results are virtually identical to Fig. 4.4.

Finally, if the zone folding picture is indeed correct, then one is forced to conclude that the inelastic scattering in the $(CuO_2)^{2-}$ planes cannot be entirely explained by the Walker-Smith Umklapp process [45]. Upon comparing the first Brillouin zones in Figs. 2.7 and 4.19, one can see that there is *no* possible Umklapp construction for relaxing charge currents attributed to the 2-dimensional bands in the $\hat{a}$-axis direction in the former case. Rather, this author suggests that more conventional inelastic scattering of quasiparticles from small $\vec{q}$ bosonic excitations will become prominent at low T in *Ortho-II* ordered $YBa_2Cu_3O_{6.5}$ because of the proximity of the nodes in the 2-dimensional bands to the first Brillouin zone boundary. As with the elastic scattering shown in Fig. 4.19, even small $\vec{q}$ inelastic scattering events can provide very effective backscattering in the $\hat{a}$-axis direction in this geometry.

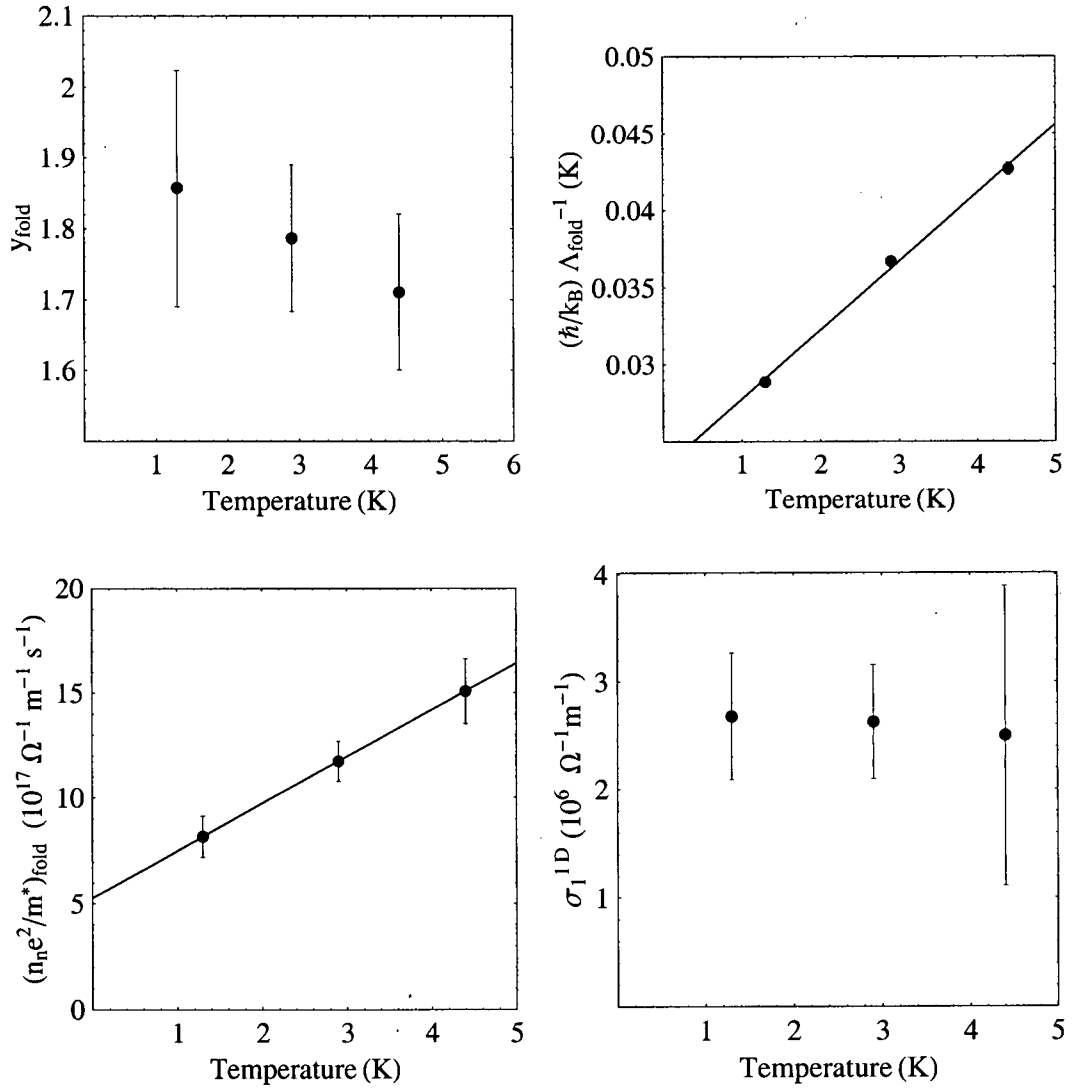

Figure 4.21: Parameterization of the 1-dimensional band from zone folding. Results obtained from fitting $\hat{b}$ axis surface resistance data on *Ortho-II* ordered $YBa_2Cu_3O_{6.5}$ from the bolometry experiment.

Chapter 5

Microscopic Models of Quasiparticle Charge Conductivity

In the first chapter of this thesis it was hypothesized that the superconducting state of the cuprates is a Fermi liquid condensate with well defined quasiparticles. This statement was verified on a qualitative level in Chapter 4 since sharp conductivity spectra were observed (which is indicative of long-lived quasiparticles) and there were no serious discrepancies between microwave conductivity data and simple spectral weight arguments. The next logical step would then be to compare the experimentally determined quasiparticle charge conductivity to a microscopic model based upon conventional many body techniques.

The fundamentals of superconductivity in a metallic system can be well described by the groundbreaking work of Bardeen, Cooper and Schrieffer [36] in which the superconducting groundstate is a phase coherent condensate of correlated electron pairs with zero net momentum. The attractive electron-electron potential $V_{\vec{k},\vec{k}'}$ (presumably peaked around $\vec{k}' = -\vec{k}$) is mediated via the exchange of bosons (phonons in the case of metallic systems) and gives rise to a mean field order parameter (OP) $\Delta_{\vec{k}}$. The resulting Hamiltonian (in Nambu notation) is written as:

$$\hat{\mathcal{H}} = \sum_{\vec{k}} C^{\dagger}_{\vec{k}} \begin{pmatrix} \xi_{\vec{k}} & \Delta_{\vec{k}} \\ \Delta_{\vec{k}} & -\xi_{\vec{k}} \end{pmatrix} C_{\vec{k}} \tag{5.1}$$

where $\xi_{\vec{k}}$ will be the electronic dispersion of a *single* 2-dimensional band from a $(CuO_2)^{2-}$ plane. For a single band the Nambu spinor will have two components and be defined as given in Eq. 2.4. The superconducting OP is defined via a self consistent equation:

$$\Delta_{\vec{k}} = \frac{1}{\nu} \sum_{\vec{k}'} V_{\vec{k},\vec{k}'} \frac{\tanh(E_{\vec{k}'}/2T)}{2E_{\vec{k}'}} \Delta_{\vec{k}'} \tag{5.2}$$

where $E_{\vec{k}} = \sqrt{\xi^2_{\vec{k}} + \Delta^2_{\vec{k}}}$. Note that a factor of $\hbar/k_B$ has been suppressed in the argument of the hyperbolic tangent if the energy $E_{\vec{k}}$ is expressed in units of angular frequency (s^{-1}). The bare quasiparticle propagator is defined as

$$\hat{\mathcal{G}}_o(\vec{k},\omega) \equiv \left\langle C_{\vec{k}} C^{\dagger}_{\vec{k}} \right\rangle = \frac{\omega\hat{\tau}^0 + \Delta_{\vec{k}}\hat{\tau}^1 + \xi_{\vec{k}}\hat{\tau}^3}{\omega^2 - \xi^2_{\vec{k}} - \Delta^2_{\vec{k}}} \tag{5.3}$$

and $\hat{\tau}^i$ are the Pauli Matrices:

$$\hat{\tau}^0 = \begin{pmatrix} 1 & 0 \\ 0 & 1 \end{pmatrix} \quad \hat{\tau}^1 = \begin{pmatrix} 0 & 1 \\ 1 & 0 \end{pmatrix} \quad \hat{\tau}^2 = \begin{pmatrix} 0 & i \\ -i & 0 \end{pmatrix} \quad \hat{\tau}^3 = \begin{pmatrix} 1 & 0 \\ 0 & -1 \end{pmatrix}$$

The reader is referred to Abrikosov and Gor'kov for a complete derivation of the BCS Hamiltonian [83]. In the case of the cuprates it is well established experimentally that the low temperature groundstate is BCS-like in that it consists of a phase coherent condensate of Cooper pairs of electrons [84, 85]. However the pairing mechanism remains elusive. Furthermore, the cuprates all display an OP symmetry that has never been seen in the more conventional superconductors, namely $d_{x^2-y^2}$ [84, 86, 87]:

$$\Delta_{\vec{k}} = \Delta_{\hat{k}} = \Delta_o \cos 2\phi \tag{5.4}$$

where ϕ is an angle within the $(CuO_2)^{2-}$ plane with respect to either the $\hat{a}$ or $\hat{b}$ axis. Note that Eq. 5.4 is a simplified form of the OP used in Chapter 2 (Eq. 2.11) and is appropriate when discussing superconductivity in only a single band.

The problem at hand will require the calculation of the quasiparticle propagator in the presence of crystalline defects. This will allow one to calculate the charge conductivity $\sigma(\Omega, T)$ at low temperatures where quasiparticle propagation is limited by elastic scattering from defect potentials. If the defects are both random and dilute, then they can be described as a perturbation to Eq. 5.1 and lead to a renormalized quasiparticle propagator:

$$\hat{\mathcal{G}}(\vec{k}, \omega) = \frac{\tilde{\omega}\hat{\tau}^0 + \tilde{\Delta}_{\hat{k}}\hat{\tau}^1 + \tilde{\xi}_{\vec{k}}\hat{\tau}^3}{\tilde{\omega}^2 - \tilde{\xi}_{\vec{k}}^2 - \tilde{\Delta}_{\hat{k}}^2} \tag{5.5}$$

where $\tilde{\omega} \equiv \omega - \Sigma_0(\tilde{\omega})$, $\tilde{\Delta}_{\hat{k}} \equiv \Delta_{\hat{k}} + \Sigma_1(\tilde{\omega})$ and $\tilde{\xi}_{\vec{k}} \equiv \xi_{\vec{k}} + \Sigma_3(\tilde{\omega})$ are the normalized quasiparticle energy, OP and electronic dispersion, respectively. Collectively the renormalizations make up a quantity known as the self energy $\hat{\Sigma}(\tilde{\omega})$ defined as

$$\hat{\Sigma}(\tilde{\omega}) = \Sigma_0(\tilde{\omega})\hat{\tau}^0 + \Sigma_1(\tilde{\omega})\hat{\tau}^1 + \Sigma_3(\tilde{\omega})\hat{\tau}^3, \tag{5.6}$$

which can in principle be calculated via Feynman diagrammatic methods [88].

5.1 Calculation of $\sigma(\Omega, T)$

The calculation of the charge conductivity tensor $\sigma_{ij}(\Omega, T)$ for a metal within linear response theory (small applied electromagnetic potential) is well documented by Mahan [88]. The calculation proceeds in a similar manner for a superconductor except that one must work with the quasiparticle propagator $\langle \mathcal{C}\mathcal{C}^\dagger \rangle$ instead of electron propagators $\langle cc^\dagger \rangle$. The starting point is the electrical Kubo formula:

$$\sigma_{ij}(\Omega, T) \overset{\lim \vec{q} \to 0}{=} \frac{1}{\Omega} \int_0^\infty dt\, e^{i\Omega t} \langle [\mathcal{J}_i(\vec{q}, t), \mathcal{J}_j(-\vec{q}, 0)] \rangle + \frac{ne^2}{m^*\Omega} i\delta_{i,j} \tag{5.7}$$

where $\langle \ldots \rangle$ denotes a thermal average and $[a,b] = ab - ba$ (commutation). The current operator $\mathcal{J}_i(\vec{q},t)$ is defined as

$$\mathcal{J}_i(\vec{q},t) = \frac{\alpha e}{2m} \sum_{\vec{k}} \left(2\vec{k} - \vec{q}\right) \cdot \hat{\imath}\, C^{\dagger}_{\vec{k}-\vec{q}}(t) C_{\vec{k}}(t) \tag{5.8}$$

where $\hat{\imath} = \{\hat{x}, \hat{y}\}$ for an isolated 2-dimensional $(CuO_2)^{2-}$ plane. I have also allowed for a Fermi liquid correction α to the electrical charge in the manner of Ioffe and Millis [89]. This calculation has been presented in the literature in a number of forms, most notably by Hirschfeld, Putikka and Scalapino [78, 79], Hettler and Hirschfeld [90, 91], Berlinsky *et al.* [92] and others [93–96]. However, in each of the above cases the authors have chosen to neglect various components of $\hat{\Sigma}(\tilde{\omega})$ so as to simplify matters. This author has repeated the calculations allowing for all three components of Eq. 5.6 to be nonzero. The result for the real part of the diagonal component of the conductivity tensor ($\{i,j\} = \hat{x}$) is as follows:

$$\begin{aligned}
\sigma_1(\Omega,T) \;=\; & -\frac{1}{2}\alpha^2 \frac{ne^2}{m^*} \int_{-\infty}^{\infty} d\omega \int_0^{2\pi} \frac{d\phi}{2\pi} \frac{\tanh(\omega/2T) - \tanh(\omega'/2T)}{2\Omega} \\
& \times \mathrm{Im}\Big[\Big\{ \frac{\tilde{\omega}'_+(\tilde{\omega}_+ + \tilde{\omega}'_+) + \tilde{\Delta}'_{\hat{k}+}(\tilde{\Delta}_{\hat{k}+} - \tilde{\Delta}'_{\hat{k}+})}{\xi_{0+}^2 - \xi_{0+}'^2} \left(\frac{1}{\xi'_{0+}} - \frac{1}{\xi_{0+}}\right) \gamma_{++} \\
& + \frac{\tilde{\omega}'_-(\tilde{\omega}_+ + \tilde{\omega}'_-) + \tilde{\Delta}'_{\hat{k}-}(\tilde{\Delta}_{\hat{k}+} - \tilde{\Delta}'_{\hat{k}-})}{\xi_{0+}^2 - \xi_{0-}'^2} \left(\frac{1}{\xi'_{0-}} + \frac{1}{\xi_{0+}}\right) \gamma_{-+} \\
& + \frac{1}{\xi_{0+}} (\gamma_{-+} - \gamma_{++}) \Big\} \Big]
\end{aligned} \tag{5.9}$$

$$\gamma_{-+} = \frac{1}{1 - \left(\frac{\Sigma'_{3-} - \Sigma_{3+}}{\xi_{0+} - \xi'_{0-}}\right)^2} \quad \gamma_{-+} = \frac{1}{1 - \left(\frac{\Sigma'_{3-} - \Sigma_{3+}}{\xi_{0+} - \xi'_{0-}}\right)^2}$$

$$\xi_{0\alpha} = \mathrm{sgn}(\omega)\sqrt{\tilde{\omega}_\alpha^2 - \tilde{\Delta}_{\hat{k}\alpha}^2} \quad \xi'_{0\beta} = \mathrm{sgn}(\omega)\sqrt{\tilde{\omega}_\alpha'^2 - \tilde{\Delta}_{\hat{k}\alpha}'^2}$$

The subscripts on the renormalized frequencies $\tilde{\omega}_\alpha$ indicate the sign of the imaginary part of $\tilde{\omega}$ ($\mathrm{Im}|\tilde{\omega}_\alpha| = -\alpha \mathrm{Im}\Sigma_0(\tilde{\omega})$). The renormalized OP's $\tilde{\Delta}_{\hat{k}\alpha}$ and electronic dispersion renormalizations $\Sigma_{3\alpha}$ are to be evaluated self-consistently with $\tilde{\omega}_\alpha$. All primed quantities are to be evaluated at $\omega' = \omega - \Omega$. Note that the above result agrees with that of Hettler and Hirschfeld [91] if one assumes $\Sigma_3 = 0$ (then $\gamma_{-+} = \gamma_{++} = 1$).

The above expression simplifies considerably if one assumes that the OP is not renormalized ($\Sigma_1 = 0$). While this may not be the case for $Bi_2Sr_2CaCu_2O_{8+x}$, as experimentally observed by STS [97], it is most likely a reasonable assumption for very clean $YBa_2Cu_3O_{6+x}$ in which the charge doping of the $(CuO_2)^{2-}$ planes appears

to be relatively uniform. The result in this particular case is then

$$\begin{aligned}\sigma_1(\Omega,T) &= -\frac{1}{2}\alpha^2\frac{ne^2}{m^*}\int_{-\infty}^{\infty}d\omega\int_0^{2\pi}\frac{d\phi}{2\pi}\frac{\tanh(\omega/2T)-\tanh(\omega'/2T)}{2\Omega}\\ &\times\mathrm{Im}\Big[\Big\{\frac{\tilde{\omega}'_+}{\tilde{\omega}'_+-\tilde{\omega}_+}\left(\frac{1}{\xi'_{0+}}-\frac{1}{\xi_{0+}}\right)\gamma_{++}\\ &+\frac{\tilde{\omega}'_-}{\tilde{\omega}_+-\tilde{\omega}'_-}\left(\frac{1}{\xi_{0+}}+\frac{1}{\xi'_{0-}}\right)\gamma_{-+}+\frac{1}{\xi_{0+}}\left(\gamma_{-+}-\gamma_{++}\right)\Big\}\Big]\end{aligned} \tag{5.10}$$

Equation 5.10 agrees with the results of Hirschfeld, Putikka and Scalapino [78, 79] if one sets $\Sigma_3 = 0$. Both Eqns. 5.9 and 5.10 give the same result in the limit of zero microwave frequency:

$$\begin{aligned}\sigma_1(\Omega\to 0,T) &= -\frac{1}{2}\alpha^2\frac{ne^2}{m^*}\int_{-\infty}^{\infty}d\omega\int_0^{2\pi}\frac{d\phi}{2\pi}\left(-\frac{\partial f}{\partial\omega}\right)\\ &\times\mathrm{Im}\left[\left\{\frac{\tilde{\omega}_+^2}{\xi_{0+}^3}+\frac{\tilde{\omega}_-}{2i\mathrm{Im}\Sigma_0}\left(\frac{1}{\xi_{0+}}+\frac{1}{\xi_{0-}}\right)\right\}\right]\end{aligned} \tag{5.11}$$

where $f(\omega) = 1/(e^{\omega/T}+1)$ is the Fermi distribution function. The width of the thermal factor $-\partial f/\partial\omega$ is roughly $3T$ and serves as a windowing function that acts upon the contents of the curled braces in Eq. 5.11. At extremely low temperatures ($T \ll -\mathrm{Im}\Sigma_0(\omega\to 0)$) the first term in curled braces dominates the integral. It can be shown that this expression reduces to the universal limit that was originally derived by Lee [98] and later modified by Durst and Lee [99] to include vertex corrections (which will be suppressed for the time being):

$$\sigma_1(\Omega\to 0, T\to 0) = \alpha^2\frac{ne^2}{\pi m^*\Delta_o} \tag{5.12}$$

Note that this quantity does not contain $\Sigma_0(\tilde{\omega})$ and so it is independent of quasiparticle scattering (hence its universality). However, the limit given in Eq. 5.12 is valid only at very low temperatures that may not even be experimentally accessible for very clean samples. Instead, a more practical limit for studying the microwave conductivity data presented in this thesis is $-\mathrm{Im}\Sigma_0(\omega\to 0) \ll T \ll \Delta_o$, in which case the second term in Eq. 5.11 dominates the integral:

$$\sigma_1(\Omega\to 0,T) \approx \frac{1}{2}\alpha^2\frac{ne^2}{m^*}\int_{-\infty}^{\infty}d\omega\left(-\frac{\partial f}{\partial\omega}\right)\frac{N(\omega)}{(-\mathrm{Im}\Sigma_0)} \tag{5.13}$$

Here $N(\omega)$ is the momentum integrated density of states (DOS) in the superconducting state,

$$N(\omega) = \frac{2}{\pi N_o}\int d^3k\,\delta\Big(\omega-\sqrt{\xi_{\vec{k}}^2+\Delta_{\vec{k}}^2}\Big) = \frac{2}{\pi}\mathrm{Re}\left[K\left(\Delta_o/\tilde{\omega}\right)\right] \tag{5.14}$$

$$K(x) \equiv \int_0^{\pi/2}d\theta\,(1-x^2\sin^2\theta)^{-1/2}$$

where πN_o is the density of states per unit cell volume at the Fermi energy in the absence of superconductivity ($\Delta_{\hat{k}} = 0$) for a cylindrical Fermi surface. At very low energies Eq. 5.14 reduces to $N(\omega) \approx \mathrm{Re}\sqrt{\tilde{\omega}^2}/\Delta_o$. In particular at $\omega = 0$, $N(\omega) = -\mathrm{Im}\Sigma_0(0)/\Delta_o$. On the other hand, if $\omega \gg -Im\Sigma_0(\tilde{\omega})$ then $N(\omega) \approx \omega/\Delta_o$ which is the usual clean d-wave single particle DOS.

The last theoretical result to be presented herein is the superfluid oscillator strength. Recall from Eqns. 3.2, 3.3 and 3.4 that at low microwave frequencies $\sigma_2(\Omega \to 0, T) \to (1/\Omega)(n_s e^2/m^*)$. Taking the imaginary part of Eq. 5.7 and multiplying it by Ω gives the desired result.

$$\frac{n_s e^2}{m^*}(T) = -\frac{1}{2}\alpha^2 \frac{ne^2}{m^*}\mathrm{Re}\left[\int_{-\infty}^{\infty} d\omega \int_0^{2\pi} \frac{d\phi}{2\pi} \tanh(\omega/2T)\frac{\Delta_{\hat{k}}^2}{\xi_{0+}^3}\right] \tag{5.15}$$

Equation 5.15 agrees with the expression of Hirschfeld, Putikka and Scalapino exactly [78, 79] and is in no way influenced by $\Sigma_3(\tilde{\omega})$. If $\mathrm{Im}\Sigma_0(\tilde{\omega}) \ll \omega$, then the angular integral $\int_0^{2\pi} d\phi(\hat{\Delta}_{\hat{k}}^2/\xi_{0+}^3)/2\pi \approx -1/\Delta_o$ for $\omega \ll \Delta_o$. For $-\mathrm{Im}\Sigma_0(\omega \to 0) \ll T \ll \Delta_o$ the first derivative of the superfluid oscillator strength with respect to temperature yields

$$\frac{d}{dT}\left(\frac{n_s e^2}{m^*}\right) = -\alpha^2 \frac{ne^2}{m^*}\int_{-\infty}^{\infty} d\omega \cosh(\omega/2T)\left(\frac{|\omega|}{2T^2}\right) = -2\ln 2\,\alpha^2 \frac{ne^2}{m^*\Delta_o}. \tag{5.16}$$

Thus the slope of the superfluid oscillator strength versus temperature gives access to the combination of microscopic parameters $\alpha^2(ne^2/m^*\Delta_o)$.

Recent insights from Franz *et al.* [35, 100] and Ioffe and Millis [89] have suggested that for hole doped cuprate superconductors the sum in Eq. 5.8 should be truncated at some finite wavevector away from the four Fermi points located along the nodes of the d-wave OP. This translates into a restriction of all ω integrals in Eqns. 5.9, 5.10, 5.11, 5.13, 5.15 and 5.16 to a finite range $\{-E_C, E_C\}$ where $E_C < \Delta_o$. If this cutoff energy is proportional to the hole doping per Cu site, δ, then it forces the $T = 0$ superfluid density to follow δ as opposed to $1 - \delta$ (electron density per Cu site):

$$\frac{n_s e^2}{m^*}(T = 0) \approx \alpha^2 \frac{ne^2}{m^*}\frac{E_C}{\Delta_o} \tag{5.17}$$

However, if $T \ll E_C$ then neither $\sigma_1(\Omega, T)$ nor $\partial(n_s e^2/m^*)/\partial T$ will be influenced by E_C; this is because the thermal factors in Eqns. 5.9, 5.10, 5.11, 5.12 and 5.16 all drop off rapidly over an energy $\sim 3T$. Therefore changes in superfluid oscillator strength, $(n_s e^2/m^*)(T) - (n_s e^2/m^*)(T = 0)$, remain unaffected by E_C. Furthermore, since $T = 0$ residual quasiparticle oscillator strength $(n_n e^2/m^*)(T = 0)$ is entirely due to defect induced quasiparticle states at $\omega = 0$, then this quantity remains unaltered as well. As a consequence of the above two conclusions, the low temperature quasiparticle oscillator strength $n_n e^2/m^*(T)$ is not influenced by the choice of E_C. On the other hand, one must redefine the oscillator strength sum rule since the total available oscillator strength will no longer be $\alpha^2 ne^2/m^*$. This can be accomplished

by assuming that all of the spectral weight ends up in the superfluid of a *clean* system where $\tilde{\omega}_+ = \omega + i0$:

$$\frac{n_n e^2}{m^*}(T) + \frac{n_s e^2}{m^*}(T) = \frac{n_s e^2}{m^*}(T=0)|_{\tilde{\omega}=\omega+i0} \tag{5.18}$$

As an interesting aside, one can calculate E_C from measurements of the in-plane penetration depth. From the ratio of Eqns. 5.16 and 5.17;

$$-\frac{\frac{n_s e^2}{m^*}(T=0)}{\frac{d}{dT}\left(\frac{n_s e^2}{m^*}\right)} = \frac{1/\mu_o \lambda_L^2(T=0)}{-d(1/\mu_o\lambda_L^2)/dT} = \frac{E_C}{2\ln 2}$$

Using the $\hat{a}$-axis values from Table 3.1, one obtains $E_C \approx 150\,K$ for $YBa_2Cu_3O_{6.5}$ and $E_C \approx 210\,K$ for $YBa_2Cu_3O_{6.993}$.

5.2 Scaling of Microwave Conductivity Data

For the sake of performing numerical calculations of $\sigma_1(\Omega, T)$ via Eqns. 5.9 and 5.10 it has proven useful to render the integral dimensionless by dividing all energies by Δ_o, which is the largest energy in the problem. These equations then take the general form

$$\sigma_1(\Omega, T) = \frac{\hbar}{k_B}\alpha^2 \frac{ne^2}{m^*\Delta_o}\int d(\omega/\Delta_o)\,\mathcal{F}\left[\frac{\tilde{\omega}}{\Delta_o}, \frac{\Omega}{\Delta_o}, \frac{T}{\Delta_o}\right]$$

Therefore, the natural unit of microwave conductivity is $(\hbar/k_B)\alpha^2 ne^2/m^*\Delta_o$, which can be conveniently obtained from penetration depth measurements (Eq. 5.17). Recall from the previous chapter that comparisons between the total quasiparticle oscillator strength and the slope of the low temperature superfluid oscillator strength are independent of the choice of $\lambda_L(T=0)$, so dividing the conductivity data by $\alpha^2 ne^2/m^*\Delta_o$ is a relatively 'safe' procedure.

To render the integrals dimensionless one must also know Δ_o to scale the independent variables Ω and T. It is easiest to determine Δ_o from an alternate experimental probe such as the zero temperature limit of the thermal conductivity, $\kappa(T)$, as measured by Sutherland *et al.* [80]. This is a particularly robust quantity in a *d*-wave superconductor that is independent of quasiparticle renormalizations *and* vertex corrections [99, 101]:

$$(\lim T \to 0)\ \frac{\kappa(T)}{T} = \frac{k_B^2}{3\hbar^2}\frac{2}{c}\left(\frac{v_F}{v_\Delta} + \frac{v_\Delta}{v_F}\right) \tag{5.19}$$

where v_F is the magnitude of the Fermi velocity at one of the Fermi points, $v_\Delta \equiv 2\Delta_o/m^*v_F$ and c is the unit cell dimension in the $\hat{c}$-axis direction. Thus if one knows the mean Fermi velocity v_F for the 2-dimensional bands of Fig. 2.5, then it is possible to extract Δ_o from thermal conductivity measurements. Sutherland *et al.* have performed such measurements on samples of $YBa_2Cu_3O_{6.5}$ and $YBa_2Cu_3O_{6.993}$ that were produced at UBC.

A summary of the scaling parameters that are relevant to $\hat{a}$-axis microwave conductivity is presented in Table 5.1. Only the $\hat{a}$-axis data will be considered henceforth because charge conduction in this direction contains contributions from neither the chain-like quasi-1-dimensional band (as argued in Chapter 2) nor any of the 1-dimensional bands derived from doubling of the unit cell in *Ortho-II* ordered $YBa_2Cu_3O_{6.5}$ (as argued in Chapter 4).

Doping (x)	$\frac{\hbar}{k_B}\alpha^2\frac{ne^2}{m^*\Delta_o}\,(\Omega^{-1}m^{-1})$	$\Delta_o\,(K)$	E_C/Δ_o
0.5	1.5×10^6	800 ± 100	0.19
0.993	4.2×10^6	400 ± 30	0.53

Table 5.1: Summary of parameters for scaling $\hat{a}$-axis microwave conductivity data. Values of Δ_o taken from Ref. [80].

The scaled $\hat{a}$-axis bolometry data from $YBa_2Cu_3O_{6.5}$ (Fig. 4.4) and $YBa_2Cu_3O_{6.993}$ (Fig. 4.10) are shown in Fig. 5.1. The left panels show the dimensionless conductivity versus Ω. The right panels demonstrate scaling of the observed lineshapes as a function of temperature. Recall from Chapter 4 that in the underdoped case both $n_n e^2/m^*$ and Λ^{-1} varied as $(T+T_o)$ but $\sigma_1(\Omega\rightarrow 0,T)$ remained fixed - therefore any gains in spectral weight with increasing temperature came from the broadening of the lineshape. Scaling the angular frequency axis as $\Omega/(T+T_o)$ (with $T_o=2K$) reveals a temperature independent lineshape. In the overdoped case $n_n e^2/m^*$ was observed to vary as $(T+T_o)$ but Λ^{-1} was roughly constant from $3K$ to $9K$. In this case the gains in spectral weight with increasing temperature result in an overall enhancement of the conductivity at any given frequency by an amount proportional to $(T+T_o)$. Scaling the dimensionless conductivity axis by the factor $T_o/(T+T_o)$ (with $T_o=0.9K$) reveals a relatively temperature independent lineshape. However, it should be noted that the $1.3\,K$ and $3\,K$ lineshapes appear slightly narrower than those at higher temperatures.

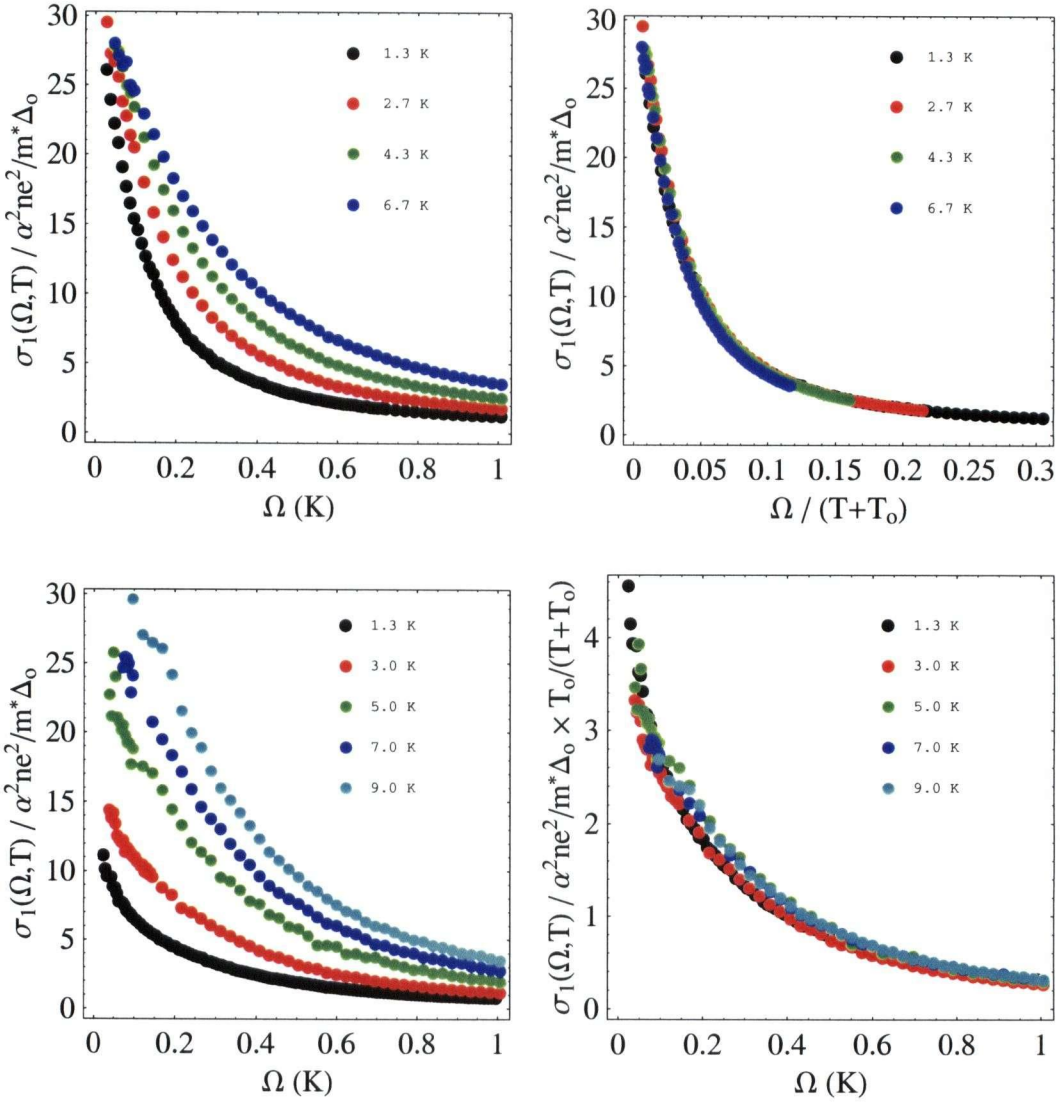

Figure 5.1: The dimensionless $\hat{a}$-axis microwave conductivity: $YBa_2Cu_3O_{6.5}$ (top panels) and $YBa_2Cu_3O_{6.993}$ (lower panels). Left panels show $\sigma_{1a}(\Omega, T)$ rendered dimensionless via a factor proportional to the slope of the superfluid oscillator strength at low temperatures. Right panels demonstrate the two different forms of $(T + T_o)$ scaling that were observed.

5.3 Point-Like Coulomb Defects

The logical starting point for studying the role of defects in d-wave superconductors is to consider a point-like Coulomb defect potential in an otherwise perfect crystal lattice. As a first approximation this seems to be a reasonable approach for studying the effect of cation substitution (Zn^{2+}, Ni^{2+} and others) into Cu^{2+} sites on the $(CuO_2)^{2-}$ planes. As such, the point-like Coulomb defect has been studied extensively in the literature [78, 79, 94, 102].

For dilute random defect potentials one can use a standard result known as the $\hat{T}$-matrix for calculating the quasiparticle self energy [88]:

$$\hat{T}(\vec{k},\vec{k}',\tilde{\omega}) = \hat{V}(\vec{k}-\vec{k}') + \sum_{\vec{k}''} \hat{V}(\vec{k}-\vec{k}'')\hat{\mathcal{G}}(\vec{k}'',\tilde{\omega})\hat{T}(\vec{k}'',\vec{k}',\tilde{\omega}) \tag{5.20}$$

$$\hat{\Sigma}(\tilde{\omega}) \equiv \pi N_o \Gamma \hat{T}(\vec{k},\vec{k},\tilde{\omega}) \tag{5.21}$$

Here, $\Gamma = nn_i/\pi N_o$ is the 'normal' state electronic scattering rate. The elements $\hat{T}(\vec{k},\vec{k}',\tilde{\omega})$ reflect how strongly the points $\vec{k}$ and $\vec{k}'$ in momentum space are connected via elastic scattering of quasiparticles by interactions with the defect potential $\hat{V}$. If the real space potential is a δ-function, then its Fourier transform will be a constant, $\hat{V}(\vec{k}-\vec{k}') = \hat{V}_o$. Therefore all points in momentum space can be accessed with equal probability and the $\hat{T}$-matrix reduces to a momentum independent scalar, $\hat{T}(\vec{k},\vec{k}',\tilde{\omega}) = \hat{T}(\tilde{\omega})$. One can then solve Eq. 5.20 for $\hat{T}(\tilde{\omega})$ and insert the result into Eq. 5.21:

$$\hat{\Sigma}(\tilde{\omega}) = \Gamma \frac{\pi N_o \hat{V}_o}{1-(\pi N_o \hat{V}_o)\hat{G}(\tilde{\omega})} \tag{5.22}$$

where the momentum integrated Green Function $\hat{G}(\tilde{\omega})$ is defined as

$$\hat{G}(\tilde{\omega}) \equiv \frac{1}{\pi N_o}\sum_{\vec{k}} \mathcal{G}(\vec{k},\tilde{\omega}) = G_0(\tilde{\omega})\hat{\tau}^0 + G_1(\tilde{\omega})\hat{\tau}^1 + G_3(\tilde{\omega})\hat{\tau}^3 \tag{5.23}$$

Referring back to the renormalized propagator Eq. 5.5, one can see that $G_3 = 0$ if $\tilde{\xi}_{\vec{k}}$ is an odd function of $\vec{k}-\vec{k}_F$ (see Ref. [102] for a robust proof). Furthermore, if the OP has the symmetry suggested by Eq. 5.4, then upon integrating over $\phi \in \{0, 2\pi\}$ one will obtain $G_1 = 0$ as well. All that remains is the $\hat{\tau}^o$ component, $G_0(\tilde{\omega})$. If one assumes a cylindrical Fermi surface (for simplicity) and replaces the sum in Eq. 5.23 by an integral, then

$$G_0(\tilde{\omega}) = -i\frac{2}{\pi}K\left(\Delta_o/\tilde{\omega}\right) \tag{5.24}$$

The next objective is to work out a form for the operator $\hat{V}_o$ in Nambu notation. For a Coulomb defect located at the origin of the form $V_{Co}\delta(\vec{r})$, the perturbation to the Hamiltonian Eq. 5.1 will have the form

$$\delta\mathcal{H} = \sum_{\vec{k},\vec{k}',\sigma} V_{Co} c^\dagger_{\vec{k}',\sigma} c_{\vec{k},\sigma} = \sum_{\vec{k},\vec{k}'} \mathcal{C}^\dagger_{\vec{k}'}\left(V_{Co}\hat{\tau}^3\right)\mathcal{C}_{\vec{k}} \tag{5.25}$$

Thus one can conclude that $\hat{V}_o = V_{Co}\hat{\tau}^3$ for this particular case. Using the convention $c \equiv 1/(\pi N_o V_{Co})$, Eq. 5.22 can now be reduced to the following:

$$\hat{\Sigma}(\tilde{\omega}) = \frac{\Gamma G_0(\tilde{\omega})}{c^2 - (G_0(\tilde{\omega}))^2}\hat{\tau}^0 - \frac{\Gamma c}{c^2 - (G_0(\tilde{\omega}))^2}\hat{\tau}^3 \tag{5.26}$$

Therefore, a point-like Coulomb potential gives rise to renormalizations to the quasiparticle energies $\tilde{\omega}$ and the electronic dispersions $\tilde{\xi}_{\vec{k}}$. Note that $\tilde{\omega}$ is an argument in $G_o(\tilde{\omega})$ so one must solve for $\Sigma_0(\tilde{\omega})$ self consistently via Eq. 5.26. The renormalizations are governed by two parameters, Γ and c^{-1}, which roughly correspond to the concentration of defects n_i and the strength of each defect potential V_{Co}. As an example, plots of $\Sigma_0(\tilde{\omega})$ and $\Sigma_3(\tilde{\omega})$ for $\Gamma/\Delta_o = 0.0025$ and $c = 0.4$ are shown in Fig. 5.2. These plots show $\hat{\Sigma}(\tilde{\omega})$ over the range $\omega > 0$, and in general $\hat{\Sigma}(\tilde{\omega}) = -\hat{\Sigma}(-\tilde{\omega})^*$. Particular attention is to be drawn to the peak in $-\mathrm{Im}\Sigma_0(\tilde{\omega})$ which is located at an energy denoted as ω_{peak}. This is a resonance due to a virtual bound state near the defect and ω_{peak} is a strong function of c^{-1}: For $c^{-1} \to \infty$ (strong on unitary scattering) $\omega_{peak} \to 0$. For $c^{-1} \to 0$ (weak or Born scattering) ω_{peak} shifts towards Δ_o.

The reader's attention is also drawn to the fact that for $\omega < \omega_{peak}$, $-\mathrm{Im}\Sigma_0(\tilde{\omega})$ is roughly linear with a slope of $\Gamma/\Delta_o c^2$. This can be seen from Eq. 5.26 by noting that for a clean d-wave superconductor $-\mathrm{Im}G_0(\tilde{\omega}) = N(\omega) \approx \omega/\Delta_o$ and by approximating the denominator to be c^2 at small ω. For $\omega > \omega_{peak}$, $-\mathrm{Im}\Sigma_0(\tilde{\omega}) \propto 1/\omega$ up to $\omega \sim \Delta_o$. For $\omega \gg \Delta_o$, $-\mathrm{Im}\Sigma_0(\tilde{\omega}) \to \Gamma$, which is the normal state electronic scattering rate.

Given values of Γ and c, one can now calculate the real part of the microwave conductivity via Eq. 5.10. This was performed numerically using procedures developed by the author. Values of $\omega/\Delta_o \in \{1 \times 10^{-9}, 15T\}$ were sampled on a logarithmic metric, thus emphasizing any low energy features in the integrand. At each value of ω, the integrand was sampled over the range of angles $\phi \in \{(1/2)\mathrm{Re}|\arccos(\tilde{\omega}/\Delta_o)| - (5/2)\mathrm{Im}|\arccos(\tilde{\omega}/\Delta_o)|, \pi/4\}$ with care taken near the angles $(1/2)\mathrm{Re}|\arccos(\tilde{\omega}/\Delta_o)|$ and $(1/2)\mathrm{Re}|\arccos(\tilde{\omega}'/\Delta_o)|$ where the integrand has sharp features due to terms of the form $1/\xi_{o\alpha}$ and $1/\xi'_{o\beta}$ (see Eq. 5.9). A cubic spline was then passed through the sampled integrand as a function of ϕ and the integral evaluated numerically. This result was then multiplied by 8 to give the desired integral over the range $\phi \in \{0, 2\pi\}$. Once this was accomplished at all of the chosen values of ω a second spline curve was constructed and the integration over ω was performed. All numerical results were chopped at 5 digits precision during the course of a calculation.

From performing a series of these calculations the author was able to make a few general observations. First, for any given c (which determines ω_{peak}), one obtains cusp-like lineshapes with a T independent value of $\sigma_1(\Omega \to 0, T)$, similar to the $YBa_2Cu_3O_{6.5}$ data, for $T \lesssim 5\omega_{peak}$. At these temperatures the thermal factor in Eq. 5.10 samples the integrand over the region where $-\mathrm{Im}\Sigma_0(\tilde{\omega}) \approx \Gamma\omega/\Delta_o c^2 \to N(\omega) \times (\Gamma/c^2)$. This is also the temperature regime in which Eq. 5.13 is expected to hold, and inserting the approximate form for the self energy yields

$$\sigma_1(\Omega \to 0, T) \approx \frac{1}{2}\alpha^2 \frac{ne^2}{m^*}\left(\frac{\Gamma}{c^2}\right)^{-1} = \frac{1}{2}\alpha^2 \frac{ne^2}{m^*\Delta_o}\left(\frac{\Gamma}{\Delta_o c^2}\right)^{-1} \tag{5.27}$$

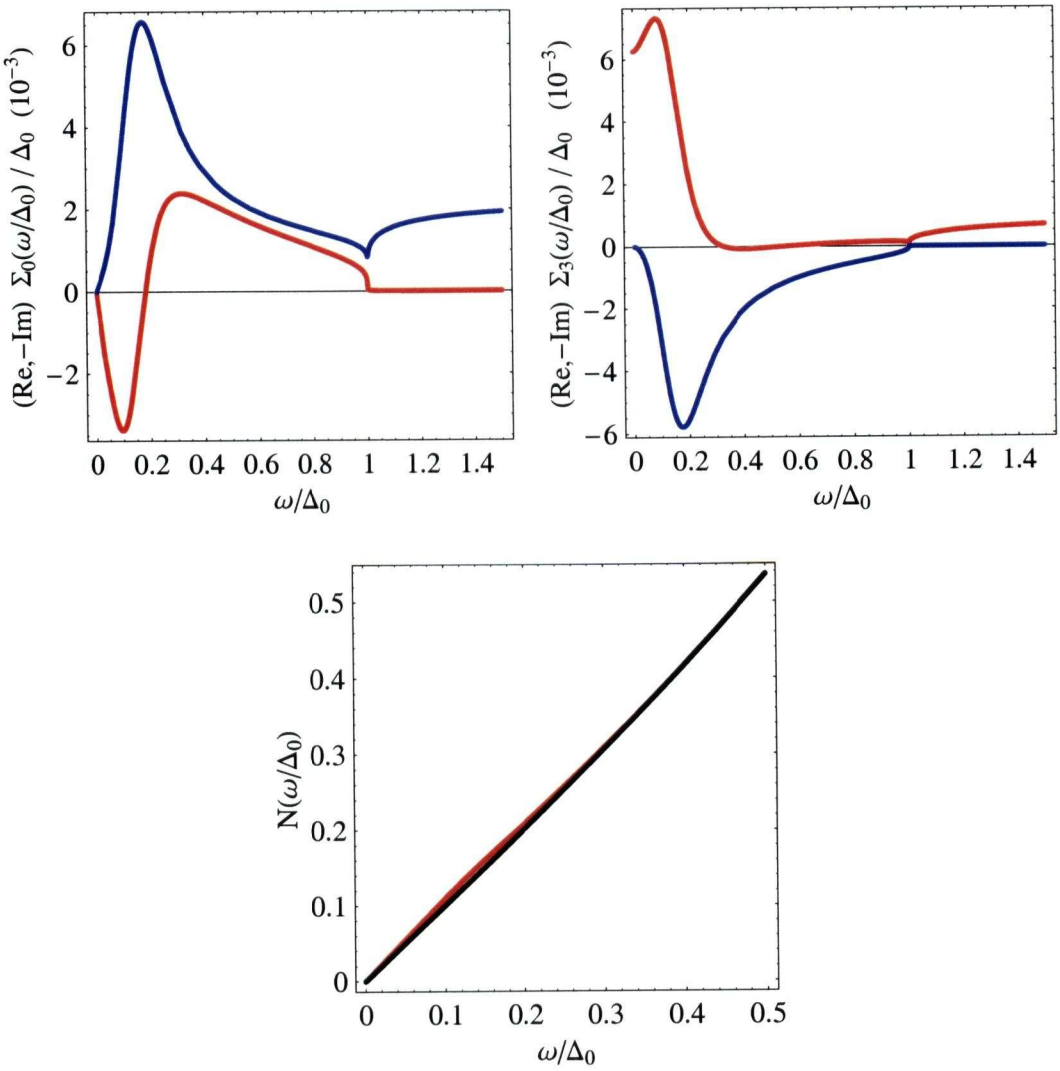

Figure 5.2: The quasiparticle self-energy and density of states (DOS) due to elastic scattering from point-like Coulomb defects using the parameters $\Gamma/\Delta_o = 2.5 \times 10^{-3}$ and $c = 0.4$. Top panels show $\hat{\Sigma}(\tilde{\omega}) = \Sigma_0(\tilde{\omega})\hat{\tau}^0 + \Sigma_3(\tilde{\omega})\hat{\tau}^3$ with the real parts shown in red and negative of the imaginary parts in blue. Lower panel displays the DOS for the system with the above scattering parameters (red) and that of a clean d-wave superconductor (black).

Furthermore, the width of the conductivity spectra obtained in this regime vary linearly with T. On the other hand, if $T > 5\omega_{peak}$ then $\sigma_1(\Omega \to 0, T)$ is observed to rise roughly as T^2 and the spectra start to narrow as $1/T$. Thus ω_{peak} represents an important crossover energy between what looks like Born limit scattering lineshapes at low temperatures to unitary limit lineshapes at higher temperatures. These observations then suggest the following recipe for fitting experimental data:

1. Look for a fixed $\sigma_1(\Omega \to 0, T)$ intercept at low temperatures. Use Eq. 5.27 to establish $\Gamma/\Delta_o c^2$.

2. Observe the temperature $T \sim 5\omega_{peak}$ at which there is a crossover from Born-like to unitary-like lineshapes. This uniquely determines c.

Thus one can determine the parameters Γ/Δ_o and c directly from scaled plots of the microwave conductivity, as shown in Fig. 5.1. For the $YBa_2Cu_3O_{6.5}$ data, one can clearly see the zero frequency intercept (~ 35). However, there is no evident crossover temperature so at best one can place a lower bound upon $\omega_{peak} \gtrsim (6.7\,K)/5$. For the $YBa_2Cu_3O_{6.993}$ data the low temperature fixed zero frequency intercept is more difficult to discern, but one can roughly estimate that the 1.3 and $3.0\,K$ spectra converge at a zero frequency intercept ~ 18 in dimensionless units. The crossover temperature is then around $3\,K$, so $\omega_{peak} \sim (3\,K)/5$. The resulting fits are shown in Fig. 5.3 and a summary of fit parameters is given in Table 5.2.

Doping (x)	$\Gamma/\Delta_o c^2$	$T \sim 5\omega_{peak}\,(K)$	Γ/Δ_o	c
0.5	1/70	$\gtrsim 6.7$	$\gtrsim 1.4 \times 10^{-4}$	$\gtrsim 0.1$
0.993	1/36	3	2.8×10^{-4}	0.1

Table 5.2: Summary of parameters for fitting $\hat{a}$-axis microwave conductivity data to a model of elastic quasiparticle scattering from point-like Coulomb defects.

As one can see, the theoretical curves give the correct qualitative behaviour, but it appears that the model cannot match the observed quasiparticle spectral weight. In both cases it can be demonstrated that the theoretical lineshapes scale with T, **not** with $(T + T_o)$. This seems to be a general result for scattering from point-like Coulomb defects, despite the suggestions of Schachinger and Carbotte [94]. While these authors have noted that very large values of Γ can give ROS, it is not possible to fit both the observed spectral weight and lineshapes simultaneously. The conclusion is that something critical is missing from the model of d-wave quasiparticles scattering elastically from point-like Coulomb defects.

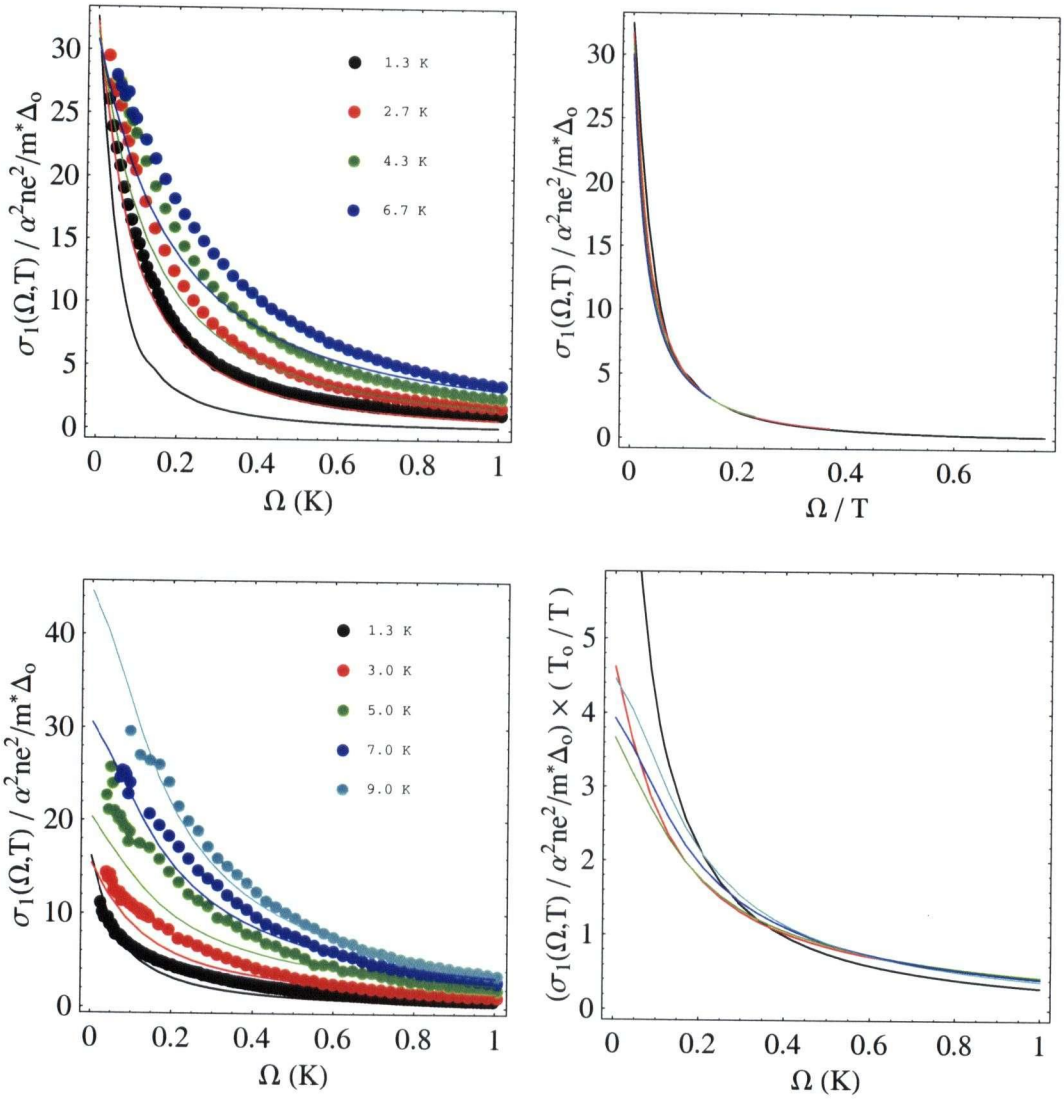

Figure 5.3: Fits to the $\sigma_{1a}(\Omega, T)$ data of Fig. 5.1 using the point-like Coulomb defect model: $YBa_2Cu_3O_{6.5}$ (top panels) and $YBa_2Cu_3O_{6.993}$ (lower panels). Left panels show the theoretical curves on top of the data. Right panels demonstrate that the theoretical curves scale with T and therefore not with $(T + T_o)$, as desired.

It should be noted that despite the values of Γ and c given in Table 5.2 being essentially identical for the two dopings studied herein, they generate very different conductivity spectra when used in conjunction with the doping dependent value of Δ_o given in Table 5.1. Recall that the scattering phase shift c determines the dimensionless quantity ω_{peak}/Δ_o. Therefore, changing Δ_o alters the energy at which the resonance peak occurs in $-\mathrm{Im}\Sigma_0(\tilde{\omega})$, and consequently changes the width of the 'Born-like' temperature regime (where $T \lesssim 5\omega_{peak}$). Thus the factor of 2 difference in Δ_o between $YBa_2Cu_3O_{6.5}$ and $YBa_2Cu_3O_{6.993}$ is most likely responsible for the the comparatively lower elastic scattering rates observed at low temperature in the underdoped compound.

As a corollary to the above conclusion, the larger value of Δ_o in the underdoped material may also be responsible for the decrease in temperature at which the maximum in $\sigma_1(\Omega \to 0, T)$ is observed, as compared to the overdoped material. As one can see in Figs. 4.6 and 4.12 the peak occurs at $\sim 8\ K$ in the former case and at $\sim 25\ K$ in the latter case. It has been hypothesized that the peak is a result of a competition between the increase in quasiparticle spectral weight $(n_n e^2/m^*)(T)$ (which augments $\sigma_1(\Omega \to 0, T)$) and the increase in quasiparticle scattering rate $\Lambda^{-1}(T)$ (which reduces $\sigma_1(\Omega \to 0, T)$) with increasing temperature [103]:

$$\sigma_1(\Omega \to 0, T) = \frac{n_n e^2}{m^*}(T) \times \frac{1}{\Lambda(T)}$$

Since $(n_n e^2/m^*)(T) \propto T/\Delta_o$ (at low temperature) then increasing Δ_o will shift the competition in favour of quasiparticle screening and $\sigma_1(\Omega \to 0, T)$ will peak at a lower T, provided that the temperature dependent scattering mechanism does not depend strongly upon Δ_o as well. Interestingly, upon comparing the slopes of the $\hat{a}$-axis superfluid density from Table 5.1 one can see that they differ by roughly a factor of 3 - this compares favourably with the roughly factor of 3 difference in temperatures at which the 1 *GHz* quasiparticle conductivity spectra peak in Figs. 4.6 and 4.12. Therefore, the temperature at which $\sigma_1(\Omega \to 0, T)$ reaches a maximum is also very dependent upon Δ_o.

5.4 'Realistic' Defects

The most common argument brought against the model presented in the previous section is that point-like Coulomb defects are not realized in condensed matter systems. For example, cation defects in metals typically become screened by conduction electrons (or holes). The charge density around the defect develops a standing wave pattern known as Friedel oscillations with an envelope that decays on a lengthscale comparable to the Fermi wavelength $\lambda_F = 2\pi/k_F$ [88]. Admittedly such a collective object will not appear to be point-like from the perspective of an electron at the Fermi surface.

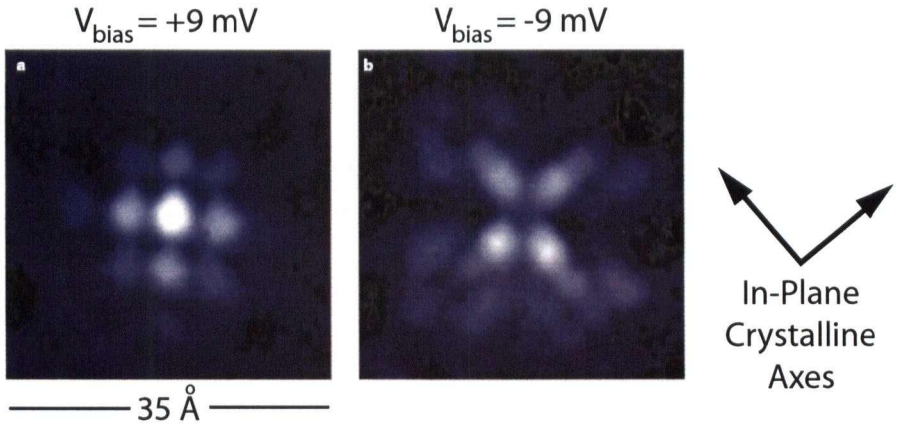

Figure 5.4: Real space STS images of a Ni^{2+} impurity in $Bi_2Sr_2CaCu_2O_{8+x}$. Bright areas correspond to high tunnelling currents. Image reproduced from Ref. [104].

Scanning tunnelling spectroscopy (STS) has indeed revealed such screening clouds around cation defects in *d*-wave superconductors [104, 105]. Figure 5.4 shows an example of a Ni^{2+} ion substituted into a planar Cu^2+ site of $Bi_2Sr_2CaCu_2O_{8+x}$ [104]. For positive tip-sample bias one resolves a pileup of the electron wavefunction on top of the defect and 4-fold symmetric Friedel oscillations emanating in the nodal directions ($\phi = \{\pm\pi/4, \pm 3\pi/4\}$ with respect to either of the in-plane crystalline axes). A negative tip-sample bias reveals a hole wavefunction that occupies the complementary parts of real space within the vicinity of the defect. Furthermore, it has been observed that magnetic cations such as Ni^{2+} ($|\vec{S}| = 1$) do not disturb the superconducting OP but nonmagnetic cations such as Zn^{2+} ($|\vec{S}| = 0$) can suppress the OP in the region surrounding the defect [105]. Therefore, ' realistic' cation defects in *d*-wave superconductors do not appear to be simple δ-function Coulomb potentials. Nonetheless, it will be demonstrated that the inclusion of these realistic features does not improve the modelling of $\sigma_1(\Omega, T)$ as compared to the simple model of the previous section.

For the sake of a demonstration, consider a defect consisting of a screened Yukawa Coulomb potential plus an exponentially decaying OP located at the origin $\vec{r} = 0$.

Such a model ignores the Friedel oscillations in Fig. 5.4 but at least captures the central part of the defect potential. The Coulomb and OP potentials will have $\hat{\tau}^3$ and $\hat{\tau}^1$ symmetry, respectively, in the space of Nambu spinors. The net real space defect potential can then be written as follows:

$$\hat{V}(\vec{r}) = \frac{eQ_i}{r} e^{-q_c r} \hat{\tau}^3 + \delta\Delta_{\hat{q}} e^{-q_{op} r} \hat{\tau}^1 \tag{5.28}$$

Here Q_i represents the charge of the defect and $\delta\Delta_{\hat{q}}$ represents the amount of suppression of the d-wave OP at the centre of the defect, $\delta\Delta_{\hat{q}} = \delta\Delta_o \cos 2\phi_{\hat{q}}$. The Coulomb defect is screened over a lengthscale $\sim 2\pi/q_c$ and the OP returns to its bulk value over a lengthscale $\sim 2\pi/q_{op}$. Upon taking the Fourier transform one obtains

$$\begin{aligned} \hat{V}(\vec{q}) &= \frac{2\pi e Q_i}{q_c^2} \frac{1}{1+(q/q_c)^2} \hat{\tau}^3 + \frac{4\pi\delta\Delta_{\hat{q}}}{q_{op}^3} \frac{1}{(1+(q/q_{op})^2)^2} \hat{\tau}^1 \\ &\equiv V_{Co} \frac{1}{1+(q/q_c)^2} \hat{\tau}^3 + V_{OPo} \frac{\cos 2\phi_{\hat{q}}}{(1+(q/q_{op})^2)^2} \hat{\tau}^1. \end{aligned} \tag{5.29}$$

Note that for $q_c \to \infty$ one returns to the point-like Coulomb defect limit. While taking this parameter to infinity decreases V_{Co}, it is at least physically possible to place a very large amount of charge (such as $1e$) on the defect to give strong point-like scattering centres. However, the magnitude of the OP supression is restricted to $-\Delta_o \leq \delta\Delta_o \leq 0$ and so in the limit $q_{op} \to \infty$ this potential becomes negligible. This latter point disagrees with the model of Hettler and Hirschfeld who take the real space OP suppression to be $\delta\Delta_{\hat{q}} \times \delta(\vec{r})$ [91]. It should be noted that $\delta(\vec{r})$ is technically infinite at the origin, which makes it a suitable substitute for truly divergent potentials (such as charge monopoles) but is not a suitable representation of mean field OP suppression at a localized site.

The problem is to now deal with the momentum dependence of the $\hat{T}$-matrix, Eq. 5.20. Rightfully one needs an $N \times N$ matrix for a system with N well defined momentum states. Attempting to solve such a model exactly for large N is impractical, but nature has been very kind in the case of a d-wave superconductor where there are only four Fermi points located along the OP nodes that need be considered. One can then concentrate upon these four points in momentum space and the wavevectors that connect them, as sketched in Fig. 5.5. This is the approach of Durst and Lee [99], but it should be noted that the calculations presented herein are far more general for they are self-consistent and applicable to calculating transport properties for nonzero external frequency Ω. The result is a 4×4 $\hat{T}$-matrix of the form

$$\hat{M} \begin{pmatrix} \hat{T}(\vec{q}_{++}) \\ \hat{T}(\vec{q}_{+-}) \\ \hat{T}(\vec{q}_{--}) \\ \hat{T}(\vec{q}_{-+}) \end{pmatrix} = - \begin{pmatrix} \hat{V}(\vec{q}_{++}) \\ \hat{V}(\vec{q}_{+-}) \\ \hat{V}(\vec{q}_{--}) \\ \hat{V}(\vec{q}_{-+}) \end{pmatrix} \tag{5.30}$$

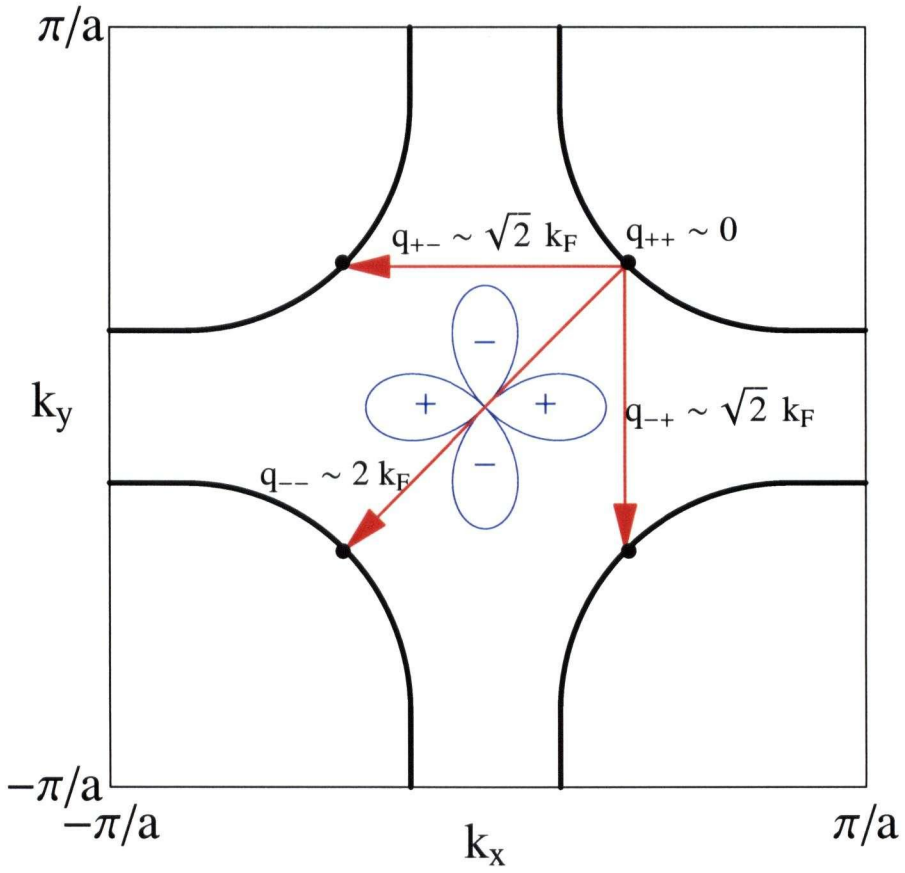

Figure 5.5: Depiction of internode scattering across the First Brillouin zone. Nodes on the Fermi surface of a 2-dimensional band are noted with black dots and the symmetry of the superconducting OP $\Delta_{\hat{k}} = \Delta_o \cos 2\phi$ is shown in blue. Internode scattering vectors $(\vec{q}_{++}, \vec{q}_{+-}, \vec{q}_{-+}, \vec{q}_{--})$ are drawn in red with their approximate magnitudes indicated.

$$\hat{M}=\begin{bmatrix} \hat{V}(\vec{q}_{++})\hat{G}_p(\tilde{\omega})-1 & \hat{V}(\vec{q}_{+-})\hat{G}_p(\tilde{\omega}) & \hat{V}(\vec{q}_{--})\hat{G}_p(\tilde{\omega}) & \hat{V}(\vec{q}_{-+})\hat{G}_p(\tilde{\omega}) \\ \hat{V}(\vec{q}_{+-})\hat{G}_p(\tilde{\omega}) & \hat{V}(\vec{q}_{++})\hat{G}_p(\tilde{\omega})-1 & \hat{V}(\vec{q}_{-+})\hat{G}_p(\tilde{\omega}) & \hat{V}(\vec{q}_{--})\hat{G}_p(\tilde{\omega}) \\ \hat{V}(\vec{q}_{--})\hat{G}_p(\tilde{\omega}) & \hat{V}(\vec{q}_{-+})\hat{G}_p(\tilde{\omega}) & \hat{V}(\vec{q}_{++})\hat{G}_p(\tilde{\omega})-1 & \hat{V}(\vec{q}_{+-})\hat{G}_p(\tilde{\omega}) \\ \hat{V}(\vec{q}_{-+})\hat{G}_p(\tilde{\omega}) & \hat{V}(\vec{q}_{--})\hat{G}_p(\tilde{\omega}) & \hat{V}(\vec{q}_{+-})\hat{G}_p(\tilde{\omega}) & \hat{V}(\vec{q}_{++})\hat{G}_p(\tilde{\omega})-1 \end{bmatrix}$$

where it has been assumed $\hat{T}(\vec{k},\vec{k}',\tilde{\omega}) = \hat{T}(\vec{k}-\vec{k}',\tilde{\omega}) = \hat{T}(\vec{k}'-\vec{k},\tilde{\omega})$. The quantity $\hat{G}_p(\tilde{\omega})$ represents a renormalized Green function (Eq. 5.5) that has been integrated over momenta near one of the Fermi points. For energies $\omega \ll \Delta_o$ one can approximate this quantity as

$$\hat{G}_p(\tilde{\omega}) \approx \hat{G}(\tilde{\omega})/4 \tag{5.31}$$

where $\hat{G}(\tilde{\omega})$ is defined by Eq. 5.23. With the given form for the scattering potential (Eq. 5.29) one expects renormalizations to all three components of the Green function Eq. 5.5. However, the renormalizations to the OP do not alter its symmetry so $G_1(\tilde{\omega}) = 0$. Furthermore, $G_3(\tilde{\omega}) = 0$ for the same reasons as those presented for the point-like Coulomb potential [102]. Thus the only nonzero component in Eq. 5.31 will be proportional to $G_0(\tilde{\omega})$ and therefore have $\hat{\tau}^0$ symmetry in Nambu space.

One can solve the above matrix *exactly* for $\hat{T}(\vec{q}=0,\tilde{\omega})$ and obtain the self-energy from Eq. 5.21. One need only determine the potential $\hat{V}(\vec{q})$ for the wavevectors $\vec{q}_{++} \approx 0$, $\vec{q}_{+-} \approx \sqrt{2}k_F\hat{k}_x$, $\vec{q}_{--} \approx \sqrt{2}k_F(\hat{k}_x+\hat{k}_y)$ and $\vec{q}_{-+} \approx \sqrt{2}k_F\hat{k}_y$, as shown in Fig. 5.5. The Coulomb part of the potential is easy to calculate because it only depends upon the magnitude of $\vec{q}$. However, one must consider the direction of $\vec{q}$ carefully when approximating the OP potential. For $\vec{q}_{++}$ and $\vec{q}_{-+}$ the wavevectors are directed along antinodal directions where $|\delta\Delta_{\hat{q}}|$ is maximized (but having opposing signs due to the OP phase). For $\vec{q}_{--}$, the wavevector is primarily directed along a nodal direction and so $\delta\Delta_{\hat{q}} \approx 0$. Finally, if the nodal dispersion is very anisotropic ($v_F/v_\Delta \gg 1$) then the majority of *intranode* scattering events will be approximately in nodal directions and one can assume $\delta\Delta_{\hat{q}} \approx 0$ for $\vec{q}_{++}$ as well. Furthermore, *intranode* scattering does not substantially alter charge currents so this matter need not be a serious concern [99]. The resulting potentials are then

$$\begin{aligned} V(\vec{q}_{++}) &= V_{Co}\hat{\tau}^3 \\ V(\vec{q}_{+-}) &= V_{Co}\frac{1}{1+2(k_F/q_c)^2}\hat{\tau}^3 + V_{OPo}\frac{1}{(1+2(k_F/q_{op})^2)^2}\hat{\tau}^1 \\ V(\vec{q}_{-+}) &= V_{Co}\frac{1}{1+2(k_F/q_c)^2}\hat{\tau}^3 - V_{OPo}\frac{1}{(1+2(k_F/q_{op})^2)^2}\hat{\tau}^1 \\ V(\vec{q}_{--}) &= V_{Co}\frac{1}{1+4(k_F/q_c)^2}\hat{\tau}^3 \end{aligned}$$

Inserting these forms in Eq. 5.30 allows one to solve for $\hat{\Sigma}(\tilde{\omega})$ self-consistently. In this case both $\tilde{\omega}$ and $\tilde{\Delta}_o$ are renormalized in the integrated Green function Eq. 5.24 and must be solved for simultaneously. As an example, consider a Coulomb potential parameterized by $\Gamma/\Delta_o = 2.5\times10^{-3}$, $c = (\pi N_o V_{Co})^{-1} = 0.4$ and $q_c = k_F$. Note that

these are the same values of Γ and c used to generate the plots in Fig. 5.2 for the point-like potential. To parameterize the OP suppression assume $N_o \sim 10^{28}\, eV^{-1}m^{-3}$, take a typical $\Delta_o \sim 40\, meV$, let $\delta\Delta_o = -\Delta_o$ (complete OP supression at the centre of the defect) and set $q_{op} = k_F \sim 0.5\,\text{Å}^{-1}$; this gives $\pi N_o V_{OPo} \sim 0.14$. The resulting self energy is plotted in Fig. 5.6 and the reader is reminded that this model should only be trusted for $\omega \ll \Delta_o$ (nodal approximation).

At small ω one can see that $-\text{Im}\Sigma_0(\tilde{\omega})$ is roughly linear with a slope $\sim (\Gamma/c^2)/6$; this factor of 6 would be deemed a vertex correction in the language of Durst and Lee [99] in that it accounts for deviations of $-\text{Im}\Sigma_0(\tilde{\omega})$ at small $\omega \ll \Delta_o$ away from the point-like defect limit (compare to Fig 5.2). Note that $\Sigma_3(\tilde{\omega})$ at small ω is not strongly influenced by the broadening of the Coulomb potential. The new piece to the self-energy is $\Sigma_1(\tilde{\omega})$ whose real part gives an energy dependent reduction in Δ_o and imaginary part that generates a Cooper pair scattering rate that follows the d-wave DOS, $N(\omega)$. This latter conclusion can be justified by noting that $\Sigma_1 \sim \Gamma|\pi N_o V_{OPo}|^2 G_0(\tilde{\omega})$ in the limit $q_{op} \to \infty$. However, the corrections to $\tilde{\Delta}_o$ are very small because the OP suppression is not a divergent potential at the site of the defect. In fact, quasiparticles can tunnel through small regions of OP suppression almost unhindered, much like a thin normal region sandwiched between two superconducting junctions that are in phase. Therefore, the realistic defect model does not substantially alter the form of $\hat{\Sigma}(\tilde{\omega})$ as compared to the point-like Coulomb defect model. As such, a calculation of $\sigma_1(\Omega, T)$ using this defect model will not reveal anything new.

The only caveat that will be mentioned here is that this defect model does not account for the physics of Andreev bound states (ABS) that will necessarily arise wherever the superconducting OP is suppressed [37]. Sheehy has demonstrated that this will give rise to a narrow band of states at the Fermi energy which will contribute to $\sigma_1(\Omega, T)$ at low temperatures [106]. However this contribution will be additive to the conductivity of the propagating quasiparticles, therefore it may be difficult to observe this effect experimentally.

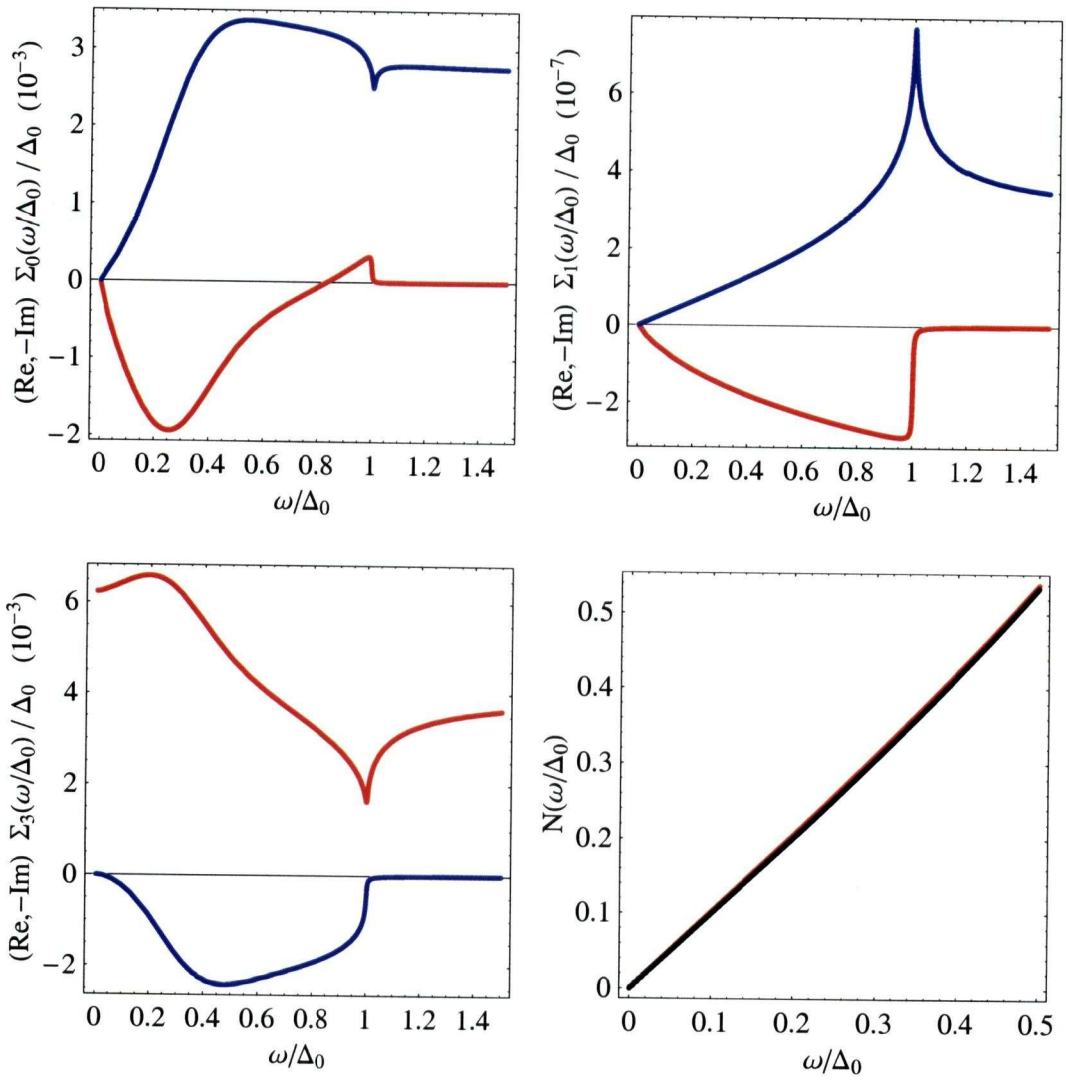

Figure 5.6: The quasiparticle self-energy and density of states (DOS) due to elastic scattering from 'realistic' defects using the parameters $\Gamma/\Delta_o = 2.5\times10^{-3}$, $c = 0.4$ and $\delta\Delta_o = -\Delta_o$. There are three components of the self energy in this case, $\hat{\Sigma}(\tilde{\omega}) = \Sigma_0(\tilde{\omega})\hat{\tau}^0 + \Sigma_1(\tilde{\omega})\hat{\tau}^1 + \Sigma_3(\tilde{\omega})\hat{\tau}^3$, with the real parts shown in red and negative of the imaginary parts in blue. The low energy DOS from this model is shown in red and that of a clean d-wave superconductor in black (lower left panel).

5.5 The Case for Magnetic Impurities

Given that neither Coulomb defects nor OP suppression seem to give a clear route to residual quasiparticle oscillator strength at zero temperature, it is a worthwhile endeavor to quest for defects that clearly behave differently than those considered thus far. In particular, this author encourages the theory community to consider the effect of magnetic defects upon charge conductivity in the cuprates more carefully. While STS has been an incredible source of inspiration for many recent models of elastic scattering of d-wave quasiparticles from Coulomb defects in the cuprates [107], it must be remembered that such experiments do not employ spin polarized currents. Therefore there is no contrast between charged or magnetic defect potentials. This should be a great concern because much of the experimental evidence points to the Cooper pairing mechanism being magnetic in origin in the cuprates. This is even more of a concern for those who subscribe to orbital ordering/slave boson theories, as described in Chapter 1. In fact, recent calculations by Wang and Lee [108] using the $SU(2)$-slave boson approach have shown that a non-magnetic ion placed in a Cu^{2+} site on a $(CuO_2)^{2-}$ plane generates a static spin-1/2 moment that is distributed amongst the four nearest neighbour Cu^{2+} sites [108]. Polkovnikov *et al.* [109] have taken the distributed spin-1/2 moment around a Zn^{2+} as given and have calculated the consequences for STS experiments. These latter authors concluded that Kondo spin dynamics have an essential role to play in the scattering of d-wave quasiparticles.

The above considerations motivated this author to advocate on behalf of magnetic defects in d-wave superconductors. For the sake of simplicity, consider a point-like (δ-function) magnetic potential in real space with some unspecified dipole moment situated at the origin. The perturbation to Eq. 5.1 can then be written as

$$\begin{aligned}\delta\mathcal{H} &\propto \sum_{\vec{k},\vec{k}',\alpha,\beta} \vec{S}\cdot c^{\dagger}_{\vec{k}\alpha}\frac{\vec{\tau}_{\alpha\beta}}{2}c_{\vec{k}'\beta} \\ &= \sum_{\vec{k},\vec{k}'}\left(\hat{S}_{-}c^{\dagger}_{\vec{k}\uparrow}c_{\vec{k}'\downarrow}+\hat{S}_{+}c^{\dagger}_{\vec{k}\downarrow}c_{\vec{k}'\uparrow}+\hat{S}_{z}\left(c^{\dagger}_{\vec{k}',\uparrow}c_{\vec{k},\uparrow}-c^{\dagger}_{\vec{k}',\downarrow}c_{\vec{k},\downarrow}\right)\right) \qquad (5.32)\end{aligned}$$

where $\vec{S}=(\hat{S}_x,\hat{S}_y,\hat{S}_z)$ is the quantum spin operator acting on the magnetic defect with $\hat{S}_{+}\equiv(\hat{S}_x+i\hat{S}_y)/2$ and $\hat{S}_{-}\equiv(\hat{S}_x-i\hat{S}_y)/2i$. The Pauli spin vector is defined as $\vec{\tau}\equiv(\hat{\tau}^1,\hat{\tau}^2,\hat{\tau}^3)$. The first two terms of Eq. 5.32 give rise to spin-flip scattering and the third term generates Zeeman splitting of electronic energy levels in the vicinity of the defect. Due to the spin-flip processes, this interaction breaks time reversal symmetry. Consequently, the quasiparticle self energy due to scattering from a potential of the form Eq. 5.32 *cannot* be expressed in terms of a simple perturbative expansion akin to the $\hat{T}$-matrix approach discussed previously. Modern theoretical methods for tackling this important problem, such as those of Cassanello and Fradkin [110] and Polkovnikov et al.[109], are beyond the scope of this thesis and will not be discussed here. All that will be stated is that there is a distinct absence in the literature of microwave conductivity calculations for d-wave quasiparticles in the presence of dilute magnetic impurities with intermediate to strong electron-impurity coupling.

One could attempt to model the scattering of quasiparticles from weak magnetic impurities using a classical approach by ignoring the spin-flip processes S_+ and S_- in Eq. 5.32, but it can be shown that this approach does not yield anything new. To demonstrate, note that the Zeeman splitting term can be expressed in terms of Nambu spinors as follows:

$$\delta\mathcal{H}_{classical} \propto \sum_{\vec{k},\vec{k}'} \hat{S}_z \left(c^\dagger_{\vec{k}',\uparrow} c_{\vec{k},\uparrow} - c^\dagger_{\vec{k}',\downarrow} c_{\vec{k},\downarrow} \right) = \sum_{\vec{k},\vec{k}'} C^\dagger_{\vec{k}'} \left(V_{Mo} \hat{\tau}^0 \right) C_{\vec{k}} \tag{5.33}$$

Thus the classical magnetic potential has $\hat{\tau}^0$ symmetry in Nambu space. However, before attempting any sort of a $\hat{T}$-matrix expansion one must acknowledge that magnetic defects ought to have random orientation and so the magnitude and sign of V_{Mo} will not be the same for all defects in a given material. As a specific example, consider a spin-1/2 defect that will then have two possible expectation values $S_z|\psi_{defect}\rangle = \pm(1/2)|\psi_{defect}\rangle$. Consequently, there will be two possible values for the potential in Eq. 5.33, $\pm V_{Mo}$. To obtain the quasiparticle self-energy one must average over the two possible orientations of the defect moment. Using Eq. 5.21 one obtains

$$\begin{aligned} \hat{\Sigma}(\tilde{\omega}) &= \frac{\Gamma}{2} \left(\frac{\pi N_o V_{Mo}}{1 - (\pi N_o V_{Mo}) G_0(\tilde{\omega})} + \frac{-\pi N_o V_{Mo}}{1 - (-\pi N_o V_{Mo}) G_0(\tilde{\omega})} \right) \hat{\tau}^0 \\ &= \Gamma \frac{(\pi N_o V_{Mo})^2 G_0(\tilde{\omega})}{1 - (\pi N_o V_{Mo} G_0(\tilde{\omega}))^2} \hat{\tau}^0 \end{aligned} \tag{5.34}$$

If one then imposes the definition $c \equiv 1/(\pi N_o V_{Mo})$ then it can be seen that Eq. 5.34 is identical to the $\hat{\tau}^0$ component of Eq. 5.26. Thus the classical limit for magnetic defects is identical to Coulomb defects and will yield nothing new.

So where does one go from here? In particular, what new physics enters the problem of quasiparticle scattering if Kondo screening of localized spin-1/2 moments has a role to play in the cuprates? While the suggestion that dynamical screening of magnetic defects has a role to play in the cuprates is entirely speculative, the reader is reminded that it has not been discounted experimentally. In this scenario the magnetic defect-electron exchange coupling approaches a divergence at low T until the a bound singlet is formed between the local moment and the conduction electrons at some finite temperature T_K [110]. Below T_K the dressed defect will no longer have a magnetic moment but will instead have a net charge, which would then appear to be a unitary scatterer. Thus it is entirely possible that the microwave conductivity data presented herein are indicative of magnetic defects struggling to maintain singlet pairing with a bath of conduction electrons above T_K. However, at the very low temperatures probed in the thermal conductivity experiments of Sutherland *et al.* [80] one would observe the effects of quasiparticles scattering from charged Coulomb defects which would then give rise to the universal limit of $(limT \rightarrow 0)\,\kappa(T)/T$, as given by Eq. 5.19. This picture provides an appealing means of reconciling the Born-like charge conductivity spectra presented in this thesis and in Ref. [26] at temperatures on the order of $1\,K$ with the near Unitary-like behaviour of the thermal conductivity at temperatures $\lesssim 100\,mK$ [80, 111]. Furthermore, it suggests an experimental signature; the sharp microwave conductivity spectra should yield to broader Unitary-like

lineshapes as $T \rightarrow 0$. A new broadband bolometry apparatus is currently being constructed in the UBC Superconductivity Laboratory will be able to measure $R_s(\Omega, T)$ at temperatures near $100\,mK$.

Chapter 6

Epilogue: Where is the New Physics?

Given the exotic nature of many of the theoretical ideas that were touched upon in Chapter 1 of this thesis, what then is the connection between these ideas and the rest of this treatise? This question must be addressed because the language that has been used in Chapters 2,4, and 5 is that of Landau quasiparticles which need not suggest anything novel. In the end, it is hoped that the reader is convinced that the devil is in the details and that the way superconductivity is influenced (or fails) near crystalline defects is suggestive of new physics in the cuprate superconductors.

One of the key themes running throughout this thesis is that an electronic band-structure approach can explain much of the microwave spectroscopy data on *Ortho-II* ordered $YBa_2Cu_3O_{6.5}$ (underdoped) and $YBa_2Cu_3O_{6.993}$ (overdoped), at least on a phenomenological level. The observation of sharp microwave conductivity spectra at low temperatures and the successful tracking of spectral weight as it is transferred between superfluid and normal fluid both indicate that the materials studied herein are clean *d*-wave superconductors with well defined quasiparticles. The anisotropy between charge transport in $\sigma_1(\Omega, T)$ in the $\hat{a}$ and $\hat{b}$-axis directions was also explained for both dopings using simple band structure: For $YBa_2Cu_3O_{6+x}$ in general one expects two effectively identical 2-dimensional bands (attributed to the two $(CuO_2)^{2-}$ planes per unit cell) to contribute equally to $\sigma_{1a}(\Omega, T)$ and $\sigma_{1b}(\Omega, T)$. To account for the $\hat{a} : \hat{b}$ anisotropy in the overdoped material all that was necessary was the inclusion of a quasi-1-dimensional band contribution to $\sigma_{1b}(\Omega, T)$ that was primarily attributed to the presence of metallic CuO chains. To account for the $\hat{a} : \hat{b}$ anisotropy in the underdoped material one needed both the above mentioned quasi-1-dimensional band that was derived primarily from CuO *chain states* and the effects of doubling the unit cell dimension in the $\hat{a}$-axis direction to produce new 1-dimensional bands from $(CuO_2)^{2-}$ *plane states.*

The presumed elastic scattering rate for $(CuO_2)^{2-}$ plane states in $YBa_2Cu_3O_{6.5}$ was observed to vary linearly with temperature; $\Lambda^{-1}(T) = a + bT$. On the other hand, $\Lambda^{-1}(T)$ was observed to be a constant at low temperatures for $YBa_2Cu_3O_{6.993}$. One may be tempted to claim that this is the result of different physics in overdoped and underdoped materials, which would seem to corroborate the quantum critical point picture presented in Chapter 1. However, it was argued in Chapter 5 of this thesis that this is most likely a crossover due to the scale of the dimensionless quantity $T/(5\omega_{peak})$ where ω_{peak} is the energy of a resonance feature in the quasiparticle self-energy. For $T < (5\omega_{peak})$ one will observe Born-like lineshapes (as seen in the $YBa_2Cu_3O_{6.5}$ data and the $1.3\,K$ $YBa_2Cu_3O_{6.993}$ data) which are characterized by a

temperature independent $\sigma_1(\Omega \rightarrow 0, T)$ and a linewidth that varies linearly with T. In the opposite temperature regime $T > (5\omega_{peak})$ one obtains unitary-like lineshapes that are characterized by a quadratic temperature dependence of $\sigma_1(\Omega \rightarrow 0, T)$ and a linewidth that varies roughly as $1/T$. Of course for $T \sim (5\omega_{peak})$ one obtains intermediate behaviour (as seen in the $YBa_2Cu_3O_{6.993}$ data above $1.3\,K$) with $\sigma_1(\Omega \rightarrow 0, T)$ varying linearly with T and linewidths that are roughly temperature independent.

In the end, the most intriguing result to come from the phenomenological analysis of the microwave charge conductivity data of $YBa_2Cu_3O_{6.5}$ and $YBa_2Cu_3O_{6.993}$ is the suggested presence of $T = 0$ residual quasiparticle oscillator strength (ROS). As it was demonstrated in Chapter 5, this feature is not amenable to either point-like or 'more realistic' Coulomb defects. Rather, it was argued that one must look beyond both Coulomb potentials and order parameter (OP) suppression.

From a theoretical standpoint, it would be a worthwhile effort to distill the work of Polkovnikov *et al* [109], Nagaosa and Lee [112] and Cassanello and Fradkin [110] to understand how Kondo screening ought to influence quasiparticle charge transport in the cuprates. From an experimental standpoint, this author's recommendation is that measurements of $\sigma_1(\Omega, T)$ be performed upon *Ortho-II* ordered $YBa_2Cu_3O_{6.5}$ (underdoped) and $YBa_2Cu_3O_{6.993}$ (overdoped) at temperatures below $1.3\,K$. If Kondo screening has a role to play in these materials, then the sharp conductivity spectra observed at $1.3\,K$ should yield to much broader unitary-like lineshapes at very low temperatures where the magnetic defects become screened.

Bibliography

[1] M. Tinkham, *Introduction to Superconductivity* (McGraw Hill, Inc. Toronto, Canada, 1996).

[2] M. P. Marder, *Condensed Matter Physics* (John Wiley and Sons, Inc. (Toronto, Canada), 2000).

[3] N. Ashcroft and N. Mermin, *Solid State Physics* (W.B. Saunders Company, Philadelphia USA, 1976).

[4] P. Anderson, Science **235**, 1196 (1987).

[5] T. Timusk and B. Statt, Rep.Prog.Phys. **62**, 61 (1999).

[6] H.Eskes and G.A.Sawatzky, Phys. Rev. Let. **61**, 1415 (1988).

[7] H.Eskes and J. Jefferson, Phys. Rev. B **48**, 9788 (1993).

[8] L. Landau, E. Lifshitz, and L.P.Pitaevskii, *Statistical Physics, 3rd Ed.* (Oxford University Press, (New York, USA), 1980).

[9] T. Timusk and W. Tanner, in *Physical Properties of High Temperature Superconductors, Vol. 1*, edited by D. Ginsberg (World Scientific, Singapore, 1994).

[10] R. Liang, D. Bonn, W. Hardy, J. C. Wynn, K. Moler, L. Lu, S. Larochelle, L. Zhou, M. Greven, L. Lurio, et al., Physica C **383**, 1 (2002).

[11] S. Hagen, T. Jing, Z. Wang, J. Horvath, and N. Ong, Phys. Rev. B **37**, 7928 (1988).

[12] T. Chien, Z. Wang, and N. Ong, Phys. Rev. Let. **67**, 2088 (1991).

[13] P. Anderson, Phys. Rev. Let. **67**, 2092 (1991).

[14] T. Pereg-Barnea and M. Franz, xxx.lanl.gov/archive/cond-mat/0306712 (2003).

[15] V. Emery, S. Kivelson, and O. Zachar, Phys. Rev. B **56**, 6120 (1997).

[16] N. Mathur, F. Grosche, S. Julian, I. Walker, D. Freye, R. Haselwimmer, and G. Lonzarich, Nature **394**, 39 (1998).

[17] F. Haldane, J.Phys.C **14**, 2585 (1981).

[18] I. Affleck and J. B. Marston, Phys. Rev. B **37**, 3774 (1988).

[19] X.-G. Wen and P. Lee, Phys. Rev. Let. **76**, 503 (1996).

[20] T. Senthil and M. Fisher, Phys. Rev. Let. **86**, 292 (2000).

[21] P. A. Lee and G. Sha, Solid State Commun. **126**, 71 (2003).

[22] M. Franz and Z. Tešanović, Phys. Rev. Let. **76**, 503 (1996).

[23] I. Herbut, Phys. Rev. Let. **88**, 047006 (2002).

[24] J. Hoffman, K. McElroy, D.-H. Lee, K. Lang, H. Eisaki, S. Uchida, and J. Davis, Nature **297**, 1148 (2002).

[25] L. Taillefer, B. Lussier, R. Gagnon, K. Behnia, and H. Aubin, Phys. Rev. Let. **79**, 483 (1997).

[26] P. Turner, R. Harris, S. Kamal, M. Hayden, D. Broun, D. Morgan, A. Hosseini, P. Dosanjh, G. Mullins, J. Preston, et al., Phys. Rev. Let. **90**, 237005 (2003).

[27] J. Jorgenson, B. Veal, A. Paulikas, L. Nowicki, G. Crabtree, H. Claus, and W. Kwok, Phys. Rev. B **41**, 1863 (1990).

[28] B. Lake, G. Aeppli, K. N. Clausen, D. F. McMorrow, K. Lefmann, N. E. Hussey, N. Mangkorntong, M. Nohara, H. Takagi, T. E. Mason, et al., Science **291**, 1759 (2001).

[29] K. McElroy, R. Simmonds, J. Hoffman, D.-H. Lee, J. Orenstein, H. Eisaki, S. Uchida, and J. Davis, Nature **56**, 7882 (1997).

[30] Z. Shen, D. Dessau, B. Wells, D. King, W. Spicer, A. Arko, D. Marshall, L. Lombardo, A. Kapitulnik, P. Dickinson, et al., Phys. Rev. Let. **70**, 1553 (1993).

[31] D. Bonn and W. Hardy, in *Physical Properties of High Temperature Superconductors, Vol. 5*, edited by D. Ginsberg (World Scientific, Singapore, 1996).

[32] R. Liang, D. Bonn, and W. Hardy, Physica C **304**, 105 (1998).

[33] R. Liang, D. Bonn, and W. Hardy, Physica C **336**, 57 (2000).

[34] D. Peets, Department of Physics and Astronomy, University of British Columbia.

[35] A. Hosseini, D. Broun, D. Sheehy, T. Davis, M. Franz, W. Hardy, R. Liang, and D. Bonn (2003), submitted to Nature.

[36] J. Bardeen, L. Cooper, and J. Schrieffer, Phys. Rev. **108**, 1175 (1957).

[37] A. M. Zagoskin, *Quantum Theory of Many-Body Systems* (Springer Verlag, New York USA, 1998).

[38] W. Atkinson, Phys. Rev. B **59**, 3377 (1999).

[39] M. C. Schabel, C.-H.Park, A. Matsuura, Z.-X. Shen, D. Bonn, R. Liang, and W. Hardy, Phys. Rev. B **57**, 6090 (1998).

[40] M. C. Schabel, C.-H.Park, A. Matsuura, Z.-X. Shen, D. Bonn, R. Liang, and W. Hardy, Phys. Rev. B **57**, 6107 (1998).

[41] D. Lu, D. Feng, N. Armitage, K. Shen, A. Damascelli, C. Kim, F. Ronning, Z.-X. Shen, D. A. Bonn, R. Liang, et al., Phys. Rev. Let. **86**, 4370 (2001).

[42] O. Andersen, O. Jepsen, A. Liechtenstein, and I. Mazin, Phys. Rev. B **49**, 4145 (1994).

[43] R. Harris, A. Hosseini, S. Kamal, P. Dosanjh, R. Liang, W. Hardy, and D. Bonn, Phys. Rev. B **64**, 064509 (2000).

[44] S. Quinlan, D. Scalapino, and N. Bulut, Phys. Rev. B **49**, 1470 (1994).

[45] M. Walker and M. Smith, Phys. Rev. B **61**, 11285 (2000).

[46] R. Liang, P. Dosanjh, D. Bonn, D. Baar, J. Carolan, and W. Hardy, Physica C **195**, 51 (1992).

[47] P. Schleger, W. Hardy, and B. Yang, Physica C **176**, 261 (1991).

[48] R. Prozorov, R. Giannetta, A. Carrington, and F. Araujo-Moriera, Phys. Rev. B **62**, 115 (2000).

[49] I. Kosztin and A. J. Leggett, Phys. Rev. Let. **79**, 135 (1997).

[50] J.-J. Chang and D. Scalapino, Phys. Rev. B **40**, 4299 (1989).

[51] P. Turner, D. Broun, S. Kamal, M. Hayden, J. Bobowski, R. Harris, D. Morgan, J. Preston, W. Hardy, and D. Bonn, Submitted to Rev.Sci.Instr. (2003).

[52] P. Turner, M.Sc. thesis, University of British Columbia (1999).

[53] S. Ramo, J. Whinnery, and T. VanDuzer, *Fields and Waves in Communication Electronics* (John Wiley and Sons, Toronto, 1994).

[54] Lakeshore Cryotronics, Inc. 575 McCorkie Blvd., Westerville, Ohio USA, 43082.

[55] D. Griffiths, *Introduction to Electrodynamics* (Prentice Hall, New Jersey USA, 1989).

[56] P. Turner, Department of Physics and Astronomy, University of British Columbia.

[57] J. D. Jackson, *Classical Electrodynamics, 3rd Ed.* (John Wiley and Sons Inc., Toronto Canada, 1999).

[58] S. Kamal, Ph.D. thesis, University of British Columbia (2002).

[59] G. Mullins, M.Sc. thesis, University of British Columbia (2003).

[60] P. Dosanjh, M.Sc. thesis, University of British Columbia (1998).

[61] A. Hosseini, M.Sc. thesis, University of British Columbia (1997).

[62] A. Hosseini, Ph.D. thesis, University of British Columbia (2002).

[63] R. Harris, M.Sc. thesis, University of British Columbia (1999).

[64] R. Waldron, *Theory of Guided Electromagnetic Waves* (Van Nostrad, New York, 1969).

[65] E. Hadge(ed.), *The Microwave Engineers' Handbook* (Horizon House Inc. Dedhan MA, USA, 1964).

[66] S. Sridhar and W. Kennedy, Rev. Sci. Instrum. **59**, 531 (1988).

[67] D. Kajfez and P. Guillon, *Dielectric Resonators* (Noble Publishing Corporation, Atlanta USA, 1989).

[68] P. Goy, *ABmm 8-350 MVNA Operation Manual*, 52 Rue Lhomond, 75005 Paris, France (1994).

[69] A. Hosseini, R. Harris, S. Kamal, P. Dosanjh, J. Preston, R. Liang, W. Hardy, and D. Bonn, Phys. Rev. B **60**, 1349 (1999).

[70] T. Pereg-Barnea, M.Sc. thesis, University of British Columbia (2001).

[71] P. Turner, Ph.D. thesis (to be written), University of British Columbia (2002).

[72] S. Kamal, R. Liang, A. Hosseini, D. Bonn, and W. Hardy, Phys. Rev. B **58**, 8933 (1998).

[73] W. Hardy, D. Bonn, D. Morgan, R. Liang, and K. Zhang, Phys. Rev. Let. **70**, 3999 (1993).

[74] T. Pereg-Barnea, P. Turner, R. Harris, G. Mullins, J. Bobowski, M. Raudsepp, D. Bonn, R. Liang, and W. Hardy (2003), (submitted to Phys.Rev. B).

[75] J. Corson, J. Orenstein, S. Oh, J. O'Donnell, and J. Eckstein, Phys. Rev. Let. **85**, 2569 (2000).

[76] M. C. Nuss, P. Mankiewich, M. O'Malley, E. Westerwick, and P. B. Littlewood, Phys. Rev. B **66**, 3305 (1991).

[77] W. H. Press, S. A. Teukolsky, W. T. Vetterling, and B. P. Flannery, *Numerical Recipes in C, 2nd Ed.* (Cambridge University Press, (New York, USA), 1992).

[78] P. Hirschfeld, W. Putikka, and D. Scalapino, Phys. Rev. Let. **71**, 3705 (1993).

[79] P. Hirschfeld, W. Putikka, and D. Scalapino, Phys. Rev. B **50**, 10250 (1994).

[80] M. Sutherland, D. Hawthorn, R. Hill, F. Ronning, S. Wakimoto, H. Zhang, C. Proust, E. Boankin, C. Lupien, L. Taillefer, et al., Phys. Rev. B **67**, 174520 (2003).

[81] D. Feng, A. Rusydi, P. Abbamonte, L. Venema, I. Elfimov, R. Liang, D. Bonn, W. Hardy, C. SchüSSler-Langeheine, S. Hulbert, et al. (2003), (preprint).

[82] Dr. Leni Bascones, Dept. of Physics, Swiss Federal lnstitute of Technology (private communication).

[83] A. Abrikosov, L. Gor'kov, and I. D. (trans. R. A. Silverman), *Methods of Quantum Field Theory in Statistical Physics* (Dover Publications (New York, USA), 1963).

[84] D. Wollman, D. V. Harlingen, J. Giapintzakis, and D. Ginsberg, Phys. Rev. Let. **74**, 797 (1995).

[85] D. Bonn, J. C. Wynn, B. W. Gardner, Y.-J. Lin, R. Liang, W. Hardy, J. Kirtley, and K. Moler, Nature **414**, 887 (2001).

[86] D. Scalapino, E. Loh, and J. Hirsh, Phys. Rev. B **34**, 8190 (1986).

[87] W. Hardy, S. Kamal, and D. Bonn, in *The Gap Symmetry and Fluctuations in High-Tc Superconductors*, edited by B. et al. (Plenum Press, New York USA, 1998).

[88] G. Mahan, *Many Particle Physics* (Plenum Press, New York,USA, 1993).

[89] L. Ioffe and A. Millis, J.Phys.Chem.Solids **63**, 2259 (2002).

[90] M. Hettler and P. Hirschfeld, Phys. Rev. B **59**, 9606 (1999).

[91] M. Hettler and P. Hirschfeld, Phys. Rev. B **61**, 11313 (2000).

[92] A. Berlinsky, D. Bonn, R. Harris, and C. Kallin, Phys. Rev. B **61**, 9088 (2000).

[93] S. Hensen, G. Muller, C. Rieck, and K. Scharnberg, Phys. Rev. B **56**, 6237 (1997).

[94] E. Schachinger and J. Carbotte, Phys. Rev. B **67**, 134509 (2003).

[95] M. Graf, M. Palumbo, and D. Rainer, Phys. Rev. B **52**, 10588 (1995).

[96] D. Xu, S. Yip, and J. Sauls, Phys. Rev. B **51**, 16233 (1995).

[97] S. H. Pan, J. P. O'Neal, R. L. Badzey, C. Chamon, H. Ding, J. R. Engelbrecht, Z. Wang, H. Eisaki, S. Uchida, A. K. Gupta, et al., Nature **413**, 282 (2001).

[98] P. Lee, Phys. Rev. Let. **71**, 1887 (1993).

[99] A. C. Durst and P. A. Lee, Phys. Rev. B **62**, 1270 (2000).

[100] D. Sheehy, T. Davis, and M. Franz, a detailed description of the theory in Ref. [35] (to be published).

[101] W. Kim, F. Marsiglio, and J. Carbotte, xxx.lanl.gov/archive/cond-mat/0307539 (2003).

[102] P. Hirschfeld, P. Wolfle, and D. Einzel, Phys. Rev. B **37**, 83 (1988).

[103] D. Bonn, S. Kamal, A. Bonakdarpour, R. Liang, W. Hardy, C. Homes, D. Basov, and T. Timusk, Proc. of the 21st Low Temp. Phys. Conf., Czech J. Phys. **46**, 3195 (1996).

[104] E. Hudson, K. Lang, V. Madhavan, S. Pan, H. Eisaki, S. Uchida, and J. Davis, Nature **411**, 920 (2001).

[105] S. Pan, E. Hudson, K. Lang, H. Eisaki, S. Uchida, and J. Davis, Nature **403**, 746 (2000).

[106] D. E. Sheehy, xxx.lanl.gov/archive/cond-mat/0303013 (2003).

[107] The reader should consult Ref. [14] for a very thorough summary of recent attempts to model FT-STS data.

[108] Z. Wang and P. A. Lee, Phys. Rev. Let. **89**, 217002 (2002).

[109] A. Polkovnikov, S. Sachdev, and M. Vojta, Phys. Rev. Let. **86**, 296 (2001).

[110] C. R. Cassanello and E. Fradkin, Phys. Rev. B **56**, 11246 (1997).

[111] R. Hill, C. Lupien, M. Sutherland, E. Boaknin, D. Hawthorn, C. Proust, F. Ronning, L. Taillefer, R. Liang, D. Bonn, et al., xxx.lanl.gov/archive/cond-mat/0307360 (2003), submitted to Phys.Rev.Lett.

[112] N. Nagaosa and P. A. Lee, Phys. Rev. Let. **79**, 3755 (1997).

[113] A. Hosseini, S. Kamal, D. Bonn, R. Liang, and W. Hardy, Phys. Rev. Let. **81**, 1298 (1998).

Appendix A

Surface Resistance Measurements at 75.4 *GHz*

The discussion in Chapter 3 explained how one can obtain values of R_s from measurements of Q via microwave cavity perturbation. However, as noted in Section 3.3, the measurement inherently involves an admixture of the surface resistance in two crystal directions because diamagnetic screening currents must traverse one of the in-plane directions across the broad $\widehat{ab}$ faces and along the $\hat{c}$-axis direction on the thin edges. Therefore, the prescribed technique results in measurements of either R_{sa} or R_{sb} with a slight admixture of R_{sc}. Nonetheless, one can disentangle the admixture of R_s from different crystal orientations through a series of carefully chosen experiments. Furthermore, one can also determine the background signals alluded to in Eq. 3.22 by altering the crystal geometry in an appropriate manner. The measurement procedure described herein was inspired by the work of Hosseini *et al.* [113] in which the authors successfully managed to extract R_{sc} by measuring R_{sb} before and after cleaving their $YBa_2Cu_3O_{6+x}$ sample parallel to the $\widehat{ac}$ plane.

This Appendix will begin with a description of measurements performed upon $YBa_2Cu_3O_{6.993}$ (overdoped), from which the surface resistance was successfully extracted. Finally, measurements performed upon $YBa_2Cu_3O_{6.5}$ (underdoped) will be presented and the reasons why they were deemed unreliable will be addressed.

A.1 Measurement Procedure: $YBa_2Cu_3O_{6.993}$

The first two measurements were performed on a single crystal of $YBa_2Cu_3O_{6.993}$ with dimensions $(x_a, x_b, x_c) = (380 \pm 6\,\mu m, 395 \pm 6\,\mu m, 23.3 \pm 2.3\,\mu m)$. In both cases the Q of the loaded (sample secured to sapphire plate with grease present) and the unloaded (sample, grease and sapphire removed) resonator were measured at each temperature. As implied by Eq. 3.22, the losses in the resonator are proportional to $1/Q$ and one can isolate the losses due to the superconducting sample and the background losses as follows:

$$M \equiv \left(\frac{1}{Q}\right)_{loaded} - \left(\frac{1}{Q}\right)_{unloaded} = \delta\left(\frac{1}{Q}\right)_{sc} + \delta\left(\frac{1}{Q}\right)_{bkgd} \tag{A.1}$$

The first measurements yielded an admixture of R_{sa} and R_{sc}. The sample was then rotated by 90° about the $\hat{c}$ axis, and measurements containing an admixture of R_{sb} and R_{sc} were obtained. The uncalibrated results may be expressed as follows:

$$M_{1a} = \delta\left(\frac{1}{Q}\right)_a + \delta\left(\frac{1}{Q}\right)_c + \delta\left(\frac{1}{Q}\right)_{bkgd} \tag{A.2}$$

$$M_{1b} = \delta\left(\frac{1}{Q}\right)_b + \gamma_c\,\delta\left(\frac{1}{Q}\right)_c + \delta\left(\frac{1}{Q}\right)_{bkgd} \tag{A.3}$$

The slight difference between the $\widehat{ac}$ and $\widehat{bc}$ surface areas on the edges of the sample is accounted for by the factor $\gamma_c = 0.96 \pm 0.02$.

The sample was then cleaved parallel to the $\widehat{bc}$ plane into 3 fragments and prepared for another $\hat{a}$-axis measurement. However, as shown in Fig. A.1, the screening currents must now traverse 6 $\widehat{bc}$ faces, which multiplies the $\hat{c}$ axis contribution to the loss by a factor of 3.

$$M_2 = \delta\left(\frac{1}{Q}\right)_a + 3\,\delta\left(\frac{1}{Q}\right)_c + \delta\left(\frac{1}{Q}\right)_{bkgd} \tag{A.4}$$

Finally, the largest of the three fragments was measured again in the $\hat{a}$-axis orientation. This portion of the crystal had dimensions $(x'_a, x'_b, x'_c) = (172 \pm 3\,\mu m, 395 \pm 6\,\mu m, 23.3 \pm 2.3\,\mu m)$, thus the $\widehat{ab}$ surface was $\gamma_a = 0.43 \pm 0.03$ of the area of the entire crystal. Assuming that the background signal was dominated by the sapphire and grease and therefore relatively independent of the change in sample size,

$$M_3 = \gamma_a\,\delta\left(\frac{1}{Q}\right)_a + \delta\left(\frac{1}{Q}\right)_c + \delta\left(\frac{1}{Q}\right)_{bkgd} \tag{A.5}$$

Equations A.2 → A.5 form a set of 4 independent equations for 4 unknowns. One can then simultaneously solve for the unknown quantities by diagonalizing a 4×4 matrix.

$$\delta\left(\frac{1}{Q}\right)_a = \frac{M_{1a} - M_3}{1 - \gamma_a} \tag{A.6}$$

$$\delta\left(\frac{1}{Q}\right)_b = M_{1b} - \gamma_c\,\delta\left(\frac{1}{Q}\right)_c - \delta\left(\frac{1}{Q}\right)_{bkgd} \tag{A.7}$$

$$\delta\left(\frac{1}{Q}\right)_c = \frac{M_2 - M_{1a}}{2} \tag{A.8}$$

$$\delta\left(\frac{1}{Q}\right)_{bkgd} = M_{1a} - \delta\left(\frac{1}{Q}\right)_a - \delta\left(\frac{1}{Q}\right)_c \tag{A.9}$$

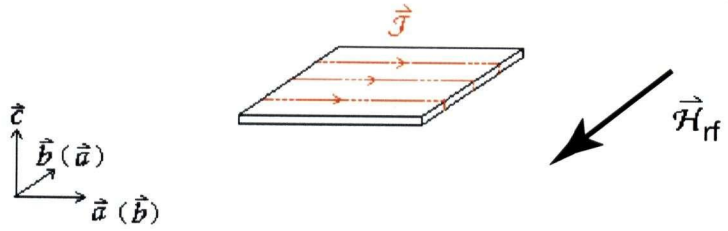

Geometry for measurement $\mathcal{M}_{1a}$ ($\mathcal{M}_{1b}$)

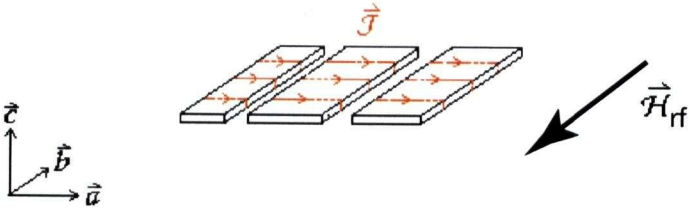

Geometry for measurement $\mathcal{M}_2$.

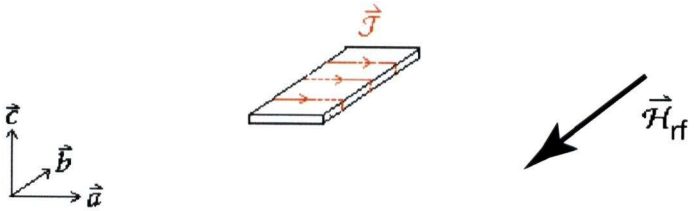

Geometry for measurement $\mathcal{M}_3$.

Figure A.1: A depiction of the measurement sequence for $YBa_2Cu_3O_{6.993}$. The first two measurements were performed upon a single piece of $YBa_2Cu_3O_{6.993}$ with crystal dimensions $(x_a, x_b, x_c) = (380 \pm 6\,\mu m, 395 \pm 6\,\mu m, 23.3 \pm 2.3\,\mu m)$. The crystal was rotated by 90^o about the $\hat{c}$-axis to obtain both $\hat{a}$ and $\hat{b}$ oriented measurements. The sample was then cleaved into three pieces and arranged for another $\hat{a}$-axis measurement, thus multiplying the $\hat{c}$-axis contribution by a factor of 3. Finally, the largest section of the crystal with dimensions $(x'_a, x'_b, x'_c) = (172 \pm 3\,\mu m, 395 \pm 6\,\mu m, 23.3 \pm 2.3\,\mu m)$ was measured.

The only remaining task is that of calibration, which was accomplished by measuring a sample of $Pb_{0.95}Sn_{0.05}$ alloy cut to $(x, y, z) = (442 \pm 7\,\mu m, 465 \pm 8\,\mu m, 20 \pm 3\,\mu m)$, which is approximately the same size as the $YBa_2Cu_3O_{6.993}$ crystal. The DC resistivity $\rho(T)$ of the calibration sample was determined independently by a four probe measurement and the normal state impedance at 75.4 *GHz* was calculated via the skin depth relation,

$$R_s(\Omega, T) = \sqrt{\mu_o\, \Omega\, \rho(T)/2}\,, \tag{A.10}$$

where Ω is the angular frequency in units of $rad \cdot s^{-1}$ and ρ has units of Ωm. The calibration constant was then determined by matching calculated values of $R_s(\Omega, T)$ with measurements of $\delta(1/Q)_{PbSn}$ over a broad temperature range by varying a multiplicative constant Γ such that $R_s(\Omega, T) = \Gamma\delta(1/Q)_{PbSn}$. This was accomplished by minimizing the function

$$\chi^2(\Gamma) = \sum_{i=1}^{N}\left(R_S(T_i) - \Gamma\,\delta\left(\frac{1}{Q}\right)_{PbSn}(T_i)\right)^2 \tag{A.11}$$

Geometric factors were calculated to account for the difference in surface areas between the $Pb_{0.95}Sn_{0.05}$ and $YBa_2Cu_3O_{6.993}$ samples. One can assume that the surface impedance of the $Pb_{0.95}Sn_{0.05}$ sample is isotropic and then scale Γ by the ratio of the total surface area of the $Pb_{0.95}Sn_{0.05}$ sample traversed by screening currents to the combined area of the two broad $\widehat{ab}$ faces of the $YBa_2Cu_3O_{6.993}$ sample to yield the calibration factor needed for both R_{sa} and R_{sb}.

$$R_{sa(b)} = \Gamma\frac{2(xy + yz)}{2x_a x_b}\,\delta\left(\frac{1}{Q}\right)_{a(b)} \tag{A.12}$$

Scaling Γ by the ratio of the total surface area of the $Pb_{0.95}Sn_{0.05}$ sample traversed by screening currents to the combined area of the two $\widehat{bc}$ edges of the $YBa_2Cu_3O_{6.993}$ sample yields the calibration factor needed for R_{sc}.

$$R_{sc} = \Gamma\frac{2(xy + yz)}{2x_b x_c}\,\delta\left(\frac{1}{Q}\right)_{c} \tag{A.13}$$

This procedure provides one with calibrated measurements of the surface impedance of $YBa_2Cu_3O_{6.993}$ in the three crystallographic orientations. Thus, by a careful measurement and cleaving programme one can account for all calibration factors and background signals.

A.2 Experimental Results: $YBa_2Cu_3O_{6.993}$

Figure A.2 displays the four measurements of $\delta(1/Q)$ prior to any data processing. Error bars have been neglected on these plots since the scatter in any measurement below 80 K proved to be less than 1%. Above 80 K the error estimates never exceeded 5%.

The individual $\hat{a}$, $\hat{b}$ and $\hat{c}$-axis contributions are depicted in the upper panel of Fig. A.3. Due to the use of the geometrical factor γ_a in Eqns. A.6 and A.8, the error estimates for $\delta(1/Q)_a$ and $\delta(1/Q)_c$ have increased to $\sim$ 5% at any point below 80K. The lower panel of Fig. A.3 displays the extracted background signal. Below 20 K, this quantity remains relatively constant at -5.5×10^{-9}, which is approximately the same size as the low temperature $\hat{c}$-axis signal. At 80 K the $\hat{c}$-axis signal exceeds the background by only a factor of 2. Therefore, $\delta(1/Q)_{bkgd}$ has a negligible effect upon measurements of $\delta(1/Q)_a$ and $\delta(1/Q)_b$, however it does complicate the extraction of $\delta(1/Q)_c$. Also shown in the lower panel of Fig. A.3 is a direct measurement of $\delta(1/Q)$ from sapphire with a minute quantity of grease. Note that this measurement yielded a positive signal, while the background signal extracted from the 4 sets of measurements is negative; a priori, one would expect these quantities to be the same. Therefore, the presence of a sample inside of the resonator alters the fields in a nonperturbative manner and the assumption that the background signal is only weakly dependent upon sample size may be questionable.

Figure A.4 displays the results of the $Pb_{0.95}Sn_{0.05}$ calibration procedure. The hollow circles represent the measured values of $\delta(1/Q)_{PbSn}$ multiplied by the fitting parameter $\Gamma = 1.72 \times 10^4 \pm 10\%$. The solid points connected by the curve represent the surface impedance calculated via Eq. A.10 from the independently measured values of $\rho(T)$. The 10% relative error in Γ due to uncertainty in the dimensions of the sample used to measure $\rho(T)$ far exceeds the error from any other measured quantity in this experiment. Thus, a more accurate means of obtaining $\rho(T)$ for the $Pb_{0.95}Sn_{0.05}$ sample is required. A critical point to note in Fig. A.4 is that at the lowest temperatures the surface resistance from $\delta(1/Q)_{PbSn}$ is reported as being negative, which is indicative of a nonperturbative background signal. The slight correction required to make these lowest points at least equal to zero has little effect upon the determination of Γ.

Subjecting the data in the upper panel of Fig. A.3 to Eqns. A.12 and A.13 then yields R_{sa}, R_{sb} and R_{sc}, as shown in Figure A.5. Representative error bars have also been included, which range from $\sim$ 10 $\rightarrow$ 14% over 1.7 to 80 K, but can be as large as 30% on $R_{S(c)}$ at 94 K. Recall that the experimental accuracy has been limited by errors in the measurement of sample dimensions - in particular x_c of the $YBa_2Cu_3O_{6.993}$ crystal and all dimensions of the $Pb_{0.95}Sn_{0.05}$ calibration sample used for the DC resistivity measurement.

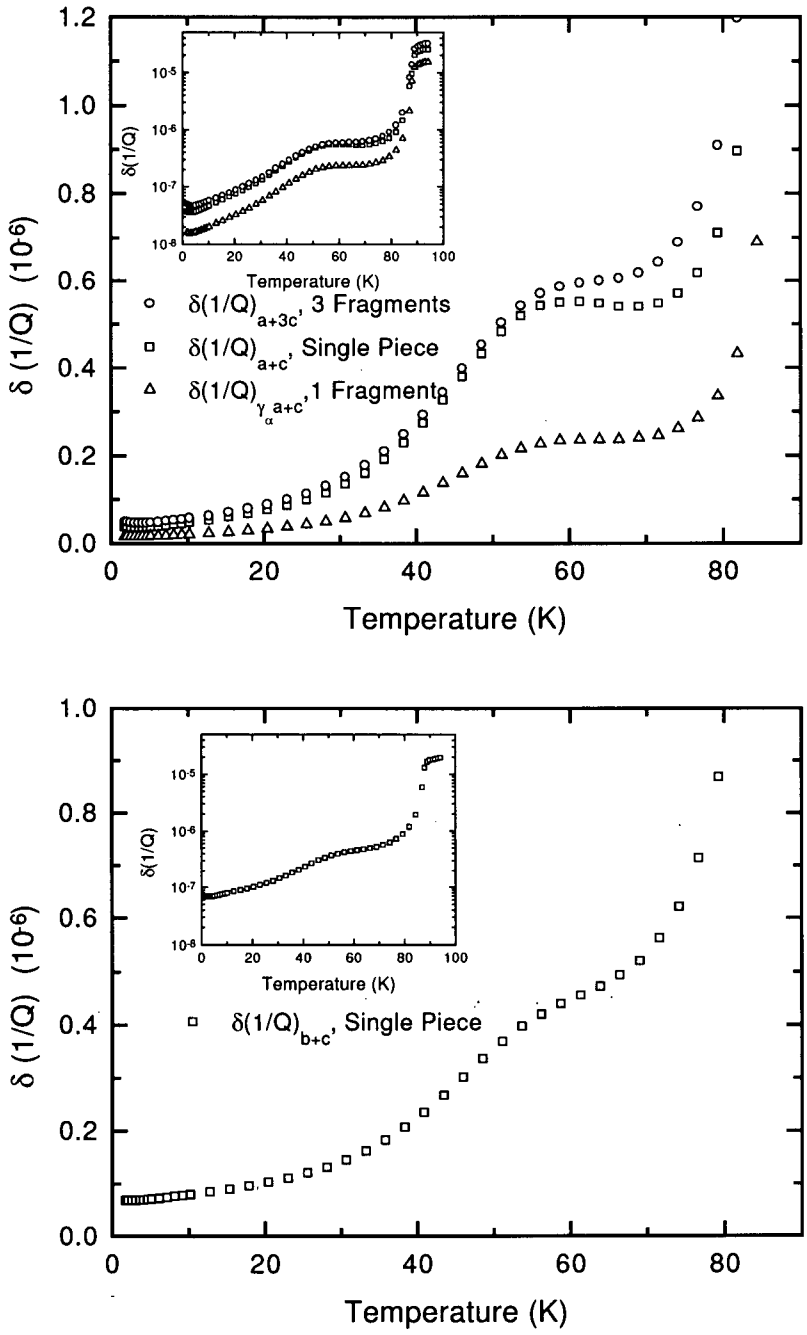

Figure A.2: Raw measurements on $YBa_2Cu_3O_{6.993}$ containing an admixture of $\hat{a}$ and $\hat{c}$-axis contributions (upper panel) and an admixture of $\hat{b}$ and $\hat{c}$-axis contributions (lower panel).

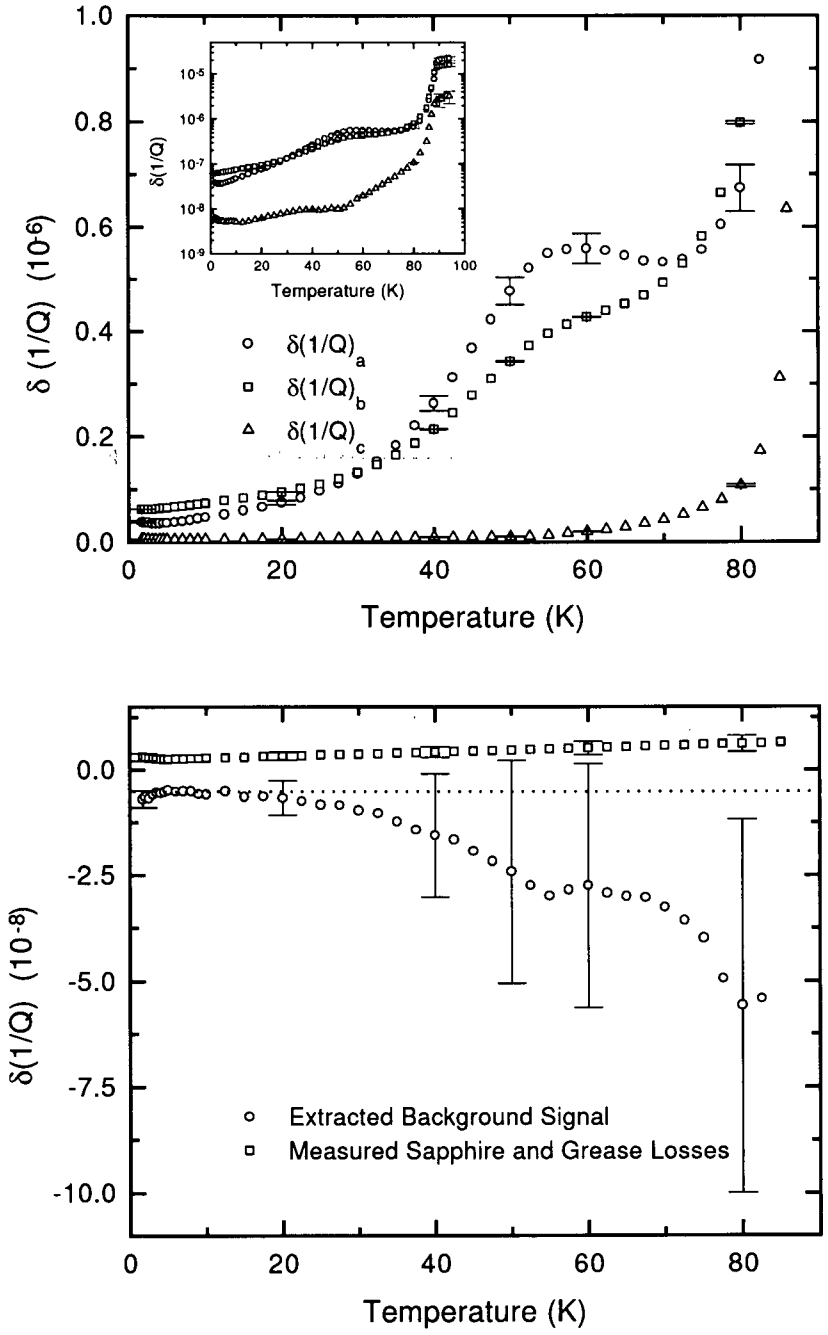

Figure A.3: The extracted losses for $YBa_2Cu_3O_{6.993}$: $\hat{a}$, $\hat{b}$ and $\hat{c}$-axis (upper panel) and background (lower panel). The lower panel also displays the directly measured losses due to the sapphire plate and the NonAq stopcock grease used to secure the sample. The dashed line indicates the low temperature nonperturbative correction $\sim -5.5 \times 10^{-9}$.

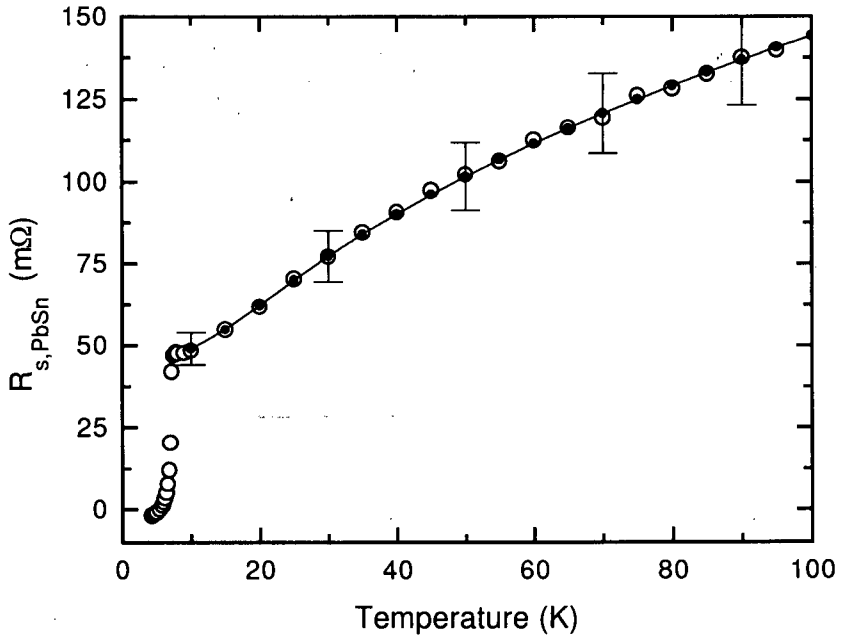

Figure A.4: Calibration of the 75.4 *GHz* apparatus using a $Pb_{0.95}Sn_{0.05}$ sample. The solid points connected by the curve represent the surface impedance calculated from the independently measured DC resistivity. The hollow circles represent $\Gamma \times \delta(1/Q)$, where $\Gamma = 1.72 \times 10^4$ was determined by a least squares fit as described in the text.

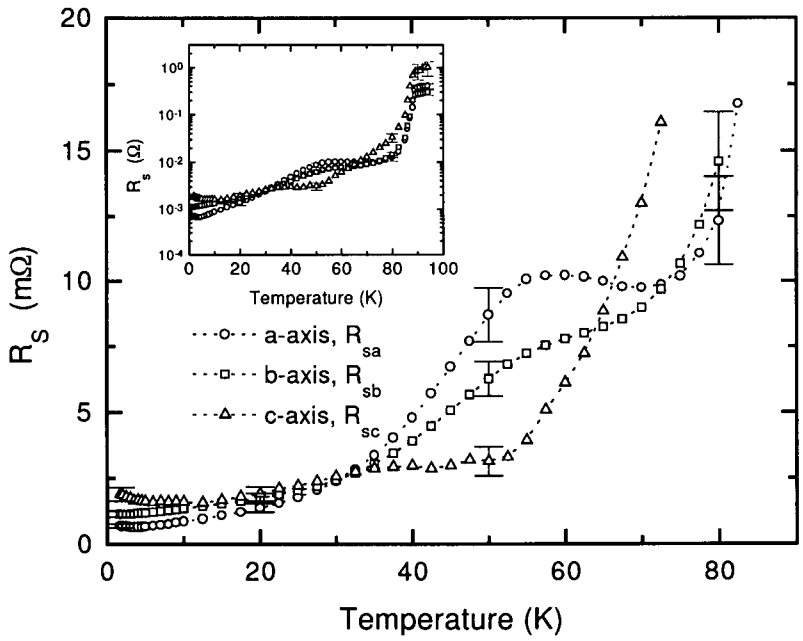

Figure A.5: The surface impedance of $YBa_2Cu_3O_{6.993}$ at 75.4 *GHz*.

A.3 Measurement Procedure: $YBa_2Cu_3O_{6.5}$

Measurements of the surface resistance of *Ortho-II* ordered $YBa_2Cu_3O_{6.5}$ were performed in a manner similar to that discussed in section A.1. However, matters were more complicated when measuring the underdoped compound due to the so called thin limit problem [58] in which the applied *rf* magnetic field penetrates into the sample on lengthscales comparable the the sample dimensions. In this scenario the interior of the sample is only partially screened form the applied fields and the effective surface resistance and surface reactance are reduced with respect to their true intrinsic values.

As a general guideline, one should always compare the sample thickness x_c to both the low temperature limit of the in-plane London penetration depth $\lambda_L^i(T \rightarrow 0)$ and the normal state skin depth just above the transition temperature, $\delta_i(T_c^+)$, where i denotes the direction of flow of the diamagnetic screening currents across the broad $\widehat{ab}$ faces of the sample, as depicted in Fig. 3.3. In the limit of local electrodynamics the skin depth above T_c can be expressed as follows:

$$\delta_i(T_c^+) \equiv \sqrt{\frac{2}{\mu_o \sigma_o(T_c^+)\Omega}} = \frac{2R_{si}(\Omega, T_c^+)}{\mu_o \Omega} \tag{A.14}$$

where $\sigma_o(T_c^+)$ is the normal state DC conductivity at temperature T_c^+. Roughly speaking the effective *rf* screening lengthscale will smoothly vary between λ_L^i at low temperatures and δ_i at high temperatures as oscillator strength is transferred between the quasiparticles and the superconducting condensate. Provided $\lambda_L^i, \delta_i \ll x_c$ then one can be assured that the thin limit is not a concern for $T < T_c$. The same arguments apply to the flow of screening currents in the $\hat{c}$-axis direction along the thin edges of a sample, as depicted in Fig. 3.3, except that one must now compare $\lambda_L^c(T \rightarrow 0)$ and $\delta_c(T_c^+)$ to the broad sample dimensions x_a and x_b.

A summary of London penetration depths and rough estimates for normal state skin depths just above T_c for $YBa_2Cu_3O_{6.5}$ and $YBa_2Cu_3O_{6.993}$ at 75.4 *GHz* is shown in Table A.1. Surface resistance measurements at 75.4 *GHz* have been used to generate $\delta_i(T_c^+)$ for the overdoped compound (see Fig. A.5). To obtain values of $\delta_i(T_c^+)$ at 75.4 *GHz* for the underdoped compound I have taken in-plane values of R_s at 22.7 *GHz* (see Fig. 3.15) to calculate the skin depth at that frequency and then scaled the results by $1/\sqrt{75.4/22.7} \sim 0.55$; this latter step should be valid if $\sigma_1(\Omega, T) \approx \sigma_o(T)$ (frequency independent) in the microwave region above T_c, which does appear to be the case from experiments. However, there were no reliable measurements of R_{sc} in the normal state for $YBa_2Cu_3O_{6.5}$ in existence at the time of writing. As one can see from Table A.1, the thin limit regime was kept at bay in the $YBa_2Cu_3O_{6.993}$ (overdoped) measurements by a wide margin. However, this was not to be the case with the $YBa_2Cu_3O_{6.5}$ (underdoped) measurements.

To begin describing the measurement procedure, the rationale for choosing particular sample geometries will be discussed. It has been learned from experience that samples with broad in-plane dimensions no greater than $\sim 500\,\mu m$ are best suited

Doping (x)	Direction	$\lambda_L(T \to 0)$ (μm)	$\delta(T_c^+)$ (μm)
0.5	$\hat{a}$	0.202	1.6
	$\hat{b}$	0.140	1.3
	$\hat{c}$	7.5	?
0.993	$\hat{a}$	0.101	1.3
	$\hat{b}$	0.078	1.0
	$\hat{c}$	0.66	3.4

Table A.1: A summary of screening lengthscales for $YBa_2Cu_3O_{6.5}$ and $YBa_2Cu_3O_{6.993}$ at 75.4 *GHz*. London penetration depth values are preliminary results from the Gd^{3+} ESR experiment and are current as of October 15, 2003 [74]. Skin depth values were determined from surface resistance measurements as described in the text.

for experiments with the 75.4 *GHz* apparatus because larger samples seem to generate substantial non-perturbative effects in the cavity. Furthermore it was observed that samples of $YBa_2Cu_3O_{6.5}$ of thickness greater than $\sim 20\,\mu m$ were too lossy to measure with this apparatus, presumably due to a very large R_{sc} as compared to the overdoped compound. The above considerations thus established the upper bounds on the dimensions of candidate samples. The lower bounds were established by considering the lengthscales presented in Table A.1 and multiplying them by a nominal factor of 10; thus the minimum allowable thickness was determined to be roughly $x_c \sim 10 \times 1.5\,\mu m = 15\,\mu m$. All that was known at the time of measurement concerning $\hat{c}$-axis electrodynamics was that both λ_L^c and δ_c would be large, with the best estimate of the London penetration depth being $\lambda_L^c(T \to 0) \sim 20\,\mu m$ at the time. As such, the absolute minimum allowable broad dimension would be $(x_a, x_b) \sim 200\,\mu m$. However the general trend in Table A.1 is that δ_i is crudely an order of magnitude greater than the corresponding value of λ_L^i, so it was inevitable that $YBa_2Cu_3O_{6.5}$ samples with broad dimensions less than $500\,\mu m$ would enter the thin limit regime at some temperature below T_c.

A series of samples were cleaved from a detwinned single crystal of *Ortho-II* ordered $YBa_2Cu_3O_{6.5}$ that was $14 \pm 2\,\mu m$ thick. These were placed in the 75.4 *GHz* apparatus in the geometry of Fig. 3.3, thus providing measurements containing an admixture of in-plane and $\hat{c}$-axis surface resistance. A summary of sample dimensions and directions of flow for diamagnetic screening currents for a selected subset of the measurements is shown in Table A.2.

It will be assumed that $\delta(1/Q)_{bkgd} \approx -5.5 \times 10^{-9}$ for all measurments, as ascertained from the measurements on the overdoped compound (see lower panel of Fig. A.3). Therefore, there are only two unknowns in measurements 1,4 and 8: $\delta(1/Q)_a$ and $\delta(1/Q)_c$. The uncalibrated results (minus the background) can then be expressed as follows:

$$M_1 = \delta\left(\frac{1}{Q}\right)_a + \delta\left(\frac{1}{Q}\right)_c \tag{A.15}$$

Measurement	Direction	x_a (μm)	x_b (μm)	x_c (μm)
1	$\hat{a}$	370 ± 6	170 ± 6	14 ± 2
4	$\hat{a}$	160 ± 6	190 ± 6	14 ± 2
7	$\hat{b}$	280 ± 6	170 ± 6	14 ± 2
8	$\hat{a}$	140 ± 6	170 ± 6	14 ± 2
9	$\hat{b}$	140 ± 6	170 ± 6	14 ± 2

Table A.2: Summary of sample dimensions for selected $YBa_2Cu_3O_{6.5}$ surface resistance measurements. Measurement number is for cataloguing purposes and Direction indicates that in which diamagnetic screening currents flowed across the broad $\widehat{ab}$ faces of the sample.

$$M_\alpha = \gamma_{a,\alpha}\,\delta\left(\frac{1}{Q}\right)_a + \gamma_{c,\alpha}\,\delta\left(\frac{1}{Q}\right)_c \tag{A.16}$$

where $\alpha \in \{4, 8\}$ and the scale factors $(\gamma_{a,\alpha}, \gamma_{c,\alpha})$ are the ratios of the $(\widehat{ab}, \widehat{bc})$ surface areas of Measurement α to those of Measurement 1. Taking either of the two possible combinations of the former measurements with Measurement 1 allows one to determine the unknown quantities:

$$\delta\left(\frac{1}{Q}\right)_a = \frac{\gamma_{c,\alpha} M_1 - M_\alpha}{\gamma_{c,\alpha} - \gamma_{a,\alpha}} \tag{A.17}$$

$$\delta\left(\frac{1}{Q}\right)_c = \frac{M_\alpha - \gamma_{a,\alpha} M_1}{\gamma_{c,\alpha} - \gamma_{a,\alpha}} \tag{A.18}$$

Measurements 7 and 9 are likewise a combination of two unknowns: $\delta(1/Q)_b$ and $\delta(1/Q)_c$. The uncalibrated results (minus the background) can then be expressed as follows:

$$M_\beta = \gamma_{b,\beta}\,\delta\left(\frac{1}{Q}\right)_b + \gamma_{c,\beta}\,\delta\left(\frac{1}{Q}\right)_c \tag{A.19}$$

where $\beta \in \{7, 9\}$ and the scale factors $(\gamma_{b,\beta}, \gamma_{c,\beta})$ are the ratios of the $(\widehat{ab}, \widehat{ac})$ surface areas of Measurement β to those of Measurement 1. Since $\delta(1/Q)_c$ can be obtained from Eq. A.18, then one can isolate $\delta(1/Q)_b$ accordingly:

$$\delta\left(\frac{1}{Q}\right)_b = \frac{1}{\gamma_{b,\beta}}\left(M_\beta - \gamma_{c,\beta}\,\delta\left(\frac{1}{Q}\right)_c\right) . \tag{A.20}$$

Finally, calibrated values of the surface resistance can be obtained via Eqns. A.12 and A.13 with the dimensions (x_a, x_b, x_c) equal to those of the sample used in Measurement 1 (see Table A.2).

A.4 Experimental Results: $YBa_2Cu_3O_{6.5}$

The measured values of $\delta(1/Q)$ (corrected for the background term $\delta(1/Q)_{bkgd} = -5.5 \times 10^{-9}$) are shown in Fig. A.6. The subset of measurements shown herein were those in which unexplained background losses were at least minimized, and therefore provided the most promising opportunites to extract the intrinsic losses of the superconducting samples. Measurements 1,4 and 8 were then used to determine $\delta(1/Q)_a$ and $\delta(1/Q)_c$, as per Eqns. A.17 and A.18, respectively. The results are shown in Fig. A.7. Note that the two $\hat{a}$-axis results are in agreement below $T_c \approx 55\,K$ but differ significantly above the superconducting transition. This is the first sign of trouble. The $\hat{c}$-axis results point to even more severe problems at lower temperatures since one of the attempts to extract $\delta(1/Q)_c$ appears to fail for $T \gtrsim 40\,K$. Fortunately there is reasonable agreement at lower temperatures. Thus $T \sim 40\,K$ must be recognized as an upper limit on T for which the data analysis presented herein can be considered reliable.

To extract $\delta(1/Q)_b$ via Eq. A.20 it has been assumed that $\delta(1/Q)_c$, as obtained from Measurements 1 and 4, will suffice. The results are shown in Fig. A.8. It is evident that the results from using Measurements 7 and 9 disagree over a broad temperature range. However, it appears that the results obtained using Measurement 9 differ from those obtained using Measurement 7 by an additive constant below $\sim 40\,K$. Since the dimensions x_b and x_c are the same for both measurements then this discrepancy cannot be blamed upon thin limit problems. Given that it is difficult to imagine how one could err in having *less* loss in a measurement, it is suspected that Measurement 9 has a systematic error in the background signal for which the data have not been properly corrected. Therefore, the results obtained using Measurement 7 must be viewed as the most reliable. However, the reader is reminded that the extraction of $\delta(1/Q)_b$ is very dependent upon knowing $\delta(1/Q)_c$, which is not to be trusted above $\sim 40\,K$.

The calibrated surface resistance of *Ortho-II* ordered $YBa_2Cu_3O_{6.5}$ at $75.4\,GHz$ is shown in Fig. A.9. Error bars have been shown at a few select points that account for the statistical scatter in the measurements, uncertainties in the various geometric factors in Eqns. A.17 - A.20 and the $\sim 10\%$ systematic error in the overall multiplicative calibration factor. These errors account for neither the uncertainty in the background $\delta(1/Q)_{bkgd}$ nor are they indicative of the author's confidence in avoiding the thin limit regime. Nonetheless, it will be reiterated that these date are certainly suspect for $T \gtrsim 40\,K$. Interestingly these data also suggest that $R_{sa} > R_{sb}$ over the entire measured temperature range. This is certainly unexpected and may very well stem from a misidentification of the crystalline axes. The standard means of determining the in-plane crystalline orientation for a microwave spectroscopy sample is to compare it to a detwinned single crystal with known orientation under polarized light, as shown in Fig. 3.2. Under such conditions there is generally some weak but discernable contrast in the colour of the two crystals if their $\hat{a}$-axes are not aligned parallel. It is conceivable (but unlikely according to this author's records) that there was an error in the identification of the crystal orientation.

The primary interest of the microwave spectroscopy programme in the UBC superconductivity laboratory at the time when these measurements were being taken was in order parameter phase fluctuations near T_c. Consequently, there was significant emphasis placed upon obtaining high temperature data. Since the 75.4 *GHz* apparatus failed to yield reliable data near T_c (presumably due to $\delta_c(T_c^+)$ being some sizeable fraction of the broad sample dimensions) then this author decided that any further measurments on underdoped $YBa_2Cu_3O_{6+x}$ samples at high microwave frequencies warranted the development of a new experimental approach that could circumvent the need to flow screening currents along the $\hat{c}$-axis oriented edges of a sample. The tasks of designing and constructing a new quasioptical millimeter wave apparatus were then taken on by this author. The construction of this new apparatus is an on-going project as of October 2003.

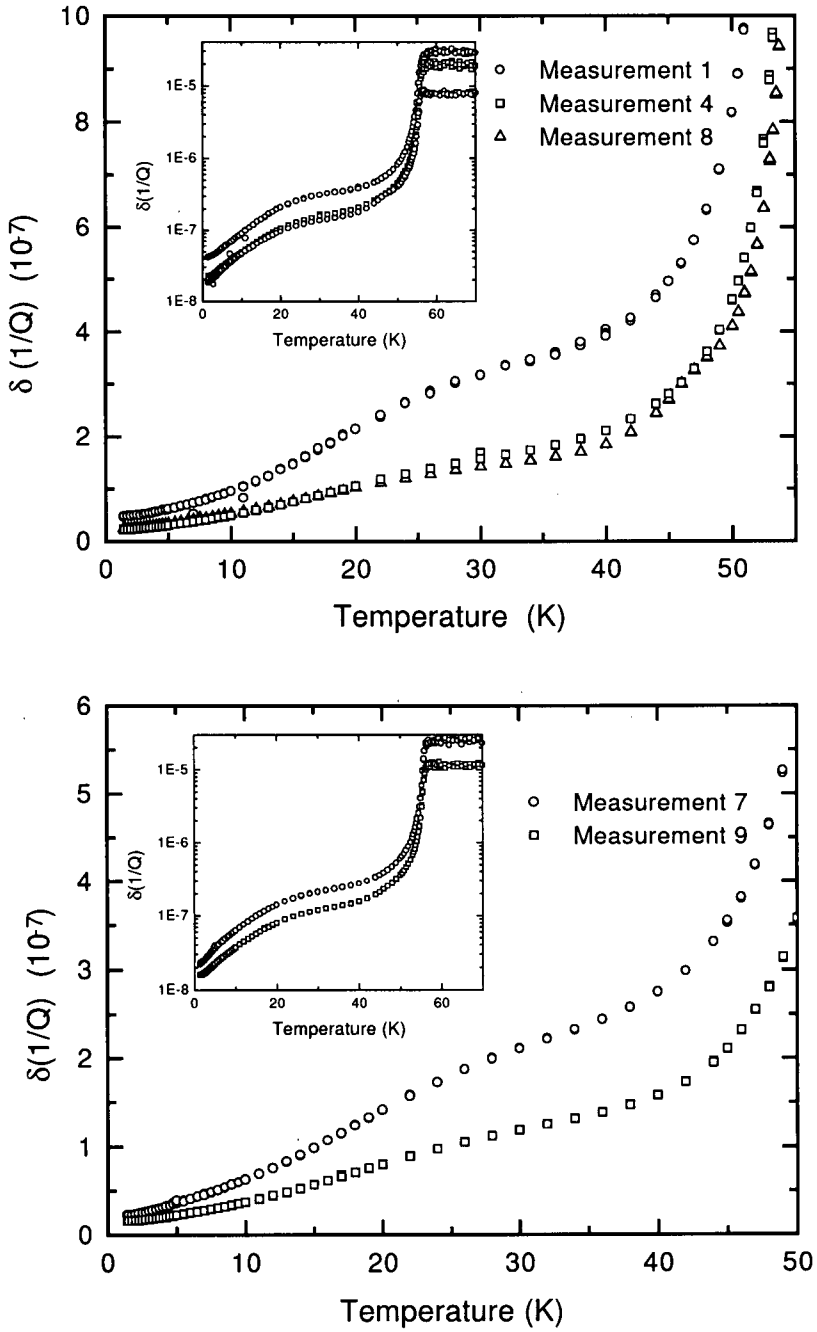

Figure A.6: Raw measurements (minus $\delta(1/Q)_{bkgd}$) on $YBa_2Cu_3O_{6.5}$ containing an admixture of $\hat{a}$ and $\hat{c}$-axis contributions (upper panel) and an admixture of $\hat{b}$ and $\hat{c}$-axis contributions (lower panel).

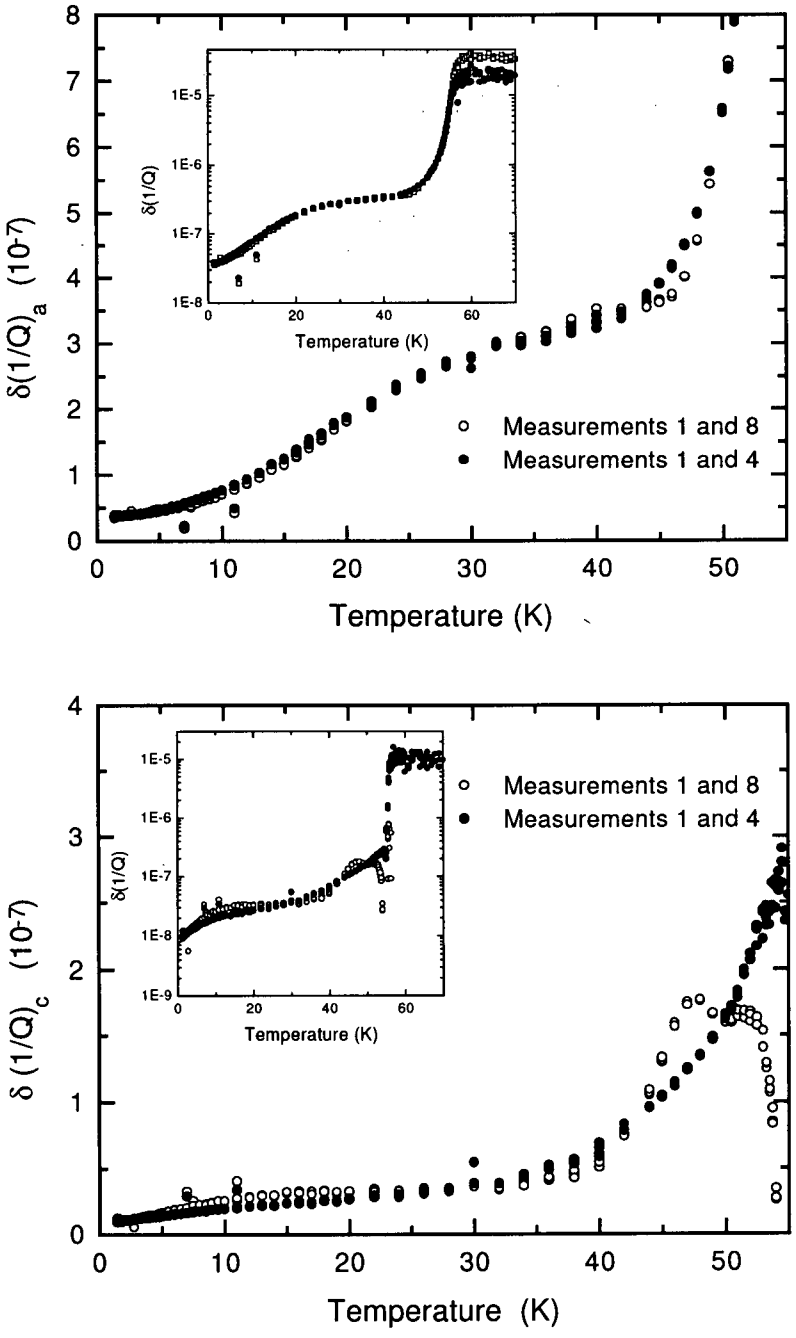

Figure A.7: The extracted losses for $YBa_2Cu_3O_{6.5}$: $\hat{a}$ (upper panel) and $\hat{c}$-axis (lower panel).

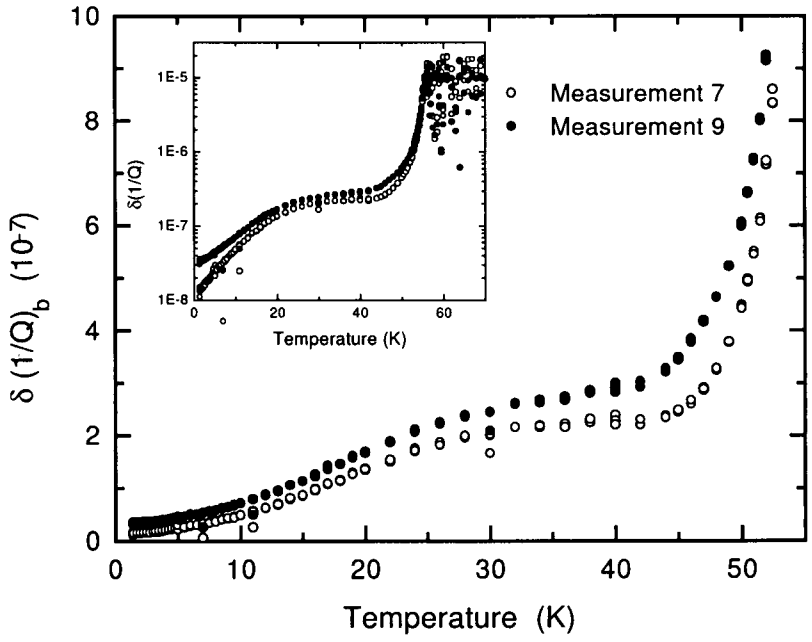

Figure A.8: The extracted $\hat{b}$-axis losses for $YBa_2Cu_3O_{6.5}$.

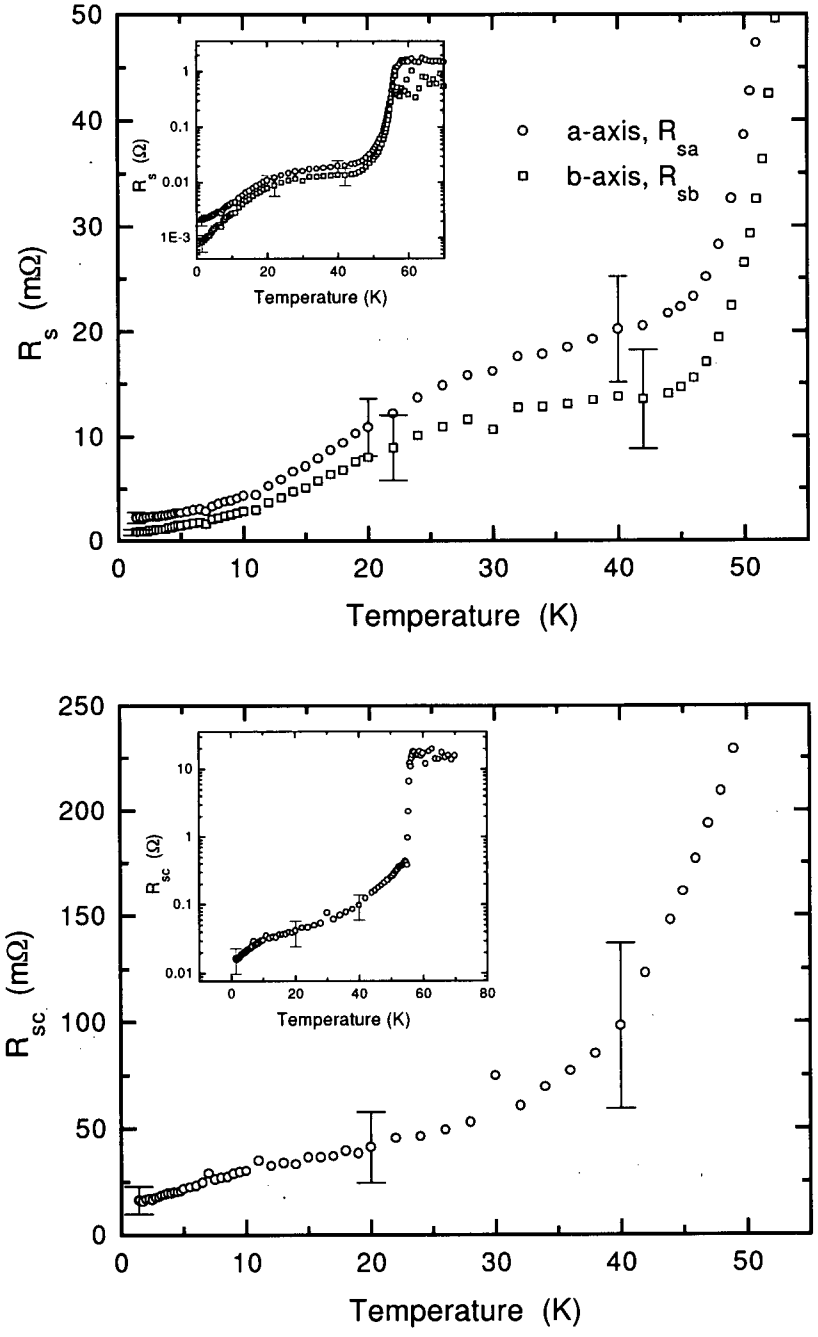

Figure A.9: The surface impedance of $YBa_2Cu_3O_{6.5}$ at 75.4 *GHz*: $\hat{a}$ and $\hat{b}$-axis (upper panel) and $\hat{c}$-axis (lower panel).